Università degli Studi di Udine

DOTTORATO DI RICERCA IN INGEGNERIA INDUSTRIALE
E DELL'INFORMAZIONE

TESI DI DOTTORATO DI RICERCA

Permanent Magnet Synchronous Motors Control: Sensorless and Field-Weakening Operation

Relatore:
Prof. Roberto Petrella

Dottorando:
Ing. Sandro Calligaro

Anno Accademico 2011-2012

"Theory is when we know everything but nothing works.
Praxis is when everything works but we do not know why.
We always end up by combining theory with praxis:
nothing works and we do not know why."

Albert Einstein (maybe)

Abstract

The Permanent Magnet Synchronous Motor (PMSM) has been adopted since the 1980s, mainly in low and medium power high-accuracy servo drives, thanks to its high power density. Moreover, the possibility of using powerful digital controllers has allowed to exploit its inherent accuracy in torque production. In the recent years, industry has shown a renewed interest in this class of machines, mainly related to the higher efficiency achievable with respect to other kinds of motor. In fact, following an increasing trend in the energy cost, the higher initial cost represented by the purchase and installation of a PMSM with respect to typical solutions (e.g. induction and DC) has started to be covered by the lifetime consumption. This, together with the improved environmental consciousness, opened the way to new applications, characterized by lower accuracy and slower dynamics, where different requirements are set, like lower production and maintenance costs, higher reliability, energy-optimized control and wider speed ranges. Among these applications, industrial ones are maybe the most relevant (e.g. fans and pumps), while emerging ones are electric and hybrid vehicles and home appliances. The impact of the adoption of these machines could be very important in the future, as most of the electrical energy consumption at present is represented by relatively low-efficiency motors, and even few percentage units of increased efficiency would lead to huge savings.

This thesis describes the work in the years 2010-2012, during the PhD course at the Electric Drives Laboratory of the University of Udine. The topics studied are mainly two, both regarding the digital control of electric drives for Permanent Magnet Synchronous Motors (PMSMs): the sensorless control and the flux-weakening control. Although the two topics have been an object of the research in electric drives for many years, and a strong development has started from that research, still many issues are open, and the industrial need for higher performances and efficiency of these drives keeps posing interesting challenges to researchers worldwide.

"Sensorless control" is the name under which the motor control techniques aiming at the avoiding the use of mechanical sensors usually adopted. For the case of PMSM, different techniques have been considered, and some improvements have been proposed both to the analytical approach and to the techniques adopted.

Different flux-weakening control feedback schemes have been compared, and a proposal for the non-linearity compensation of the loop dynamics has been proposed for a class of these, mainly applicable to Interior-PMSM.

A perspective on the practical implementation issues has been kept all over the work, favoring simpler schemes with the less possible parameter dependence, in order to avoid the need for extensive off-line tests on the single machine.

Table of contents

Chapter 1
Introduction

Permanent Magnet Synchronous Motors (PMSMs) have been adopted, since the 1980s, in precision servo systems or applications characterized by high dynamic requirements. Although their principle of operation was known since decades before, it was only with the discovery of rare-earth magnetic materials (in the 1980s) and the introduction of relatively low-cost digital controllers and power electronic devices, that the use of PMSMs started to be quite common in the automation industry. They are known for their inherent high-efficiency, high-accuracy torque characteristics and high power/torque density with respect to other motor classes. Their relatively high production cost is one of the reasons that have historically limited their diffusion. One other reason can be identified in the fact they need more complex controllers, even for achieving a very basic motion control. More specifically, beyond the algorithms complexity, the Permanent Magnet (PM) axis position information is needed, which represents an important issue. Since the added cost and reduced reliability related to the use of a position sensor, research on the so-called "*sensorless control*" has been carried on with the aim of operating synchronous motors without any mechanical sensors.

In the last years many factors, energy cost increase, availability of powerful controllers and environmental consciousness among them, have renewed the industry and academic research interest on PMSMs. Besides their mature application to machine automation applications, some other fields, for which PMSMs were not considered in the past, are now emerging. Home appliances are an excellent example: in some cases, while the requirements regarding dynamic and accuracy performances are usually not very high, the cost, efficiency and power density targets have become very stringent. Since many devices are nowadays being equipped with an electronic controller, this makes it possible to integrate the motor control, reducing the associated cost. Moreover, it has been demonstrated

that, especially for large power machines, the initial cost for a motor purchase and installation is only a small part of the overall lifetime cost, being energy consumption and maintenance the largest components. This rather important change in the cost perspective allows more sophisticated and expensive solutions to be applied, in order to achieve reduced power losses and lower maintenance requirements (which calls for a higher reliability).

Another quite recent trend related to environmental reasons and energy cost increase is the demand of renewable energy production, where an important role is played by wind power generators. Also in this case, the highest power density and efficiency is achieved by means of PMSMs.

The Automotive traction is one of the fields where perhaps the most important innovation massively involving PMSMs electric drives is happening. Although some hybrid and electrical solutions have been in the market since the 1990s, the technology (which also covers many other technical fields) is only now reaching a maturity point that will make it possible for this kind vehicles to be present on the mass market. Also in this case, the capability to achieve high power density and efficiency is a key factor, since the need to accommodate the system in constrained spaces, to reduce the vehicle inertia and to manage the stored energy in the best way possible. Besides the possible future developments, the PMSM is already adopted in some conventional internal combustion powered vehicles, with the function of Integrated Starter Alternator (ISA).

Many of the new applications of the PMSM have in common the requirements of a relatively large operating speed range. This is especially true for electric and hybrid powertrain and some home appliances. Some peculiar issues arise, where low supply voltage is available (e.g. in battery operated drives) or in the case particularly high speeds must be reached. Proper techniques, which go under the name of "flux-weakening" or "field-weakening" control, need to be adopted, and depending on the method different dynamical and steady-state performances can be achieved in terms of maximum torque vs. speed, control response times, current ripples or efficiency.

From the control point of view, many interesting research topics are still open. In this thesis, most of the work has been devoted to some techniques for sensorless control of PMSMs, and to the high-speed operation, where "*flux-weakening*"

methods must be adopted to overcome the issues related to the phase voltage limitation imposed by the limited supply voltage.

1.1 Efficiency regulation and demand

Recently, the increasing cost of energy and the consciousness of environmental problems related energy production have driven both market and regulatory authorities in the direction of improving the systems efficiency. In particular, the electric area is a good candidate for energy consumption reduction for many reasons. As a first aspect, a large portion of the whole energy demand is due to conversion into electric energy, since its easy transportation and versatility. It is worth noting that, in average, the present efficiency in the production and delivery of electric energy is quite low (nearly 40%). This makes losses reduction in electric energy utilization a key factor, since the multiplication ratio that causes energy need at the source. Moreover, the high levels of efficiency already achievable by proper electric design and manufacturing and the opportunities of improvement due to the fast technological development let us forecast the reach of further important efficiency goals for the future. The exploitation of renewable energy is also becoming an important factor in the reduction of air pollution, greenhouse gases and dependence on fossil sources.

Motion generation from electrical energy is a very important application, looking at the energy volumes involved. For example, according to a study from the US Department of Energy [1], more than half of the electrical energy consumed in the United States is used by electric motors. In particular, motors convert nearly 70% of all electric energy industrial demand, with industry using 20% of the total amount. Hence, efficiency in electrical to mechanical energy conversion, especially in the industrial field, has a very important impact, and could result in considerable environmental advantages and economical savings. For these reasons, USA and the European Union have recently enforced new regulations for new

motor installations of medium to high-power, which set higher minimum efficiency levels and define efficiency classes. Also from the user point of view, the energy cost associated to the operation of a medium-power motor during a single year is usually many times greater than its initial purchase price. This arguments justify the research efforts aiming at reducing power losses, even at the expense of more sophisticated or expensive motors and driving devices.

One of the technological and economic factors that, quantitatively, will probably have the largest impact on energy consumption in the near future is the electrification of transportation, that is slowly starting in these years. In fact the energy consumption for transportation represents around 20% of the global world primary energy demand and, moreover, it must be noticed that, internal combustion engines, largely the most common powertrain have peak thermal efficiency levels that reach (for optimized two-stroke large ship Diesel engines) about 50%, while land transportation engines have much lower efficiency. The strong dependence on speed and load operating conditions, the idle losses and the exclusively dissipative braking lead to much worse results, on a typical drive cycle. After a quite long marginal history of electric and hybrid cars, in 1997 Toyota, a major Japanese car manufacturer, introduced to the market the Prius model, a modern hybrid gasoline-electric car. The relatively large success of this car is probably opening the way to a massive introduction of electric and hybrid models in the near future, and has already stimulated an important research in the fields involved in the development of these cars. From the point of view of potentialities, besides the very high difference in efficiency (both peak and at the various operating conditions), the absence of idle losses and the bidirectional conversion capability (regenerative braking) offered by electric powertrain are out of reach for combustion engines, thus electrification of transportation could lead to large energy savings.

Maybe the most important obstacle to the improvements in energy efficiency is represented by the investments needed for the installation of new plants and devices and the substitution of inefficient existing ones. As mentioned, the increasing cost of energy and technological development is rapidly reducing return times for large power. For lower power applications, the efficiency demand is related both to economic and environmental reasons, where the second ones are recently becoming a market driving factor (especially in consumer goods).

In this scenario, the importance of electric motors and of their control techniques is evident, since they are involved in many of the energy optimization or generation innovations that are taking place. Since the inherent advantages in energetic efficiency and power density offered by PMSMs, an increment in their diffusion can be expected in the near future. In fact, despite their higher initial cost, if the whole lifetime power consumption (motor lifetime is about 20 years on average) and maintenance is taken into account, which represents typically the largest part of the expenses associated to a large electrical motor, in some applications the adoption of PMSMs can be convenient with respect to the induction competitor. As an example, in a study published on the IEEE Industry Applications Magazine ([2]), the energy costs for the operation of a cooling tower fan (about 30 kW motor power) were compared between the case of a classical gearbox-coupled induction motor and an innovative PMSM direct-drive solution. The results, shown in Table 1.1, demonstrated that annual savings can be consistent even for non-continuous duty.

Table 1.1. Cooling tower fan drive case study, annual energy cost savings [US$] adopting direct-drive PMSM with respect to gearbox-coupled line-start induction motor.

Application	Hours/day	Full vs. half speed duty-cycle		
		100% - 0%	75% - 25%	50% - 50%
Petrochemical	24	3,154	2,488	1,822
Hospital	18	2,365	1,866	1,367
University	12	1,577	1,244	911

Fig. 1.1. Industrial cooling towers in a power plant.

According to the report [3], both in Industrial and Tertiary sectors fans, pumps and compressors (see Fig. 1.1) are by far the main electrical loads, accounting for 62% and 66% of the motor electricity consumption, respectively. Since these applications usually have low dynamics and low accuracy requirements, PMSMs could be profitably adopted also with simple sensorless control techniques, while nowadays the largest majority of these applications are covered by induction motors. The sure advantages of asynchronous motors (line-start capability among them) could however become less important since the increasing cost of energy and the decreasing cost of power converters and controllers. In fact, both pumps and fans usually represent a peculiar load, which make it possible to achieve large power savings if operation on larger duty-cycle at intermediate speeds is imposed instead of shorter running periods at high speeds.

In medium-low power civil applications such as HVAC (Heat, Ventilation, Air Conditioning), the particular characteristics of the load (from the thermodynamical point of view) make it particularly convenient to vary the operating speed in a continuous manner (rather than operating in on-off), thus the use of Adjustable Speed Drives (ASD) cannot be avoided. In this case, the switch to PM brushless motors has already happened in the past years, demonstrating that these cost-effective, efficient and reliable solutions can be widely adopted in industry.

1.2 Classification of the most common electric motors

Among the many electric motor working principles and geometries, few of them have dominated the scene till now. Some classes of motors, despite being built in large numbers, have a very limited application field. This is for example the case of some very small power synchronous motors like single-phase AC synchronous motors and other timing motors, like those used in electro-mechanical energy meters. In this work, the focus will be of course on Permanent Magnet Synchronous Motors, but introducing their main "competitors" can be useful to understand the importance of some aspects like efficiency, accuracy and control complexity.

1.2.1 Induction motors

Induction motors are the actual workhorse of industry, converting approximately 70–80% of all electrical energy to mechanical. Their structure is quite simple, their manufacturing relies on commonly available materials (copper, steel, aluminum), and their diffusion has led to a deep engineering effort through many years of production. However, only in the last decades magnetic and thermal Finite Element Method (FEM) simulations helped the design improvement.

Their large success is due to the capability of operation from a fixed-frequency and fixed-voltage line. In fact, three phase motors are able to be started and kept at a quite accurate speed by just connecting them to the grid line, since they tend to rotate in synchronism with the supply voltage, showing a self-regulating characteristic in speed (i.e. null torque at synchronism speed and negative slope in its neighborhood).

On the other hand, induction motors, with respect to their competitors (i.e. PM brushless motors) show poorer dynamic performances and efficiency, and achieving an accurate control of their speed or position is more difficult than with DC or PMSM motors, since the impossibility to exactly know the rotor field.

Variable speed drives for induction motors have been commercially available since the 1970s, and also sensorless control is nowadays a mature technology, but the research on some topics, like dynamic response improvement and operation at very low-speed is still active.

1.2.2 DC motors

Direct Current motors have been widely used in those applications where variable speed, high power density operation is needed, or in those where only DC sources are available (e.g. battery powered). DC motors can be classified in two major classes, depending on the kind of stator field excitation, which can be either from a permanent magnet or winding. Usually, low-power DC motors are provided with magnet excitation, while large size ones rely on a field generating winding, since manufacturing and cost issues related to large permanent magnets. The first class provides relatively high power density and efficiency, while the second offer a second degree of freedom for regulation.

They allow an easy control, since steady-state speed is in first approximation determined by armature supply voltage, and torque is proportional to field and armature current. The major disadvantage of DC motors is the need for a slip ring, which also acts as a commutator, supplying the correct winding depending on position. The commonly used devices for slip ring connection, called brushes, are subject to wear (causing added reliability issues and maintenance costs), produce sparks and dust, besides causing quite important friction and vibrations, which deteriorate the motion performances of the motor.

1.2.3 Synchronous motors

Among the synchronous motors, different classes can be distinguished for construction and torque generation principle. While PMSMs and wound rotor synchronous machines (typically used as generators) rely on the interaction between flux provided by the rotor and (by means of a permanent magnet or

orientated winding) and stator current, torque in Synchronous Reluctance Motors (SRMs) is due to the presence of minimum reluctance paths in the rotor, and the rotor field is provided by stator windings only. However, some motors, like IPMSMs, can resemble both the rotor characteristics of the PMSM and SRM, and thus can produce torque according to both the two operation principles.

Permanent Magnet Synchronous Motors (PMSMs) are a wide class of machines, mainly known as "brushless motors", although this term hardly describes their peculiarities. In fact, besides the absence of brushes, which is also common to AC induction and reluctance machines, the presence of permanent magnets in the rotor is the main difference with respect to other brushless machines. Although in this work sinusoidal flux-linkage is considered, other shapes of the field can be obtained, e.g. in the case of Brush-Less DC (BLDC) motors, where a trapezoidal back-EMF is considered, thus allowing, ideally, a constant torque to be obtained by driving piecewise constant currents in the stator windings. These machines have wide use in low-demanding applications, where torque ripple and dynamical performances are not critical. However, modeling of these machines usually is conducted by using similar analytical tools as for the case of sinusoidal machines. It is also worth mentioning that the very common hybrid stepper motors can be, under some approximations, considered as two-phase PMSMs, and can represent for some applications a viable low-cost alternative.

With respect to induction and variable reluctance motors, the use of permanent magnets allows to obtain rotor induced flux-linkage on the stator avoiding the losses associated with additional currents for rotor flux generation. This simple peculiarity is fundamental, since it determines the higher efficiency and power density achievable by this kind of motors, especially with respect to induction ones. Motors offering combinations of reluctance torque and PM torque (Interior Permanent Magnet Synchronous Motors, IPMSMs or PM-Assisted Synchronous Reluctance Motors, PMASR) can achieve even higher torque densities at high efficiency levels.

Another important characteristic of PMSMs is that since rotor field is due to the rotor mounted PMs (mechanically bound in fixed positions), PM flux can be accurately known from the mechanical rotor position. For sinusoidal PMSMs (i.e. those in which flux-linkage is sinusoidally distributed), this means that, if the rotor magnetic axis angular position is correctly known, the generated torque is proportional to the orthogonal component of the current vector, and so an accurate

torque control can be achieved. For this reason, PMSMs have been used since the 80s (when rare-earth magnets were discovered) in low-power automation applications where high precision is required, and especially for position servo control.

The use of permanent magnets in the construction of electrical machines brings the following advantages:

- The field excitation requires no power absorption from the supply, thus eliminating the related losses
- A higher power (and torque) density can be achieved with respect to electromagnetic excitation machines, leading to better dynamic performances
- Simplified construction
- Reduced maintenance

The increased power density represents a double advantage, which needs to be pointed out. On one side, some space-constrained applications require the use of mechanical transmission or gear when adopting a larger motor, such as an asynchronous one. It is also worth noting that, to achieve a high peak efficiency (like for the new IEC energy efficient and premium efficiency classes), induction motor usually needs larger size with respect to a normal efficiency one, then the large ratio between the volume of a classical induction motor and that of a PMSM of the same power is further increased. A second advantage is of course the reduction in the quantity of material used, both for magnetic steel and conductive metal (copper and aluminum) and the reduced weight, although the production cost of a PMSM is generally higher due to the use of the expensive permanent magnet materials.

Moreover, since the very low rotor losses (ideally null, but induced currents and hysteresis dissipation exists) heat transfer from the rotor to ambient does not need to be high, making it possible to avoid ventilation, and fully enclosing the motor structure. This allows operation in heavily contaminated (dust, moisture, chemical agents) or dangerous (explosion risk) environments and a longer lifetime. Also these factors can be important in the choice of a motor for a certain application, since it may reduce costs associated with maintenance and replacing.

However, the utilization of PMSMs encounters many difficulties, mainly related to the usually higher initial cost and more complex control. In particular, the possibility of straight line-start of asynchronous motors, although with extremely high electrical, thermal and mechanical stresses, together with relatively poor efficiency, will probably make the induction motor be the most common machine in a long future, even if on a decreasing trend.

Moreover, PMSM have an important advantage from the thermal point of view, with respect to induction and DC motors. In fact, stator generated heat can be easily dissipated to the free air, while rotor path to ambient is quite resistive. Since their negligible rotor losses, there is no need for forced ventilation, and smaller dimensions can be achieved. This is compatible with the fact that some permanent magnet materials must be protected from chemical agents, thus PMSM are usually packed in a dust and water resistant enclosure.

1.3 Contribution of this work

Although the Permanent Magnet Synchronous Motor has been an important topic in the electric drives research during the last decades, from the control point of view, many interesting topics are still open. The work described in this thesis has been devoted to two main topics, both representing important aspects of PMSM control. As a contribution towards a wide adoption of sensorless PMSM drives, different techniques for position and speed estimation have been studied, resulting in some original analytical characterization and improvement proposals. The other main topic, which is more important for particular applications where wide operating speed ranges are required (for example in washing machines and electrical traction drives), relates to the operation of IPMSMs at very-high speed, where “flux-weakening” techniques must be applied to overcome the issues related to the phase voltage limitation imposed by the limited inverter supply capability.

About the model-based techniques for isotropic motors (i.e. where anisotropy-based estimation is not possible), a project for the development of a

sensorless strategy for general-purpose PMSM industrial drives has been carried out. Some analytical tools for the tuning of the estimation process have been obtained, together with a proposal on the improvement of robustness at low-speed, where in normal conditions the control fails. Also, an injection-based technique valid for isotropic motors has been proposed, for both initial position detection and tracking.

For the control of motors characterized by a salient rotor, the well-known techniques involving sinusoidal signal injection have been studied, and an original technique, which avoids the demodulation carrier phase tuning issue has been proposed. Moreover, a detailed analytical description and a preliminary implementation of a technique relying only on the PWM ripple excitation has been presented, which takes advantage of the adoption of simple Rogowsky coils for current derivative sensing.

After this introduction, Chapter 2 briefly introduces the PMSM two-phase model (in both the stationary and synchronous reference frames) and the fundamentals of vector control, where the main symbols will also be defined.

Chapters 3 and 4 describe the activity in the sensorless field, dividing the two chapters according to the two main classes of techniques, i.e. model-based and injction-based methods. In the first of the two, the development of a sensorless strategy for a general-purpose Surface Mount-PMSM industrial drive will be described, where a back-EMF observer in the stationary reference frame has been adopted for position and speed estimation. A simple approach to the modeling of the estimation process will be exploited, obtaining a full analytical description of the dynamics involved. Moreover, a stabilization technique based on the injection of a constant direct-axis current will be analyzed, and the overall performances of the system tested on the hardware of a commercial drive. In the fourth chapter, the study of injection-based methods will lead to the original contributions that have been proposed, namely an alternative demodulation exploiting the Discrete Fourier Transform principle, a PWM excitation technique making use of Rogowsky coils and, finally, a novel injection-based technique suitable for the control of isotropic machines at very low-speed and stand-still.

In Chapter 5 a few state-of-art algorithms for flux-weakening control of Interior-PMSM drives have been compared. The advantages of the techniques relying on the synchronous current frame, in terms of performances and

implementation, will be demonstrated. For this class of methods, a novel theoretical investigation will be presented, allowing to develop a simple approach for voltage command regulation on-line gain adaptation. The experimental results, obtained on a prototype motor drive for washing machines, will demonstrate the feasibility of the method and the related improvements.

The work described in this thesis has been mainly developed within the Electric Drives Laboratory of the University of Udine (EDLab Udine), during the three years of the PhD course in Industrial and Information Engineering. The laboratory is part of a network that comprises other two groups, and works in a close partnership with the Electric Drives Laboratory of the University of Padova (EDLab Padova). While the motivation of some of the work just came from the emerging results of state-of-art research, part of the work has been carried out in the frame of partnerships with external companies, which allowed to maintain a perspective on the possible fields of application of the research, and on the implementation issues, costs and robustness associated to the different techniques. For this reason, as a choice towards the applicability and robustness of the results, the simpler methods have been favored against more complex ones, especially where a good dynamical characterization was not available, they required large implementation resources or were based on data from extensive off-line testing of the single machine.

As almost all of the research results, the small original contribution coming from this work leaves important issues open. However, it is hopefully going to be useful for further study and development.

1.4 List of publications

Several parts of the work reported in this thesis have been presented in international conferences and journals, together with marginal contributions on different topics. Hereafter these publications are listed in a chronological order.

- S. Bolognani, S. Calligaro, R. Petrella, and M. Tursini, "Sensorless Control of IPM Motors in the Low-Speed Range and at Standstill by HF Injection and DFT Processing," *IEEE Transactions on Industry Applications*, vol. 47, no. 1, pp. 96 –104, Feb. 2011.
- S. Bolognani, S. Calligaro, R. Petrella, and F. Pogni, "Flux-weakening in IPM motor drives: Comparison of state-of-art algorithms and a novel proposal for controller design," in *Proceedings of the 2011-14th European Conference on Power Electronics and Applications (EPE 2011)*, 2011, pp. 1 –11.
- S. Bolognani, S. Calligaro, and R. Petrella, "Design issues and estimation errors analysis of back-EMF based position and speed observer for SPM synchronous motors," in *2011 Symposium on Sensorless Control for Electrical Drives (SLED)*, 2011, pp. 138 –145.
- S. Bolognani, S. Calligaro, R. Petrella, and M. Sterpellone, "Sensorless control for IPMSM using PWM excitation: Analytical developments and implementation issues," in *2011 Symposium on Sensorless Control for Electrical Drives (SLED)*, 2011, pp. 64 –73.
- S. Bolognani, S. Calligaro, and R. Petrella, "Adaptive flux-weakening controller for IPMSM drives," in *2011 IEEE Energy Conversion Congress and Exposition (ECCE)*, 2011, pp. 2437 –2444.
- S. Bolognani, S. Calligaro, and R. Petrella, "Optimal voltage feed-back flux-weakening control of IPMSM," in *IECON 2011 - 37th Annual Conference on IEEE Industrial Electronics Society*, 2011, pp. 4170 –4175.
- M. Morandin, S. Bolognani, R. Petrella, A. Pevere, and S. Calligaro, "Mild-hybrid traction system based on a bidirectional half-bridge interleaved converter and a three-level active NPC inverter-fed PMSM," presented at the 2012 Twenty-Seventh Annual IEEE Applied Power Electronics Conference and Exposition (APEC), 2012, pp. 1644 –1651.
- S. Calligaro and R. Petrella, "Accuracy and robustness improvement in sensorless PMSM drives at low-speed by direct-axis current injection," in *2012 Symposium on Sensorless Control for Electrical Drives (SLED)*, 2012, pp. 138 –145.
- S. Calligaro, R. Petrella, and S. Bolognani, "Sensorless quasi-standstill and very low-speed position detection in non-salient PMSMs based on current injection and back-EMF observer," in *2012 Symposium on Sensorless Control for Electrical Drives (SLED)*, 2012, pp. 138 –145.

- S. Bolognani, S. Calligaro, and R. Petrella, "A novel proposal for sensorless speed control of non-salient PMSMs at standstill and low-speed based on current injection and constant direct-axis current stabilization effect," accepted for presentation at the *2013 Twenty-Eighth Annual IEEE Applied Power Electronics Conference and Exposition (APEC)*, 2013.
- A. Pevere, F. Pasut, R. Petrella, and S. Calligaro, "Modulation Techniques for Three-Phase Three-Level NPC Inverters: a Review and a Novel Solution for Switching Losses Reduction and Optimal Neutral-Point Balancing in Photovoltaic Applications," accepted for presentation at the *2013 Twenty-Eighth Annual IEEE Applied Power Electronics Conference and Exposition (APEC)*, 2013.
- S. Calligaro and R. Petrella, "General-Purpose Full-Speed-Range Sensorless SPM Drive: Low-Frequency Injection and Robustness Improvement," accepted for presentation at *PCIM Europe 2013*, 2013.

Chapter 2
PMSM model and control

While the DC motors dominated the field of servo drives for decades, at the end of the 1960s, K. Hasse introduced the field oriented control of AC motor. Based on the theory developed by R.H. Park in the early 1930s, it was pointed out that in theory the induction motor could be controlled in the same way as the DC motor. Further developments of this method, together with the important leaps ahead made by the semiconductor industry (both power and digital devices) made it possible for PMSM servo drives to be present on the market in the 1980s. With the establishment of digitally controlled architectures and the decreasing cost of computing power, abstraction from the simple machine could be achieved, allowing many sophisticated control techniques to be implemented also in standard drives and reaching high levels of accuracy and dynamic responses with easy commissioning procedures.

In the model of an electric drive, two subsystems can be identified, an electrical and a mechanical one. The equations linking the two subsystems are the electromagnetic torque expression and the position and speed dependent induced voltages (back-EMF). The expression "motor control", regardless of the considered class of motor, driving devices and control schemes, indicates a set of techniques aiming at obtaining a desired mechanical behavior from the motor by providing the proper electrical inputs at its electrical terminals.

For all electrical rotating machines, torque is obtained as an interaction between current and magnetic flux. In particular, in the ideal model of the PMSM, torque can be expressed as a function of currents and rotor position only (besides constant parameters), then allowing to control torque production by means of current control. Based on torque control, speed and/or position can be easily controlled, unless very peculiar mechanical loads are applied. In the majority of cases, in fact, a simple first order (inertia-damping) model describes the mechanical

subsystem, which makes the dynamic behavior of load versus input torque very straightforward.

2.1 PMSM model

This brief recall to the model of synchronous machines, and in particular to Permanent Magnet Synchronous Motors (PMSMs), will be functional to the comprehension of the rest of this thesis, also helping in the definition of the most used symbols. The ideal model is considered, which allows an easy analytical study, while in most of the cases non-idealities will be seen as model disturbance.

An electric motor is a machine able to perform a power conversion from electrical to mechanical, and vice versa. While the term "motor" is commonly used for indicating generically such a machine, more properly operation can be distinguished, depending on the energy flow direction, between motoring operation and generating, which are from electrical to mechanical or reversed, respectively. An identical machine is usually called a generator or a motor depending on which is the main operating condition in its application.

The system dynamics point of view will be often adopted. A mechanical and an electrical subsystem, which are physically linked each other, will be sometimes separately considered, when this is allowed by the kind of study to be done. In particular, in the electrical subsystem the motor has to be often considered together with its supply connection, while on the mechanical side the load must be taken into account, since at least the rotor inertia and viscous friction are present.

The far most common motor construction is represented by three-phase topologies, although some exceptions exist, like single-phase and two-phase motors in low-power applications, and multi-phase ones, proposed for fault-tolerant systems. Apart from single-phase systems, two-phase and multi-phase machines can be mapped into the same model used for three-phase motors, making it possible to take advantage of the same modeling and control techniques. An interesting case is represented by the widely used hybrid stepper motors, which can be modeled as two-phase PMSMs.

Where not otherwise noted, the anisotropic rotor model will be adopted, where inductances seen from the motor phases depend on the rotor position. Usually, this means that the permanent magnet axis shows lower inductance than in its electrically orthogonal direction. The model is, of course, also valid for isotropic rotor machines, provided that inductances on the two axes are set equal, and in this case can be greatly simplified.

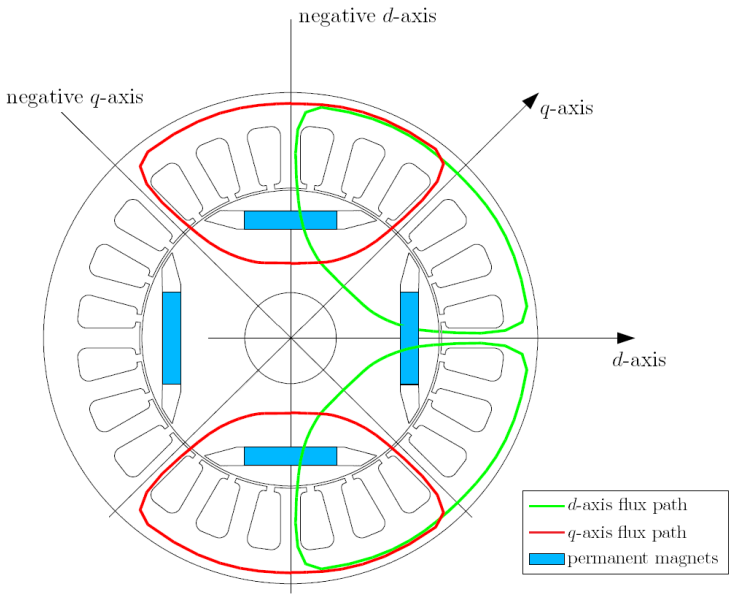

Fig. 2.1. Example of a four-pole IPMSM cross section.

2.1.1 Two-phase representation of the three-phase PMSM

Although the three-phase model of the machine can be studied, an important innovation in the theory of AC machines was the introduction of two-phase models for the three-phase systems [4],[5], which result in very convenient sets of equations. Two main representations have been developed, in the stationary and in the synchronous reference frame; the first being a simple transformation to orthogonal

coordinates, while the second reveals the deep relation between the rotor position and the phase of sinusoidal electrical quantities in a synchronous machine. The construction of the model exploits the fact that the three phase voltages and currents, for a non-connected neutral system, are not linearly independent, since their sum is null. The most obvious transformation is towards an equivalent system consisting of two orthogonal phases. In this short recall of the ideal PMSM model, that will be used where no additional hypothesis or non-ideal aspects are introduced, the considered machine has the following characteristics:

- Magnetic saturation phenomena are negligible;
- The permanent magnets are supposed to have constant total flux amplitude, and a linear demagnetization curve;
- Magnet flux-linkage, stator phase windings distribution and resulting self and mutual inductances are sinusoidally distributed according to the angle variation, but their behavior is modeled by means of ideally concentrated windings;
- The stator phases are identical, symmetrically positioned and wye connected, so that the available terminals corresponds to each of the three windings, and a neutral connection is not present (so that homopolar current cannot flow);
- The interesting frequencies are sufficiently low, so that wavelengths and penetration depths are in the winding conductors are not subject to skin effect, then inductance and resistance are not dependent on frequency;
- The iron losses due to hysteresis and parasite currents are negligible, so rotor induced currents are considered null;
- The time constants associated with the mechanical system are much larger than the electrical ones;
- System parameters are considered to be constant, thus neglecting their dependence on the operating conditions (e.g. temperature).

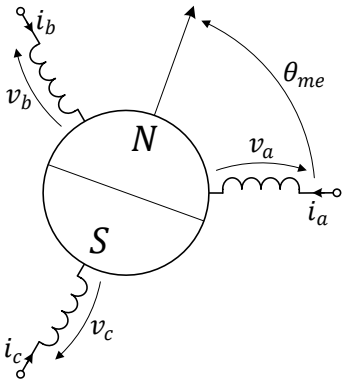

Fig. 2.2. Schematic representation of the three-phase PMSM.

An anisotropic rotor motor is considered, since it has a more complex model; the isotropic rotor PMSM will be considered as a special case, and a simplified model will be used where more convenient. The reduction from the three-phase system (Fig. 2.2) to the equivalent two-phase one is performed by applying the Clarke transformation [4], named after E. Clarke. A generic electrical quantity x, defined for each phase, is represented in a vector form and transformed in a two-element variable by calculating:

$$\underline{x}_{\alpha\beta} = \begin{bmatrix} x_\alpha \\ x_\beta \end{bmatrix} = \begin{bmatrix} 1 & -1/2 & -1/2 \\ 0 & \sqrt{3}/2 & -\sqrt{3}/2 \end{bmatrix} \begin{bmatrix} x_a \\ x_b \\ x_c \end{bmatrix} \tag{2.1}$$

As above mentioned, the common mode component has been neglected, since the sum of phase currents and phase-to-phase voltages is null (thus it has no influence on the three motor phases). The transform has an easy geometric explanation, as it represents the contribution of each of the three phases a, b, c (placed at $0, 2\pi/3, 4\pi/3$, respectively) on two orthogonal axes α and β (placed at 0 and $\pi/2$, respectively). An illustration of the two-phase stationary reference frame model is shown in Fig. 2.3. voltage equation in these axes, in the Laplace domain, has the form

$$\underline{V}_{\alpha\beta} = \begin{bmatrix} V_\alpha \\ V_\beta \end{bmatrix} = R_S \begin{bmatrix} I_\alpha \\ I_\beta \end{bmatrix} + s \begin{bmatrix} \lambda_\alpha \\ \lambda_\beta \end{bmatrix} \tag{2.1}$$

Where $V_{\alpha,\beta}$ and $I_{\alpha,\beta}$ are the voltage and current vector, respectively, and R_S is the stator phase resistance. The flux derivative terms $s\lambda_\alpha$,$s\lambda_\beta$ can be divided into the contribution of self and mutual inductances and of the permanent magnet flux-linkage. Flux linkage consists of current induced flux, expressed by means of an inductance matrix (which depends on the rotor position), and permanent magnet flux (having magnitude Λ_{mg}), projected on the two axes:

$$\underline{\lambda}_{\alpha\beta} = \begin{bmatrix}\lambda_\alpha \\ \lambda_\beta\end{bmatrix} = \begin{bmatrix}L_\Sigma + L_\Delta \cos 2\theta_{me} & -L_\Delta \sin 2\theta_{me} \\ -L_\Delta \sin 2\theta_{me} & L_\Sigma + L_\Delta \cos 2\theta_{me}\end{bmatrix}\begin{bmatrix}I_\alpha \\ I_\beta\end{bmatrix} + \Lambda_{mg}\begin{bmatrix}\cos\theta_{me} \\ \sin\theta_{me}\end{bmatrix} \tag{2.2}$$

where L_Σ is the average inductance seen from the stator phases, and L_Δ is the amplitude of the sinusoidal variation of stator inductance.

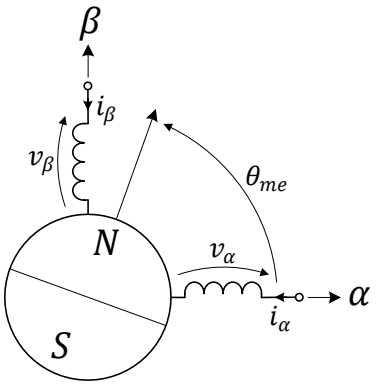

Fig. 2.3. Schematic representation of the PMSM model in the two-phase stationary reference frame.

The mechanical-electrical rotor position θ_{me} is an angle representing the electrically equivalent position of rotor magnetic axis (South to North direction) with respect to the first winding axis (α, which corresponds to the first motor physical phase). Since the number of motor pole pairs can be higher than one, the magnetic model is periodic in a fraction of the mechanical angle, then mechanical-electrical equivalent position θ_{me} and speed ω_{me} are defined, with respect to their mechanical counterparts θ_m and ω_m, as

$$\theta_{me} = pp\ \theta_m \ ,\ \ \omega_{me} = pp\ \omega_m \tag{2.3}$$

where pp represents the number of pole pairs. The voltage equation (2.1) can now be expressed as

$$\begin{bmatrix} V_\alpha \\ V_\beta \end{bmatrix} = R_S \begin{bmatrix} I_\alpha \\ I_\beta \end{bmatrix} + sL_{\alpha\beta} \begin{bmatrix} I_\alpha \\ I_\beta \end{bmatrix} + \omega_{me} \Lambda_{mg} \begin{bmatrix} -sin\,\theta_{me} \\ cos\,\theta_{me} \end{bmatrix} \tag{2.4}$$

after defining the stationary frame inductance matrix

$$L_{\alpha\beta} = \begin{bmatrix} L_\Sigma + L_\Delta\, cos\, 2\theta_{me} & -L_\Delta\, sin\, 2\theta_{me} \\ -L_\Delta\, sin\, 2\theta_{me} & L_\Sigma + L_\Delta\, cos\, 2\theta_{me} \end{bmatrix} \tag{2.5}$$

and the back Electro-Motive Force (back-EMF) vector

$$\underline{E}_{\alpha\beta} = \begin{bmatrix} E_\alpha \\ E_\beta \end{bmatrix} = \omega_{me} \Lambda_{mg} \begin{bmatrix} -sin\,\theta_{me} \\ cos\,\theta_{me} \end{bmatrix} \tag{2.6}$$

It is worth noticing that, for the particular case of the isotropic rotor machine (i.e. an ideal SM-PMSM, where saturation induced saliency is not present), the model can be written in a very compact and useful form, thanks to the simplification of the inductance matrix $L_{\alpha\beta}$ (since $L_\Delta = 0$). Vectors can also be substituted by complex variables, i.e. for a generic variable X among the ones previously defined:

$$\boldsymbol{X}_{\alpha\beta} = X_\alpha + jX_\beta \tag{2.7}$$

obtaining

$$\boldsymbol{V}_{\alpha\beta} = R_S \boldsymbol{I}_{\alpha\beta} + sL_{SS} \boldsymbol{I}_{\alpha\beta} + \boldsymbol{E}_{\alpha\beta} \tag{2.8}$$

where the synchronous phase inductance is $L_{SS} \triangleq L_\Sigma$. The back-EMF variable can be expressed as a complex exponential quantity:

$$\boldsymbol{E}_{\alpha\beta} = j\omega_{me} \Lambda_{mg} e^{j\theta_{me}} \tag{2.9}$$

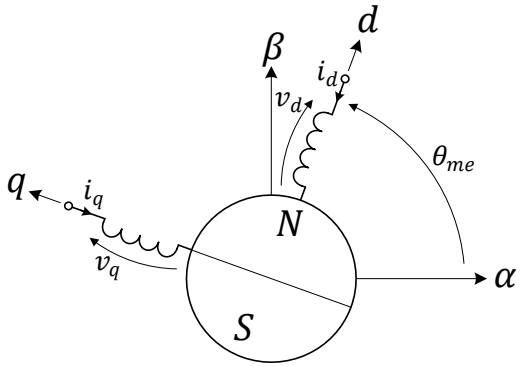

Fig. 2.4. Schematic representation of the PMSM model in the synchronous reference frame.

By means of the Park transformation, which was introduced by R. H. Park in 1929, [5], allowing the study of synchronous machines behavior in a way similar to the DC motor, a two-phase model in the synchronous reference frame is obtained. In this case, the motor is represented by two windings (direct, d and quadrature, q) rotating with the rotor. The direct-axis is set as aligned with the rotor magnetic axis. This model has many advantages, since the quantities related to torque generation are more easily studied in this domain, and steady-state variables assume constant values. The voltage equation in matrix form becomes

$$\underline{V}_{dq} = \begin{bmatrix} V_d \\ V_q \end{bmatrix} = R_S \begin{bmatrix} I_d \\ I_q \end{bmatrix} + \begin{bmatrix} s & \omega_{me} \\ -\omega_{me} & s \end{bmatrix} \begin{bmatrix} \lambda_d \\ \lambda_q \end{bmatrix} \tag{2.10}$$

The terms $\omega_{me}\lambda_d$ and $-\omega_{me}\lambda_q$ are called axes cross-coupling.

The flux-linkage expression now becomes

$$\underline{\lambda}_{dq} = \begin{bmatrix} \lambda_d \\ \lambda_q \end{bmatrix} = \begin{bmatrix} L_\Sigma - L_\Delta & 0 \\ 0 & L_\Sigma + L_\Delta \end{bmatrix} \begin{bmatrix} I_d \\ I_q \end{bmatrix} + \begin{bmatrix} \Lambda_{mg} \\ 0 \end{bmatrix} \tag{2.11}$$

The absence of mutual terms and variable terms in the inductance matrix shows how the two phases dynamically see only a constant self-inductance. The inductance values can be defined as direct-axis and quadrature-axis inductance

$$L_d \triangleq L_\Sigma - L_\Delta \ , \ L_q \triangleq L_\Sigma + L_\Delta \tag{2.12}$$

Equation (2.10) can be then rewritten in the more explicit form

$$\underline{V}_{dq} = \begin{bmatrix} V_d \\ V_q \end{bmatrix} = R_S \begin{bmatrix} I_d \\ I_q \end{bmatrix} + \begin{bmatrix} sL_d & \omega_{me}L_q \\ -\omega_{me}L_d & sL_q \end{bmatrix} \begin{bmatrix} I_d \\ I_q \end{bmatrix} + \omega_{me} \begin{bmatrix} 0 \\ \Lambda_{mg} \end{bmatrix} \tag{2.13}$$

The term $\omega_{me}\Lambda_{mg}$ represents the permanent magnet induced voltage, then, in analogy to the stationary reference frame equations, a back-EMF can be defined as:

$$\underline{E}_{dq} \begin{bmatrix} E_d \\ E_q \end{bmatrix} = \begin{bmatrix} 0 \\ \omega_{me}\Lambda_{mg} \end{bmatrix} \tag{2.14}$$

The dependence on rotor position has been eliminated, or, in other terms, moved into the calculation of the d, q terms from the actual stationary reference phase values, which is a simple coordinates transformation (backward rotation of θ_{me}):

$$\begin{bmatrix} V_d \\ V_q \end{bmatrix} = \begin{bmatrix} cos\,\theta_{me} & sin\,\theta_{me} \\ -sin\,\theta_{me} & cos\,\theta_{me} \end{bmatrix} \begin{bmatrix} V_\alpha \\ V_\beta \end{bmatrix} \tag{2.15}$$

$$\begin{bmatrix} I_d \\ I_q \end{bmatrix} = \begin{bmatrix} cos\,\theta_{me} & sin\,\theta_{me} \\ -sin\,\theta_{me} & cos\,\theta_{me} \end{bmatrix} \begin{bmatrix} I_\alpha \\ I_\beta \end{bmatrix} \tag{2.16}$$

Also in this case, complex notation can be useful. In fact, rotation matrix translates in an exponential, which is very simple to deal with for derivation and integration. In the case $L_\Delta = 0$ (isotropic rotor) the voltage equation (2.13) becomes:

$$\boldsymbol{V}_{dq} = R_S \boldsymbol{I}_{dq} + (s + j\omega_{me})L_{ss}\boldsymbol{I}_{dq} + j\omega_{me}\Lambda_{mg} \tag{2.17}$$

and obviously

$$\boldsymbol{E}_{dq} = j\omega_{me}\Lambda_{mg} \tag{2.18}$$

2.1.2 Electro-mechanical model

As mentioned, the electrical motor can be seen as bidirectional energy converter, and is therefore equipped with two power ports, the electrical and the mechanical one. The electrical part model has been introduced in 2.1.1 while, in

the present paragraph, the comprehensive electro-mechanical model will be recalled, describing the motor torque production characteristic.

In the previous voltage equations (2.4),(2.8),(2.13),(2.17), the dependence on speed and position represents the effect of the mechanical sub-model on the electrical one. The corresponding can be found in the relation of torque generated by the motor and phase currents. Electro-magnetic torque can in fact be expressed as the cross product of current and flux vector:

$$T_e = \frac{3}{2} pp \begin{bmatrix} \lambda_\alpha \\ \lambda_\beta \end{bmatrix} \times \begin{bmatrix} I_\alpha \\ I_\beta \end{bmatrix} \tag{2.19}$$

By substituting the expressions of flux, the more common torque expression, based on the synchronous reference frame, can be obtained

$$T_e = \frac{3}{2} pp \begin{bmatrix} \lambda_d \\ \lambda_q \end{bmatrix} \times \begin{bmatrix} I_d \\ I_q \end{bmatrix} = \frac{3}{2} \left[pp\, \Lambda_{mg}\, I_q + \left(L_d - L_q\right) I_d I_q \right] \tag{2.20}$$

In this equation, two contributions can be recognized, which result from different principles: the torque related to the interaction between rotor permanent magnet flux and stator current, and the reluctance torque, which implies only stator-generated field.

The mechanical system is not limited to the motor, but the load coupled to the rotor shaft is also modeled. This is normally represented by a first order inertia-friction passive system and a generic braking torque T_L (independent source), which can represent any other kind of load:

$$\omega_{me} = \frac{T_e - T_L}{B + sJ} \tag{2.21}$$

2.2 Typical drive architecture

The impressive improvements in semiconductors technology (both in power and logic devices, cost and performances), starting from the 1980s allowed the implementation and commercialization of drives controlled according to principles

developed in the previous years, including vector control. In particular, the increased availability of powerful microprocessors allowed more complex algorithms to be adopted, achieving reliable and accurate sensorless vector control. In this scenario, the induction motor was the main target, since its wide utilization, relatively low cost and high reliability.

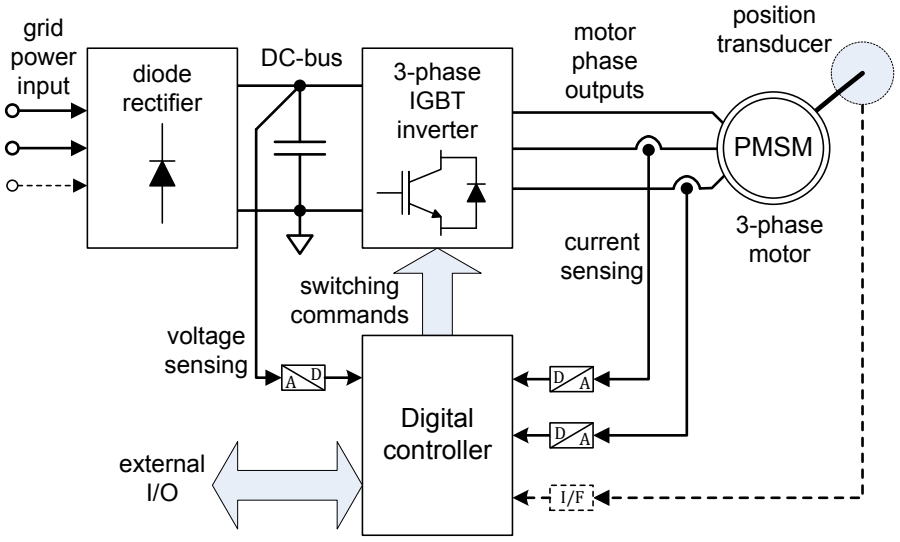

Fig. 2.5. Typical architecture of an electric drive.

The vast majority of three-phase electric drives share a similar hardware architecture, which is depicted in Fig. 2.5. The scheme comprises a DC power supply (usually a grid connected diode rectifier), which supplies a three-phase power inverter (usually consisting of six Insulated Gate Bipolar Thyristors, IGBTs, or Metal-Oxide Semiconductor Field Effect Transistors, MOSFETs), Fig. 2.6, by means of the DC-bus, i.e. a capacitor bank filtering the rectified voltage. In some cases, a controlled DC source is present or, in high-power applications, a bidirectional rectifier (Active Front-End, AFE) is adopted. In fact, during motor braking, the DC-bus is charged and, in the case of an unidirectional supply from the grid, a dissipation device must also be present in order to avoid the DC-bus overvoltage.

The control algorithms for the specific kind of motor are usually implemented as software on a digital microcontroller (firmware), where inverter switching

commands are generated, aiming at controlling the motor to follow a desired torque, speed or position behavior. The measurements that are available to the controller comprise usually at least two of the three phase currents and the DC bus voltage, although speed, position and other sensors can also be present. Acquisition of the measurements is performed by means of analog to digital converters (ADC or A/D converters) or other interfaces dedicated to peculiar measurements (as for the case of incremental encoders for position sensing), after a proper signal conditioning. Insulation between the controller and the power sections is required for reliability or safety reasons, also because of the presence of external user interfaces or input/output (I/O) connections to other devices, which provide the communication of commands, parameter settings or feedback from the controller to external supervising units.

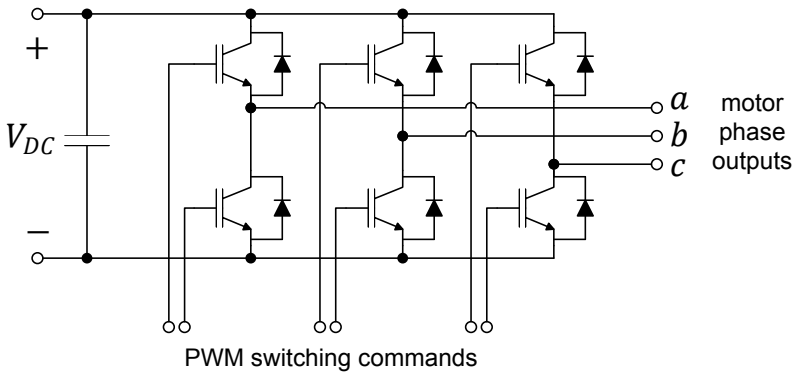

Fig. 2.6. Typical three-phase inverter configuration.

Of course, the elimination of non-necessary hardware is desirable, even at the cost of some loss in robustness and performances, since it allows to reduce production, installation and maintenance costs. It is worth noticing that, among the various connections described, some of them are critical for several reasons. Depending on the power rating and application field, the physical distance between the controller, power stage and motor can substantially vary. In particular, small power dedicated drives (as those found in home appliances and HVAC) controller and power stage are often integrated into the motor case, while in large power

drives (fitted in large electrical cabinets) the connections can be quite long, especially for the motor phase wires and mechanical sensors.

2.3 Vector control

For most of the cases studied in this thesis, a rotor speed control will be considered. The term "control" or "regulation" is usually meant as feed-back loop control, in which the controlled variable is measured (or estimated) and compared to a reference value. On the basis of the control error, the controller or regulator rule generates a proper value for the input to the plant, in order to drive the output to reproduce the reference input with a certain bandwidth. In many cases, the dynamic behavior of each state-variable is mainly linked to a single input or state-variable. For this reason, one of the common schemes adopted for the control of plants of dynamics order higher than one (i.e. having more than one pole in the plant's transfer function) consists of concentric feed-back loops, each regulating one state variable. In the case of speed control of an electric drive, in addition to the speed loop, usually a torque or torque-related current inner control is implemented, thus simplifying the speed regulator task. One of the most common, if not the most common, control topology of this kind is based on a vector representation of electrical quantities, and is thus called vector control. In particular, the relation between currents and flux-linkage on one side and torque on the other is exploited to control the generation of the torque as required by the speed controller.

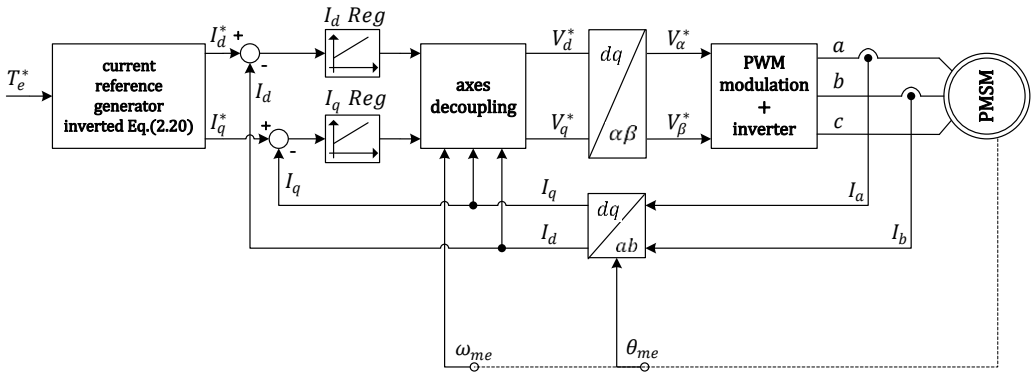

Fig. 2.7. Torque control loop.

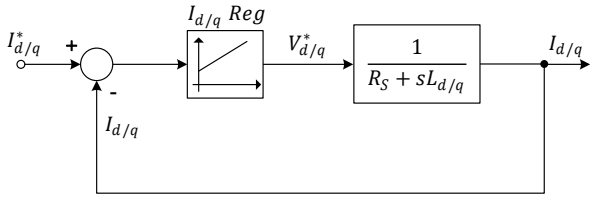

Fig. 2.8. Simplified current control loop dynamics (considering exact decoupling and ideal inverter behavior).

The most common approach to torque control of the PMSM is the vector control, which refers to the synchronous quantities, i.e. those defined in the dq synchronous reference frame. Although some different proposals are present (the most common one being Direct Torque Control, DTC, also called Direct Self Control, DSC, [6]), Field Oriented Control is almost a standard in this field. Its operating principle, introduced by K. Hasse and F. Blaschke, [7], exactly follows the Park transformation model (introduced in 2.1.1), in which the direct axis is linked to the rotor permanent magnet axis (South to North direction). It is worth noticing that position signal is needed not only for speed measurement, but also in order to achieve proper torque regulation. In fact, from (2.20) it can be easily seen that, once the angular position of the rotor magnetic axis is known, torque can be simply obtained from the d, q currents and the motor physical parameters of rotor magnet flux Λ_{mg} and inductances L_d, L_q. This means that a proper current control, operated on the synchronous reference frame components, enables torque control (Fig. 2.7). Moreover, the motor phases electrical dynamics results in a simpler plant with respect to the case of the stationary frame, in which model is sinusoidally varying with rotor position. Also, thanks to the Park transformation, a transposition in the frequency domain is done, so that the signals at the rotation frequency in the stationary reference frame are moved to null frequency in the synchronous one. This is an important advantage, since the widely adopted Proportional-Integral regulator (PI regulator) ensures null DC error. Current control is then actually achieved by imposing to the inverter proper logic commands. The voltage vector reference can be simply obtained from the current

regulators outputs, but usually dynamics is linearized by summing the expected value of the coupling terms ($\omega_{me}L_qI_q$ and $\omega_{me}\left(L_dI_d+\Lambda_{mg}\right)$ terms in the voltage equations), which results in the ideal equivalent scheme shown in Fig. 2.8. The translation of vector voltage request into Pulse Width Modulation (PWM) duty-cycles for the inverter switches is called "*modulation*". The actual PWM signal is then generated by a dedicated peripheral, whose input duty-cycles are updated at regular intervals (each control period or half period). Many techniques can be found on this topic, one of the most common ones is Space Vector - PWM (SV-PWM), where possible inverter configurations are mapped as vectors (Fig. 2.9). The application duty-cycles of the two vectors adjacent to the reference one correspond to their projections on the same vector directions. It is worth mentioning that output voltage is usually not measured, but only deduced from the imposed voltages (which result in PWM duty-cycles) and from the voltage measurement on the inverter DC bus (which is the inverter supply). Unfortunately, this information is not accurate, since it is distorted by the non-ideal behavior of the inverter. One of the most significant is due to the fact that simultaneous commutation on the inverter switches on the same leg cannot be applied (high probability to result in a leg short circuit), so turn-on delays (dead-times) must be introduced in the PWM pattern. This means that, for each inverter phase, during the time between the two commanded transitions, voltage will be clamped by one of the two leg free-wheeling diodes, depending on the current direction. Many techniques for the compensation of this effect have been developed, [8]–[10].

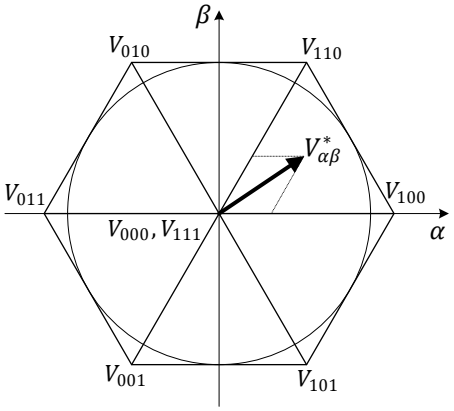

Fig. 2.9. Inverter modulation in the space vector representation.

When the speed regulator output needs to be actuated, of course different current vectors could result in the same output torque, thus they can be considered completely equivalent from the speed control point of view. Efficiency maximization and electrical limits impose the adoption of some current characteristics in the dq current plane with respect to others. With reference to the graph in Fig. 2.10, which is drawn for steady-state, all points laying inside the current magnitude limit circle (related to thermal limits) are admissible at low-speed (i.e. when inverter voltage maximum capability is not reached), and all points on the hyperbolas result is the same torque. However, it can be easily seen that, for each torque value, on point ensures the minimum current vector magnitude, and is said to lie on the Maximum Torque Per Ampere curve (MTPA).

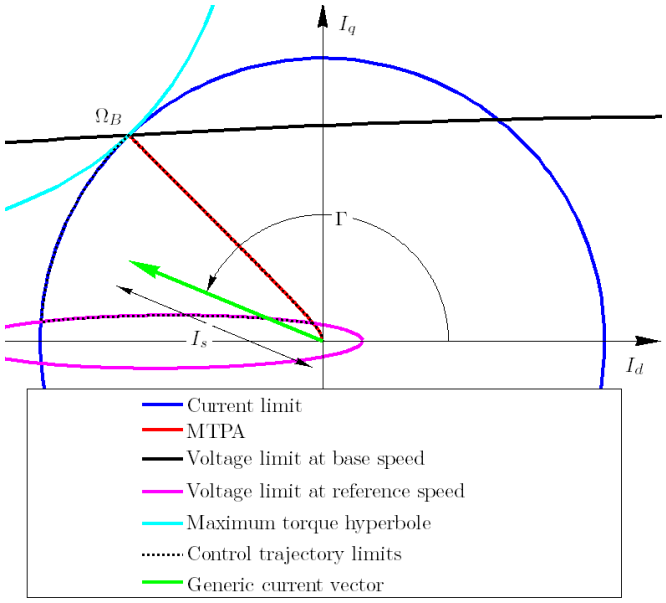

Fig. 2.10. Control trajectories and limit loci in the I_d vs. I_q plane.

If Joule dissipation is considered the main portion of losses, operation on the MTPA curve results in a minimum losses strategy, and also allows to fully exploit the torque producing capability of the motor. MTPA can be analytically obtained by finding the minimum of current amplitude for a given torque, while using the

phase angle as the independent variable. This results in a simple expression representing the curve:

$$I_d = \frac{\Lambda_{mg}}{4(L_d - L_q)} - \sqrt{\frac{\Lambda_{mg}^2}{16(L_d - L_q)} + I_q^2} \tag{2.2}$$

In the case of non-salient PMSM, i.e. where $L_d = L_q$, the reluctance torque is not present, thus torque expression becomes proportional to the q-axis current:

$$T_e = K_T\, I_q \tag{2.3}$$

having defined $K_T = \frac{3}{2} pp\Lambda_{mg}$, which is a parameter usually found on the nameplate of PMSM for servo applications. Only the q-axis current is involved to actual torque control (being proportional to it), while the d-axis current, normally regulated at null value, at high-speed is used for the reduction of the flux-linkage ("flux-weakening" control), to reduce the necessary voltage magnitude. Similar considerations can be applied to the case of the anisotropic motor (normally for IPMSM, in which saliency is intentionally designed), even if, in this case, torque depends on both the current components, and then a more complex algorithm is needed for translating the speed controller request into a vector current reference. Obviously, the relation between current vector value and torque is entirely dependent on the motor magnetic parameters, which are subject to dispersion (statistically among the same production model) and variation due to the operating conditions (saturation, temperature influence). To overcome the possible mismatches between the analytically found MTPA curve and the actual maximum torque curve, the usual techniques are based on off-line extensive or limited measurements on the machine. However, the need for off-line measurements and their incorporation into the drive controller represents an additional cost and can be impractical in some applications. A viable alternative to these issues has been proposed in [11], where an on-line tracking method for the MTPA trajectory, is presented. While the first version of the algorithm relied on mechanical vibration sensing as a consequence of a current injection, further developments were introduced in [12], [13], where only electrical measurements are involved (exploiting active power calculation). The on-line obtained data can be periodically acquired and stored when in steady-state conditions, and then used also during transient

operation. The described topology is depicted in Fig. 2.11, where a mechanical transducer is adopted for position and speed sensing.

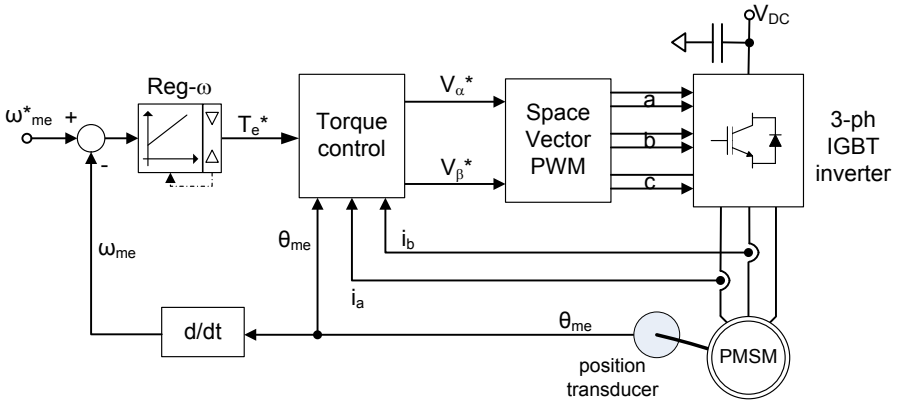

Fig. 2.11. Typical PMSM drive speed control topology.

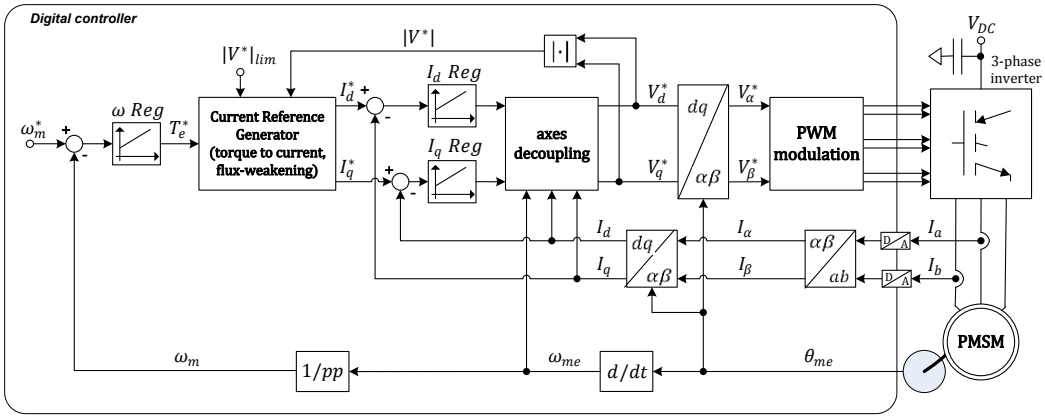

Fig. 2.12. Typical scheme for the speed vector control of a sensored PMSM drive.

The typical FOC scheme for a sensored PMSM drive is represented in Fig. 2.12. The *Current Reference Generator* block provides direct and quadrature current values so that, from the motor knowledge, the resulting torque reaches the reference value coming from the speed regulator. Direct and quadrature currents are then regulated by means of two separate feed-back paths, while the *axes*

decoupling sums the cross voltage components linear with speed (see (2.13)), simplifying the plant for the synchronous current control, which ideally results in an inductive impedance. An additional feed-back path is drawn, involving voltage vector magnitude for flux-weakening. This has a role only at high-speed, where voltage reaches the inverter maximum capability, and a proper modification of the current references (with respect to the MTPA trajectory) is needed to reduce the total flux-linkage (and then voltage) amplitude. More details will be reported in Chapter 5, where some issues and proposals related to this kind of control will be studied.

From the dynamical point of view, the system under study consists of a SM-PMSM, its mechanical load, the inverter hardware supplying motor phases and the control algorithm. For the sake of a simple analytical and practical description, in the complete electro-mechanical system different interacting subsystems can be identified, distinguishing between the controller, the electrical subsystem and the mechanical one. The various subsystems act on different time domains: the motor and mechanical load are clearly continuous-time, the control algorithm is updated at discrete time intervals, while the inverter can be considered both continuous or discrete-time, depending on the purpose of the model.

In this work, the common SV-PWM will be considered. PWM can be seen as a technique aiming at approximating a voltage level by means of the average value of a square-wave signal. Since the square-wave is characterized by constant frequency (same as the control update) and its duty-cycle is set at the start of each period, the inverter can be conveniently considered as a discrete-time system having PWM period as the sampling time. Of course, this is a simple model which only considers the averaged voltage output in an ideal condition, completely neglecting other factors like the unavoidable dead-time effects, DC bus fluctuations and discretization of the duty-cycle value, which can be considered as noise sources. While the last two usually have low influence, as it will be shown hereafter dead-time is very important during operation at low voltage (which normally corresponds to low speed), having a detrimental effect on sensorless capabilities, thus a compensation technique is usually adopted in order to mitigate its effects.

Besides the inverter modeling, the interactions between a discrete-time and a continuous-time system need to be dealt with. As for most of the digitally controlled systems, if the sampling frequency has been chosen properly (i.e. the sampling period is sufficiently shorter than the smallest time constant in the

controlled continuous-time system), a continuous-time model of the entire system can be adopted. Although this is an approximation, it allows to use much simpler analytical tools and to easily design the various regulation gains in the widely adopted terms of bandwidth and damping, which also goes in the direction of an easier commissioning and fine-tuning of the drive. In many cases, the effect of sampling and inverter delay can be neglected, in others they will be simply represented by a first-order approximation (low-pass filter).

2.4 Sensorless control

As seen in 2.3, the need for position and speed sensing in the vector control of PMSM electric drives, both for feedback purposes and FOC limits their applicability in some areas. In some cases this is due to the added cost (e.g. consumer devices), while in others the reduced reliability of the sensor itself or of its connection to the controller are the most important reasons for eliminating the use of mechanical sensors (e.g. in industrial plants).

It is worth noticing that electrical sensors, that in an industrial drive (for vector control) are usually a DC bus voltage measurement and current transducers on two of the three phases, cannot be avoided, but have lower cost and higher reliability than mechanical sensors. Another important difference is the fact that, while the former can be easily fitted into the inverter (physically near the controller), the last must be mechanically coupled to the rotor, which in some cases (especially for large power machines) means that quite long cables must be deployed between motor and inverter controller stage. This signal connections, differently from the phase supply cables, consist of many conductors (mechanically weak and relatively difficult to connect) that bring electrically weak signals, resulting in a higher fault probability of the entire system.

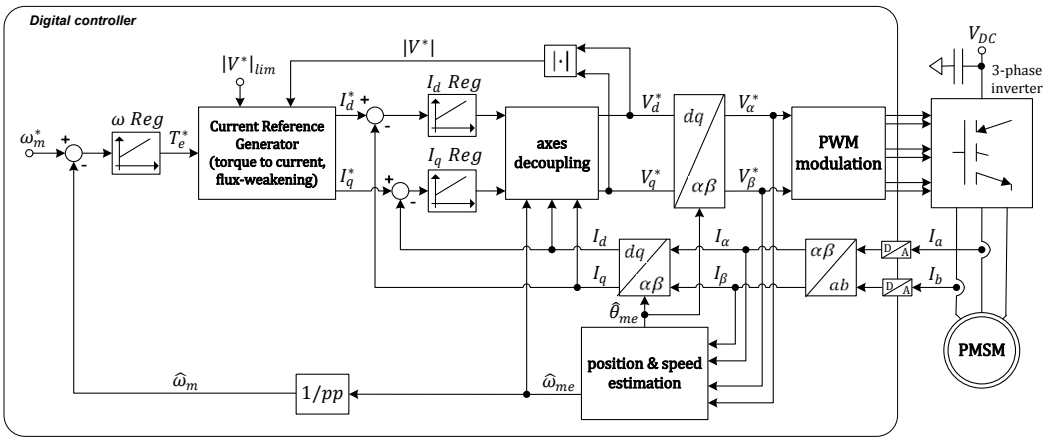

Fig. 2.13. Typical scheme for the speed vector control of a sensorless PMSM drive.

In some peculiar cases, safety issues require both sensored and sensorless redundance, while in others the use of the same drive hardware for different motors prevents from the use of mechanical sensors (e.g. aerospace).

The most common solution for controlling adjustable speed drives without mechanical sensors is the adoption of induction motors, which can be easily controlled by means of the so-called "V/f" control, where (as a first approximation) three-phase supply frequency is set equal to the reference value and voltage is proportional to it. Since this is an open-loop approach, depending on the motor characteristics a certain steady-state accuracy can be achieved, relying on the self-regulating behavior of the induction machine and on the fact that full torque is reached for small frequency slip values. In applications where speed accuracy and dynamics requirements are not high (as in the driving of fans), or the purpose is to slowly regulate, by varying motor speed, a different quantity (e.g. flow or pressure at a pump output), this can be a good solution. Besides the poor regulation performances, the main disadvantages are usually related to the low efficiency of the motor (or to the cost for achieving a good efficiency machine), while the most important advantages are reliability and simplicity. However, this kind of control leads to insufficient performances for many applications, and so a great effort has been done in research. Most of the techniques developed to overcome the poor performances of sensorless V/f fall under the category of vector control and, beyond the superior dynamical performances, they also allow to estimate with

better accuracy the mechanical rotor speed in order to perform closed-loop speed regulation.

The simplest techniques adopted for PMSMs, called sensorless BLDC (Brushless-DC) for the analogy with a mechanical commutator, switch motor currents at 120 degrees intervals, supplying two motor phases and sensing the back-EMF on the third at each sector. This technique is still widespread for very low-cost applications (e.g. small fans or compressors) where high efficiency is required or the adoption of brushes is not allowed. These methods have poor performances at low-speed and often show heavy torque ripple, due to the square-shaped currents. Since the first approaches to the sensorless control of PM motors, important developments have been done, in particular with the adoption of model-based estimation and signal injection techniques applied to vector control. Since the recent strong interest in efficiency improvement (following the energy cost increase and environmental consciousness) and the expansion of some new fields of application (e.g. electric and hybrid vehicles), sensorless control of PM motors is establishing as an effective technology, as has already happened for induction motors.

It is important to notice that, when FOC is adopted, the position of rotor or stator flux needs to be known also for torque control, since correct orientation of current vector has to be performed. To overcome the disadvantages related to the mechanical sensors, a constant effort has been devoted by research towards the development of controllers replacing measurement with estimation, resulting in the so-called "sensorless" control. Sensorless control capabilities can be quite impressive: state-of-art systems (especially for PMSMs) can achieve steady-state accuracies in the order of less than a mechanical degree in position and few rpm in speed [14]–[16], based on these few electrical measurements and quite accurate model parameters of the machine. This is possible thanks to the accuracy in the machine construction, which makes it possible to use it indirectly as a sensor. This concept is referred to as "self-sensing", which is an alternative (and more clear) term for "sensorless". However, in this work the "sensorless" will be used, since it is far more widely used, both in past literature and as a present commercially known feature.

The decrease in the cost of processing power of modern digital microcontrollers has allowed to introduce sophisticated sensorless techniques aiming at reaching similar performances with respect to their sensored counterparts, usually

estimating rather than measuring the mechanical quantities from the measurements and model knowledge of the electrical dynamic subsystem. Many years of research have led to a large variety of schemes, but they can be mainly divided between those relying on the fundamental (torque production aimed) electrical quantities and those involving special signals superimposed to the system with the only purpose of position and speed estimation.

2.4.1 Classification of the most common position and speed estimation methods

Since the development of digital controlled motor drives, many techniques have been developed and implemented with the aim of controlling speed without the use of a mechanical sensor. Despite the large variety of methods and of their names (which sometimes can be misleading), they fall into few categories, if classified according to their operating principle. Model-based techniques exploit the knowledge of the dynamic behavior of the electro-mechanical system to deduce in some way the mechanical quantities related to the rotor (speed and/or position) from the measured or imposed electrical quantities, just considering the fundamental signals needed for torque generation. The other large class of techniques can be identified as injection-based, meaning that peculiar electrical signals are imposed to the motor just for the purpose of estimation, ideally being not involved in the production of torque. These two approaches have strongly different application areas and operation characteristics, but in some cases share a common ground.

Almost all of the model-based methods for speed and position detection rely on the PM flux or back-EMF estimation, since these are directly linked to the rotor. These can be detected under any current condition (thus allowing detection under the normal control), but require a minimum back-EMF voltage level to be present, which means a certain minimum speed. The injection methods, on the other hand, usually exploit inductance dependence on the rotor position (magnetic anisotropy), which can be designed (e.g. in IPM motors) or present as a secondary-

order effect. Estimation requires in this case a current variation to be generated, in order to make the inductance visible from the motor phases terminals.

It is worth remembering that, apart from some peculiar cases, the development of sensorless control is constrained by the fact that additional costs or devices must be avoided in the hardware, with respect to a typical sensored drive. The hardware of a classical three-phase drive (by far the most common topology) relies on few electrical measurements, which consist of current transducers on two of the three phases and a DC bus sensing.

Both classes of methods suffer from an ambiguity issue about the polarity detection. In the case of anisotropy, the sinusoidal model of a salient motor ($L_d \neq L_q$) shows that rotor angle information can be extracted from the inductance map, but an ambiguity about the direction is present (since, according to the ideal model, the rotor is magnetically symmetrical). In this case, a simple alignment procedure (forcing constant current) or detection of higher order magnetic harmonics (related to saturation) is needed in order to perform control. On the other hand, PM-based techniques exploit induced voltage from the PM flux on the motor phases. Besides the fact that this quantity is null at stand-still, an additional issue is related to the confusion between rotation direction and rotor orientation (permanent magnet North vs. South pole). This means that a discontinuity must be introduced in the control, so that speed and position estimates based on back-EMF or PM flux are not used for control across null speed, where injection methods or some form of open-loop control must be adopted.

Depending on the application, this can be acceptable or not. In simple applications, initial alignment through forcing of a constant current is sufficient, while in some cases, where uncontrolled movement must be avoided, these issues can be overcome by exploiting some secondary effects (not included in the usual ideal model). One example is the exploitation of the second harmonic behavior in injection-based techniques, which reflects magnetic saturation and then the direction of the permanent magnet field [17], [18].

Chapter 3
Model-based sensorless control

Sensorless control of non-salient PM synchronous motors is typically based on back-EMF or PM flux linkage estimation in the stationary or synchronous reference frame, although many variants are present, which include the use of linear ([19]–[24]), nonlinear ([25]–[27]), Kalman filtering ([22], [28]) and phase-locked loop processing ([29]). Almost all of the model-based methods for speed and position detection rely on the PM flux or back-EMF estimation, since these are directly linked to the rotor, and can be detected also at null current. The injection methods, on the other hand, usually exploit inductance dependence on the rotor position (magnetic anisotropy), which can be designed (e.g. in IPM motors) or present as a secondary-order effect.

Both classes of methods suffer from an ambiguity issue about the polarity detection. In the case of anisotropy, the sinusoidal model of a salient motor ($L_d \neq L_q$) shows that rotor angle information can be extracted from the inductance map, but an ambiguity about the direction is present (since, according to the ideal model, the rotor is magnetically symmetrical). In this case, a simple alignment procedure (forcing constant current) or detection of higher order magnetic harmonics (related to saturation) is needed in order to perform control. On the other hand, PM-based techniques exploit induced voltage from the PM flux on the motor phases. Besides the fact that this quantity is null at null speed, an additional issue is related to the confusion between rotation direction and rotor orientation (North vs. South pole). This means that a discontinuity must be introduced in the control, so that speed and position estimates based on back-EMF or PM flux are not used for control across null speed, where some form of open-loop control is used, or injection-based estimation methods are adopted.

3.1 Industrial general-purpose sensorless drive for SM-PMSM

One of the projects carried out during the PhD course, which was supported by a private company, consisted in the development of a sensorless control strategy for SM-PMSM, to be implemented on a general-purpose industrial drive. The company was already present on the market with a sensored PMSM drive, which had to be used as a platform for the new algorithm. The target applications could have been mainly pumps, fans, compressors and some machinery (conveyors, extrusion), or any cases where low-accuracy speed or torque control is required. Also, since in these applications normal operating cycle comprises only short periods at low-speed, and relatively low and slowly-varying load torque is present at startup, an open-loop starting procedure can be acceptable, so that the development had to be focused on the medium-high speed control.

The new control had to be built on the basis of a commercially available drive, keeping unchanged hardware and part of software (signal sampling, PWM generation, parameters identification, architecture), which had been developed for the sensored control. The drive had to be able to control any generic SM-PMSM (commercially identified as "brushless AC motor", and usually available for automation applications) matched to the inverter power capability. The same controller board had to be used for different motor sizes, running the same firmware (except for some data related to the inverter size). These requirements related to the general-purpose nature of the controller, had an important impact on the choice of the techniques to be adopted. In particular, any method involving off-line measurement with equipment other than that already present on a normal electric drive had to be discarded. Moreover, the only parameters that had to be inserted at the commissioning stage had to be the ones present on the motor nameplate, namely nominal values of voltage, current, speed or frequency, number of poles and, since the particular class of motors targeted, torque constant. This meant that, for the other necessary parameters, the values obtained by means of

the initial estimation procedure (stand-still or very low-speed rotation) had to be used.

An important effort has been devoted to the study of the dynamical properties of the sensorless algorithm and to the development of tuning criterions, with the aim of making the commissioning operation as simple as possible for the operator, while obtaining acceptable performances over a vast range of motors. This implied both analytical and experimental work to be done in order to characterize the various factors influencing dynamical and steady-state operation (sections 3.2 and 3.3, also presented in [29]). Besides the novel analytical approach adopted, as a result of this work simple formulas for the estimation process gains as a function of required bandwidth and damping factor have been obtained.

Moreover, some hints on the implementation of self-diagnostics solutions have been studied, especially for startup and low-speed operation, which are certainly the most critical conditions. In fact, for the possible applications of the considered drive, it is very important to ensure reliability and to detect any control faults (which cannot be totally prevented, since the heavy influence of random variables such as load fluctuations and other "noise" sources, including in this case parametric variations), and signal or report it to a supervisor device if needed.

Finally, the dramatic improvement in the low-speed control robustness and accuracy at low-speed obtained by adding a constant direct-axis current, which was previously adopted in other works and also in a commercial drive, but not analytically described, has been analyzed in detail from the dynamical point of view ([30]).

The experimental tests that will be described in this chapter have been performed on a test bench comprising two similar PM motors driven by two 5.5 kW general-purpose industrial drives, the one under test and one acting as a braking load (see section A.1).

3.2 Adopted estimation algorithm

As seen in 3.1, many different and sometimes very sophisticated sensorless algorithms for PMSM control have been developed and studied in the last decades.

Among these, many techniques introduce important implementation issues, or need a specific knowledge about the motor to be controlled, since they require heavy offline parameter identification. Some show poor performances and could need much work to become reliable or their principle of operation suffers from poor analytical explanation (based on second order effects). Since all these considerations, the focus was concentrated on quite simple and proven methods, with a particular focus on their reliability, parameter dependence and dynamical characterization, so that a good method for automatic gain tuning could be implemented with confidence for a large range of motors, and stability could be ensured with a good confidence.

Taking into account that the project involved a generic surface mount motor, the methods exploiting anisotropy were discarded, although they have been applied to this class of machines, as also reported in many papers in literature. In fact, in these cases, the estimation relies on what is formally an unwanted parasitic characteristic (due to the permanent magnet flux induced saturation) and, typically, shows a strong variability with the operating conditions (currents in particular). This last factor leads to the necessity of a previous knowledge on the motor characteristics (which requires off-line testing) to achieve a good control while, in some cases, can make it impossible to estimate position and speed. A further step could be the implementation of algorithms for the automatic detection and exploitation of anisotropy, but of course this was outside the scope of this project.

A first distinction among estimation techniques is the formal difference between estimators and observers, which can be both adopted for the purpose of position and speed estimation. Both algorithms act on the basis of model and measurements, aiming at obtaining an estimate of a variable which is not measured (or has a noise affected measurement). Estimators act by simply exploiting the dynamical system equations, and explicitly obtaining the term needed. Observers, on the other hand, are basically a virtual copy of the model, which is fed with the same inputs as the real one. The state estimation is then corrected by using the comparison between measured and estimated outputs, in a feed-back fashion. In the case of sensorless, according to some methods estimators are adopted to obtain stator flux from integration of the non-resistive voltage, or back-EMF is deduced by simply subtracting the resistive and inductive voltage drops from the phase supply. These techniques, although very simple, are usually

affected by calculation-related issues, thus requiring particular attention when applied. In the case of integration, any unavoidable measurement or actuation offset will result in estimate drift, while derivative operation exalts the always present high-frequency noise. For these reasons, observers are widely adopted, since the measurement-based feedback allows to reduce the impact of non-idealities, at the cost of a usually higher computational cost and possible stability issues. Moreover, the feedback gains allow to design a proper filtering action on the estimates, while providing consistent outputs at steady-state, once stability is ensured.

Another major classification among the various estimation algorithms based on PM flux or back-EMF can be done on the basis of their reference frame of operation, either synchronous or stationary. While, for stationary frame model-based observers or estimators, electrical and mechanical subsystems can be separately treated, the intrinsic nature of the synchronous ones leads to a deep coupling between the two sets of equations. In fact, since measured electrical quantities come from the real-world stationary frame (transposition from two to three coordinates is a pure algebraic matter), transformation to the synchronous axes involves the knowledge of the rotor position, or its hypothetical value. Moreover, the phase equations contain terms proportional to speed, which indeed is not known, but needs to be estimated by the same scheme. This translates into indirect loops, which are not easy to be modeled and often overlooked. The choice of a stationary reference frame back-EMF based algorithm is motivated by the possibility to separately analyze and design the various observer parts, also maintaining electrical subsystem observation under any condition, included zero speed.

An important disadvantage of the stationary reference frame observer is that, since sinusoidal signals are involved, the back-EMF estimation at steady-state depends on the rotation speed, and it will be demonstrated in 3.3.1 that the behavior can be represented by a second-order low-pass filter. In the case heavy estimation noise (which is the limitation factor for bandwidth increase) imposes a relatively low bandwidth, the estimated back-EMFs can suffer from a non-negligible phase lag, which corresponds to a position error, which is only relevant at high-speed. Since, in this case, the high level of the back-EMF signal ensures reliable speed estimation, thanks to the modified algorithm proposed in [19], null phase-lag can be obtained with the use of a speed dependent term. However, the

application of this improvement has been shown experimentally to be detrimental for the control robustness at low-speed, so mixed approaches, where both the basic and the speed-compensated version of the observer are used could be a solution, and could represent one of the future developments of the present estimation algorithm.

The back-EMF observation is of course just one of the possible approaches to model-based speed and position estimation. Among the many methods that have been proposed, linear observers have been preferred for their intrinsic robustness, simplicity (also from the implementation point of view), and easiness of analysis (which also leads to simple gain setting procedures). Moreover, as can be seen from the voltage equations (2.8)(2.17), valid for an isotropic rotor PMSM, the observed system equations only involve two parameters, namely the stator resistance and inductance. Some different observers also require the use of the PM flux magnitude parameter, which makes the estimation sensitive to the accuracy of one more parameter. The observation of flux, although widely adopted, suffers heavily from any current measurement or voltage actuation offset, since these contributions result (as a result of integration) in an estimation drift. Many techniques have been proposed for the elimination of offset effects, but they increase complexity and decrease robustness.

3.2.1 Analytical description of the position and speed estimation process

Since an isotropic motor model is considered, it is convenient to make use of a simplified notation, using a complex notation instead of a vector one (matrices for inductance are not needed). This leads to an interesting compact notation that, in the Laplace domain, allows to obtain a dynamical characterization of position and speed estimation based on back-EMF observation, by means of a straightforward linearization.

The electrical subsystem can be described by the equation in the stationary reference frame

$$\boldsymbol{U}_{\alpha\beta} = R_s \boldsymbol{I}_{\alpha\beta} + sL_{ss}\boldsymbol{I}_{\alpha\beta} + \boldsymbol{E}_{\alpha\beta} \tag{3.1}$$

or, in the synchronous axes,

$$\boldsymbol{U}_{dq} = R_s \boldsymbol{I}_{dq} + sL_s \boldsymbol{I}_{dq} + j\omega_{me} L_s \boldsymbol{I}_{dq} + \boldsymbol{E}_{dq} \tag{3.2}$$

The coupling between mechanical and electrical subsystems is described by the back-EMF definition (for sinusoidally distributed flux-linkage)

$$\boldsymbol{E}_{\alpha\beta} = s\boldsymbol{\lambda}_{mg\,\alpha\beta} = j\omega_{me}\Lambda_{mg} \cdot e^{j\theta_{me}} \tag{3.3}$$

or

$$\boldsymbol{E}_{dq} = 0 + j\omega_{me}\Lambda_{mg} \tag{3.4}$$

As already mentioned, the notation adopted for electrical quantities is complex, where the orthogonal components of a generical quantity X are represented as $\boldsymbol{X}_{\alpha\beta} = X_\alpha + jX_\beta$ in the stationary reference frame and $\boldsymbol{X}_{dq} = X_d + jX_q$ for the synchronous one. The derivative operator $^{d}/_{dt}$ is expressed by the Laplace operator s.

A dynamic equation of the back-EMF is also necessary. If motor electrical speed ω_{me} is considered as constant, motor back-EMF dynamics can be approximated by:

$$s\boldsymbol{E}_{\alpha\beta} = j\omega_{me}\boldsymbol{E}_{\alpha\beta} \tag{3.5}$$

Estimation of motor back-EMF can be therefore carried out by the extension of a classical Luenberger linear observer of motor currents, which can be built by considering the model (3.1) and using measured currents as feedback values, i.e.:

$$s\hat{\boldsymbol{I}}_{\alpha\beta} = \frac{1}{L_{ss}}\left(\boldsymbol{U}^*_{\alpha\beta} - R_s\hat{\boldsymbol{I}}_{\alpha\beta} - \hat{\boldsymbol{E}}_{\alpha\beta}\right) + K_1\left(\boldsymbol{I}_{\alpha\beta} - \hat{\boldsymbol{I}}_{\alpha\beta}\right) \tag{3.6}$$

$$s\hat{\boldsymbol{E}}_{\alpha\beta} = j\tilde{\omega}_{me}\hat{\boldsymbol{E}}_{\alpha\beta} + K_2\left(\boldsymbol{I}_{\alpha\beta} - \hat{\boldsymbol{I}}_{\alpha\beta}\right) \tag{3.7}$$

where K_1 and K_2 are (real) gains, $\hat{\boldsymbol{I}}_{\alpha\beta}$ and $\hat{\boldsymbol{E}}_{\alpha\beta}$ are current and back-EMF estimates respectively. The term (parameter) $\tilde{\omega}_{me}$ can be set equal to the estimated electrical speed or kept null. This choice affects the steady-state error and leads to a different small-signal position and speed estimation transfer functions. The two operating modes (i.e. the substitution $\tilde{\omega}_{me} = \hat{\omega}_{me}$ or $\tilde{\omega}_{me} = 0$)

show different robustness and noise propagation behavior. As a first approximation, it is simple to guess that the choice $\widetilde{\omega}_{me} = \widehat{\omega}_{me}$ is critical and suffers from noise and dynamic instability. The observer dynamics described by (3.6) and (3.7) is in this last case non-linear due to the presence of angular speed, but can be approximated to a linear system, considering that speed is relatively slowly varying. However, this simplification is critical because transient conditions are difficult to analyze, since an implicit feedback loop takes place due to the dependence of $\widehat{\omega}_{me}$ on the back-EMF estimates, which again depends on the estimated speed, in this case. Preferring stability and robustness, the solution adopts the $\widetilde{\omega}_{me} = 0$ solution, which can also be fully analytically characterized. The resulting position estimation error is discussed in 3.3.1.

The block diagram of the estimation system is shown in Fig. 3.1.

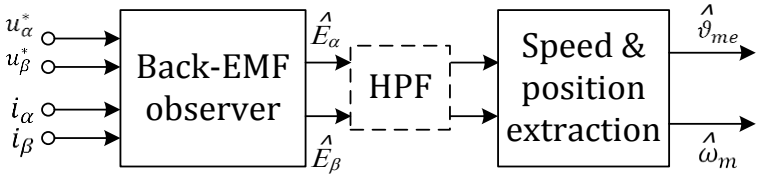

Fig. 3.1. Position and speed estimation block diagram.

The reference voltage vector $\boldsymbol{U}_{\alpha\beta}^*$ is considered as a measured value, so considering an ideal inverter able to accurately reproduce reference to the output ($\boldsymbol{U}_{\alpha\beta} = \boldsymbol{U}_{\alpha\beta}^*$). However, non-idealities (dead-time, switch devices voltage drop) affect actual stator voltage and could lead to wrong estimates, as it will be shown hereafter. Although ideally not necessary, the presence of a high-pass filtering action on the estimated back-EMF components (before speed and position extraction) is needed to remove any DC component that could affect the reliability of position and speed estimation. This filtering, as will be shown in 3.3.4, introduce a position estimation error. Its influence is however usually negligible since its pole frequency is very low with respect to the lowest operation electrical frequency (corresponding to the lowest speed). Thus, distortion is non-negligible only at very low-speed (where they are not useful for position and speed estimation due to the low amplitude).

The motor electrical model (3.1) can be written in a state space model (explicitly expressing the current derivative):

$$s\boldsymbol{I}_{\alpha\beta} = \frac{1}{L_{ss}}\left(\boldsymbol{U}_{\alpha\beta} - R_s\boldsymbol{I}_{\alpha\beta} - \boldsymbol{E}_{\alpha\beta}\right) \tag{3.8}$$

Then, algebraic manipulation of this last equation together with the observer updates (3.5)-(3.7) it is possible to obtain the transfer function linking the estimated and actual back-EMFs. The first step consists in the subtraction of (3.8) and (3.6), which leads to

$$\boldsymbol{I}_{\alpha\beta} - \hat{\boldsymbol{I}}_{\alpha\beta} = \frac{-\left(\boldsymbol{E}_{\alpha\beta} - \hat{\boldsymbol{E}}_{\alpha\beta}\right)}{sL_{ss} + R_s + K_1L_{ss}} \tag{3.9}$$

The substitution of last obtained result ($\boldsymbol{I}_{\alpha\beta} - \hat{\boldsymbol{I}}_{\alpha\beta}$) in the back-EMF estimation update (3.7)

$$s\hat{\boldsymbol{E}}_{\alpha\beta} = j\tilde{\omega}_{me}\hat{\boldsymbol{E}}_{\alpha\beta} + K_2\frac{-\left(\boldsymbol{E}_{\alpha\beta} - \hat{\boldsymbol{E}}_{\alpha\beta}\right)}{sL_{ss} + R_s + K_1L_{ss}} \tag{3.1}$$

and extraction of the estimation transfer function yields:

$$\frac{\hat{\boldsymbol{E}}_{\alpha\beta}}{\boldsymbol{E}_{\alpha\beta}}(s) = \frac{-K_2}{(s - j\tilde{\omega}_{me})(sL_{ss} + R_s + K_1L_{ss}) - K_2} \tag{3.10}$$

Further manipulation of (3.10) allows the calculation of transfer function as the sum of separate real and imaginary contributions on a common real denominator, having with $\mathcal{R}(s) \triangleq \mathbb{Re}\left\{\frac{\hat{\boldsymbol{E}}_{\alpha\beta}}{\boldsymbol{E}_{\alpha\beta}}\right\}$ and $\mathcal{I}(s) \triangleq \mathbb{Im}\left\{\frac{\hat{\boldsymbol{E}}_{\alpha\beta}}{\boldsymbol{E}_{\alpha\beta}}\right\}$:

$$\begin{aligned}&\frac{\hat{\boldsymbol{E}}_{\alpha\beta}}{\boldsymbol{E}_{\alpha\beta}}(s)\\ &= \frac{-K_2[s(sL_{ss} + R_s + K_1L_{ss}) - K_2] \;\; - \;\; j\;\; K_2\tilde{\omega}_{me}(sL_{ss} + R_s + K_1L_{ss})}{[s(sL_{ss} + R_s + K_1L_{ss}) - K_2]^2 + [\tilde{\omega}_{me}(sL_{ss} + R_s + K_1L_{ss})]^2}\\ &= \mathcal{R}(s) + j\mathcal{I}(s)\end{aligned} \tag{3.11}$$

Since the back-EMF can be expressed as

$$\boldsymbol{E}_{\alpha\beta} = \Lambda_{mg}\omega_{me}(-\sin\theta_{me} + j\cos\theta_{me}) \tag{3.12}$$

instantaneous estimation of the position estimation can be obtained as the argument angle of the estimated back-EMF vector:

$$\hat{\theta}_{me} = tan^{-1}\left(-\frac{\hat{\boldsymbol{E}}_{\alpha}}{\hat{\boldsymbol{E}}_{\beta}}\right) \tag{3.13}$$

If this model is adopted for the rotor position extraction starting from the observed back-EMF and the transfer function (3.11) is considered, the estimation path model shown in Fig. 3.2 can be simply obtained.

To obtain a characterization of the position and speed estimation process (from the estimated back-EMF), a small-signal approximation around steady-state rotor position value $\boldsymbol{\Theta}_{me}$ is applied. The transfer function linking the actual and estimated angular position can be calculated through linearization of the arctangent function, leading to two separate contributions on the estimated angle, due to the real and imaginary parts of $\hat{\boldsymbol{E}}_{\alpha\beta}$, i.e.

$$\begin{aligned}\frac{\hat{\theta}_{me}}{\theta_{me}} = &\frac{\partial}{\partial \hat{E}_{\alpha}}\left[tan^{-1}\left(\frac{-\hat{E}_{\alpha}}{\hat{E}_{\beta}}\right)\right]\Bigg|_{\theta_{me}=\Theta_{me}} \cdot \frac{\hat{E}_{\alpha}}{\theta_{me}} \\ &+ \frac{\partial}{\partial \hat{E}_{\beta}}\left[tan^{-1}\left(\frac{-\hat{E}_{\alpha}}{\hat{E}_{\beta}}\right)\right]\Bigg|_{\theta_{me}=\Theta_{me}} \cdot \frac{\hat{E}_{\beta}}{\theta_{me}}\end{aligned} \tag{3.14}$$

The estimated components of the back-EMF can be expressed by means of the real and imaginary parts of the transfer function (3.11), i.e.:

$$\hat{\boldsymbol{E}}_{\alpha\beta} = \hat{E}_{\alpha} + j\hat{E}_{\beta} = \left(\mathcal{R}(s)E_{\alpha} - \mathcal{I}(s)E_{\beta}\right) + j\left(\mathcal{I}(s)E_{\alpha} + \mathcal{R}(s)E_{\beta}\right) \tag{3.15}$$

that, after substitution in (3.14), leads to

$$\begin{aligned}\frac{\hat{\theta}_{me}}{\theta_{me}} = &\frac{\partial}{\partial \hat{E}_{\alpha}}\left[tan^{-1}\left(\frac{-\hat{E}_{\alpha}}{\hat{E}_{\beta}}\right)\right]\Bigg|_{\theta_{me}=\Theta_{me}} \cdot \frac{\left(\mathcal{R}(s)E_{\alpha} - \mathcal{I}(s)E_{\beta}\right)}{\theta_{me}} + \frac{\partial}{\partial \hat{E}_{\beta}}\left[tan^{-1}\left(\frac{-\hat{E}_{\alpha}}{\hat{E}_{\beta}}\right)\right]\Bigg|_{\theta_{me}=\Theta_{me}} \cdot \\ &\frac{\left(\mathcal{I}(s)E_{\alpha} + \mathcal{R}(s)E_{\beta}\right)}{\theta_{me}}\end{aligned} \tag{3.16}$$

The corresponding estimation path model is shown in Fig. 3.3.

The derivative terms can be calculated as follows:

$$\frac{\partial}{\partial \hat{E}_{\alpha}}\left[tan^{-1}\left(\frac{-\hat{E}_{\alpha}}{\hat{E}_{\beta}}\right)\right]\Bigg|_{\theta_{me}=\Theta_{me}} = \frac{-\cos\Theta_{me}}{\Lambda_{mg}\omega_{me}} \tag{3.17}$$

$$\frac{\partial}{\partial \hat{E}_\beta}\left[tan^{-1}\left(\frac{-\hat{E}_\alpha}{\hat{E}_\beta}\right)\right]\Big|_{\theta_{me}=\Theta_{me}} = \frac{-sin\,\Theta_{me}}{\Lambda_{mg}\omega_{me}}$$

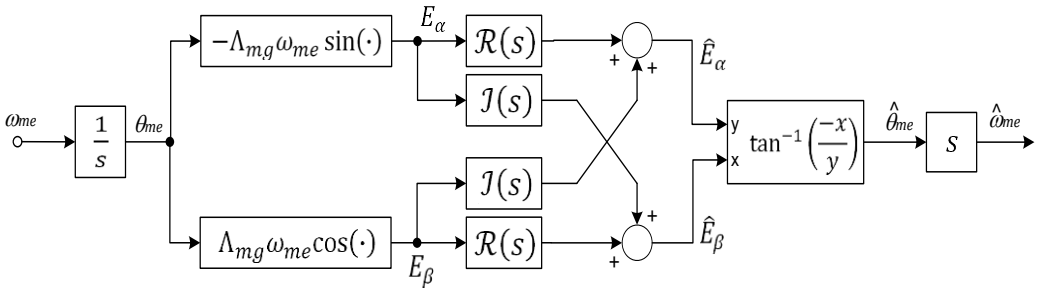

Fig. 3.2. Estimation path model (non-linear system).

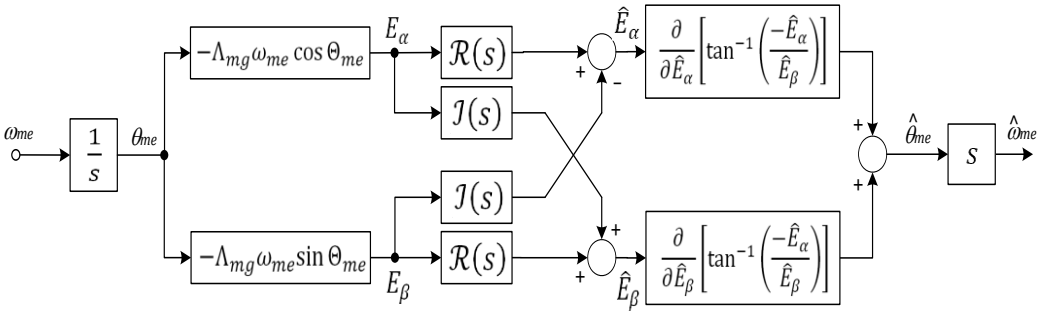

Fig. 3.3. Estimation path model (small-signal linearized system).

while the back-EMF terms E_α and E_β can be substituted by their small-signal gain with respect to θ_{me}

$$\frac{\hat{\theta}_{me}}{\theta_{me}} = \frac{-\cos\Theta_{me}}{\Lambda_{mg}\omega_{me}} \cdot \left(\mathcal{R}(s)\frac{\partial E_\alpha}{\partial \theta_{me}}\Big|_{\theta_{me}=\Theta_{me}} - \mathcal{I}(s)\frac{\partial E_\beta}{\partial \theta_{me}}\Big|_{\theta_{me}=\Theta_{me}}\right) + \frac{-sin\,\Theta_{me}}{\Lambda_{mg}\omega_{me}} \cdot \left(\mathcal{I}(s)\frac{\partial E_\alpha}{\partial \theta_{me}}\Big|_{\theta_{me}=\Theta_{me}} + \mathcal{R}(s)\frac{\partial E_\beta}{\partial \theta_{me}}\Big|_{\theta_{me}=\Theta_{me}}\right) \quad (3.18)$$

By considering the simple derivatives

$$\left.\frac{\partial E_\alpha}{\partial \theta_{me}}\right|_{\theta_{me}=\Theta_{me}} = -\cos\Theta_{me}\,\omega_{me}\Lambda_{mg}$$
$$\left.\frac{\partial E_\beta}{\partial \theta_{me}}\right|_{\theta_{me}=\Theta_{me}} = -\sin\Theta_{me}\,\omega_{me}\Lambda_{mg} \tag{3.19}$$

expression (3.18) can be expanded

$$\begin{gathered}\frac{\hat{\theta}_{me}}{\theta_{me}} = \left[-\cos\Theta_{me}\,\omega_{me}\Lambda_{mg}\cdot\mathcal{R}(s) + \sin\Theta_{me}\,\omega_{me}\Lambda_{mg}\cdot\mathcal{I}(s)\right]\cdot \\ \left(\frac{-\cos\Theta_{me}}{\Lambda_{mg}\omega_{me}}\right) + \left[-\cos\Theta_{me}\,\omega_{me}\Lambda_{mg}\cdot\mathcal{I}(s) - \sin\Theta_{me}\,\omega_{me}\Lambda_{mg}\cdot\mathcal{R}(s)\right]\cdot \\ \left(\frac{-\sin\Theta_{me}}{\Lambda_{mg}\omega_{me}}\right) = \\ \cos^2\Theta_{me}\cdot\mathcal{R}(s) - \sin\Theta_{me}\cos\Theta_{me}\cdot \\ \mathcal{I}(s) + \cos\Theta_{me}\sin\Theta_{me}\cdot\mathcal{I}(s) + \sin^2\Theta_{me}\cdot\mathcal{R}(s)\end{gathered} \tag{3.20}$$

obtaining, as expected, a transfer function having null imaginary part and no dependence on the position, which has the form of a second-order low-pass filter:

$$\frac{\hat{\theta}_{me}}{\theta_{me}} = \mathcal{R}(s) = \frac{1}{1 + s\left(\frac{R_s - K_1 L_{ss}}{K_2}\right) - s^2\,L_{ss}/K_2} \tag{3.21}$$

The dynamics can thus be described by means of natural frequency and damping factor:

$$\omega_o = \sqrt{-\frac{K_2}{L_{ss}}},\ \xi = \frac{R_s - K_1 L_{ss}}{2K_2}\omega_0 \tag{3.22}$$

These parameters can be used to design observer's gains as a function of desired closed-loop bandwidth, this last being a function of natural frequency and damping factor themselves. At the observer gains tuning, a constant ratio (more than unity, of course, e.g. 3 times or more) rule between required speed control bandwidth and observer crossing frequency can be adopted, together with a proper damping factor (e.g. Butterworth or unity).

Although analytical description of the observer dynamics has been already obtained [24], this approach can give a contribution to simplification and understanding of the design of the observer's gains, since the easier manipulation of the classical frequency response expression, with respect to the previously used eigenvalues. Moreover, differently from previous work on this method for position

and speed estimation, in this case the actual dynamics of position and speed information contained in the observed back-EMF is studied, rather than just the observed back-EMF itself. This is possible thanks to the complex representation of the electrical quantities and their estimated counterparts (which greatly simplifies calculation and notation), and by the application of small-signal linearization to the ideal position and speed extraction process (based on the arctangent calculation). In the following sections, a simple analysis of some non-idealities effects is obtained by means of the same approach.

3.2.2 PLL for position and speed extraction

A first approach to position estimation can be the use of an inverse trigonometric function directly from the back-EMF space vector (e.g. arctangent function), while speed can be obtained as a derivative of position angle. Although this method has been used in many cases, resulting estimation noise represents an important issue. Low-pass filtering can be applied to speed estimate, while position filtering is quite critical, due to the dependence on speed and steady-state error introduced. An efficient alternative is the adoption of a quadrature phase-locked loop (Q-PLL or simply PLL, Fig. 3.4), [31], which has widespread use in many fields as a means for extracting phase and/or frequency from a sinusoidal signal affected by noise or distortion.

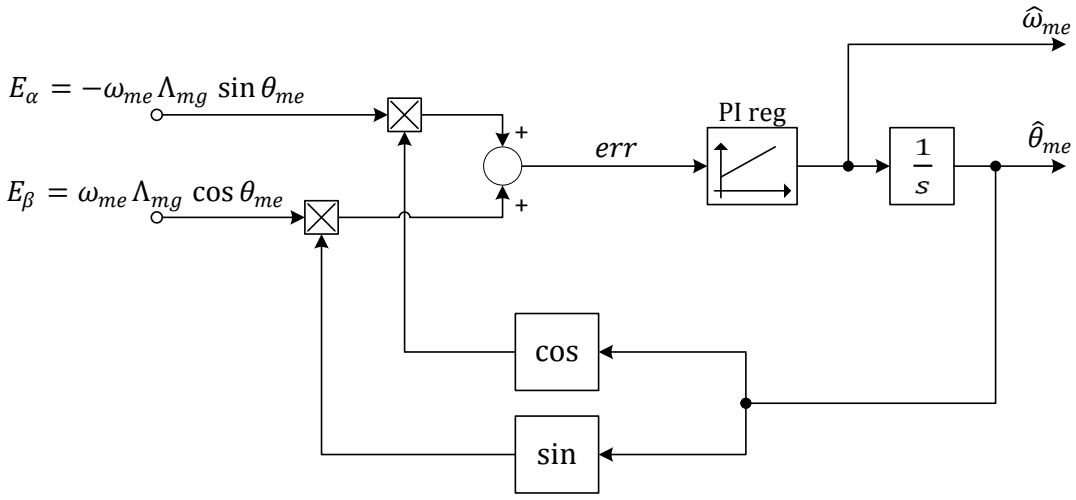

Fig. 3.4. Block diagram of the quadrature PLL.

As it will be shown hereafter, Quadrature-PLL can be seen as a band-pass filter which is tuned on the present estimated frequency, thus following variations around the steady-state with a certain constant bandwidth. From a different point of view, Q-PLL is a closed-loop algorithm able to track, with a certain bandwidth, the phase and frequency of a complex exponential signal, which in the case of sensorless position and speed estimation is the back-EMF:

$$\hat{\boldsymbol{E}}_{\alpha\beta} \cong \boldsymbol{E}_{\alpha\beta} = j\omega_{me}\Lambda_{mg}(\sin\theta_{me} - j\cos\theta_{me}) = j\omega_{me}\Lambda_{mg}\, e^{j\theta_{me}} \tag{3.23}$$

giving a filtered estimation for the electrical position and speed, with null steady-state error.

As depicted in Fig. 3.5, a simple linearized model can be obtained, which is valid in the neighborhood of the steady-state condition (i.e. around null error point). The scheme can also be seen as an observer of part of the mechanical system which describes the relation between speed and position ($s\,\theta_{me} = \omega_{me}$). It can be intuitively guessed that, since a double integrator is present in the loop, both speed and position estimates will track the observed quantities with null error at steady-state. The error signal feeding the PI regulator is:

$$err = -E_\beta \sin\hat{\theta}_{me} + E_\alpha \cos\hat{\theta}_{me} \tag{3.24}$$

that can be written as

$$err = -\omega_{me}\Lambda_{mg}\cos\theta_{me}\sin\hat{\theta}_{me} + \omega_{me}\Lambda_{mg}\sin\theta_{me}\cos\hat{\theta}_{me} = \\ = \omega_{me}\Lambda_{mg}\sin(\theta_{me} - \hat{\theta}_{me}) \tag{3.25}$$

The Q-PLL open-loop transfer function can be expressed as

$$G_{PLL_{OL}}(s) = \omega_{me}\Lambda_{mg}Reg_{PLL}(s)\frac{1}{s} = \omega_{me}\Lambda_{mg}\left(K_{P_{PLL}}\frac{1+\tau_{PLL}s}{\tau_{PLL}s}\right)\frac{1}{s} \tag{3.26}$$

where $Reg_{PLL}(s)$ is the PI regulator transfer function and $K_{P_{PLL}}, \tau_{PLL}$ are its proportional gain and time constant.

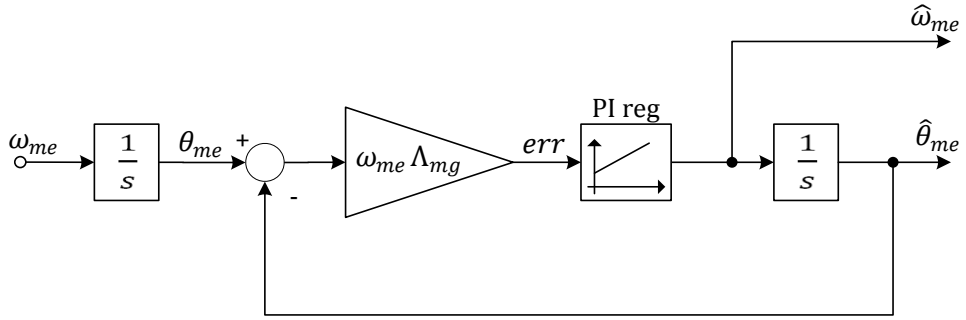

Fig. 3.5. Equivalent linearized scheme for the quadrature PLL.

Using one of the simplest approximated approaches to stability analysis, the transition frequency must be set to lying in the region after the regulator zero, so having $20\ dB/dec$ slope. The open-loop unity gain match frequency corresponds to the closed-loop bandwidth:

$$\omega_T = K_{P_{PLL}}\omega_{me}\Lambda_{mg} \tag{3.27}$$

which depends on the speed value. Considering the continuous-time domain, there is no upper limit to the bandwidth, while a lower boundary is set by the approximated condition:

$$K_{P_{PLL}}\omega_{me}\Lambda_{mg} > {}^{1}/_{\tau_{PLL}} \tag{3.28}$$

Since the worst case for satisfying this last condition is the lowest operating speed, one must ensure

$$K_{P_{PLL}} > \frac{1}{\omega_{me_{min}} \Lambda_{mg} \tau_{PLL}} \tag{3.29}$$

If sampling is taken into account, of course a bandwidth must be limited at a fraction of the sampling frequency. This is usually not a restrictive condition, since maximum speed control bandwidth is orders of magnitude lower than sampling frequency.

From a theoretical point-of-view, the loop gain should be adapted to the varying frequency condition of the motor in order to maintain the same bandwidth of PLL. Normalization could be done by scaling gain either with the vector amplitude or with the estimated speed, but in both cases compensation is critical to be done on-line (as it introduces an inherent feed-back loop having a quite complex dynamic behavior), and would lead to very limited benefits. In fact, the signal-to-noise ratio increases almost linearly with speed, due to the growth in the back-EMF vector amplitude. This leads to the possibility to widen the position and speed estimation bandwidth, given a constant noise level. Moreover, if a high-pass filter is introduced on the estimated back-EMFs, aiming at improving robustness against measurement and actuation offsets, the estimation bandwidth is limited by the filter pole, thus naturally increasing with speed. These points lead to state that a gain normalization is not needed, as it would limit the bandwidth at the worst case possible (low-speed operation), which has been experimentally proven. An intermediate approach could be the application of an upper saturated normalization factor, so that constant dynamics is obtained at low-speed, while at speeds over a certain threshold bandwidth is improved.

While simulations did not point out severe issues related to normalization, experimental implementation showed a robustness degradation. A quite obvious explanation for this can be found by considering that the speed value used for division is indeed an estimate, which in turn depends on the PLL behavior. This means that an intrinsic feedback loop is built, by linking scaling of the PLL inputs and speed estimate output. A simple and effective solution to this issue is the use of estimated back-EMF magnitude as the scaling factor, which avoids the undesired feedback loop. However, this normalization technique adds further noise to the PLL input, as a result of the nonlinear mixing of back-EMF estimates and their magnitude. For this reason, a modified vector magnitude calculation is introduced, which is based on a synchronous frame filtering, as in Fig. 3.6.

Supposing a small speed estimation error, the magnitude of fundamental components is maintained, while higher order harmonics are filtered out.

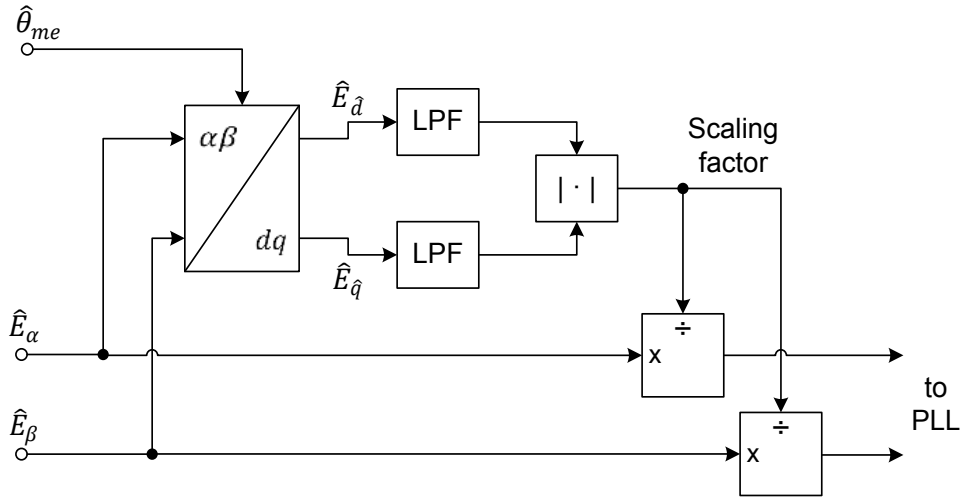

Fig. 3.6. Back-EMF estimates magnitude normalization for constant-bandwidth PLL.

An important aspect about position and speed extraction from the back-EMF is the polarity vs. speed ambiguity issue. In fact, back-EMF contain the angle exponential term multiplied by speed, which results in a sign inversion between positive and negative speed.

$$j\omega_{me}\Lambda_{mg}\, e^{j\theta_{me}} = -j\omega_{me}\Lambda_{mg}\, e^{j(\theta_{me}\pm\pi)} \tag{3.30}$$

Unfortunately, the same waveforms are obtained for negative speed or phase opposition ($\pm\pi$ difference), which means that the difference between these two conditions is not observable. A proper startup procedure must take this into account, avoiding the utilization of speed and position estimates around zero speed, and forcing rotation in a known direction by means of an open-loop procedure. If speed sign is reliably known, Q-PLL input signals can be taken as straight or reversed, achieving correct estimation.

3.3 Steady-state estimation error analysis

In an actual drive system, non-ideal elements in the measurement (currents and DC-bus voltage) and actuation (three-phase inverter), together with the uncertainty about the motor electrical parameters, can represent different estimation error sources. Excluding motor model non-idealities, the main causes of steady-state position estimation error can be recognized:

- estimation phase lag due to observer's response;
- current measurement and voltage actuation offsets;
- parameters uncertainty;
- phase advance due to high-pass filtering.

Speed estimation error can be easily obtained from the position one, since the simple derivative relation linking the two quantities. The synchronous nature of the machine makes constant speed estimation error unlikely to occur, except for the case of estimation and control loss ("*phase loss*", as it will be called in 3.6.1) which, however, cannot be correctly considered as a steady-state condition.

In this section, the effects of the various estimation error sources listed above will be described analytically. In the cases of the observer's response lag and high-pass filter advance this analysis can be used for compensation, while in the other cases the results can be used for worst-case determination, on the basis of parameters accuracy and system current or voltage offsets.

3.3.1 Estimation phase lag due to observer's response

The response of the closed-loop estimation transfer function (3.21) directly provides the steady-state phase delay of the observer:

$$\theta_{me} - \hat{\theta}_{me} = \angle \boldsymbol{E}_{\alpha\beta} - \angle \widehat{\boldsymbol{E}}_{\alpha\beta} = -\angle \frac{\widehat{\boldsymbol{E}}_{\alpha\beta}}{\boldsymbol{E}_{\alpha\beta}} = -\angle \left\{ \frac{-K_2}{(j\omega_{me} - j\tilde{\omega}_{me})(j\omega_{me}L_{ss} + R_s + K_1 L_{ss}) - K_2} \right\} \tag{3.31}$$

It can be pointed out that, in the case $\tilde{\omega}_{me} = \omega_{me}$ (as at steady-state the estimated speed $\hat{\omega}_{me}$ is always equal to the actual one ω_{me}) and no error in measurement or in the parameters are considered, the position estimation error is zero. This can be intuitively demonstrated by considering model (3.7), leading to null current estimation error. Therefore the estimated back-EMF in (3.6) has to be equal to the actual one.

3.3.2 Current measurement and voltage actuation offsets

The back-EMF observer is fed with current and voltage measurements. Very often, voltage measurements are replaced by reference voltages outputs of current controllers, due to difficulties in measuring actual PWM modulated voltages. Both current and voltage signals are normally affected by noise, distortion (linear or non-linear), gain mismatching between different channels and offsets, caused by the measuring circuitry or inverter's non-ideal behavior. In particular, voltage accuracy is heavily affected by dead-times and non-ideal behavior of the power switches, which usually need to be compensated with the aim of reducing the equivalent voltage disturbance, [8], [32], [33]. In this work, the combination of two non-ideal cases is considered, in which voltage actuation and/or current measurement offsets are present. The common cases of voltage or current gain non-ideality (gain different from specified value or unbalanced between sensors) will not be addressed.

It is supposed in the following that offsets are experienced both in current measurements and voltage actuation, i.e.:

$$\boldsymbol{I}_{\alpha\beta} = \boldsymbol{I}_{\alpha\beta_{act}} + \boldsymbol{\Delta I} \quad , \quad \boldsymbol{U}_{\alpha\beta} = \boldsymbol{U}_{\alpha\beta_{act}} + \boldsymbol{\Delta U} \tag{3.32}$$

where the subscript act is introduced to identify the actual values and $\boldsymbol{\Delta I}$ and $\boldsymbol{\Delta U}$ represent the measuring offsets as complex constants (which can map any combination of offset values found in a two-phase sensor based measurement).

The response of the back-EMF observer is calculated in those cases in order to understand its sensitivity.

Equation (3.1) can be rewritten as

$$s\boldsymbol{I}_{\alpha\beta_{act}} = \frac{1}{L_{ss}}\left[\boldsymbol{U}_{\alpha\beta_{act}} - R_s\boldsymbol{I}_{\alpha\beta_{act}} - \boldsymbol{E}_{\alpha\beta}\right] \tag{3.33}$$

Substitution of (3.32) into (3.33) and considering sinusoidal conditions for stator currents, leads to

$$j\omega_{me}\boldsymbol{I}_{\alpha\beta} = \frac{1}{L_{ss}}\left[\boldsymbol{U}_{\alpha\beta} - R_s\boldsymbol{I}_{\alpha\beta} - \boldsymbol{E}_{\alpha\beta}\right] - \frac{\boldsymbol{\Delta U}+R_s\boldsymbol{\Delta I}}{L_{ss}} \tag{3.34}$$

where the derivative of the current offset $\boldsymbol{\Delta I}$ has been considered null (constant offset).

The difference between (3.34) and (3.6) is then calculated:

$$j\omega_{me}\left(\boldsymbol{I}_{\alpha\beta} - \hat{\boldsymbol{I}}_{\alpha\beta}\right) = \frac{1}{L_{ss}}\left[-R_s\left(\boldsymbol{I}_{\alpha\beta} - \hat{\boldsymbol{I}}_{\alpha\beta}\right) - \left(\boldsymbol{E}_{\alpha\beta} - \hat{\boldsymbol{E}}_{\alpha\beta}\right)\right] - \frac{\boldsymbol{\Delta U}+R_s\boldsymbol{\Delta I}}{L_{ss}} - K_1\left(\boldsymbol{I}_{\alpha\beta} - \hat{\boldsymbol{I}}_{\alpha\beta}\right) \tag{3.35}$$

If the second set of equations of the observer, i.e. (3.7), is rewritten when considering sinusoidal conditions for stator currents

$$\left(\boldsymbol{I}_{\alpha\beta} - \hat{\boldsymbol{I}}_{\alpha\beta}\right) = \frac{\hat{\boldsymbol{E}}_{\alpha\beta}(s-j\tilde{\omega}_{me})}{K_2} \tag{3.36}$$

and then substituted into (3.35), the following expression is obtained:

$$j\omega_{me}\frac{\hat{\boldsymbol{E}}_{\alpha\beta}(s-j\tilde{\omega}_{me})}{K_2} = \frac{1}{L_{ss}}\left[-R_s\frac{\hat{\boldsymbol{E}}_{\alpha\beta}(s-j\tilde{\omega}_{me})}{K_2} - \left(\boldsymbol{E}_{\alpha\beta} - \hat{\boldsymbol{E}}_{\alpha\beta}\right)\right] - \frac{\boldsymbol{\Delta U}+R_s\boldsymbol{\Delta I}}{L_{ss}} - K_1\frac{\hat{\boldsymbol{E}}_{\alpha\beta}(s-j\tilde{\omega}_{me})}{K_2} \tag{3.37}$$

The estimated back-EMF is supposed to be decomposed into AC and DC components, i.e.

$$\hat{\boldsymbol{E}}_{\alpha\beta} = \hat{\boldsymbol{E}}_{\alpha\beta_{AC}} + \hat{\boldsymbol{E}}_{\alpha\beta_{DC}} \tag{3.38}$$

Substitution into (3.37) and after some manipulation, the expression of the back-EMF estimation error is obtained:

$$\boldsymbol{E}_{\alpha\beta} - \widehat{\boldsymbol{E}}_{\alpha\beta_{AC}} - \widehat{\boldsymbol{E}}_{\alpha\beta_{DC}} = -\left[j(\omega_{me} - \tilde{\omega}_{me})\widehat{\boldsymbol{E}}_{\alpha\beta_{AC}}\right]\frac{j\omega_{me}L_{ss}+R_s+K_1L_{ss}}{K_2} + j\tilde{\omega}_{me}\widehat{\boldsymbol{E}}_{\alpha\beta_{DC}}\frac{j\omega_{me}L_{ss}+R_s+K_1L_{ss}}{K_2} - (\boldsymbol{\Delta U} + R_s\boldsymbol{\Delta I}) \tag{3.39}$$

Two different cases are now considered, i.e. the speed value $\tilde{\omega}_{me}$ entering in second set of equations of the observer, i.e. (3.7), is zero or equal to the actual speed ω_{me} (at steady-state). As previously stated these two conditions correspond to two different variants of the back-EMF observer. It is important to notice that, since ω_{me} is not measured, but estimated, the condition $\tilde{\omega}_{me} = \omega_{me}$ is actually an approximation, which is however valid at steady-state (coherently with the kind of analysis) and a correct estimation has been already achieved.

Case $\tilde{\omega}_{me} = 0$

Equation (3.39) can be rewritten as

$$\boldsymbol{E}_{\alpha\beta} - \widehat{\boldsymbol{E}}_{\alpha\beta_{AC}} - \widehat{\boldsymbol{E}}_{\alpha\beta_{DC}} = -j\omega_{me}\widehat{\boldsymbol{E}}_{\alpha\beta_{AC}}\frac{j\omega_{me}L_{ss}+R_s+K_1L_{ss}}{K_2} - (\boldsymbol{\Delta U} + R_s\boldsymbol{\Delta I}) \tag{3.40}$$

Therefore the DC component of the estimated back-EMF has to be equal to the last term of the previous equation, i.e.:

$$\widehat{\boldsymbol{E}}_{\alpha\beta_{DC}} = (\boldsymbol{\Delta U} + R_s\boldsymbol{\Delta I}) \tag{3.41}$$

and the overall estimation error can be calculated as

$$\begin{aligned}\boldsymbol{E}_{\alpha\beta} - \widehat{\boldsymbol{E}}_{\alpha\beta} &= \frac{-j\omega_{me}\boldsymbol{E}_{\alpha\beta}\dfrac{j\omega_{me}L_{ss}+R_s+K_1L_{ss}}{K_2}}{1 - j\omega_{me}\dfrac{j\omega_{me}L_{ss}+R_s+K_1L_{ss}}{K_2}} - (\boldsymbol{\Delta U} + R_s\boldsymbol{\Delta I}) \\ &= \frac{\widehat{\boldsymbol{E}}_{\alpha\beta}}{\boldsymbol{E}_{\alpha\beta}}\,\boldsymbol{E}_{\alpha\beta} - \widehat{\boldsymbol{E}}_{\alpha\beta_{DC}}\end{aligned} \tag{3.42}$$

which is the sum of the previously calculated steady-state error (3.31) in the case of null offset and the offset-related component (3.41).

Case $\tilde{\omega}_{me} = \omega_{me}$

Equation (3.39) can be rewritten as

$$\boldsymbol{E}_{\alpha\beta} - \widehat{\boldsymbol{E}}_{\alpha\beta_{AC}} - \widehat{\boldsymbol{E}}_{\alpha\beta_{DC}} = -j\omega_{me}\widehat{\boldsymbol{E}}_{\alpha\beta_{DC}}\frac{j\omega_{me}L_{SS}+R_S+K_1L_{SS}}{K_2} - (\boldsymbol{\Delta U} + R_S\boldsymbol{\Delta I}) \quad (3.43)$$

As the right side of previous equation is a DC component, is has to be equal to the last term $\widehat{\boldsymbol{E}}_{\alpha\beta_{DC}}$ of the left side, leading to:

$$\widehat{\boldsymbol{E}}_{\alpha\beta_{DC}} = \frac{\boldsymbol{\Delta U}+R_S\boldsymbol{\Delta I}}{1+j\omega_{me}\frac{j\omega_{me}L_{SS}+R_S+K_1L_{SS}}{K_2}} \quad (3.44)$$

and the overall estimation error can be calculated as

$$\boldsymbol{E}_{\alpha\beta} - \widehat{\boldsymbol{E}}_{\alpha\beta} = -\widehat{\boldsymbol{E}}_{\alpha\beta_{DC}} = \frac{-(\boldsymbol{\Delta U}+R_S\boldsymbol{\Delta I})}{1+j\omega_{me}\frac{j\omega_{me}L_{SS}+R_S+K_1L_{SS}}{K_2}} \quad (3.45)$$

which represents a DC term, confirming the previous supposition.

By taking into account the position and speed estimation extraction method applied, it can be pointed out that, for both $\tilde{\omega}_{me}$ choices, the DC component causes an harmonic error at the electrical frequency. In fact, considering a PLL processing, at steady-state a small offset causes a sinusoidal component on the phase error calculation (i.e. complex cross-product):

$$err = \widehat{\boldsymbol{E}}_{\alpha\beta} \times e^{j\hat{\theta}_{me}} = \left(\boldsymbol{E}_{\alpha\beta}+\widehat{\boldsymbol{E}}_{\alpha\beta_{DC}}\right)e^{j\hat{\theta}_{me}} \cong j\left|\widehat{\boldsymbol{E}}_{\alpha\beta_{DC}}\right| sin\,\hat{\theta}_{me} \quad (3.46)$$

However, a similar result is obtained if an inverse trigonometric function is adopted for obtaining the position estimate from a DC-offset affected back-EMF signal.

3.3.3 Parameters uncertainty

The back-EMF estimation error will be calculated in the case the knowledge of both synchronous inductance and resistance are uncertain. When sinusoidal steady-

state conditions are considered (i.e. $s = j\omega_{me}$), the model of the observer and of the motor can be rewritten:

$$j\omega_{me}\hat{\boldsymbol{I}}_{\alpha\beta} = \frac{1}{\hat{L}_{ss}}\left(\boldsymbol{U}_{\alpha\beta} - \hat{R}_s\hat{\boldsymbol{I}}_{\alpha\beta} - \hat{\boldsymbol{E}}_{\alpha\beta}\right) + K_1\left(\boldsymbol{I}_{\alpha\beta} - \hat{\boldsymbol{I}}_{\alpha\beta}\right) \tag{3.47}$$

$$j\omega_{me}\hat{\boldsymbol{E}}_{\alpha\beta} = j\tilde{\omega}_{me}\hat{\boldsymbol{E}}_{\alpha\beta} + K_2\left(\boldsymbol{I}_{\alpha\beta} - \hat{\boldsymbol{I}}_{\alpha\beta}\right) \tag{3.48}$$

$$j\omega_{me}\boldsymbol{I}_{\alpha\beta} = \frac{1}{L_{ss}}\left(\boldsymbol{U}_{\alpha\beta} - R_s\boldsymbol{I}_{\alpha\beta} - \boldsymbol{E}_{\alpha\beta}\right) \tag{3.49}$$

where $\hat{R}_s$ and $\hat{L}_{ss}$ are the estimated values of stator resistance and synchronous inductance adopted in the observer, that are supposed to be in general different from the actual values.

Also in this case the two conditions $\tilde{\omega}_{me} = 0$ and $\tilde{\omega}_{me} = \omega_{me}$ will be considered. In the following equations, the parametric errors will be defined as

$$\Delta L_{ss} \triangleq \hat{L}_{ss} - L_{ss} \quad , \quad \Delta R_s \triangleq \hat{R}_s - R_s \tag{3.50}$$

Case $\tilde{\omega}_{me} = 0$

Substitution of current estimation error $\boldsymbol{I}_{\alpha\beta} - \hat{\boldsymbol{I}}_{\alpha\beta}$ from (3.48) into (3.47) and subtraction of the obtained equation from motor model (3.49), allows the calculation of the following expression for the back-EMF estimation error:

$$\boldsymbol{E}_{\alpha\beta} - \hat{\boldsymbol{E}}_{\alpha\beta} = \frac{-j\omega_{me}\boldsymbol{E}_{\alpha\beta}\frac{j\omega_{me}\hat{L}_{ss}+\hat{R}_s+K_1\hat{L}_{ss}}{K_2} + \boldsymbol{I}_{\alpha\beta}(\Delta R_s + j\omega_{me}\Delta L_{ss})}{1 - j\omega_{me}\frac{j\omega_{me}\hat{L}_{ss}+\hat{R}_s+K_1\hat{L}_{ss}}{K_2}} \tag{3.51}$$

One can notice that a steady-state error is present also in the case no uncertainty on motor parameters are considered, i.e. both ΔR_s and ΔL_{ss} are zero. That error is due to the phase lag of the observer at the considered angular frequency ω_{me}, as discussed in a previous section.

Case $\tilde{\omega}_{me} = \omega_{me}$

Calculation of the difference between (3.49) and (3.47), with $\hat{\boldsymbol{I}}_{\alpha\beta} - \boldsymbol{I}_{\alpha\beta} = 0$ (this last coming directly from (3.48) at steady-state and $\tilde{\omega}_{me} = \omega_{me}$) leads to

$$\boldsymbol{E}_{\alpha\beta} - \hat{\boldsymbol{E}}_{\alpha\beta} = \boldsymbol{I}_{\alpha\beta}\Delta R_s + \frac{\Delta L_{ss}}{L_{ss}}\left(-R_s\boldsymbol{I}_{\alpha\beta} - \boldsymbol{E}_{\alpha\beta} + \boldsymbol{U}_{\alpha\beta}\right) \tag{3.52}$$

The last term is $j\omega_{me}\boldsymbol{I}_{\alpha\beta}$ (from (3.49)), hence:

$$\boldsymbol{E}_{\alpha\beta} - \hat{\boldsymbol{E}}_{\alpha\beta} = (\Delta R_s + \Delta L_{ss} j\omega_{me})\boldsymbol{I}_{\alpha\beta} \tag{3.53}$$

Considering that the position estimation error is independent from rotor position itself and under the following hypothesis (corresponding vector diagram is sketched in Fig. 3.7):

- current control is at steady-state ($\boldsymbol{I}_{dq} = \boldsymbol{I}^*_{dq}$);
- position estimation error is low enough (the estimated synchronous reference frame $\hat{d}\hat{q}$ is close to the actual one dq);
- control below the base speed is considered (no flux-weakening condition, i.e. $I^*_d = 0$, $I^*_q = |\boldsymbol{I}_{\alpha\beta}| \Rightarrow \boldsymbol{I}_{\alpha\beta} = jI^*_q e^{j\theta_{me}} = jI_q e^{j\theta_{me}}$);

Rotor position estimation error is calculated for $\theta_{me} = 0$ ($\boldsymbol{E}_{\alpha\beta} = j|\boldsymbol{E}_{\alpha\beta}|$, $\boldsymbol{I}_{\alpha\beta} = j|\boldsymbol{I}_{\alpha\beta}|$) as follows:

$$\begin{aligned}\theta_{me} - \hat{\theta}_{me} &= \angle\boldsymbol{E}_{\alpha\beta} - \angle\hat{\boldsymbol{E}}_{\alpha\beta} = {}^{\pi}/_{2} - \angle\left[\boldsymbol{E}_{\alpha\beta} - \left(\boldsymbol{E}_{\alpha\beta} - \hat{\boldsymbol{E}}_{\alpha\beta}\right)\right] \\ &= tan^{-1}\frac{\omega_{me}\Delta L_{ss}|I_{\alpha\beta}|}{\omega_{me}\Lambda_{mg} - \Delta R_s|I_{\alpha\beta}|} \approx tan^{-1}\frac{\Delta L_{ss}|I_{\alpha\beta}|}{\Lambda_{mg}}\end{aligned} \tag{3.54}$$

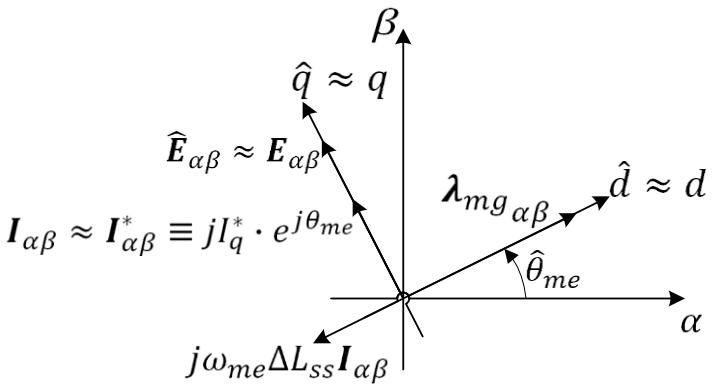

Fig. 3.7. Back-EMF and currents vector diagram at steady-state.

One can notice that the position estimation error is null when motor parameters are accurately known or (theoretically) at no load, which is consistent with the result obtained in the previous error analysis for the case where no parametric errors were present.

Indeed only phase estimation errors have been considered in this analysis, completely neglecting the amplitude of the estimated back-EMF. In [24] it is demonstrated that, when parameters deviations are considered, the estimated back-EMF amplitude could become zero even at relatively high values of motor speed. This means that, under those conditions, the signal-to-noise ratio of the estimates could be very low and then prevent reliable sensorless operations.

3.3.4 Phase advance due to high-pass filtering

The presence of a high-pass filtering action on the estimated back-EMF components (before speed and position extraction, see Fig. 3.1) could be needed to remove any DC component that could affect the reliability of position and speed estimation. The high-pass filtering action provides a phase advance, especially at low speed values. This advance can be easily calculated by considering the filter pole ω_{HPF}, i.e.:

$$HPF_E(s) = \frac{s}{s+\omega_{HPF}} \Rightarrow \angle HPF_E(j\omega_{me}) = {}^{\pi}/_{2} - tan^{-1}\left({}^{\omega_{me}}/_{\omega_{HPF}}\right) \qquad (3.55)$$

It is worth mentioning that, differently from the typical case of flux observer based methods, where a voltage integration drift arises, the back-EMF observer is not subject to this issue, both for the nature of the variable observed (which is not the integral of measured variables) and thanks to the current feedback. In this case, the high-pass filtering is just used to remove the possible DC components introduced by measurement or actuation offsets (described in 3.3.2). For this reason, pole frequencies as low as $0.1\,Hz$ can be adopted in the control of a motor having $200\,Hz$ nominal frequency (from experimental testing), meaning that

negligible phase errors are introduced even at the lowest operating speeds ($\sim 75\, rpm$ or $5\, Hz$).

3.4 Observer dynamics simulation results

Reliability of the proposed analysis has been verified by comparing the results of a complete electro-mechanical dynamical model simulation of the drive system, including sampled-time control and PWM modulation, and the analytical models discussed in the previous sections. Simulations have been carried out principally with the aim of verifying the correctness of the theoretical work on the dynamics and error sources identification. The observer and PLL gains choice have been analytically proven to be acceptable, then confirmed by simulation and tuned empirically, since the system noise plays a very relevant role in the estimation performances (practically limiting the usable bandwidth), and a noise model is very difficult to obtain. The observer with $\tilde{\omega}_{me} = 0$ has been considered in this results.

In Fig. 3.8 a comparison among actual, estimated and theoretical estimated back-EMFs and rotor electrical positions is shown with the observer off-line (i.e. estimates are not fed back to motor control, which is bases on measured position and speed). The aim of this test is to obtain a validation of the developed analytical models, i.e. the linearized version of (3.11) and (3.20), both in steady-state ($200\, rpm$) and in transient speed conditions (200 to $1000\, rpm$). The actual and the estimated variables are those coming from the dynamical simulation, implementing a complete model of motor, discrete-time controller and observer. The theoretical estimated variables are calculated on-line by dynamically feeding the analytical transfer functions with the actual variables (i.e. either back-EMFs or rotor position). It is shown that an optimal match is obtained, confirming the reliability of the theoretical analysis.

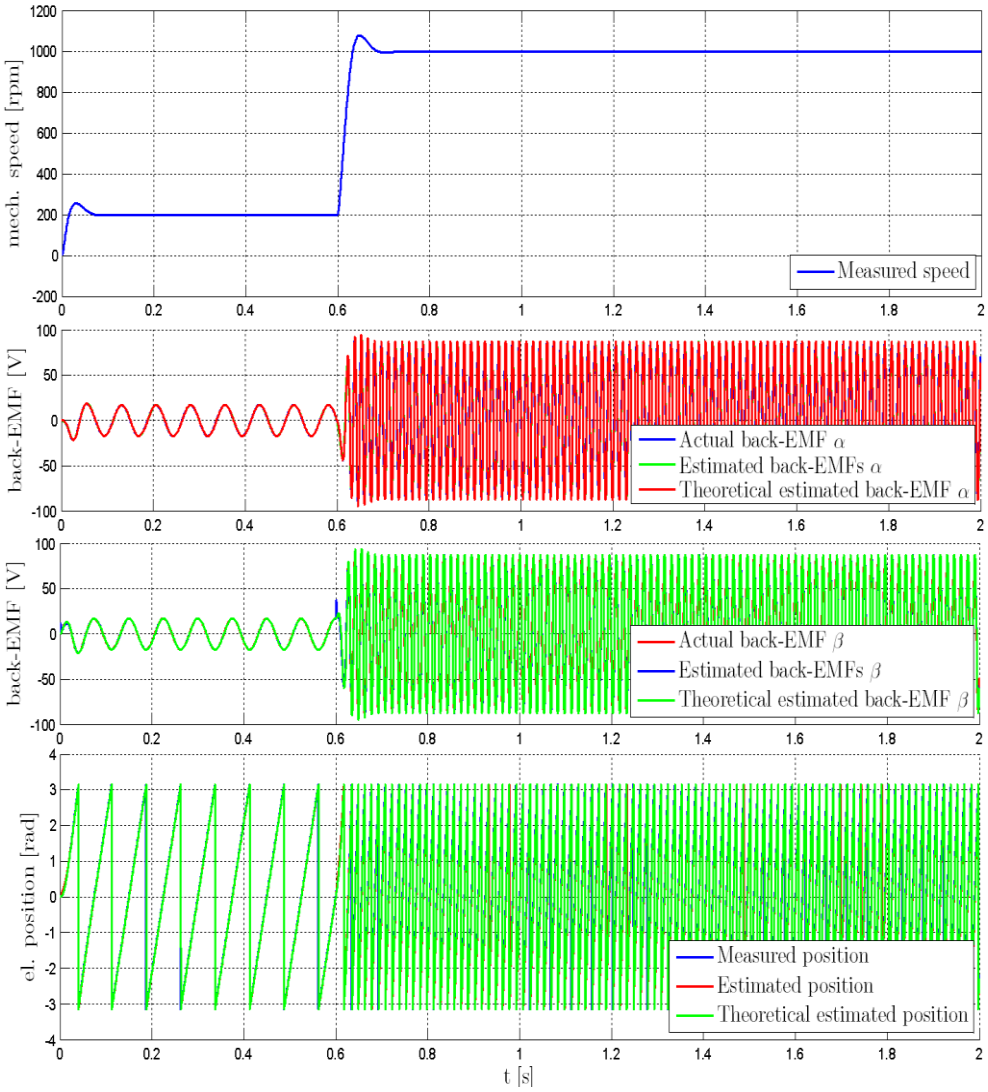

Fig. 3.8. Comparison among actual, dynamical estimated and theoretical (linearized) estimated back-EMFs and rotor position (simulation) at different steady-state speeds and during transients.

The aim of Fig. 3.9 is to verify the rotor position estimation errors as a function of rotor speed and synchronous inductance variations during full sensorless operations. The drive is started-up till $200\,rpm$ with the correct value of the

synchronous inductance used in the observer. The rotor position estimation error is both due to the presence of the high-pass filter in the estimation chain and due to the phase response of the back-EMF transfer function at the considered frequency. The speed reference is then increased up to $1000\,rpm$. Estimation error is therefore raising. At time $t = 1.5\,s$ a variation of $+2\,mH$ in the synchronous inductance (the value inside the observer) is simulated, resulting in an variation of estimation error of about $+2\,deg$, being in good agreement with the theoretical analysis, (3.54).

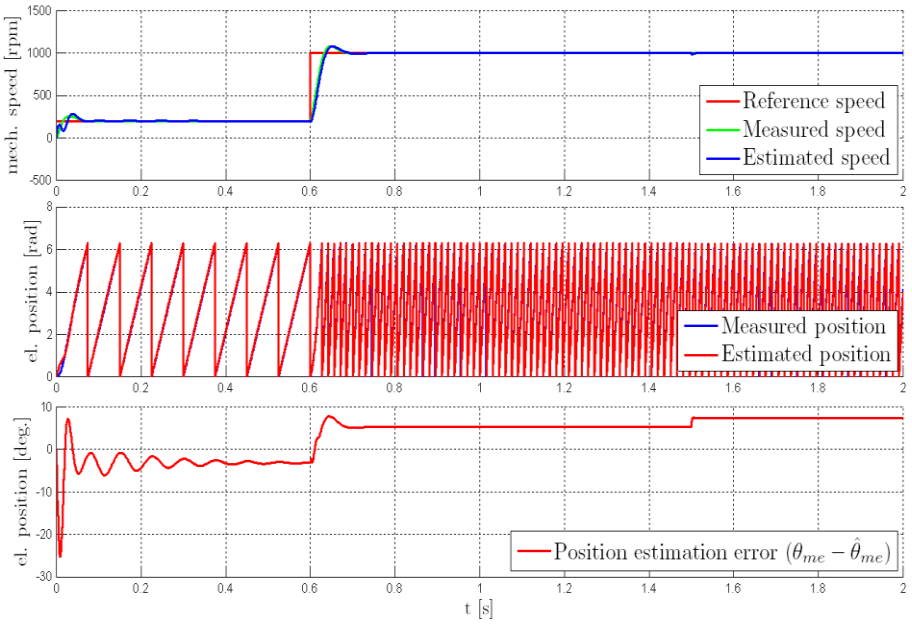

Fig. 3.9. Response to inductance variation ($\Delta L_{ss} = +2\,mH$, simulation).

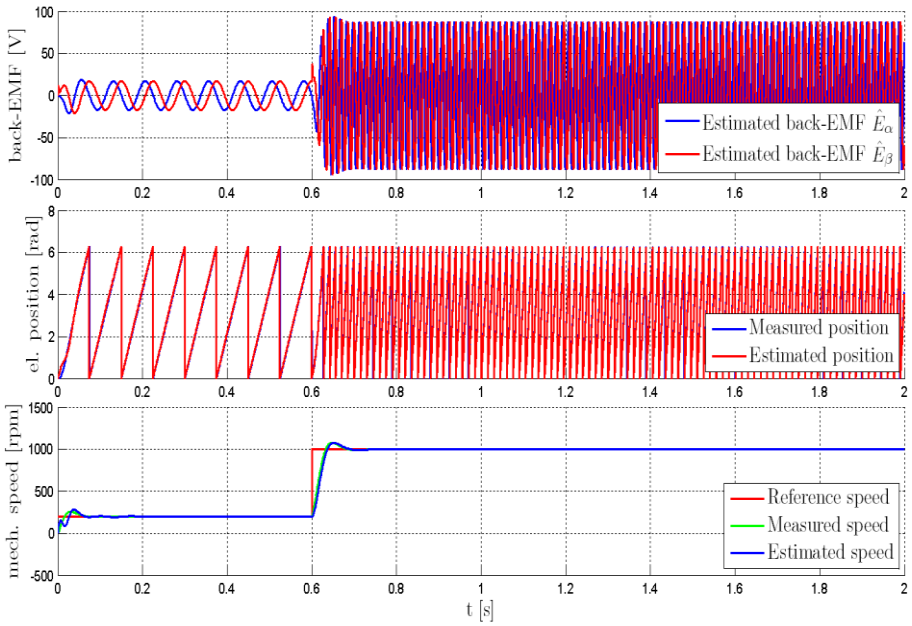

Fig. 3.10. PLL operations during a fast transient (simulation).

3.5 Experimental results

A general purpose industrial drive has been considered for the experimental investigation (Fig. A.1 and Table A.1). Both speed and torque transient and steady-state conditions have been considered. Estimation errors will be measured and used to validate the theoretical analysis.

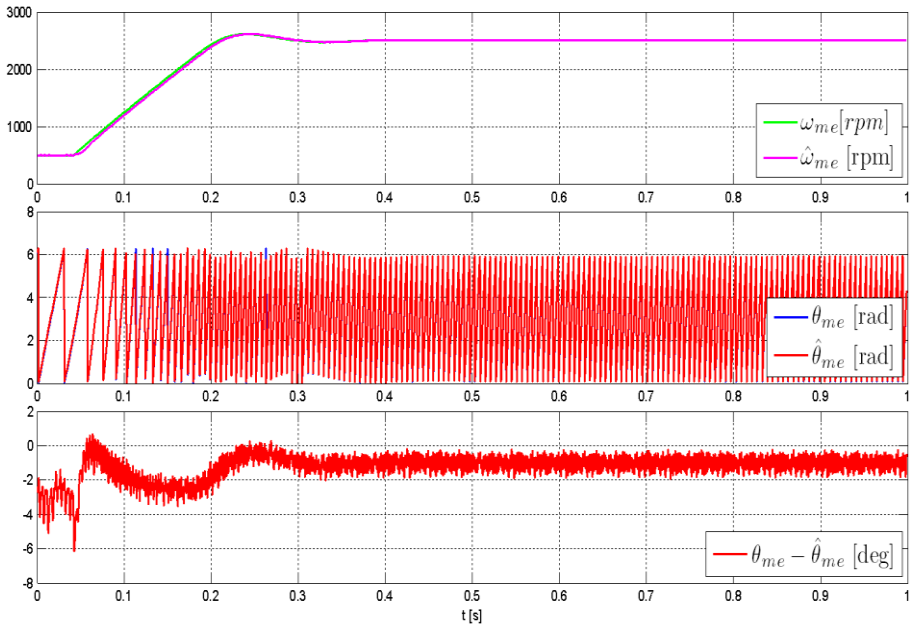

Fig. 3.11. Speed transient (**500** to **2500** rpm), half rated load (experimental).

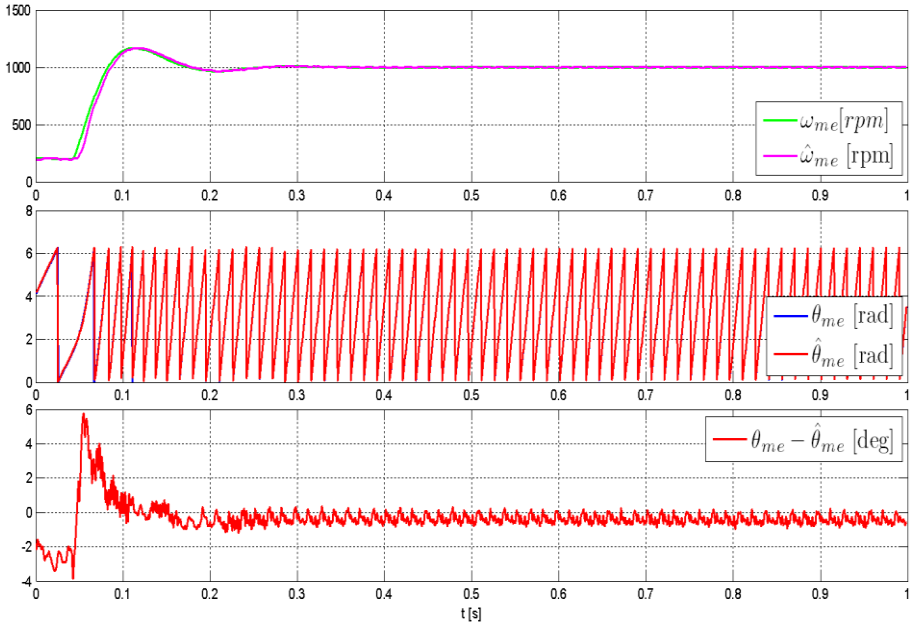

Fig. 3.12. Speed transient (**200** to **1000** rpm), no load (experimental).

The results of a first test are shown in Fig. 3.11 and refer to a transient speed condition from 500 to $2500\,rpm$ under half the rated load torque. Differently from simulation tests, ramp speed reference has been considered instead of a step. Actual and estimated speed (this last being the feedback of the speed controller) are shown in the first subplot, confirming good tracking performance and reduced estimation delay. In the second subplot actual and estimated position are reported, while the position estimation error is shown in the third subplot. One can notice the reduced value of the estimation error and its dependency with speed, as discussed in the theoretical analysis. The absolute values of estimation errors are not comparable as a different set of parameters has been adopted in the experimental investigations due to the presence of hard measurements noise. A similar test is reported in Fig. 3.12 showing that sensorless operation is possible even at very low values of speed (but not zero). Although it is not shown, same synchronous inductance variation considered in simulation (see Fig. 3.9) has been tested, experiencing same position estimation error deviation.

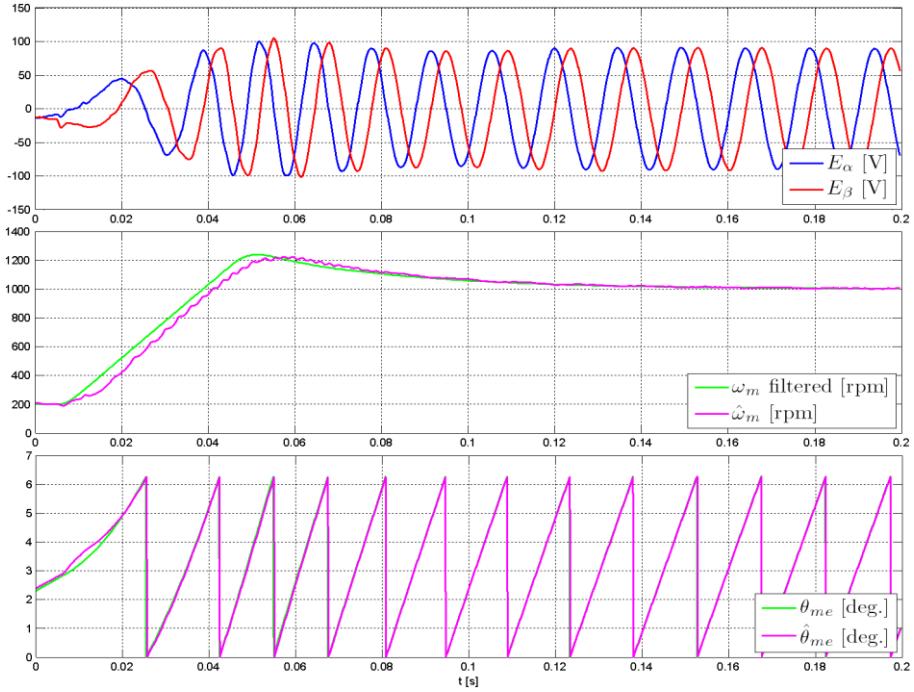

Fig. 3.13. Observer and PLL speed tracking capabilities under fast speed transient (experimental, observer is off-line).

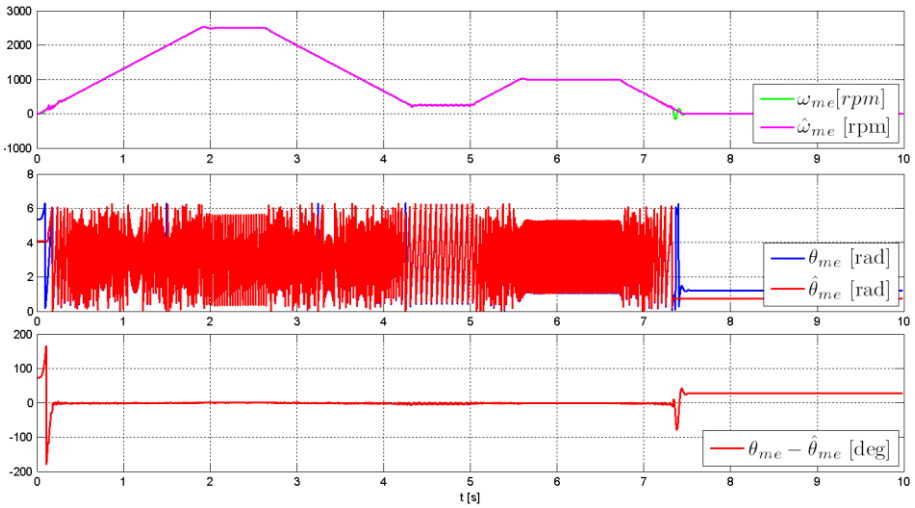

Fig. 3.14. Sensorless startup from stand-still, ramp control and braking to zero, 33% rated load (experimental).

In Fig. 3.13 fast speed transient condition is considered. The response of the estimated back-EMFs (first subplot), actual and estimated speed (second subplot) and position (third subplot) are shown. The motor is controlled with sensor feedback, therefore a transient from standstill is possible, also to understand the behavior of the observer in the very low speed range. Estimated back-EMF is the output of the observer, that feeds the PLL and provides the estimated position and (after a low-pass filtering) the estimated speed. The position response of this test is directly comparable to the one shown in Fig. 3.10, showing the fast and accurate dynamics of the PLL.

Finally in Fig. 3.14 sensorless operation for a startup from standstill, ramp up, and braking. Start-up from stand-still and very low-speed operation has been achieved by means of an open-loop control, consisting in the generation of a large current vector, rotating at the reference speed. Actual and estimated position experience displaying problems due to decimation of the acquired samples.

3.6 Sensorless drive management and supervision

During the last part in the development of the sensorless drive control, some important aspects other than the essential estimation issue have been dealt. In particular, the necessary open-loop startup and management of the transition to closed-loop, the stabilization of speed control at low-speed, some alternative speed estimation techniques for control fault detection and an initial position detection to improve startup robustness have been studied.

In fact, attention to the reliability (robustness) of control also under the worst load conditions is an important factor in the actual usability of the drive. Experimental tests pointed out that startup at high loads or load disturbance withstanding at low speed are the most demanding conditions. While open-loop startup is, obviously, very prone to the random initial position and load, control at low-speed is also critical, since a sudden load increase can cause speed to decrease to values where insufficient back-EMF amplitude is present (leading to low SNR on the speed estimation). This situation can easily cause control loss (stall) and needs to be managed with particular care. As a minimum reliability requirement, it must be possible to detect stall, to prevent it from persisting and to signal a fault event to an operator or supervising system. Even if fault detection and managing was out of the scope of the project, some signal processing schemes that will enable malfunction recognition were developed, mainly based on alternative speed measurements, avoiding the use of the PLL block. In fact, experimental tests showed that most fault conditions cause a large speed control error (difference between reference and estimated value), so this signal can also be used for a simple fault detection, which is normally implemented in commercial drives (speed reference lost threshold comparison). However, in some fault cases, in the presence of an estimated speed value stably near reference, actual speed revealed that control was lost and PLL was locked to an incorrect value. This condition can occur when speed oscillations at frequencies above the estimation bandwidth build up as a consequence of control loss.

In particular, in some cases, following a transient where a large estimation error has occurred, estimated speed can remain at a high value (over the minimum open-loop operating mode threshold) while actual speed is nearly zero, with rotor oscillation. The closed-loop control would not be possible in these conditions but, since a low-speed is not detected, the operating mode is not switched to open-loop, thus the rotor can stall permanently. A reason for this behavior can be found in the particular position and speed estimate extraction process, involving a PLL which, under large "slip" conditions, detects a high-frequency error correction signal having null average, thus does not allow estimation tracking, leaving the speed estimate locked (since the high-frequency error is simply filtered out).

The quantities that have been exploited for an indirect speed estimation are the back-EMF vector magnitude and active electrical power, since they are constantly available or easily obtainable. The use of a stationary frame back-EMF observer has, from this point of view, an advantage over its synchronous counterpart, i.e. the possibility to maintain observation under any speed condition, since the electrical subsystem is current controlled (based on measurements) and thus will not diverge. This means that, at least, an acceptable estimation of the back-EMF amplitude can be performed also at null or low-speed.

3.6.1 Startup and low-speed control mode and optimization

Startup from stand-still is a critical condition, as already seen. In fact, depending on the noise level of speed estimation, control under a certain speed can result in a very oscillatory speed behavior, also showing very low stiffness to load variations. Although the influence of noise can be reduced by the technique described in 3.7, extending the control range to a lower speed, a different control algorithm must be applied for startup.

Besides startup, a different critical condition is represented by the effect of sudden load changes during control at the low speed range limit, which can cause the control to enter a region where speed and position estimation becomes prohibitive. Deteriorated position estimation results in lower torque capability, and

mechanical load and friction tend to brake the rotor down to zero speed, thus estimation and control is normally lost.

A proper managing of the different control conditions is needed, guaranteeing correct switch from one mode to the other. In the implementation, the main control modes are open-loop and closed-loop speed control. When control is enabled, back-EMF observer is always updated, since the current control prevents divergence of the estimates. For the PLL, instead, the probability of divergence is much higher, in the case of a low SNR on its inputs.

In the open-loop mode, a constant magnitude current vector is imposed, while position is obtained as integration of the reference speed. If a proper current value and acceleration is imposed (depending on load braking torque and inertia), the rotor can be accelerated and steady-state average speed equal to the reference one can be obtained (although strong oscillations can be present). This common technique is also known as "I/f", which recalls the more famous open-loop approach to induction motor control (V/f), even if in this case a constant vector magnitude is applied, instead of a constant ratio with frequency. The implementation of this control mode integration inside a normal vector control scheme is quite straightforward, i.e. imposing a constant $\boldsymbol{d}$-axis current and using a fictitious position (as above explained) for axes transformations.

Despite the simplicity of this control scheme, various aspects need to be taken into account to ensure proper operation, especially at the switching between the two control modes. In Fig. 3.15 the behavior that the main control variables and mode flags follow is represented. The graph is symmetrical for positive or negative speed, and the most important variable is the control mode, which is switched according to an hysteresis that is applied to the speed estimation and reference. The condition for passing to the closed-loop is more restrictive, requiring both reference and estimated speed to assume values above the maximum open-loop control threshold (AND condition), while the change to open-loop control is determined by either reference or estimate going under the minimum closed-loop control threshold (OR condition). The reason behind this logic is preventing control loss until possible, and relying on open-loop at low-speed as a safe mode. Unfortunately, open-loop can be considered as a safe mode only when slip speed (the difference between stator current rotation speed and rotor speed) is limited and load is sufficiently low. Thus the maximum open-loop control threshold must be set as low as possible, still guaranteeing proper startup.

Obviously, an analytical way for determining the two thresholds is not available, since it is related to the noise level affecting estimates (which has both deterministic and random sources). However, an interesting approach is the one proposed in [34], where the inverter dead-times are considered as the main back-EMF estimation noise source. Following this assumption, the speed and position estimates are used for control when the back-EMF magnitude is higher than that of the dead-time distortion voltage, thus the condition for reliably adopting the closed-loop control based on back-EMF estimation becomes:

$$\omega_{me}\Lambda_{mg} \geq \frac{T_{DT}}{T_{SW}}V_{DC} \tag{3.56}$$

where T_{DT} and T_{SW} are the inverter dead-time and PWM switching period length.

As already mentioned, following a sudden load increase, recovery of control from a large undershoot can be problematic in the case speed follows below the minimum closed-loop control threshold and open-loop control is activated. This peculiar condition, which has been called "*phase loss*" in this text, needs a particular recovery procedure based on open-loop ramp control. In fact, switching to the open-loop mode causes the current vector to rotate at the reference speed. If the actual rotor speed is much lower than the reference, the excessive slip can cause a rotor stall, since low average torque is produced by the rotating current vector. To overcome this severe problem, a simple transient control strategy has been implemented. The phase loss condition is detected when a change to the open-loop mode has occurred due to the estimated speed reaching the minimum threshold and the reference speed is higher than the maximum open-loop threshold. This triggers the generation of an open-loop speed ramp (which is used for the current vector rotation) starting from the estimated speed sampled at the control mode change instant and rising at constant rate up to the reference speed. At the end of the ramp, closed-loop control is restored, allowing normal operation. This simple solution allows the drive control to recover from estimation loss after a speed decrease not commanded. The ramp slope must be equal or lower than the slope maximum limit used for the normal control at startup, allowing the load to be contrasted and position and speed estimation to converge before entering closed-loop. The phase loss recovery should be an alert event for fault detection, since the

control could enter an infinite sequence of phase loss recovery attempts, while rotor is indeed stalling.

Another problematic condition that needs to be considered takes place when a steep ramp is imposed towards zero speed, starting in closed-loop control operation, and the reference speed reaches null value while the actual speed is relatively high. In this case, a non-rotating current vector is imposed, while the kinetic energy stored in the rotor inertia is quite high. For low resistance mechanical load (i.e. having low friction coefficient), and a relatively low open-loop current vector magnitude, multiple oscillations are generated. Examples of this undesired behavior are reported in Fig. 3.18 and Fig. 3.21. In fact, the phenomenon arises when excessive ramp slope is selected for reference. However, further study in the management of control modes could lead to an effective solution.

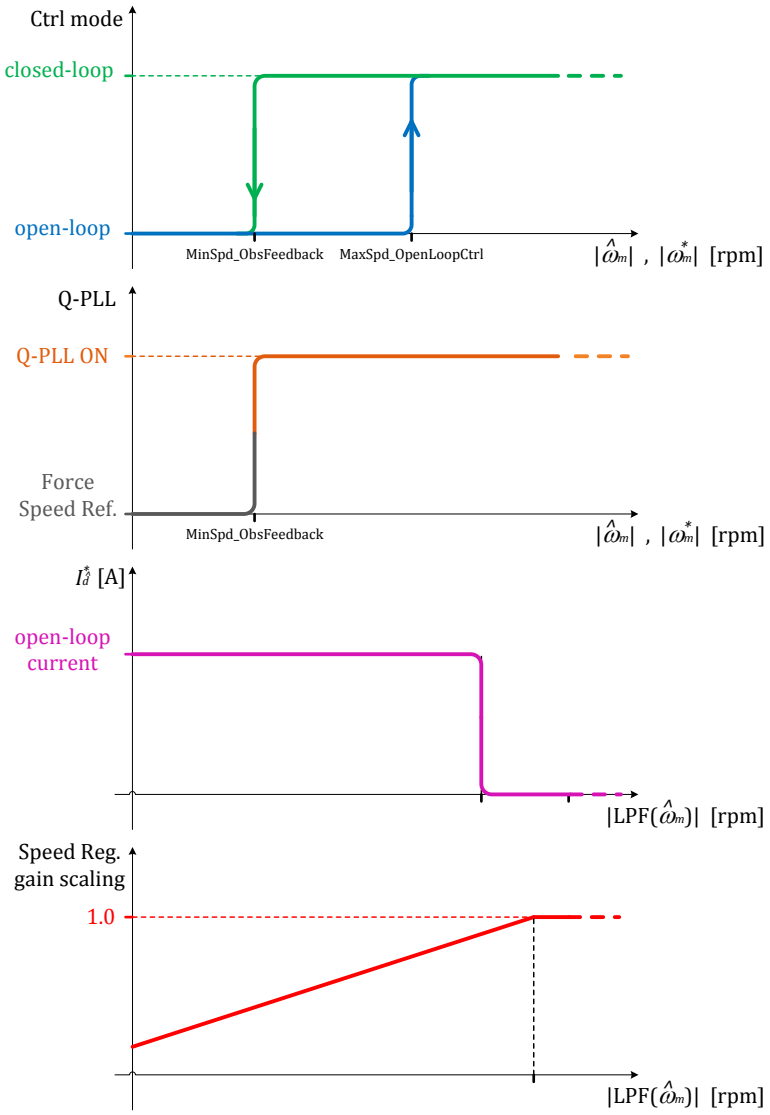

Fig. 3.15. Control modes managing and optimization of reactive current and speed regulator gains for optimization.

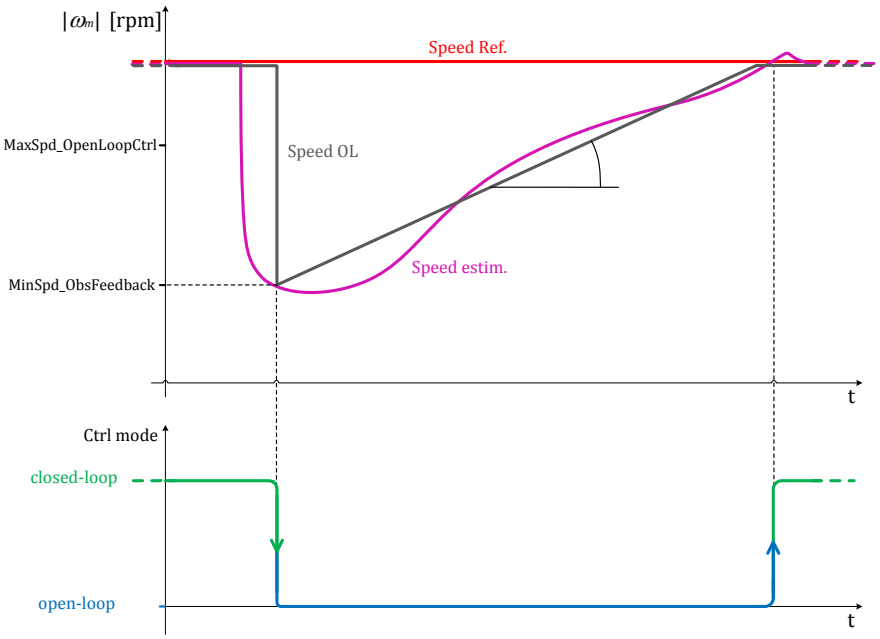

Fig. 3.16. Phase loss recovery control example.

3.6.2 Back-EMF magnitude monitoring for indirect speed estimation

From equation (3.3), the back-EMF vector magnitude is easily obtained as

$$\left|\boldsymbol{E}_{\alpha\beta}\right| = |\omega_{me}|\Lambda_{mg} \tag{3.57}$$

which is proportional to the absolute value of speed. Actually, the control algorithm only provides a noisy estimation of the back-EMF, so simply applying an approach similar to a tachometric dynamo, i.e. calculating speed as

$$\left|\widehat{\omega}_{me_{E_{\alpha\beta}}}\right| = \frac{\left|\widehat{\boldsymbol{E}}_{\alpha\beta}\right|}{\Lambda_{mg}} \tag{3.58}$$

would be hardly useful for the purpose of monitoring speed control correctness. Transformation to the synchronous reference frame brings at least to advantages:

the possibility to apply a low-pass filter on the estimated back-EMF signals without any steady-state accuracy loss and an easy way for determining the rotation direction (Fig. 3.17). In particular, due to the non-linear nature of the modulus operator, filtering the two components before the magnitude calculation results in a better noise rejection. If processing is done in the synchronous reference frame, almost speed-independent behavior can be obtained from the low-pass filtering, differently from what would be in the stationary axes. As mentioned above, rotation direction can be obtained considering that steady-state back-EMF in the dq axes are DC signals, and the q-axis component sign is the speed sign

$$\widehat{\omega}_{me_{E_{dq}}} = \frac{sign(\hat{E}_q) \cdot |\hat{\boldsymbol{E}}_{dq}|}{\Lambda_{mg}} \tag{3.59}$$

It is worth pointing out that the actual rotor axis direction is not known, but only its estimation is available. While a small constant phase error would cause no effect on this kind of estimation, a variable phase (either a DC speed estimation error or a large oscillating position error) will lead to oscillating $\hat{d}\hat{q}$-axes signals, that can be filtered out resulting in a low estimated speed. A large constant position error (i.e. over $\pi/2$) also implies a sign reversal of the estimated speed.

While for the purpose of estimation this is strictly a disadvantage, for supervision and control fault detection this means that both the conditions of excessive position error (torque inversion) or speed error can be detected by setting thresholds on a low-pass filtered $\widehat{\omega}_{me_{E_{dq}}}$ signal, both considering the gap with respect to the reference speed or, during operation at low speed, an abnormally low value.

Obviously, accuracy of this estimation is strongly dependent on a good back-EMF observation and on PM flux magnitude parameter matching (Λ_{mg}). Although this second factor is important, it must be considered that a low accuracy requirement is present, since the estimation is only needed for a fault monitoring. Moreover, the peak PM flux parameter can usually be obtained from nameplate, where torque constant is reported ($K_T = \frac{3}{2} pp\Lambda_{mg}$), or easily estimated during steady-state operation at a sufficiently high speed (where control reliability is very high).

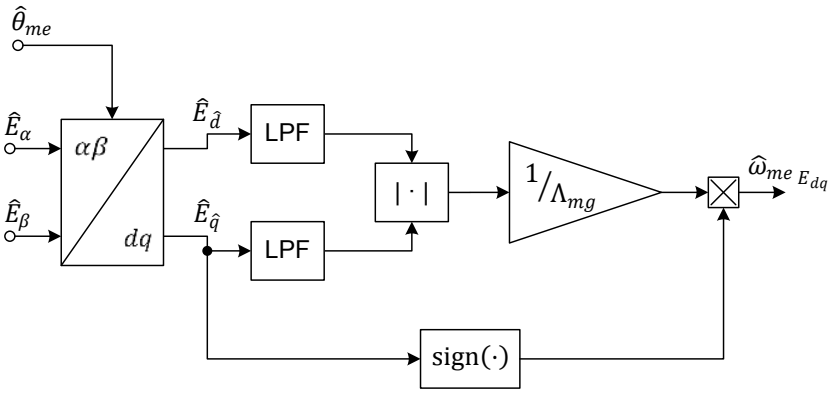

Fig. 3.17. Speed estimation from estimated back-EMF amplitude.

Experimental results

Some significant tests have been performed to show the potential of this alternative measurement for control fault detection. In the following tests, the PM flux value is set to the datasheet value. The estimation shows very good steady-state accuracy (in the order of few rpm), demonstrating the reliability of the manufacturer measurements on this parameter.

While the three speed values (estimation from PLL and from back-EMF magnitude processing, encoder measurement) show good agreement during correct operation, in the case of control loss (following a steep ramp from stand-still, under load) the PLL estimation does not properly track speed, while the estimation from the back-EMF magnitude can detect an incorrect speed. For achieving a correct detection, proper speed difference and duration time thresholds should be determined based on statistical information.

In the final part of traces in Fig. 3.18 and Fig. 3.21, an abnormal open-loop commutation can be seen, which causes a strong and persistent speed oscillation. This issue has been already reported in 3.6.1. The particularly good speed tracking that can be obtained by the back-EMF magnitude processing during open-loop speed control is a very interesting result, that could lead to further development of an intermediate control mode (keeping some characteristics common to open-loop

and some from closed-loop), where this speed estimation could be effectively exploited.

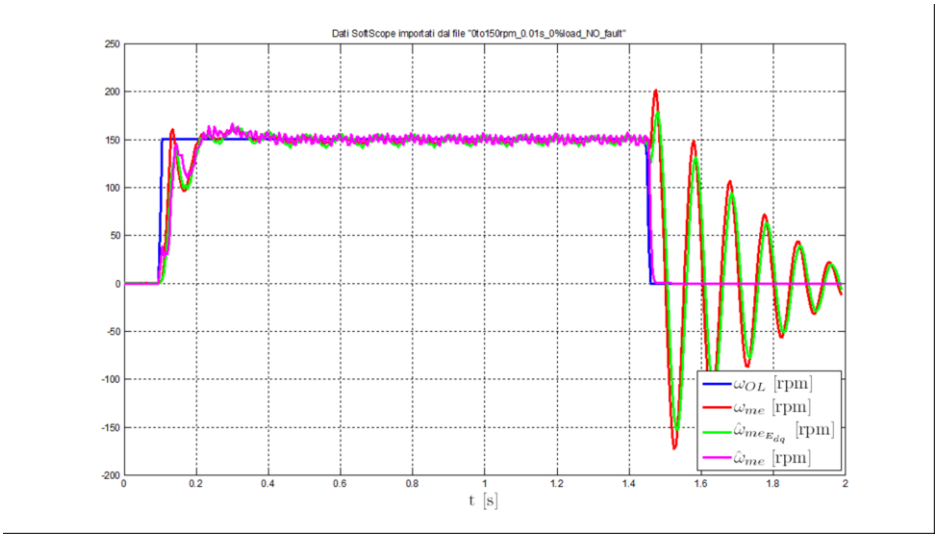

Fig. 3.18. Speed transient from stand-still to 150 rpm and vice versa, correct control (no faults).

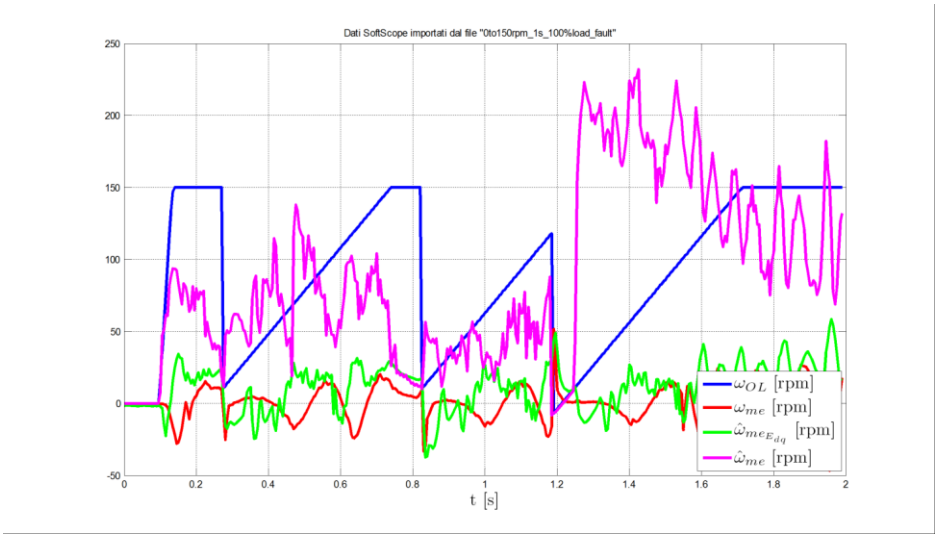

Fig. 3.19. Speed transient from stand-still to 150 rpm and vice versa, control loss (fault) not recovered.

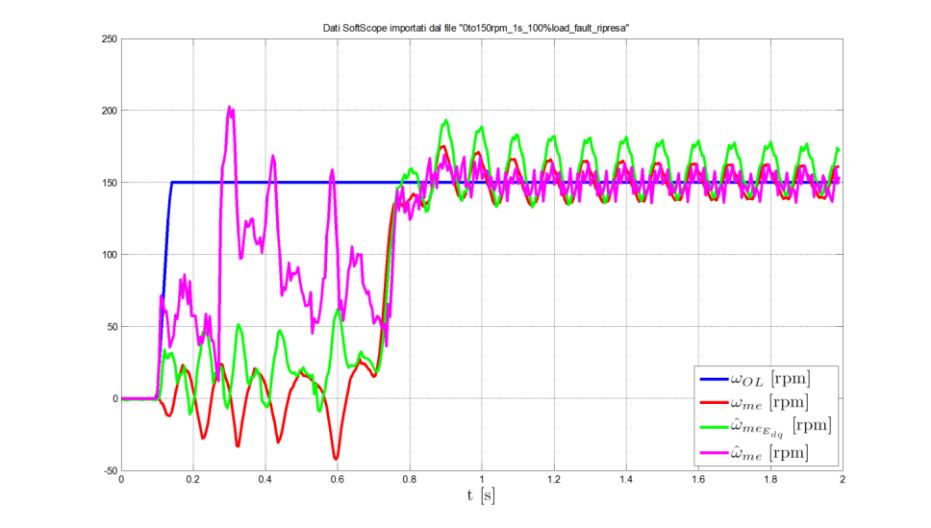

Fig. 3.20. Speed transient from stand-still to 150 rpm, control loss followed by recovery.

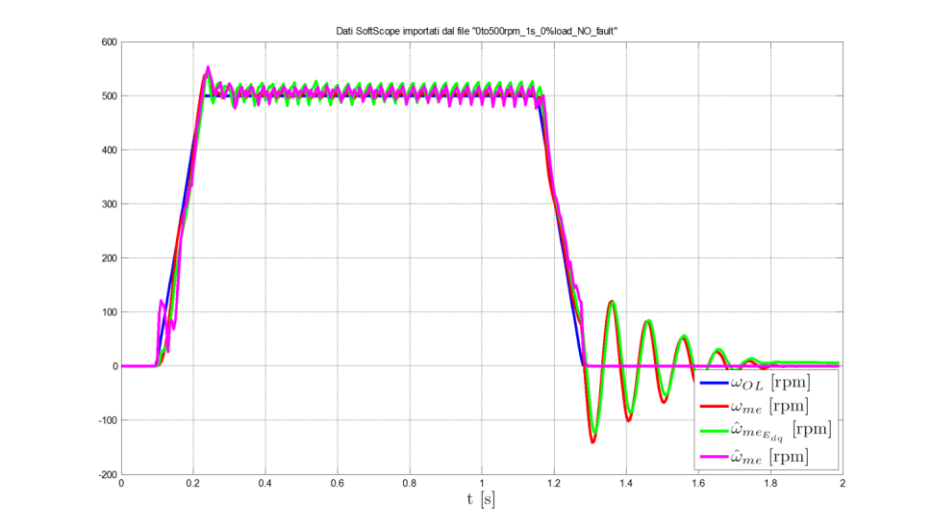

Fig. 3.21. Speed transient from stand-still to 500 rpm and vice versa, correct control (no faults).

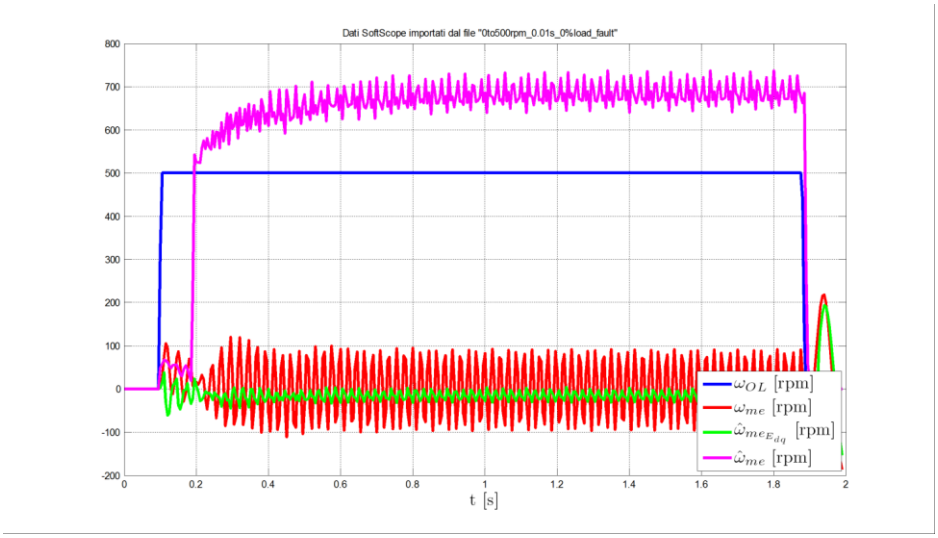

Fig. 3.22. Speed transient from stand-still to 500 rpm, control loss (fault) not recovered.

3.7 Control robustness and accuracy improvement by constant direct-axis current injection

As already mentioned the critical issue of all of the sensorless position and speed estimation methods based on the fundamental quantities (back-EMF, PM flux-linkage) is the linear dependence of the induced voltage on rotor speed. In fact, this results in estimated speed and position affected by heavy noise at low speed (due to estimation noise on back-EMF, e.g. caused by current measurement noise and distortion from the feeding inverter), which prevents accurate and reliable closed-loop control. Although open-loop techniques can be adopted, they do not ensure proper robustness against load torque disturbance and cannot achieve the

control stability and accuracy required for some applications. Thus, the extension to the very low-speed control region (e.g. below 5% of the base speed) with full feedback control is highly desirable.

Using the common torque control ($I_d^* = 0$), at very low-speed the trade-off between regulation dynamics on one side and robustness or steady-state speed accuracy on the other often results in poor performance. Reducing control bandwidth will lead to poor load torque disturbance rejection, and then a sudden increase in load torque can cause a deceleration out of the reliable estimation speed region, eventually causing loss of control. It has been shown experimentally that, given a certain estimation noise level, the superimposition of a positive direct-axis current component to current reference improves control capabilities, [20], [22]. The minimum speed limit for closed-loop control can be substantially lowered, and the speed ripple at low-speed steady-state is also dramatically reduced. While this effect was already known and reported, an analytical explanation was not available in literature. Assuming some simplifications (mainly a small position error and an independent source modeling for noise), identification and characterization of the principle behind this stabilizing action has been obtained through small-signal analysis, and the work has been published in [30]. Simulation and experimental investigations demonstrate the effectiveness of the adopted approach, and show the advantages resulting from constant direct-axis injection on the sensorless drive system. Of course, the most important disadvantage can be easily pointed out in the increased losses produced by the additional current, so this important factor influences the choice of whether this technique is applicable and which is the proper value for reactive current.

3.7.1 Analytical description

To obtain an analytical description of the system dynamics, an approximated approach has been applied to the equations relating torque production and speed control in the estimated position reference frame. Operation under small position estimation error and ideal current control is considered. Modeling of a classical speed control loop with superimposed estimation noise allows to highlight the effect of an additive direct-axis current component.

Let $I_{\hat{d}}^*$ e $I_{\hat{q}}^*$ be the current control references in the estimated rotor reference frame (electrical position being $\hat{\theta}_{me}$), which are provided by a closed-loop speed control having ω_m^* as the set-point value and a speed feed-back (estimated speed) $\hat{\omega}_m$. If all distortions and noise are modeled as an additive signal n, the estimated speed can be expressed as

$$\hat{\omega}_m = \omega_m + n \tag{3.60}$$

The generated electromagnetic torque

$$T_e = \frac{3}{2} pp \Lambda_{mg} I_q \tag{3.61}$$

is proportional to the actual quadrature component of the stator current, which can be expressed as a function of the estimated reference frame components $I_{\hat{d}}$ and $I_{\hat{q}}$, and the rotor position estimation error:

$$I_q = I_{\hat{d}} \, sin\left(\hat{\theta}_{me} - \theta_{me}\right) + I_{\hat{q}} \, cos\left(\hat{\theta}_{me} - \theta_{me}\right) \tag{3.62}$$

A current controller having sufficient bandwidth is considered, leading to:

$$I_{\hat{d}\hat{q}} \approx I_{\hat{d}\hat{q}}^* \tag{3.63}$$

Therefore the torque equation becomes:

$$T_e = \frac{3}{2} pp \Lambda_{mg} \left[I_{\hat{d}}^* \, sin\left(\hat{\theta}_{me} - \theta_{me}\right) + I_{\hat{q}}^* \, cos\left(\hat{\theta}_{me} - \theta_{me}\right) \right] \tag{3.64}$$

where pp is the polar pairs number and Λ_{mg} is the flux-linkage amplitude.

If a first-order mechanical system Laplace model is considered, having inertia J and friction B, the mechanical speed becomes:

$$\omega_m(s) = \frac{T_e - T_L}{B + sJ} \tag{3.65}$$

If a small-signal approach is considered and the load torque is constant or slowly varying, position estimation error, the electromagnetic torque (3.64) can be substituted into (3.65), leading to:

$$\omega_m(s) = \frac{1}{B + sJ} \cdot \frac{3}{2} pp \Lambda_{mg} \left[I_{\hat{d}}^* \, sin\left(\hat{\theta}_{me} - \theta_{me}\right) + I_{\hat{q}}^* \, cos\left(\hat{\theta}_{me} - \theta_{me}\right) \right] \tag{3.66}$$

Under small position estimation error conditions, linear approximation of the above expression results in

$$\omega_m(s) \approx \frac{1}{B+sJ} \cdot \frac{3}{2} pp \Lambda_{mg} \left[I_{\hat{d}}^* \left(\hat{\theta}_{me} - \theta_{me} \right) + I_{\hat{q}}^* \right] \tag{3.67}$$

The estimated and actual position can be written as speed integral, i.e.:

$$\theta_{me} = pp \frac{1}{s} \omega_m \quad , \quad \hat{\theta}_{me} = pp \frac{1}{s} \hat{\omega}_m \tag{3.68}$$

while the q-axis current reference is provided by the speed regulator:

$$I_{\hat{q}}^* = Reg(s)(\omega_m^* - \hat{\omega}_m) \tag{3.69}$$

where the regulator transfer function $Reg(s)$ can be defined as the typical continuous-time proportional-integral:

$$Reg(s) \triangleq K_P + {}^{K_I}/_{s} \tag{3.70}$$

Substitution of (3.68) and (3.69) into (3.67) leads to:

$$\omega_m(s) \approx \frac{1}{B+sJ} \cdot \frac{3}{2} pp \Lambda_{mg} \left[I_{\hat{d}}^* \frac{1}{s} pp(\hat{\omega}_m - \omega_m) + Reg(s)(\omega_m^* - \hat{\omega}_m) \right] \tag{3.71}$$

It can be highlighted that the last expression is a function of the speed estimation error, instantaneous speed control error and the direct-current reference.

Recalling the definition of the estimation noise n in (3.60), speed expression becomes:

$$\begin{aligned} \omega_m(s) = & \frac{1}{B+sJ} \\ & \cdot \frac{3}{2} pp \Lambda_{mg} \left[I_{\hat{d}}^* \frac{1}{s} pp(\omega_m + n - \omega_m) + Reg(s) \right. \\ & \left. \cdot (\omega_m^* - \omega_m - n) \right] \end{aligned} \tag{3.72}$$

The closed-loop speed response to the speed reference ω_m^* and to the estimation disturbance n is therefore:

$$\omega_m(s) = \frac{\frac{1}{B+sJ}\frac{3}{2}pp\Lambda_{mg}\cdot Reg(s)}{1+\frac{1}{B+sJ}\frac{3}{2}pp\Lambda_{mg}Reg(s)}\cdot\omega_m^*(s) + \frac{\frac{1}{B+sJ}\frac{3}{2}pp\Lambda_{mg}\cdot\left[I_{\hat{d}}^*\frac{1}{s}pp - Reg(s)\right]}{1+\frac{1}{B+sJ}\frac{3}{2}pp\Lambda_{mg}Reg(s)}\cdot n(s) = \left.\frac{\omega_m(s)}{\omega_m^*(s)}\right|_{n(s)=0}\cdot\omega_m^*(s) + \left.\frac{\omega_m(s)}{n(s)}\right|_{\omega_m^*(s)=0}\cdot n(s) \tag{3.73}$$

It can be seen that the noise effect (i.e. the sensitivity) on the actual rotor speed is weighted by the transfer function $I_{\hat{d}}^*\frac{1}{s}pp - Reg(s)$ and can therefore be adjusted by selecting the reference direct-axis current $I_{\hat{d}}^*$. If a proper value is chosen, a damping effect on the estimation noise can be achieved, as it will be highlighted in the next section.

3.7.2 Simulation results

Reliability of the proposed analysis has been verified by comparing the results of a complete electro-mechanical dynamical model simulation of the drive system, including sampled-time control and PWM modulation, and the analytical models discussed in the previous sections. Simulations have been carried out to verify the correctness of the analytical method, and to evaluate the expected impact of a d-axis current on the control stability and accuracy. The observer and PLL gains choice have been chosen according to the developed analytical investigation reported in [21]. The observer with $\tilde{\omega}_{me} = 0$ has been considered in this results.

A simple preliminary analysis for a given speed regulator tuning and three different values of $I_{\hat{d}}^*$ is drawn in Fig. 3.23, where $\frac{\omega_m(s)}{n(s)}$ transfer function is represented. The expected lower influence of the estimation noise on the mechanical speed when a non-negligible direct-axis current $I_{\hat{d}}^*$ is selected is clearly visible. It can also be noted that for an arbitrary frequency range, there exist a minimum of the sensitivity, i.e. the noise has the minimum effect. In the considered results the value $I_{\hat{d}}^* = 3\,A$ provides the minimum noise effect in the frequency range up to about $6\,Hz$.

In the results of Fig. 3.24 a speed reference $\omega_m^* = 100\,rpm$ has been considered with the observer operating off-line, i.e. the motor is controlled with the measured speed. A noise with a frequency of $1\,Hz$ with $1\,rpm$ amplitude is added

to the measured speed and the integral of that signal is also added to the measured rotor position needed for current vector control. Therefore feedback speed and position entering into the control loop are affected by the injected noise. The response of the drive to that noise is analyzed as a function of three different values of current component along the d-axis. The top diagram shows the reference and actual d-axis current, the bottom one the feedback, actual and reference speed.

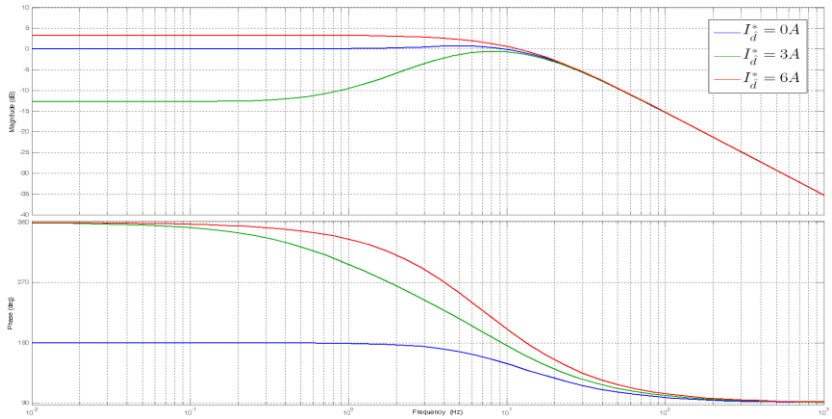

Fig. 3.23. Speed estimation noise effect on mechanical speed $\left.\frac{\omega_m(s)}{n(s)}\right|_{\omega_m^*(s)=0}$.

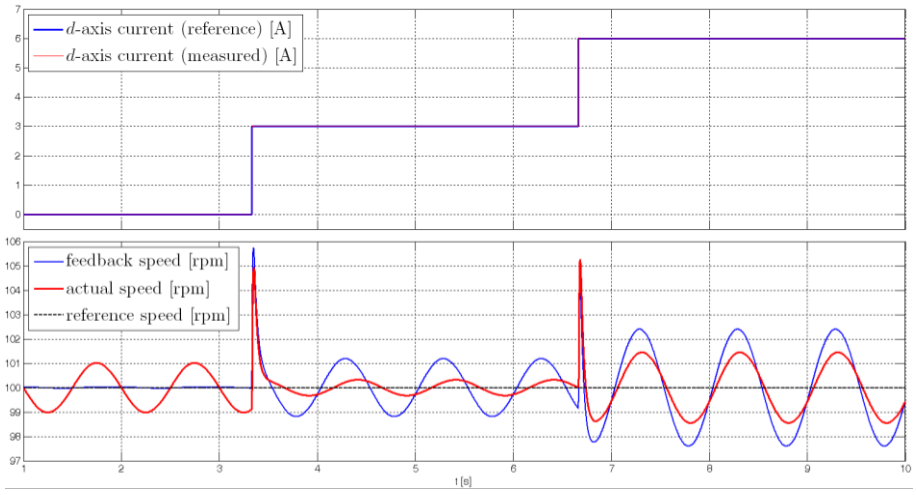

Fig. 3.24. Speed control noise sensitivity at steady-state ($100\ rpm$) with three different values of (estimated) d-axis (noise is $1\ Hz$ and $1\ rpm$).

The test results confirm the analytical calculations and the results shown in Fig. 3.23. In fact, without any injection of d-axis current (i.e. the most left part of the diagram), the injected noise is present on the actual speed, while it is not present on the feedback speed as the control rejects that disturbance. As the injected current is increased (i.e. to $3\,A$ in the middle part of the diagram), the feedback speed changes, and the actual speed oscillations are reduced. A further increase of d-axis current will provide worse results and also amplify the effect of the injected noise (most right part of the diagram).

3.7.3 Experimental results

Experimental results are based on an actual industrial drive system (Fig. A.1 and Table A.1) and confirm the importance of this effect on the control capabilities, demonstrating the extension of closed-loop control range towards zero, with respect to conventional techniques.

In the results of Fig. 3.25 and Fig. 3.26 the same test previously discussed in the simulation section is realized, i.e. Fig. 3.24. The drive system is operated at constant speed reference $\omega_m^* = 100\,rpm$ with the measured speed and position as feedbacks. A noise with a frequency of $1\,Hz$ is added to the measured speed and the integral of that signal is also added to the measured rotor position needed for current vector control. The injected noise amplitude is $1\,rpm$ and $5\,rpm$ in Fig. 3.25 and Fig. 3.26 respectively. The presence of other system noises (e.g. effects of dead time, measurement noise and offsets, quantization) requires low-pass filtering of the actual speed in order to extract only the injected noise component and understand the effect of the d-axis current injection. The results are comparable to those in Fig. 3.24, i.e. a proper value of the injected current provides a reduction of overall noises, while a further increase would amplify the noise effect.

The results in Fig. 3.27 are referred to sensorless operations in the same speed condition ($100\,rpm$). The additional current component is obviously performed in this case along the estimated d-axis and feedback position and speed going into the controller are the estimates coming out of the observer.

System noises provide a poor estimation and control in that low-speed condition and with no injection, leading to large oscillations on the actual speed (i.e. about $70\,rpm$ peak-to-peak) and almost unstable behavior, as shown in the most left part of the diagrams. A non-zero value of the additional current, i.e. $3\,A$, reduces the noise on the actual as far as on the estimated speed, allowing reliable sensorless operations. A further increase of the reference current, i.e. $6\,A$, provides worse results, as previously discussed.

Fig. 3.28 and Fig. 3.29 further show the effects of two different values of the injected current at steady-state. For the chosen speed regulator gains, the conventional technique ($0\,A$ $\hat{d}$-axis current, Fig. 3.28) shows almost unstable behavior at $100\,rpm$, as it can be seen from the large oscillations present, while speed is controlled within about $\pm 3\,rpm$ in the second case, i.e. with $4\,A$ $\hat{d}$-axis current, Fig. 3.29.

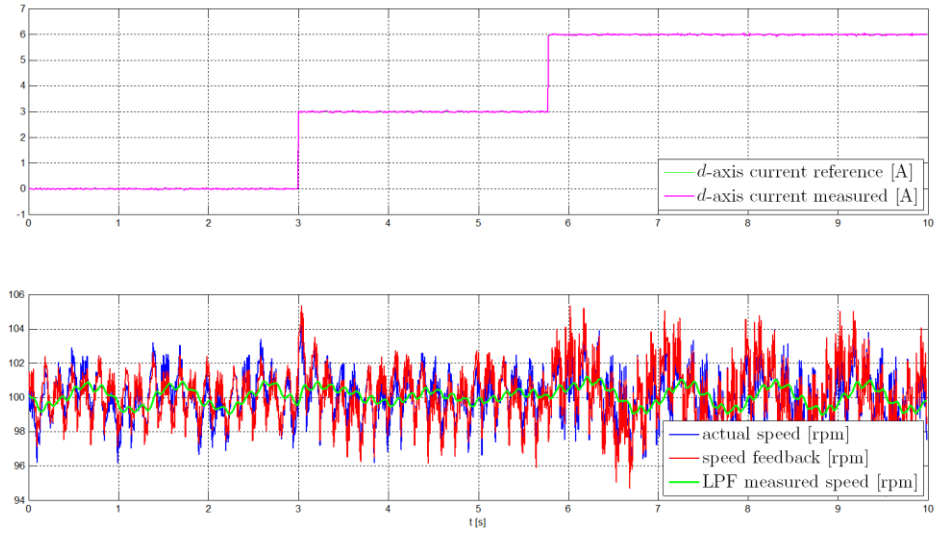

Fig. 3.25. Speed control noise sensitivity at steady-state ($100\,rpm$) with three different values of (estimated) d-axis (noise is $1\,Hz$ and $1\,rpm$).

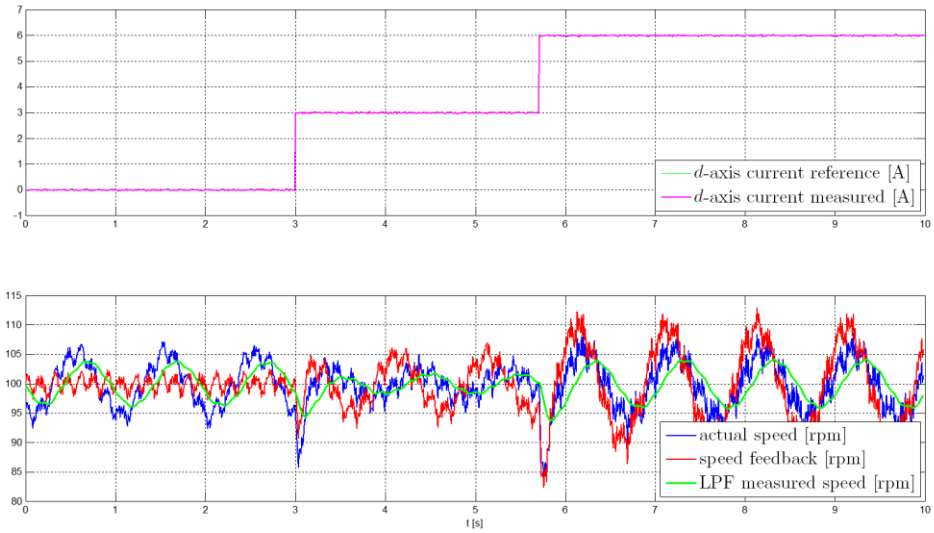

Fig. 3.26. Speed control noise sensitivity at steady-state ($100\,rpm$) with three different values of (estimated) d-axis (noise is $1\,Hz$ and $5\,rpm$).

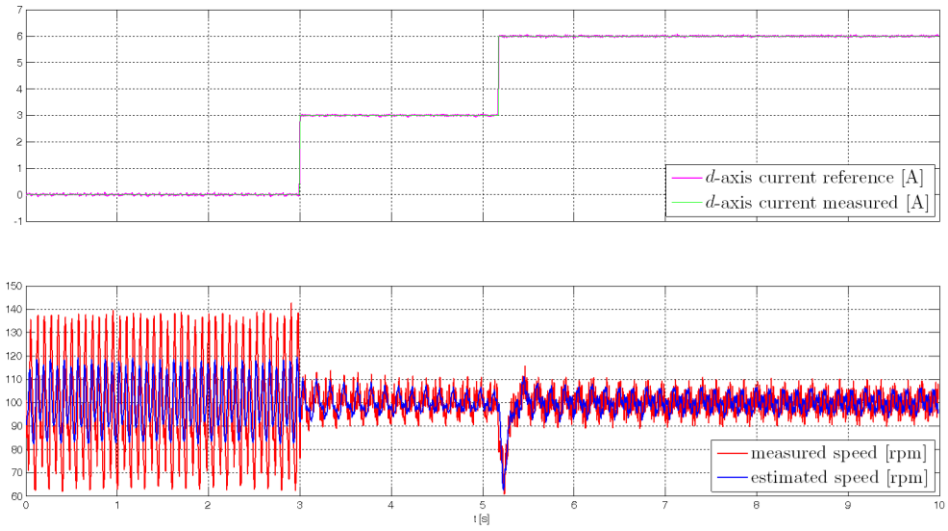

Fig. 3.27. Sensorless speed control at steady-state ($100\,rpm$) with three different values of (estimated) d-axis current.

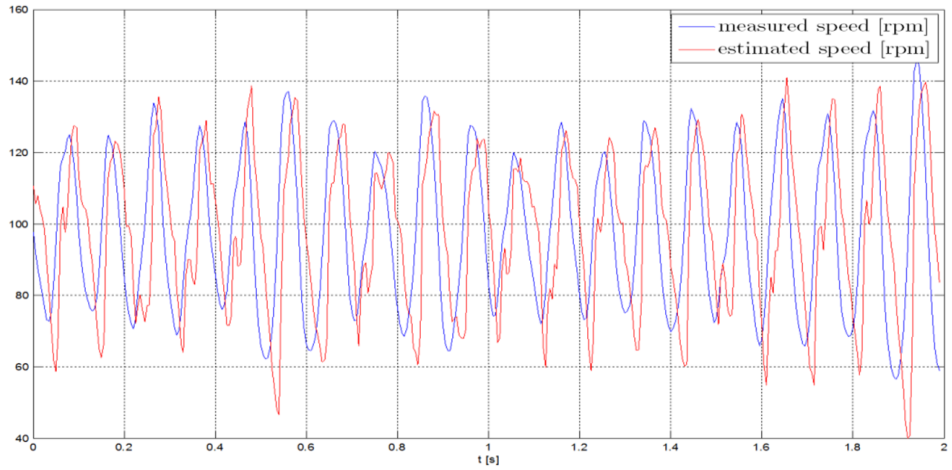

Fig. 3.28. Sensorless speed control at steady-state ($100\,rpm$) and $0\,A$ (estimated) d-axis current

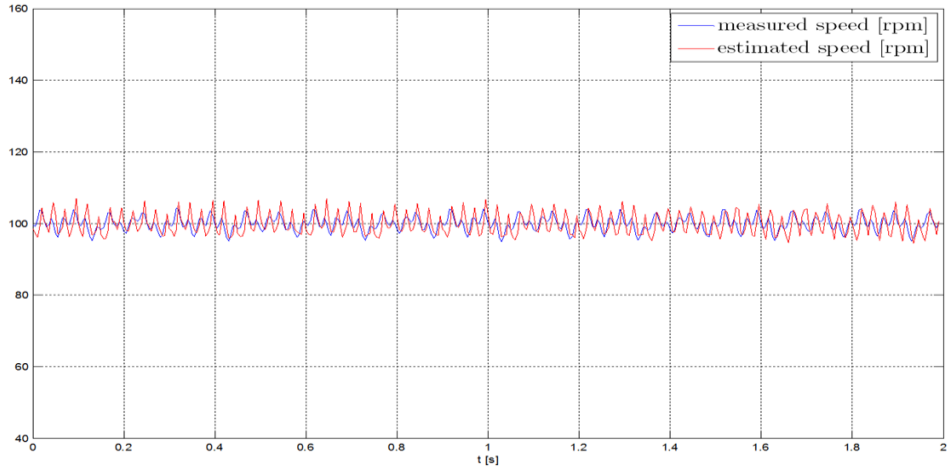

Fig. 3.29. Sensorless speed control at steady-state ($100\,rpm$) and constant $4A$ (estimated) d-axis current.

3.8 Conclusions

A back-EMF based sensorless technique for SPMSM drive systems has been considered and studied in this chapter. With respect to previous proposals, normally adopting a state-state representation, the analysis of the observer and the design of the observer's gains is developed using complex phase variables in the Laplace domain, and represents an original feature of this study. Steady-state errors are calculated from a theoretical point-of-view, including the effects of the most common non-idealities affecting the drive system (e.g. DC offsets) and parameters sensitivity. Simulation and experimental characterization of the sensorless drive is provided with reference to a general purpose industrial drive, i.e. both in transient and steady-state conditions and in the whole speed/torque operating range. Start-up from standstill and braking is handled through a simple but effective open-loop control.

Since the back-EMF based position and speed estimation is critical at very low-speeds (due to the low amplitude of back-EMF), operation of speed control in this condition can be quite unstable and non-robust. The effect of a constant direct-axis current component, is shown to be improving accuracy and stability in the case of noise-affected estimation or measurement, and an analytical explanation of this phenomenon can be found if considering a linearized model. It has been proved that a reduction of the estimation noise entering into the control loop is attainable with a proper choice of the value of the injected current.

Extensive simulation and experimental investigations have been provided to demonstrate the effectiveness of the adopted approach and the resulting advantages in an actual drive system, also for a sensored system. In the case of sensorless control based on a back-EMF observer, reduction of noise sensitivity of the controller, especially at low-frequency, allows to dramatically reduce speed oscillations, extending the closed-loop control range at the low-speed. Reliable operation of the drive is possible even in the case of step rated torque load insertion and removal. Standard filtering methods would be partially ineffective, as they will also provide a reduction of the control bandwidth and increase the possibility to enter into a speed operating range where estimates are very low and signal to noise ratio is therefore too low for a proper control of the motor.

Chapter 4
Injection-based sensorless estimation

In this chapter, three different position and speed estimation techniques, based on the exploitation of non-fundamental (i.e. not needed for torque generation) voltage or current signals will be described. The first two described methods are suitable for motors featuring an anisotropic rotor.

In the first case, a proposal related to the signal demodulation issues in high-frequency pulsating carrier injection will be presented, aiming at eliminating the dependence of the closed-loop estimation gain on the high-frequency carrier. This novel approach to demodulation was published in [35].

In the second section, excitation resulting from the PWM voltage ripple only (i.e. avoiding an actual injection) will be considered. The current transient response introduced by standard (or slightly modified) SV-PWM excitation will be considered as a means for extracting information on the rotor position, by means of Rogowsky coil derivative measurements. With respect to the past literature adopting similar approaches, a more detailed model is considered. The results of this study, which confirm the feasibility of the approach, but also highlight an unmodeled effect related to the permanent magnet, have been also presented in [36].

The last section deals with a technique relying on the back-EMF resulting from a low-frequency current injection, which can be also adopted for isotropic motors. This method, also described in [37], represents a viable possibility for low-performance sensorless startup and low-speed operation of non-salient motors.

4.1 Introduction to anisotropy based estimation

The basic principle behind the classical position and speed estimation methods based on signal injection is the relation between rotor magnetic anisotropy and position, similarly to what is done in magnetic rotary position sensors (resolvers). Since the behavior of the rotor iron geometry reflects into stator inductance, a direct or indirect sensing of the phase inductance results in a position-dependent quantity. The usual model representing a motor having magnetically salient rotor is a sinusoidal inductance contribution on the stationary frame inductance matrix, which is very similar to a rotation matrix. From direct inductance measurements or inductance-related signals, the rotor position can be easily estimated, extracting position information and consequently obtaining a speed estimate. Anisotropy-based estimation was conceived mainly for IPMSMs, but soon was applied also to SM-PMSMs, since anisotropy is almost always present also in this case (although it is usually lower).

Measurement or testing of inductance requires a current variation (non-null current derivative), which is incompatible with the normal torque control currents. Moreover, to achieve good exploitation of anisotropy, a constant and recognizable excitation (i.e. a signal distinguishable from the fundamental) is desired, thus additional signals must be considered for estimation. In the classical signal injection based methods, a rotating or pulsating carrier signal is superimposed to fundamental voltage (persistent carrier based excitation) and demodulation of the resulting high frequency induced currents is exploited to obtain rotor position information, [38], [39]. To achieve a sufficient bandwidth of the information carried by the measured signal, and to avoid the introduction of large disturbance to the control loop, a high-frequency carrier is preferred, which is the reason for the name "HF-injection", which is usually associated with these techniques. In Fig. 4.1, a scheme representing the principle of operation of the most common techniques is shown. The figure is only intended to intruduce how injection, motor magnetic model and signal processing interact in loops, while implementations are usually far more complex, at least comprising demodulation and filtering blocks. An excitation voltage signal is injected (depending on the method, direction can be dependent on

the estimation position or not). The resulting current vector is then compared in direction to the expected one (based on the estimated rotor position), by means of what is, in principle, a vector product calculation. The result is proportional to the sine of twice the angular difference between the estimated and actual rotor position which, for a small difference, can be approximated to a linear gain. Thus, an error signal is obtained, that can be used as a correction term in a Luenberger-style observer (PLL-type scheme).

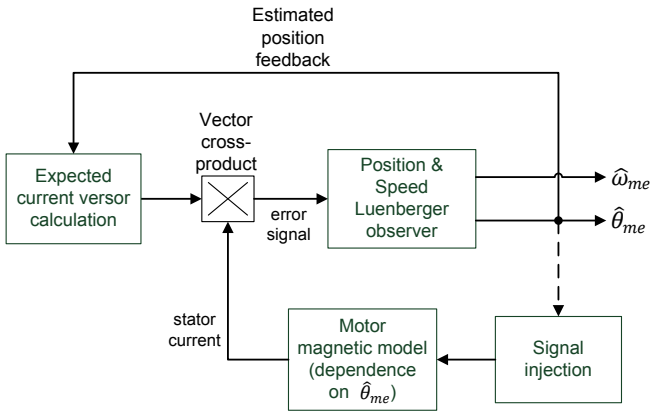

Fig. 4.1. Principle of operation of anisotropy-based methods.

The simpler methods imply sinusoidal flux injection (which is simply translated into voltage injection, [40]), mainly according to two variants: a pulsating injection along one of the two estimated rotor axes Fig. 4.2 or a constant magnitude vector rotating at high frequency Fig. 4.3. The first technique provides a simpler implementation and some other advantages [41], then is more widely adopted.

Other techniques have also been adopted, the well-known INFORM method among them, based on intermittent excitation [42]. In this case, the injection consists in the application of two separate and opposite test vectors during a null space voltage vector. More recently, the development of techniques relying on the PWM voltage ripple only as the injected signal have been proposed, as the one described in 4.3, that has been presented in [36]. Of course, in these cases more complex algorithms and measurements need to be implemented, and achieving high accuracy and dynamical performances is usually more difficult than with

sinusoidal excitation, due to the spread-spectrum characteristic of the exploited signal. In particular, oversampling and current derivative sensing have been introduced in some proposals, in order to overcome the issues introduced by the particular signal considered for inductance testing.

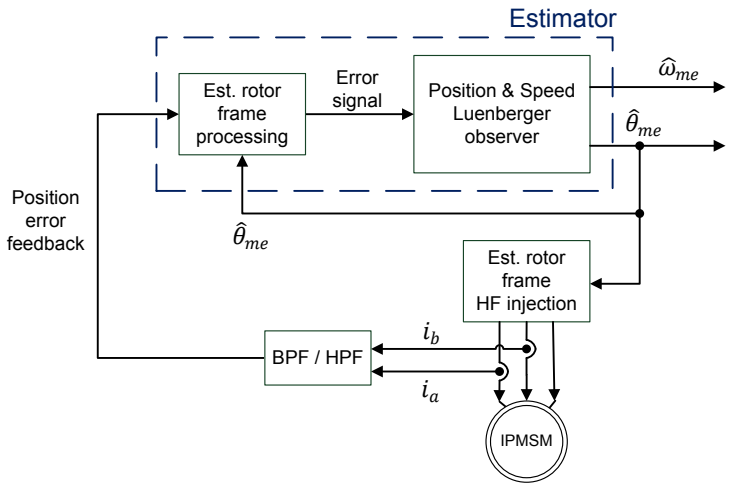

Fig. 4.2. Principle of operation of pulsating signal injection estimation technique.

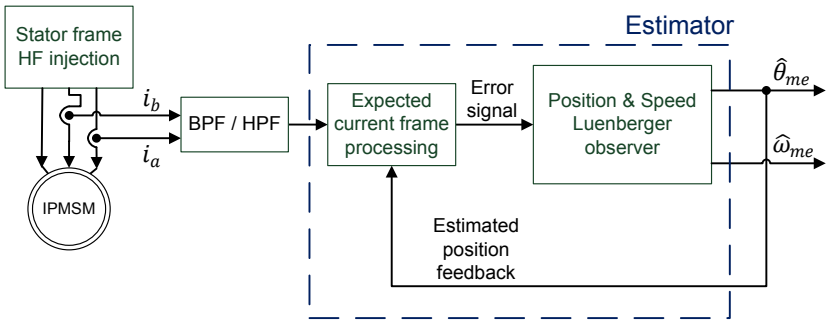

Fig. 4.3. Principle of operation of rotating signal injection estimation technique.

Despite the many years of research and development on these topics, and the presence on the market of some drives implementing high-frequency injection based estimation [43], many issues are still open. An important one can be identified in the effects of saturation on the anisotropy map of the rotor (i.e. in the relation

between position and inductance), which is, especially for certain motors, heavily affected by the operating conditions (current magnitude and phase). In the case of the Surface Mount PMSM, for example, which is the most diffused rotor configuration, the anisotropy is mostly saturation-induced, and then the stator current conditions usually play an important role on anisotropy. Although many compensation techniques have been developed, which can be adopted for specific motors, application to general-purpose drives is almost impossible, since extensive off-line measurements are not available. Also for these reasons, a combined approach from both the machine design and control point of view is making its way, in which the sensorless requirements are taken into account from the early stages of development.

Recently, some methods have been proposed in which the tracking is performed on high-frequency stator-reflected resistance, in place of the usually tracked inductance, which is mainly related to the presence of the permanent magnets and their conductivity, [44]–[47]. Investigation on this field is however quite new, and measurements on more different rotors would be interesting to confirm the feasibility on standard Surface Mount PMSMs.

4.2 Demodulation techniques for pulsating vector HF injection

This section will introduce a novel approach based on Discrete Fourier Transform (DFT) and a non-conventional reference frame transformation for pulsating vector high-frequency injection, which was published in [35]. The method allows a simple and robust non-coherent demodulation, i.e. in which no information about the carrier phase is needed. In the classically adopted coherent approaches, in fact, uncertainty about carrier phase reflects in uncertainty in the demodulated signal amplitude, affecting observer gains and signal-to-noise ratio, definitively providing a degradation of the performance of the estimator. After an analytical recall of the reference sensorless algorithm (based on pulsating

flux/voltage injection), a novel demodulation technique will be introduced and investigated by means of simulations and experiments, based on a prototype motor drive for city-scooters.

From a magnetic point of view, IPM motors exhibit a saliency ratio different from unity, i.e. the direct d-axis inductance is substantially different from the quadrature q-axis inductance, where the d-axis is usually selected to be aligned with the PM flux axis. This characteristic is particularly suited for extending the speed operating region by proper field-weakening control techniques [48] and, also, it allows the application of some interesting approaches to position and speed estimation, i.e. high-frequency signal injection techniques, suitable for low-speed and stand-still sensorless control of the machine, [39], [49], [50]. According to this approach a high-frequency flux is superimposed to the fundamental one. The resulting high-frequency current is sine-carrier amplitude-modulated by a function of the position estimation error. Demodulation of this signal and its closed loop control to zero provides a mean for the dynamic estimation of the rotor position, [51]–[54],[55]–[57], [41].

The impact of rotor geometry on sensorless rotor position detection by high frequency signal injection have been investigated recently, [55], [58]. It has been found that the effectiveness of the sensorless rotor position detection strongly depends on the PM rotor geometry.

In this section, a demodulation approach based on Discrete Fourier Transform (DFT) will be presented. The method allows a simple and robust non-coherent demodulation, i.e. in which no information about the carrier phase is needed. In the classically adopted coherent approaches, in fact, uncertainty about carrier phase reflects in uncertainty in the demodulated signal amplitude (which is proportional to the sine of the error between real and known phase), thus affecting observer gains and signal to noise ratio and definitively providing a degradation of the performance of the dynamical position estimator. Also, square-wave based demodulation techniques allow only two points per period of the injected signal to be sampled and their accuracy is similarly dependent on the uncertainty about carrier phase. The analytical development of the sensorless algorithm including the demodulation technique is provided. A complete simulation investigation is carried out aiming at showing the performance of the proposed method, also in comparison with state-of-the-art approaches. Finally experimental results are presented based on a prototype motor drive system for city-scooters.

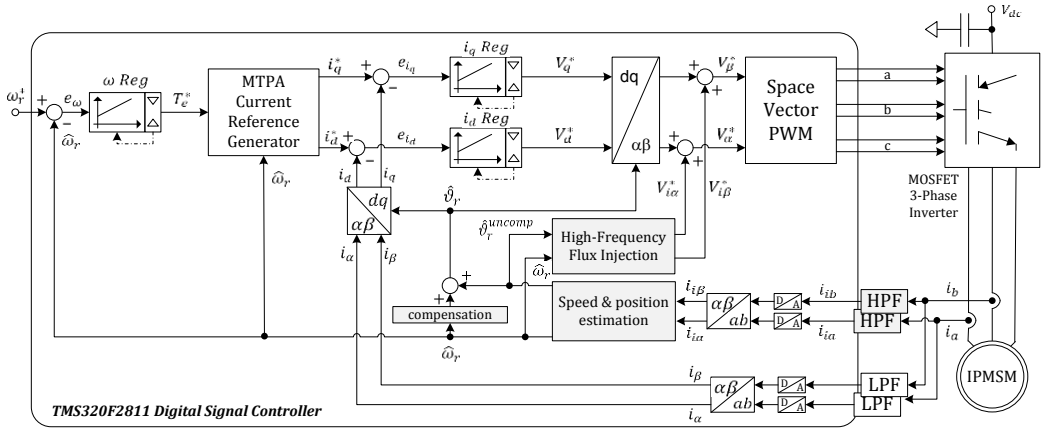

Fig. 4.4. Drive system scheme.

4.2.1 Sensorless control scheme

The sensorless control scheme considered in this work is shown in Fig. 4.4. It is implemented by a 32-bit fixed-point digital signal controller performing all the processing needed for rotor position and speed estimation as well as the motor control algorithms. The current control loops are arranged in the two-phase synchronously rotating reference frame d-q aligned with the predicted/estimated rotor flux. Current references are provided by an maximum torque per ampere (MTPA) reference generator as a function of the required torque reference and actual (estimated) rotor speed. Proportional and integral regulators are used for both the current and speed control loops. An adjacent-vector space vector pulse width modulator (AV-SVPWM) is used to apply the voltage commands. Low-pass and high-pass filters are used respectively for the acquisition of the fundamental currents (needed for current control loops) and high-frequency currents (needed for the speed and position estimator), allowing to improve both control and estimation performance by enhancing the signal-to-noise ratio of the acquisition chain.

In the actual implementation the high-pass filtering is realized by digitally programmable switched-capacitance analogical filters, thus obtaining high filtering performance and allowing to adapt very easily the pass band to the adopted frequency used for the flux-injection. During system development and testing, a

steady-state position estimation error being a function of speed has been pointed-out, which in our experience is due to estimation loop delays (mainly represented by inverter timing and current sampling). It has been shown that this is linearly dependent on speed, then a simple compensation has been introduced, whose coefficient has been tuned empirically.

Further developments of next section will show that an additional component compensating for cross-saturation effects should be introduced on rotor position estimation, [59]–[61].

4.2.2 Injection-based estimation method principle of operation

The technique adopted in this work is similar to the one originally proposed by Corley and Lorenz for salient-rotor motors, [39]. According to this method, the direct rotor axis (the direction of permanent magnet field) is being tracked thanks to an error signal which comes from a superimposed high frequency flux, whose angular frequency being ω_i.

The conventional voltage equation of IPM motor in the dq reference frame synchronous with permanent magnet flux-linkage is considered first, i.e.:

$$\begin{bmatrix} u_d \\ u_q \end{bmatrix} = R \begin{bmatrix} i_d \\ i_q \end{bmatrix} + \frac{d}{dt} \begin{bmatrix} \lambda_d \\ \lambda_q \end{bmatrix} + \omega_{me} \begin{bmatrix} -\lambda_q \\ \lambda_d \end{bmatrix} \tag{4.1}$$

where $[u_d \quad u_q]^T$, $[i_d \quad i_q]^T$ and $[\lambda_d \quad \lambda_q]^T$ are respectively the vectors of stator voltage, current and flux-linkage in the dq rotor oriented synchronous reference frame aligned with the permanent magnet flux and ω_r is the electrical angular speed. Electromagnetic torque is therefore:

$$T_e = \frac{3}{2} pp \left[\lambda_d i_q - \lambda_q i_d \right] \tag{4.2}$$

where pp is the number of pole-pairs.

Let us consider flux-current relationships $\lambda_d(i_d)$ and $\lambda_q(i_q)$, where mutual inductance due to cross-saturation effects is ignored. If small (e.g. high-frequency)

variations around a steady-state operating point are considered, the following expressions can be written:

$$\begin{bmatrix}\lambda_{id}\\ \lambda_{iq}\end{bmatrix}=\begin{bmatrix}\dfrac{d\lambda_d(i_d)}{di_d} & 0\\ 0 & \dfrac{d\lambda_q(i_q)}{di_q}\end{bmatrix}\begin{bmatrix}i_{id}\\ i_{iq}\end{bmatrix}=\begin{bmatrix}l_d & 0\\ 0 & l_q\end{bmatrix}\begin{bmatrix}i_{id}\\ i_{iq}\end{bmatrix} \tag{4.3}$$

where l_d and l_q are the self differential inductances, [60], and i_{id} and i_{iq} are the current components generating the perturbation around the steady-state point.

Equation (4.3) can be referred to an unknown rotating reference frame $\hat{d}\hat{q}$ by the transformation:

$$\begin{bmatrix}\lambda_{i\hat{d}}\\ \lambda_{i\hat{q}}\end{bmatrix}=T^{-1}_{\hat{d}\hat{q}\to dq}\cdot\begin{bmatrix}l_d & 0\\ 0 & l_q\end{bmatrix}\cdot T_{\hat{d}\hat{q}\to dq}\cdot\begin{bmatrix}i_{i\hat{d}}\\ i_{i\hat{q}}\end{bmatrix} \tag{4.4}$$

where

$$T_{\hat{d}\hat{q}\to dq}=\begin{bmatrix}cos(\Delta\theta_{me}) & sin(\Delta\theta_{me})\\ -sin(\Delta\theta_{me}) & cos(\Delta\theta_{me})\end{bmatrix} \tag{4.5}$$

and $\Delta\theta_{me}=\theta_{me}-\hat{\theta}_{me}$ is the error between the actual (dq) and the unknown ($\hat{d}\hat{q}$) reference frames.

Inversion of (4.4) allows to calculate current components as a function of flux:

$$\begin{aligned}\begin{bmatrix}i_{i\hat{d}}\\ i_{i\hat{q}}\end{bmatrix}&=T^{-1}_{\hat{d}\hat{q}\to dq}\cdot\begin{bmatrix}l_d & 0\\ 0 & l_q\end{bmatrix}^{-1}\cdot T_{\hat{d}\hat{q}\to dq}\cdot\begin{bmatrix}\lambda_{i\hat{d}}\\ \lambda_{i\hat{q}}\end{bmatrix}\\ &=\frac{1}{l_d l_q}\begin{bmatrix}(l_\Sigma+l_\Delta)cos(2\Delta\theta_{me}) & l_\Delta sin(2\Delta\theta_{me})\\ l_\Delta sin(2\Delta\theta_{me}) & (l_\Sigma-l_\Delta)cos(2\Delta\theta_{me})\end{bmatrix}\cdot\begin{bmatrix}\lambda_{i\hat{d}}\\ \lambda_{i\hat{q}}\end{bmatrix}\end{aligned} \tag{4.6}$$

where $l_\Sigma=\frac{l_d+l_q}{2}$ and $l_\Delta=\frac{l_q-l_d}{2}$.

The injection of an alternating flux space vector along the $\hat{q}$-axis only, i.e.:

$$\begin{bmatrix}\lambda_{i\hat{d}}\\ \lambda_{i\hat{q}}\end{bmatrix}=\frac{V_i}{\omega_i}sin(\omega_i t)\begin{bmatrix}0\\ 1\end{bmatrix} \tag{4.7}$$

will then result in a $\hat{d}$-axis current whose amplitude is proportional to the sine of twice the position error $\Delta\vartheta$:

$$\begin{aligned} i_{i\hat{d}} &= I_{i1} sin(\omega_i t) \cdot sin(2\Delta\theta_{me}) \\ i_{i\hat{q}} &= [I_{i0} - I_{i1} \cdot cos(2\Delta\theta_{me})] \cdot sin(\omega_i t) \end{aligned} \tag{4.8}$$

where $I_{i1} = \frac{V_i l_\Delta}{\omega_i (l_\Sigma^2 - l_\Delta^2)}$ and $I_{i0} = \frac{V_i l_\Sigma}{\omega_i (l_\Sigma^2 - l_\Delta^2)}$.

The injected voltage needed to provide flux (4.7) can be simply calculated from (4.1) by neglecting the resistance voltage drop and derivation of (4.7), yielding:

$$\begin{bmatrix} v_{i\hat{d}} \\ v_{i\hat{q}} \end{bmatrix} = V_i \begin{bmatrix} -\hat{\omega}_{me}/\omega_i \, sin(\omega_i t) \\ cos(\omega_i t) \end{bmatrix} \tag{4.9}$$

where $\hat{\omega}_{me}$ is the (estimated) angular speed of the $\hat{d}\hat{q}$ estimated reference frame and V_i is a proper amplitude. The voltage locus is an ellipse in the estimated reference plane, [39], [51], [54].

The $\hat{d}$-axis current (4.8) caused by injection, once filtered (to eliminate fundamental components involved in torque production), is a high-frequency sine *carrier*, amplitude-modulated by a function of the position error $\Delta\theta_{me}$ and can be adopted to estimate rotor position θ_{me} (by driving this component to zero in closed-loop fashion as a function of $\hat{\theta}_{me}$). Although the dependency from the angle is sinusoidal, it is normally considered linear (this is almost true when estimation error is enough small).

Then one needs to demodulate that signal and to feed it into a proper dynamical system (usually a *Luenberger-style observer* of the mechanical subsystem, [53]), providing speed and position estimates. Details about demodulation process will be provided in a next specific section, where the novel contribution of this work will be analysed in details and compared to standard solutions.

4.2.3 Cross-saturation effects

Magnetic coupling between d and q axes leads to the dependence of the flux of each axis on both currents, i.e.:

$$\begin{aligned}\lambda_d &= \lambda_d(i_d, i_q)\\ \lambda_q &= \lambda_q(i_d, i_q)\end{aligned} \tag{4.10}$$

Equation (4.3) can therefore be rewritten to take this effect into account:

$$\begin{bmatrix}\lambda_{id}\\ \lambda_{iq}\end{bmatrix} = \begin{bmatrix}\dfrac{\partial\lambda_d(i_d,i_q)}{\partial i_d} & \dfrac{\partial\lambda_d(i_d,i_q)}{\partial i_q}\\ \dfrac{\partial\lambda_q(i_d,i_q)}{\partial i_d} & \dfrac{\partial\lambda_q(i_d,i_q)}{\partial i_q}\end{bmatrix}\begin{bmatrix}i_{id}\\ i_{iq}\end{bmatrix} = \begin{bmatrix}l_d & l_M\\ l_M & l_q\end{bmatrix}\begin{bmatrix}i_{id}\\ i_{iq}\end{bmatrix} \tag{4.11}$$

and mutual differential inductance l_M is introduced.

By repeating similar calculations to those of the previous section, the expression of the currents in response to an injected flux in an unknown $\hat{d}\hat{q}$ reference frame can be calculated:

$$\begin{aligned}&\begin{bmatrix}i_{i\hat{d}}\\ i_{i\hat{q}}\end{bmatrix} = T^{-1}_{\hat{d}\hat{q}\to dq}\cdot\begin{bmatrix}l_d & l_M\\ l_M & l_q\end{bmatrix}^{-1}\cdot T_{\hat{d}\hat{q}\to dq}\cdot\begin{bmatrix}\lambda_{i\hat{d}}\\ \lambda_{i\hat{q}}\end{bmatrix} =\\ &= \frac{1}{l_d l_q - l_M^2}\cdot\\ &\cdot\begin{bmatrix}l_\Sigma + l_\Delta cos(2\Delta\theta_{me}) + l_M sin(2\Delta\theta_{me}) & l_\Delta sin(2\Delta\theta_{me}) - l_M cos(2\Delta\vartheta)\\ l_\Delta sin(2\Delta\theta_{me}) - l_M cos(2\Delta\theta_{me}) & l_\Sigma - l_\Delta cos(2\Delta\theta_{me}) - l_M sin(2\Delta\vartheta)\end{bmatrix}\cdot\begin{bmatrix}\lambda_{i\hat{d}}\\ \lambda_{i\hat{q}}\end{bmatrix}\end{aligned} \tag{4.12}$$

The injection of an alternating flux space vector along the $\hat{q}$-axis, i.e. (4.7), will result in the following components of currents:

$$\begin{aligned}i_{i\hat{d}} &= \frac{V_i}{\omega_i(l_d l_q - l_M^2)}[l_\Delta sin(2\Delta\theta_{me}) - l_M cos(2\Delta\theta_{me})]\cdot sin(\omega_i t)\\ i_{i\hat{q}} &= \frac{V_i}{\omega_i(l_d l_q - l_M^2)}[l_\Sigma - l_\Delta\cdot cos(2\Delta\theta_{me}) - l_M sin(2\Delta\theta_{me})]\cdot sin(\omega_i t)\end{aligned} \tag{4.13}$$

Same approach as before can be adopted to estimate actual rotor position θ_{me}, i.e. by driving the $\hat{d}$-axis current component to zero as a function of $\hat{\theta}_{me}$:

$$0 = l_\Delta sin(2\Delta\theta_{me}) - l_M cos(2\Delta\theta_{me}) \tag{4.14}$$

leading to

$$\Delta\theta_{me} = \frac{1}{2}arctan\left(-\frac{l_M}{l_\Delta}\right). \tag{4.15}$$

One can notice that rotor position estimation error is a function of self and mutual differential inductances, [59].

4.2.4 Coherent demodulation

An important issue is represented by the demodulation, which is typically done coherently, as shown in the block diagram of Fig. 4.5. In the classical heterodyning technique, the amplitude modulated signal is first mixed (multiplied) with a sine wave at the same frequency as the carrier (an arbitrary phase shift $\widehat{\Phi}$ may be present). The result is the sum of a signal proportional to the original modulating one (low frequency) and a component modulated at twice the frequency. Low-pass filtering the mixer output then allows to recover the desired information.

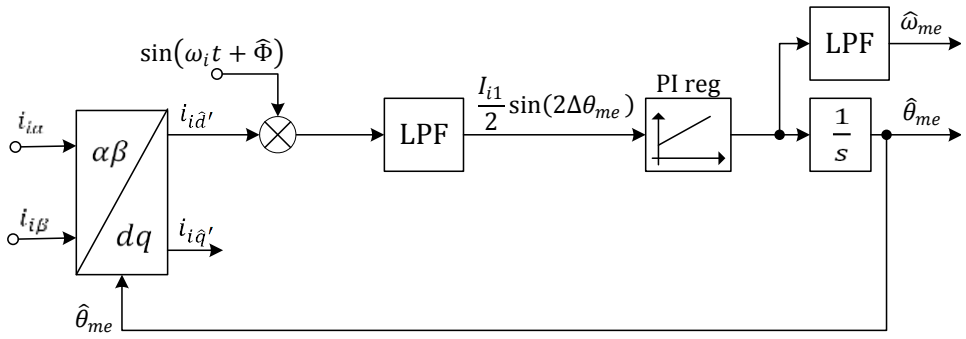

Fig. 4.5. Block diagram of the coherent demodulation engine and position/speed estimator.

The loop filter (PI regulator) may be replaced by a more complex estimation observer, [49].

This implies that the actual phase of superimposed high-frequency signals has to be known, but this is not true in practical implementations. In fact, if a telecommunications approach is considered, even if the control system acts like both transmitter and receiver, inverter and sample timing introduce non negligible

delays that are hardly analytically predictable. Uncertainty about carrier phase reflects in uncertainty in the demodulated signal amplitude (which is proportional to the sine of error between real and known phase), affecting observer gains and signal to noise ratio. An interesting approach to carrier recovery of the carrier signal needed for the demodulation process is presented in [50]. A short resume is presented hereafter.

A more realistic model for the $\hat{q}$-axis high frequency current component (neglecting cross-saturation effects) must then take into account the previous considerations and could be expressed in the form:

$$i_{i\hat{q}} = [I_{i0} - I_{i1} \cdot cos(2\Delta\theta_{me})] \cdot sin(\omega_i t + \Phi) \tag{4.16}$$

being Φ an unknown phase shift between the injected high frequency voltage (carrier signal) and the correspondent current. When the position estimation error is kept constant, that is the estimation procedure is inhibited, the amplitude of the high-frequency components of that current is constant and could be expressed in the form:

$$i_{i\hat{q}} = a \cdot sin(\omega_i t + \Phi) \tag{4.17}$$

being a its constant amplitude. The demodulation process must be synchronous with this current component, that is a suitable strategy for carrier extraction must be found (Φ is to be known). One can notice that the quadrature current component (4.16) is always present independently from the rotor position estimation error, as the term I_{i0} is always non-zero, allowing the carrier recovery process always to be applied.

The basic idea is to implement a simple digital phase locked loop (Fig. 4.6): the measured $\hat{q}$-axis current component is first multiplied by an auxiliary numerically phase-controlled (Φ) fixed-frequency (ω_i) oscillator (NPCO), whose frequency is equal to that of the injected voltage/flux:

$$\varepsilon_\Phi = i_{i\hat{q}} \cdot cos\left(\omega_i t + \hat{\Phi}\right) = \frac{1}{2} a\left[sin\left(2\omega_i t + \hat{\Phi} + \Phi\right) + sin\left(\Phi - \hat{\Phi}\right)\right] \tag{4.18}$$

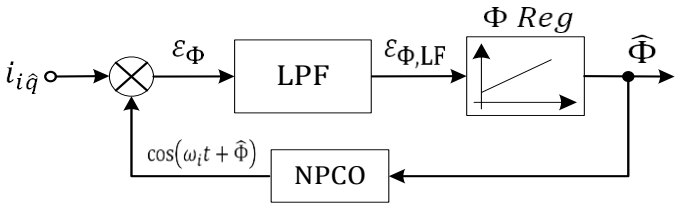

Fig. 4.6. Digital PLL adopted for carrier recovery.

Then the error signal ε_Φ is passed through a low-pass filter in order to remove the (double) high-frequency content, thus obtaining the low-frequency error signal:

$$\varepsilon_{\Phi,LF} = \frac{1}{2} a \cdot sin\left(\Phi - \widehat{\Phi}\right) \tag{4.19}$$

The actual implementation considers a 4th order $800\,Hz$ cut-off frequency IIR low-pass filter.

Note that $\varepsilon_{\Phi,\mathrm{LF}}$ is a function of the phase difference between the two input signals and it is zero when the received carrier and internally generated waves are exactly matched in phase (and in frequency). When this condition is met, the corresponding phase shift $\widehat{\Phi}$ equals the unknown one Φ and a correct carrier recovery is accomplished.

4.2.5 DFT-based demodulation

The use of a digital implementation makes it possible to use more complex signal processing algorithms. One possible approach is to adopt the Discrete Fourier Transform (DFT) to identify the amplitude of the modulated signal in real-time. Although the approach that will be described in the following is actually based on a DFT approach, the use of the term DFT might be confusing, thus some clarification is needed. Since information on a single harmonic is needed (injection frequency), the Fourier algorithm will only be used to determine the amplitude of one frequency component of two different signals. This will result in a computational effort which is very limited, since it can be considered as the application of simple FIR (Finite Impulse Response) filtering.

The advantage represented by this kind of demodulation consists in avoiding phase recovery algorithms needed to implement a coherent demodulation, since the DFT-based algorithm is a simple and robust non-coherent demodulation technique, i.e. does not need any information about the carrier phase. If a signal contains only a sine term at a known frequency, calculating the modulus of the complex DFT at that frequency is equivalent to extracting the amplitude of the wave. Considering the DFT calculated over a flat *running-window* (i.e. selecting the last samples at each time step) of a modulated sine wave, it is known that the modulus term corresponding to the injection (carrier) frequency f_i is the instant amplitude except for a small phase-lag. It is important to notice that this amplitude is always positive, so the remaining problem is the determination of sign of the desired signal, whose accuracy is extremely important for estimation purposes. A simple solution to this problem can therefore be obtained in making the modulated signal never change its sign. This can be easily accomplished by the original feature here introduced, i.e. a new rotor reference frame (e.g. $\hat{d}'\hat{q}'$ frame) which is phase shifted by $-\pi/4$ from the usual one, and processing both direct and quadrature currents. Both projections on these axes contain a term I_{i0} related to the average inductance, and a term I_{i1} related to the differential inductance modulated by the rotor position estimation error, as shown in the following expression:

$$\begin{aligned}\begin{bmatrix} i_{i\hat{d}'} \\ i_{i\hat{q}'} \end{bmatrix} &= T_{\alpha\beta\to dq}\left(\hat{\theta}_{me} - \frac{\pi}{4}\right)\cdot i_{i_{\alpha\beta}} = \\ sin(\omega_i t)&\begin{bmatrix} I_{i0}sin\left(-\frac{\pi}{4}\right) + I_{i1}sin\left(2\Delta\theta_{me} + \frac{\pi}{4}\right) \\ I_{i0}cos\left(-\frac{\pi}{4}\right) - I_{i1}cos\left(2\Delta\theta_{me} + \frac{\pi}{4}\right) \end{bmatrix} = \\ sin(\omega_i t)&\begin{bmatrix} -\frac{\sqrt{2}}{2}I_{i0} + I_{i1}sin\left(2\Delta\theta_{me} + \frac{\pi}{4}\right) \\ \frac{\sqrt{2}}{2}I_{i0} - I_{i1}cos\left(2\Delta\theta_{me} + \frac{\pi}{4}\right) \end{bmatrix}.\end{aligned} \tag{4.20}$$

As I_{i1} is usually smaller than I_{i0}, both modulation signals maintain their signs no matter about the estimation error value and/or sign (as in the classical Amplitude Modulation).

As a consequence, the envelope (given by the DFT modulus) of each one gives back the modulating signal including an offset:

$$\left|DFT_{f_i}\left(\begin{bmatrix} i_{i\hat{d}'} \\ i_{i\hat{q}'} \end{bmatrix}\right)\right| \cong \begin{bmatrix} \left|-\frac{\sqrt{2}}{2} I_{i0} + I_{i1} sin\left(2\Delta\theta_{me} + \frac{\pi}{4}\right)\right| \\ \left|\frac{\sqrt{2}}{2} I_{i0} - I_{i1} cos\left(2\Delta\theta_{me} + \frac{\pi}{4}\right)\right| \end{bmatrix} = \begin{bmatrix} \frac{\sqrt{2}}{2} I_{i0} - I_{i1} sin\left(2\Delta\theta_{me} + \frac{\pi}{4}\right) \\ \frac{\sqrt{2}}{2} I_{i0} - I_{i1} cos\left(2\Delta\theta_{me} + \frac{\pi}{4}\right) \end{bmatrix}. \tag{4.21}$$

The difference between the outputs of the two DFT signals neglects this constant term, giving back the error signal:

$$\begin{aligned} &\left|DFT_{f_i}(i_{i\hat{q}'})\right| - \left|DFT_{f_i}(i_{i\hat{d}'})\right| \\ &= {\sqrt{2}}/{2}\, I_{i0} - I_{i1} cos\left(2\Delta\theta_{me} + \frac{\pi}{4}\right) - \frac{\sqrt{2}}{2} I_{i0} + I_{i1} sin\left(2\Delta\theta_{me} + \frac{\pi}{4}\right) \\ &= I_{i1} sin\left(2\Delta\theta_{me} + \frac{\pi}{4}\right) - I_{i1} cos\left(2\Delta\theta_{me} + \frac{\pi}{4}\right) \\ &= cos\left(\frac{\pi}{4}\right) \cdot I_{i1} sin(2\Delta\theta_{me}) = \sqrt{2} I_{i1} sin(2\Delta\theta_{me}) \end{aligned} \tag{4.22}$$

This approach is, from the dynamical point of view, equivalent to the classical heterodyning process followed by a running window averaging (i.e. a filter whose pulse response has the same shape of the DFT windowing function), but does not require any information about the carrier phase. To show the dynamic properties of the considered processing, an intuitive demonstration is provided hereafter for a generic signal $x(t)$. Before the modulus calculation, the DFT algorithm consists in the convolution with a filter whose impulse response is the sine-cosine exponential signal at f_i windowed by a rectangular signal. Since the modulus is kept the same also in the frequency domain, this corresponds to a multiplication between the Fourier transform of the input signal $X(f)$ and the convolution of the transforms of the two impulse response functions composing the filter:

$$\left|DFT_{f_i}(x)\right| = \left|x(t) * [rect(\tau) \cdot e^{j2\pi f_i \tau}]\right| \tag{4.23}$$

Since the Fourier transform of an exponential signal is a Dirac delta function δ (in this case translated by f_i) and that of a rectangular one is a sinc, the following expression can be obtained:

$$\left|DFT_{f_i}(x)\right| = |X(f) \cdot [sinc(f) * \delta(f - f_i)]| \tag{4.24}$$

which represent the processing by a band-pass filter centered on f_i and shaped as a sinc function.
Simulations demonstrate that the best dynamic results can be achieved by using a window whose length is half a period of the injected sine wave (window duration equal to $0.5/f_i$). The adoption of this technique introduces a weak constraint when choosing the injected and sampling frequencies, to avoid aliasing phenomenon.

The overall block diagram of the proposed demodulation engine adopting DFT is shown in Fig. 4.7.

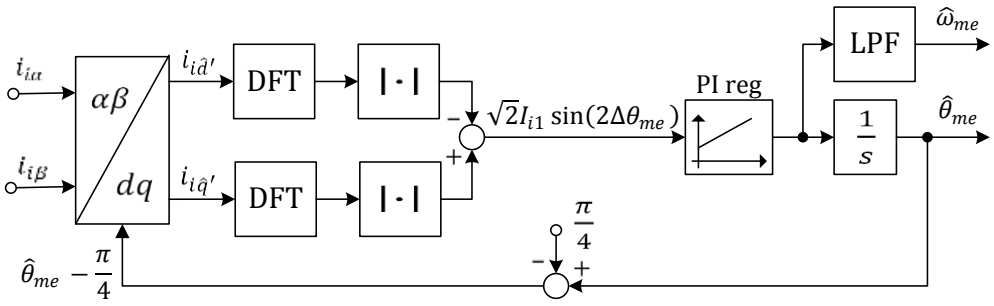

Fig. 4.7. Block diagram of the non-coherent DFT-based demodulation engine and position/speed estimator.

From a computational point of view, it is important to notice that, at each control step, the DFTs of two signals have to be calculated for a single frequency value. This requires a low number of math operations, (each DFT is a filter whose order is equal to the window length), if done with pre-calculated coefficients.

A simplification can be applied to the calculation, since the two high-frequency dq modulated signals are in-phase (because they are a consequence of the same injected flux):

$$\left|DFT_{f_i}(i_{i\hat{q}'})\right| - \left|DFT_{f_i}(i_{i\hat{d}'})\right| = \left|DFT_{f_i}(i_{i\hat{q}'} - i_{i\hat{d}'})\right| \tag{4.25}$$

allowing the calculation of complex magnitude once instead of twice. A rough comparison between the implementation requirements of the proposed demodulation approach and conventional heterodyne with carrier recovery shows that the DFT based approach needs about four times the number of cycles, that is

about $2\,\mu s$ execution time in the considered implementation, which is absolutely acceptable, as it corresponds to the 2% of the control cycle.

4.2.6 Simulation results

Simulation results are shown in order to demonstrate the system performance and the proposed DFT-based demodulation process properties. A commercial IPM synchronous motor has been considered, rating 2 pole pairs, $80\,Hz$ (base electrical frequency), $50\,Arms$, $17.11\,Vrms$, $L_d = 0.2245\,mH$, $L_q = 0.8115\,mH$ and $R = 0.023\,\Omega$. The simulation takes into account the actual motor drive implementation, i.e. digital control, inverter, etc.. The injection frequency is chosen to $f_i = 1250\,Hz$.

The first result shown in Fig. 4.8 refers to a standstill operation (with initial rotor position error equal to 45 electrical degrees) followed by a step variation of the speed reference from zero to $0.25\,p.u.$ ($600\,rpm$) with 2 Nm passive load torque. Top graph shows reference (black, dashed), measured (blue), estimated (green) and speed error (red). Bottom graph is related to rotor position estimation error. Peaks at around time $t = 0$ on both speed and position estimation errors are due to the initial rotor position error of $\pi/4$ imposed in the estimator. It can be seen that, even with a fast transient slope in speed, the position error has a maximum value of about 3 (electrical) degrees, and becomes very small after $50\,ms$, when steady-state condition is reached. Looking at the fact that considerable error is only present during acceleration, it is easy to yield that estimator phase-lag is the main cause of imprecision. This suggests that a complete mechanical observer involving commanded torque feed-forward could gain better dynamical performances, [39], [49].

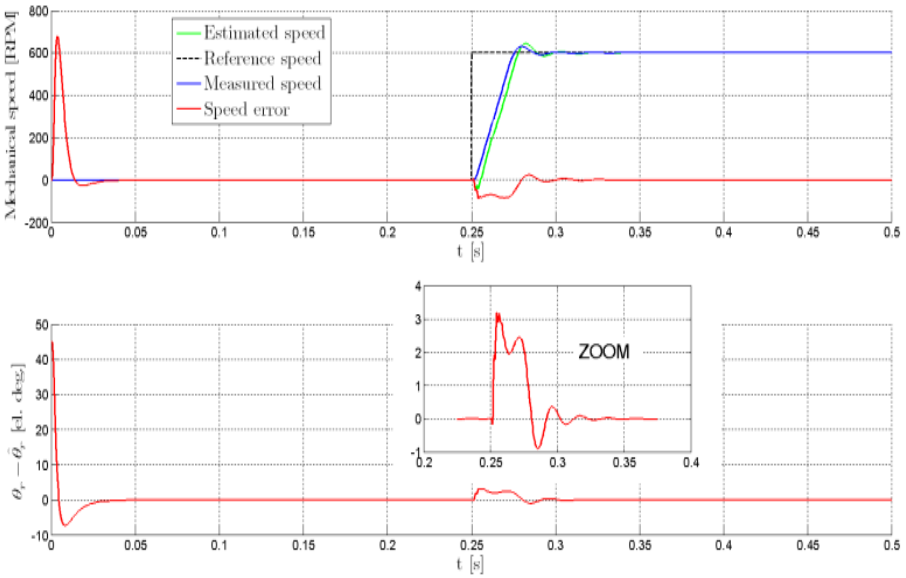

Fig. 4.8. Simulation results: 0.25 p.u. speed step response and related position estimation error.

The performance of the demodulation engine adopting DFT is shown in Fig. 4.9, showing the high-frequency currents $i_{i\hat{d}'}$ and $i_{i\hat{q}'}$ (blue traces) and the DFT modula (red traces). Fig. 4.10 presents again the DFT modula (blue and red traces) and their difference (green trace, i.e. the error signal $\sqrt{2}I_{i1}\sin(2\Delta\theta_{me})$ driving the PI regulator of Fig. 4.7), used to estimate rotor speed and position.

The result demonstrates that a correct and fast position estimation error signal can be achieved without any knowledge of the demodulating carrier that can be phase shifted with respect to the modulating one.

In the results of Fig. 4.11 a first step start-up and a speed reversal is commanded. Top graph shows reference (black, dashed), measured (blue), estimated (green) and speed error (red). Bottom graph is related to rotor position estimation error. Even in this case a very low position estimation error is obtained.

Finally in Fig. 4.12 a test case is considered having a initial rotor position estimation error equal to $\pi/2$. As it is clearly visible, the estimated position error converges to a value being π instead of becoming zero. A simple start-up procedure has therefore been implemented aiming at verifying that the convergence of the estimate is toward the right value, [53]. Otherwise a correction to the initial

estimate is forced driving the error to zero. Then the speed step response is considered as in other test cases shown previously.

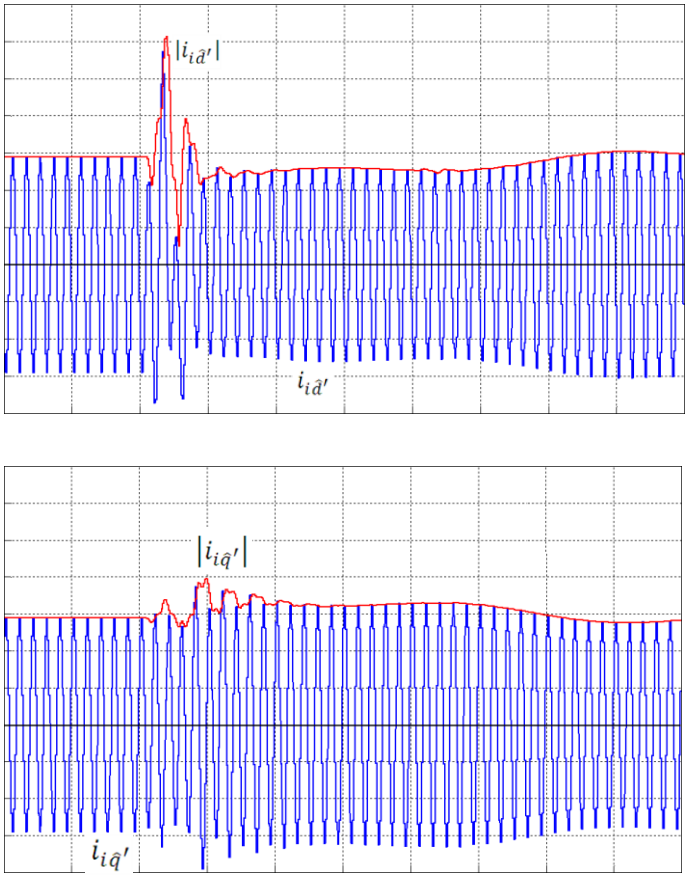

Fig. 4.9. Simulation results: example of the demodulation process by DFT. Vertical scale: current [$\mathbf{0.5}\ \boldsymbol{A/div}$], horizontal scale: time $\mathbf{5}\ \boldsymbol{ms/div}$.

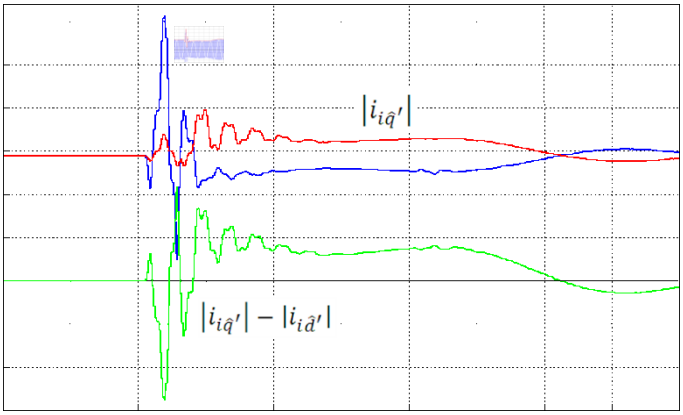

Fig. 4.10. Simulation results: estimation error calculation by DFT modula calculation. Vertical scale: current [**0.5 *A/div***], horizontal scale: time **5 *ms/div***.

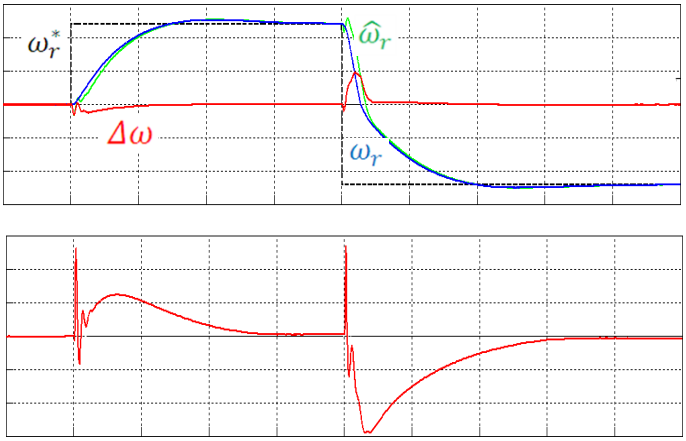

Fig. 4.11. Simulation results: start-up and speed reversal. Vertical scale top: speed [**100 *rpm/div***], vertical scale bottom: position error [**1 *deg/div***], horizontal scale: time **50 *ms/div***.

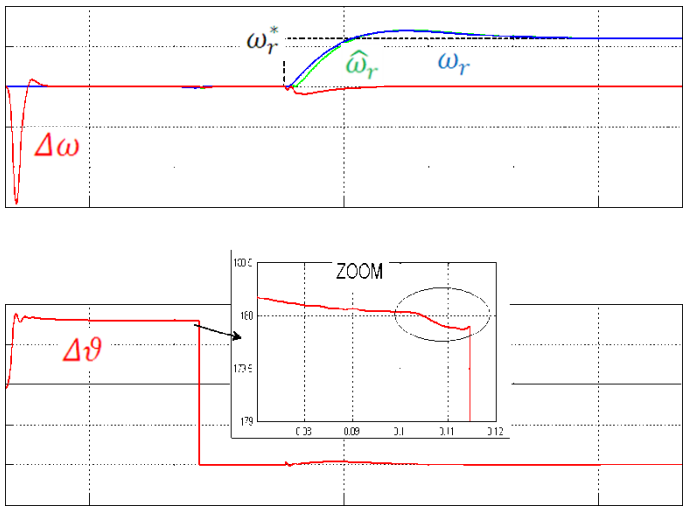

Fig. 4.12. Simulation results: start-up with large initial rotor position estimation error. Vertical scale top: speed [**500 *rpm/div***], vertical scale bottom: position error [**50 *deg/div***] (zoom is [**0.5 *deg/div***]), horizontal scale: time **50 *ms/div***.

4.2.7 Experimental results

The described sensorless algorithm has been tested on a prototype drive for an electric city-scooter, shown in Fig. A.2, comprising the motor described by Table A.2. The drive system embodies a digital control board based on the Texas Instruments *TMS320F2811* digital signal controller, a MOSFET-based voltage-source inverter and all the electronics subsystems needed for current and DC-bus voltage measurements, signalling and communicating with remote human-machine interface.

The results of Fig. 4.13 and Fig. 4.14 are equivalent to those of Fig. 4.8 and Fig. 4.9 respectively. The oscillation of the difference between the two components DFT modulus (i.e. the error signal $\sqrt{2}I_{i1}\sin(2\Delta\theta_{me})$ driving the PI regulator of Fig. 4.7), is probably due to cross-saturation effects or higher-order spatial saliency harmonics.

Fig. 4.15A comparison between actual and estimated rotor position at $0.1\,p.u.$ ($240\,rpm$) commanded speed is shown in Fig. 4.15. It can be noticed that

estimation is rather accurate, but the analysis of the estimation error (purple trace) shows that cross-saturation provides a periodic influence on estimate, whose amplitude is less than 10 electrical degrees.

In Fig. 4.16 the step response of sensorless speed control is considered. Actual (measured) and estimated rotor speed are shown. Measured speed has a superimposed ripple due to the low-resolution of the position sensor adopted in the experimental system. Also estimated speed has some oscillations at a frequency higher that the speed control loop bandwidth (in fact measured speed does not track those oscillations) and could therefore be easily removed by low-pass filtering.

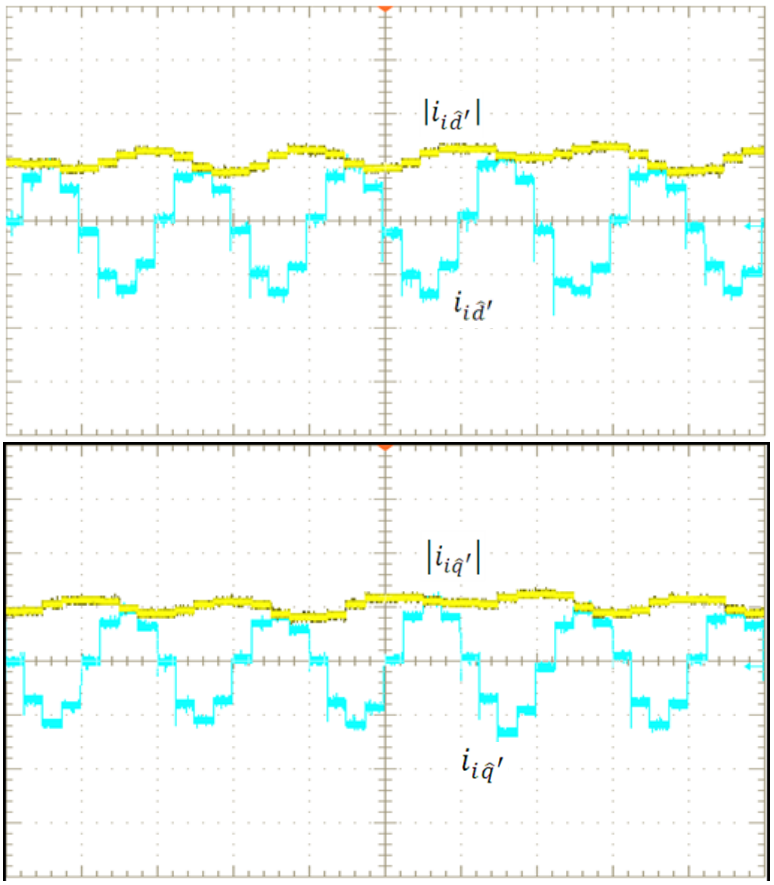

Fig. 4.13. Experimental results: demodulation process by DFT during sensorless control at steady-state. Vertical scale: current 0.5 A/div; horizontal scale: time 400 µs/div.

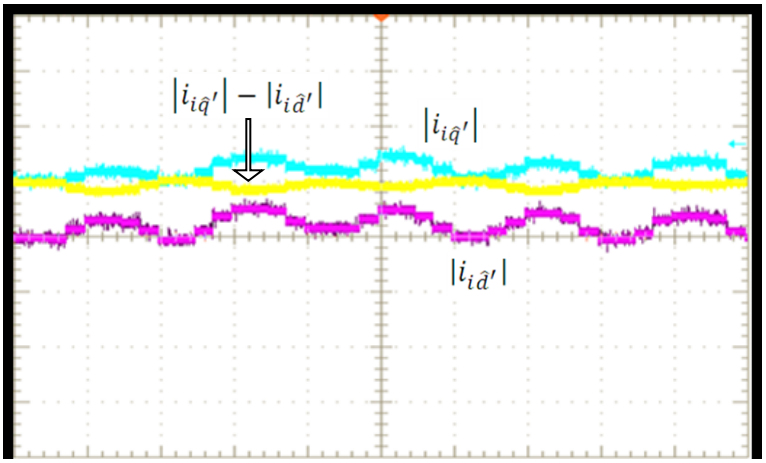

Fig. 4.14. Experimental results: estimation error calculation by DFT modula during sensorless control. Vertical scale: current 0.5 A/div; horizontal scale: time 400 µs/div.

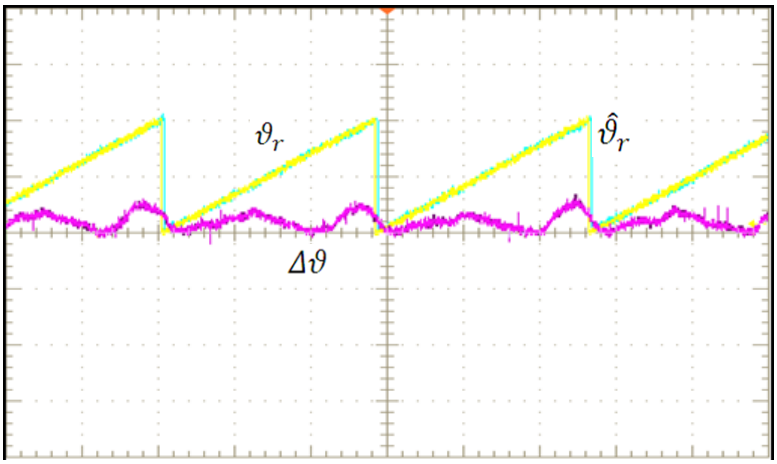

Fig. 4.15. Experimental results: actual (yellow) and estimated (blue) rotor position, rotor position estimation error (purple) during sensorless control. Vertical scale: position 180 deg/div; position error 17 deg/div; horizontal scale: time 40 ms/div.

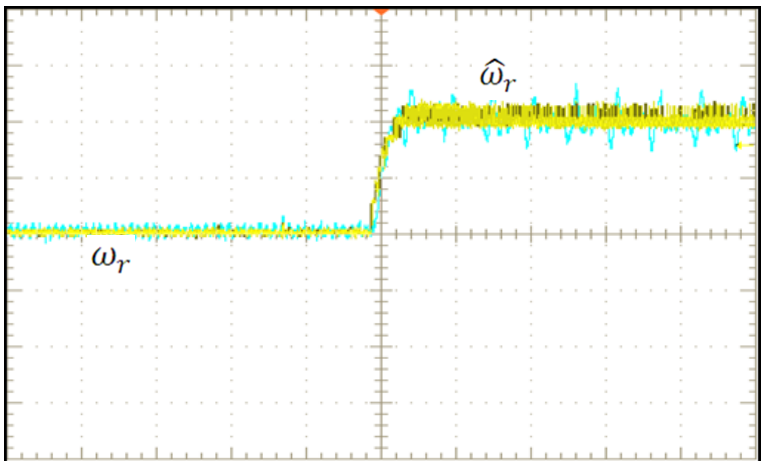

Fig. 4.16. Experimental results: sensorless control step response. Measured (yellow) and estimated (blue) speed. Vertical scale: position 120 rpm/div; horizontal scale: time 200 ms/div.

Finally, in Fig. 4.17 speed state-steady conditions are considered at two different values of load torque. Rotor position, q-axis fundamental current (without any high-frequency content) and error signal $\sqrt{2}I_{i1}\sin(2\Delta\theta_{me})$ driving the PI regulator of the tracking loop (see Fig. 4.7) are shown. The results refer to sensored control with the estimated angle kept equal to the measured one, thus forcing a null estimation error. Under this condition the error signal would always be null, according to the ideal model (4.8). From the results of Fig. 4.17 it is possible to notice that the estimation correction signal shows periodic oscillations which increase as the torque current increases. This can be considered an indirect proof of the effect of cross-saturation on the reliability and accuracy of position and speed estimation.

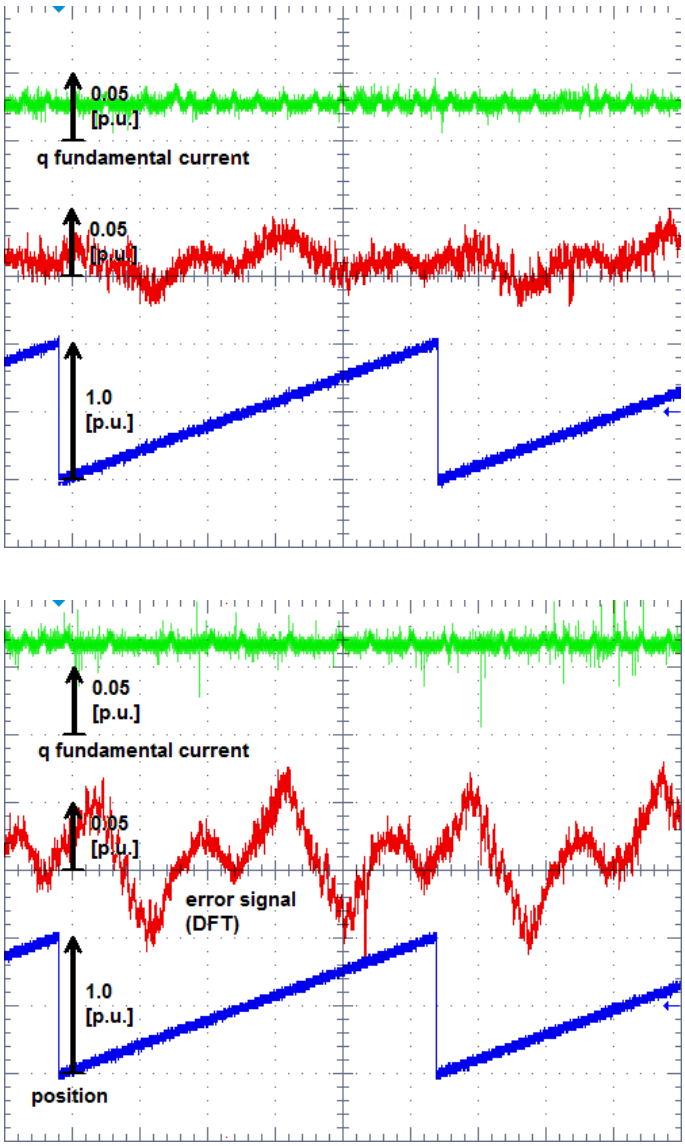

Fig. 4.17. Experimental results: measured position (blue), demodulated estimation correction signal (red), torque currend (green) during sensored control (estimation error forced to null value). Vertical scale: position 180 el. deg/div, correction signal 0.05 p.u./div, torque current 0.05 p.u./div; horizontal scale: time 200 ms/div).

4.3 PWM excitation

Some of the disadvantages of the typical signal injection techniques can be found in the additional current ripple (resulting in a torque ripple and audible noise) and losses caused by the test signal. To avoid or reduce the importance of these issues, some very recent approaches have been proposed, based on the measurement of the current transient response introduced by standard (or slightly modified) PWM excitation, i.e. without any additional test voltage, [62]–[66]. References [62] and [63] consider a non-salient PM machine and adopt a persistent excitation within standard space vector PWM, exploiting magnetic saturation induced saliencies. Since the application of null or very low voltage vectors, in standard SV-PWM, results in null or very low voltage high-frequency content (ripple), a small degree of modification is needed when short voltage vectors occur, i.e. near a sector transition or when the modulation index is very low. The methods relying on the PWM excitation only are based on the measurement of current derivatives (i.e. a term related to motor inductance) during the PWM cycle that, similarly to what happens in other anisotropy-based methods, contain components with sinusoidal dependence on the rotor position.

In this work, a contribution to the analysis and implementation of this method has been proposed. The analytical relation between phase current derivatives, inductance and rotor position is obtained, and a complete mathematical model is developed for the case of IPMSM. Differently from past literature regarding the same sensorless approach, in this case the dependence of the rotor position estimation error on the mutual inductance has been taken into account. Another original feature of the technique consists in the fact that the entire estimation is performed within a single PWM period, although multiple measurements are needed. To avoid derivative calculation from current samples, the sensing of current derivatives is obtained from dedicated Rogowski coils or similar, as already reported in previous works ([62], [63], [67]). The issues associated to the acquisition during short voltage vector application times (e.g. under null and low-voltage output operation) have been overcome by means of a proper edge-shifting technique on the PWM signals. A motor drive system for fractional power high speed IPM motor is considered as a test bench to prove the effectiveness of the proposal.

4.3.1 Analytical model of IPM machine and current derivatives expression

In this section a mathematical model of the IPMSM is recalled in order to illustrate the possibility of estimating rotor position by means of current derivatives measurements under space vector PWM excitation.

Differently from the approach presented in [62], the complete model also takes into account for the spatial variation of the total inductance is introduced, thus obtaining a more general result.

The analytical model of the IPMSM is considered in the dq synchronous reference frame oriented according to the flux linkage due to permanent magnet, including cross-coupling terms.

$$\begin{aligned} \underline{u_{dq}} &= R\underline{i_{dq}} + \frac{d\underline{\lambda_{dq}}}{dt} + \omega_{me}\underline{J}\,\underline{\lambda_{dq}} \\ \underline{\lambda_{dq}} &= \underline{\lambda_{i,dq}}\left(\underline{i_{dq}}\right) + \underline{\lambda_{mg,dq}} = \underline{L_{dq}}\left(\underline{i_{dq}}\right)\cdot\underline{i_{dq}} + \underline{\lambda_{mg,dq}} \end{aligned} \tag{4.26}$$

$\underline{u_{dq}}$, $\underline{i_{dq}}$ and $\underline{\lambda_{dq}}$ are voltage, current and flux linkage vectors, and R is the phase resistance, i.e.

$$\underline{u_{dq}} = \begin{bmatrix} u_d \\ u_q \end{bmatrix}, \underline{i_{dq}} = \begin{bmatrix} i_d \\ i_q \end{bmatrix}, \underline{\lambda_{dq}} = \begin{bmatrix} \lambda_d \\ \lambda_q \end{bmatrix} \tag{4.27}$$

The flux-linkage has been divided into the two terms, the former $\underline{\lambda_{i,dq}}\left(\underline{i_{dq}}\right)$ depending on the motor currents, and the latter due to the permanent magnet, $\underline{\lambda_{mg,dq}}$. $\underline{J}$ is the anti-diagonal unity matrix.

$$\underline{\lambda_{mg,dq}} = \begin{bmatrix} \Lambda_{mg} \\ 0 \end{bmatrix}, \underline{J} = \begin{bmatrix} 0 & -1 \\ 1 & 0 \end{bmatrix} \tag{4.28}$$

Matrix $\underline{L_{dq}}\left(\underline{i_{dq}}\right)$ is related to motor apparent self and mutual inductances, i.e.:

$$\underline{L_{dq}}\left(\underline{i_{dq}}\right) = \begin{bmatrix} L_d(i_d, i_q) & M_{qd}(i_d, i_q) \\ M_{dq}(i_d, i_q) & L_q(i_d, i_q) \end{bmatrix} \tag{4.29}$$

In general, self and mutual dq inductances depend on the dq currents, because of saturation and cross-magnetization.

Substitution of flux expression inside voltage equation leads to a more complex expression considering the variation of the flux linkage $\underline{\lambda_{i,dq}}\left(\underline{i_{dq}}\right)$ with respect to motor currents, i.e.:

$$\begin{aligned}\underline{u_{dq}} &= \underline{R}\underline{i_{dq}} + \frac{\partial \underline{\lambda_{i,dq}}\left(\underline{i_{dq}}\right)}{\partial \underline{i_{dq}}}\frac{d\underline{i_{dq}}}{dt} + \omega_{me}\underline{J}\underline{\lambda_{dq}} \\ &= \underline{R}\underline{i_{dq}} + \underline{\tilde{L}_{dq}}\left(\underline{i_{dq}}\right)\frac{d\underline{i_{dq}}}{dt} + \omega_{me}\underline{J}\left(\underline{L_{dq}}\left(\underline{i_{dq}}\right)\underline{i_{dq}} + \underline{\lambda_{mg,dq}}\right)\end{aligned} \tag{4.30}$$

Differential self and mutual inductance matrix $\underline{\tilde{L}_{dq}}\left(\underline{i_{dq}}\right)$ can therefore be defined, i.e.:

$$\begin{aligned}\frac{d\underline{\lambda_{i,dq}}\left(\underline{i_{dq}}\right)}{d\underline{i_{dq}}} &= \begin{bmatrix}\frac{\partial \lambda_{i,d}}{\partial i_d} & \frac{\partial \lambda_{i,d}}{\partial i_q} \\ \frac{\partial \lambda_{i,q}}{\partial i_d} & \frac{\partial \lambda_{i,q}}{\partial i_q}\end{bmatrix} = \\ &= \begin{bmatrix}\tilde{L}_d(i_d,i_q) & \tilde{M}_{qd}(i_d,i_q) \\ \tilde{M}_{dq}(i_d,i_q) & \tilde{L}_q(i\_,i_q)\end{bmatrix} = \underline{\tilde{L}_{dq}}\left(\underline{i_{dq}}\right)\end{aligned} \tag{4.31}$$

Voltage equation in the synchronous reference frame therefore becomes:

$$\begin{aligned}\begin{bmatrix}u_d \\ u_q\end{bmatrix} &= R\begin{bmatrix}i_d \\ i_q\end{bmatrix} + \begin{bmatrix}\tilde{L}_d(i_d,i_q) & \tilde{M}_{qd}(i_d,i_q) \\ \tilde{M}_{dq}(i_d,i_q) & \tilde{L}_q(i_d,i_q)\end{bmatrix}\frac{d}{dt}\begin{bmatrix}i_d \\ i_q\end{bmatrix} + \\ &+\omega_{me}\begin{bmatrix}0 & -1 \\ 1 & 0\end{bmatrix}\left[\begin{bmatrix}L_d(i_d,i_q) & M_{qd}(i_d,i_q) \\ M_{dq}(i_d,i_q) & L_q(i_d,i_q)\end{bmatrix}\begin{bmatrix}i_d \\ i_q\end{bmatrix} + \begin{bmatrix}\Lambda_{mg} \\ 0\end{bmatrix}\right]\end{aligned} \tag{4.32}$$

Finally if the rotating (dq) to stationary $(\alpha\beta)$ reference frames transformation is applied, the motor model (4.33) is obtained, where θ_{me} is the rotor electrical position:

$$\begin{aligned}\underline{u_{\alpha\beta}} = &\underbrace{\begin{bmatrix}\tilde{L}_\Sigma - \tilde{L}_\Delta cos(2\theta_{me}) - \tilde{M}_{qd}sin(2\theta_{me}) & -\tilde{L}_\Delta sin(2\theta_{me}) + \tilde{M}_{qd}cos(2\theta_{me}) \\ -\tilde{L}_\Delta sin(2\theta_{me}) + \tilde{M}_{qd}cos(2\theta_{me}) & \tilde{L}_\Sigma + \tilde{L}_\Delta cos(2\theta_{me}) + \tilde{M}_{qd}sin(2\theta_{me})\end{bmatrix}\frac{d}{dt}\begin{bmatrix}i_\alpha \\ i_\beta\end{bmatrix}}_{inductive\ voltage\ drop} + \underbrace{\omega_{me}\Lambda_{mg}\begin{bmatrix}-sin(\theta_{me}) \\ cos(\theta_{me})\end{bmatrix}}_{backe.m.f.due\ to\ permanent\ magnet\ flux} \\ &+\underbrace{\omega_{me}\begin{bmatrix}(L_\Delta + \tilde{L}_\Delta)sin(2\theta_{me}) - (M_{qd} + \tilde{M}_{qd})cos(2\theta_{me}) & -(L_\Sigma - \tilde{L}_\Sigma) - (L_\Delta + \tilde{L}_\Delta)cos(2\theta_{me}) - (M_{qd} + \tilde{M}_{qd})sin(2\theta_{me}) \\ (L_\Sigma - \tilde{L}_\Sigma) - (L_\Delta + \tilde{L}_\Delta)cos(2\theta_{me}) - (M_{qd} + \tilde{M}_{qd})sin(2\theta_{me}) & -(L_\Delta + \tilde{L}_\Delta)sin(2\theta_{me}) + (M_{qd} + \tilde{M}_{qd})cos(2\theta_{me})\end{bmatrix}\begin{bmatrix}i_\alpha \\ i_\beta\end{bmatrix}}_{induced\ voltage\ due\ to\ anisotropy}\end{aligned} \tag{4.33}$$

The following inductive terms have been defined:

$$\begin{aligned} \tilde{L}_\Sigma &= \frac{\tilde{L}_q + \tilde{L}_d}{2} \quad \tilde{L}_\Delta = \frac{\tilde{L}_q - \tilde{L}_d}{2} \\ L_\Sigma &= \frac{L_q + L_d}{2} \quad L_\Delta = \frac{L_q - L_d}{2} \end{aligned} \tag{4.34}$$

The contribution of different sources of induced voltage is clearly shown in (4.33), the most interesting to our purposes is the one proportional to the derivative of stator currents. In fact a proper measurement and processing of current derivatives allows the estimation of the rotor position, as demonstrated in the next sections.

4.3.2 Rotor position estimation basis

A symmetric double edge PWM pattern is taken into account, as shown in Fig. 4.18.

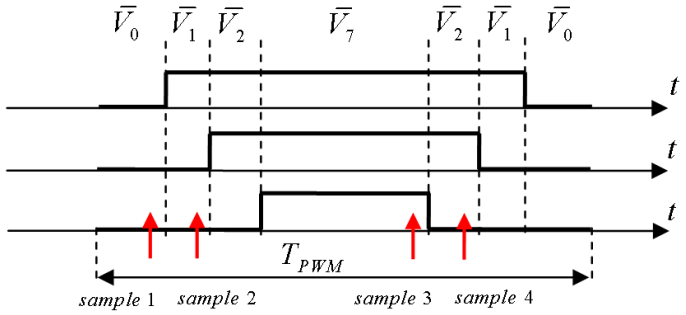

Fig. 4.18. Sampling instants within a symmetric double-edge PWM pattern.

The four (generic) measuring points of motor current derivatives are indicated by the red arrows. Sample 1 is acquired during null voltage vector $\bar{V}_0$ and sample 2 is taken in the next active vector (i.e. $\bar{V}_1$ in this example). We have a similar situation with respect to samples 3 and 4, where sampling is done during $\bar{V}_7$ and the next active vector $\bar{V}_2$. This is a different approach with respect to literature, [62], as four current derivative samples are measured within the same PWM period. Hereafter it will be shown that the sampling task is not so easy as described (e.g.

due to the presence of parasitic effects and variation of the PWM pattern as a function of the motor operating conditions).

A first simplifying hypothesis is to consider rotor electrical speed ω_{me} to be relatively low and to assume that rotor position θ_{me} is constant within the modulation period. In the next subsection it will be analytically demonstrated that the method is still valid when high speed operation is considered (i.e. when a variation of the rotor position is experienced between the four current samples) by means of a proper simplified model of the rotor position variation, representing one of the original features of this work. In fact, the set of equations generated by the motor model provides additional speed-dependent terms. It will be proved that they can be eliminated by proper processing of current derivative signals.

Low speed operation

If the four current derivatives measurements shown in Fig. 4.18 are considered and resistive voltage drop and back-EMFs (both due to permanent magnet and saliency related) are neglected as they are assumed constant within the modulation period, (4.33) can be rewritten for each sample. The difference between the obtained equations can be considered, leading to (4.35):

$$\begin{aligned}
\underline{u_{\alpha\beta}}^{(21)} &= \\
\begin{bmatrix} \tilde{L}_\Sigma - \tilde{L}_\Delta cos(2\theta_{me}) - \tilde{M}_{qd} sin(2\theta_{me}) & -\tilde{L}_\Delta sin(2\theta_{me}) + \tilde{M}_{qd} cos(2\theta_{me}) \\ -\tilde{L}_\Delta sin(2\theta_{me}) + \tilde{M}_{qd} cos(2\theta_{me}) & \tilde{L}_\Sigma + \tilde{L}_\Delta cos(2\theta_{me}) + \tilde{M}_{qd} sin(2\theta_{me}) \end{bmatrix} & \\
\underline{u_{\alpha\beta}}^{(43)} &= \\
\begin{bmatrix} \tilde{L}_\Sigma - \tilde{L}_\Delta cos(2\theta_{me}) - \tilde{M}_{qd} sin(2\theta_{me}) & -\tilde{L}_\Delta sin(2\theta_{me}) + \tilde{M}_{qd} cos(2\theta_{me}) \\ -\tilde{L}_\Delta sin(2\theta_{me}) + \tilde{M}_{qd} cos(2\theta_{me}) & \tilde{L}_\Sigma + \tilde{L}_\Delta cos(2\theta_{me}) + \tilde{M}_{qd} sin(2\theta_{me}) \end{bmatrix} &
\end{aligned} \tag{4.35}$$

Superscripts indicate the difference between the two values within the sampling instants shown in Fig. 4.18. This represents a set of four equations linking voltage and current derivatives (known values), rotor position and inductances. Rearranging (4.35) the following two sets of equations can be obtained:

$$\begin{bmatrix} \frac{di_\alpha^{(21)}}{dt} & \frac{di_\beta^{(21)}}{dt} \\ \frac{di_\alpha^{(43)}}{dt} & \frac{di_\beta^{(43)}}{dt} \end{bmatrix} \begin{bmatrix} A \\ B \end{bmatrix} = \begin{bmatrix} u_\alpha^{(21)} \\ u_\alpha^{(43)} \end{bmatrix}$$
$$\begin{bmatrix} \frac{di_\alpha^{(21)}}{dt} & \frac{di_\beta^{(21)}}{dt} \\ \frac{di_\alpha^{(43)}}{dt} & \frac{di_\beta^{(43)}}{dt} \end{bmatrix} \begin{bmatrix} C \\ D \end{bmatrix} = \begin{bmatrix} u_\beta^{(21)} \\ u_\beta^{(43)} \end{bmatrix} \tag{4.36}$$

where

$$\begin{aligned} A &= \tilde{L}_\Sigma - \tilde{L}_\Delta cos(2\theta_{me}) - \tilde{M}_{qd} sin(2\theta_{me}) \\ B &= C = -\tilde{L}_\Delta sin(2\theta_{me}) + \tilde{M}_{qd} cos(2\theta_{me}) \\ D &= \tilde{L}_\Sigma + \tilde{L}_\Delta cos(2\theta_{me}) + \tilde{M}_{qd} sin(2\theta_{me}) \end{aligned} \tag{4.37}$$

The solution of the two sets of equations by a simple linear combination provides two signals being respectively proportional to the sine and cosine of twice the (electrical) rotor position, i.e.:

$$\begin{aligned} -A + D &= 2\left(\tilde{L}_\Delta cos(2\theta_{me}) + \tilde{M}_{qd} sin(2\theta_{me})\right) = \\ &= 2\sqrt{\left(\tilde{L}_\Delta{}^2 + \tilde{M}_{qd}{}^2\right)} cos(2\theta_{me} + \alpha) = \\ &= -au_\alpha^{(21)} - bu_\alpha^{(43)} + cu_\beta^{(21)} + du_\beta^{(43)} \\ -B - C &= 2\left(\tilde{L}_\Delta sin(2\theta_{me}) - \tilde{M}_{qd} cos(2\theta_{me})\right) = \\ &= 2\sqrt{\left(\tilde{L}_\Delta{}^2 + \tilde{M}_{qd}{}^2\right)} sin(2\theta_{me} + \alpha) = \\ &= -au_\beta^{(21)} - bu_\beta^{(43)} - cu_\alpha^{(21)} - du_\alpha^{(43)} \end{aligned} \tag{4.38}$$

where

$$\begin{bmatrix} a & b \\ c & d \end{bmatrix} = \frac{\begin{bmatrix} \frac{di_\beta^{(43)}}{dt} & -\frac{di_\beta^{(21)}}{dt} \\ -\frac{di_\alpha^{(43)}}{dt} & \frac{di_\alpha^{(21)}}{dt} \end{bmatrix}}{\frac{di_\alpha^{(21)}}{dt}\frac{di_\beta^{(43)}}{dt} - \frac{di_\alpha^{(43)}}{dt}\frac{di_\beta^{(21)}}{dt}} \tag{4.39}$$

$$\alpha = tan^{-1}\left(-\frac{\widetilde{M}_{qd}}{\tilde{L}_{\Delta}}\right) \tag{4.1}$$

By processing signals (4.38), i.e. by application of the inverse trigonometric function tan^{-1} or a phase-locked-loop based approach, rotor position estimation can be achieved. No knowledge of motor inductance is needed, except for the mutual terms, due to the presence of the phase delay α in the argument of the sine and cosine functions in (4.38). A compensation is however possible if a map of the motor fluxes is known.

High speed operation

At high speed, a discontinuity of sine and cosine signals is experienced every time the voltage vector crosses sector borders. So it is not related to the variation of the back-EMF in the four ideal sampling instants. However the estimated rotor position as obtained by the ratio of sine and cosine signals is always correct. The analytical proof and results will be presented and discussed hereafter. Also it will be shown that a speed dependent term arises, that can be compensated, leading to the possibility to adopt a more robust approach (e.g. phase locked loop) for rotor position estimation instead of direct tan^{-1} calculation.

In order to continue to deal with linear equations, the following simplifying hypothesis have been introduced (see also Fig. 4.19):

- the electrical rotor position is assumed to be constant within each couple of ideal sampling instants, i.e. 1 and 2 or 3 and 4 (θ'_{me} and θ''_{me}, blue arrows);
- the electrical rotor position is assumed to be linearly varying between the first two samples of current derivatives and the last two samples; this means that rotor speed is constant within each period;
- a linear variation for each term of $\underline{L}_{\alpha\beta}$ matrix with Taylor series expansion is considered; this means the two vector equations (4.33) can be rewritten, each one referring to a mean sampling instant ($sample\ 12$ and $sample\ 34$ in Fig. 4.19, blue arrows) corresponding to the mean time of the original sampling instants.

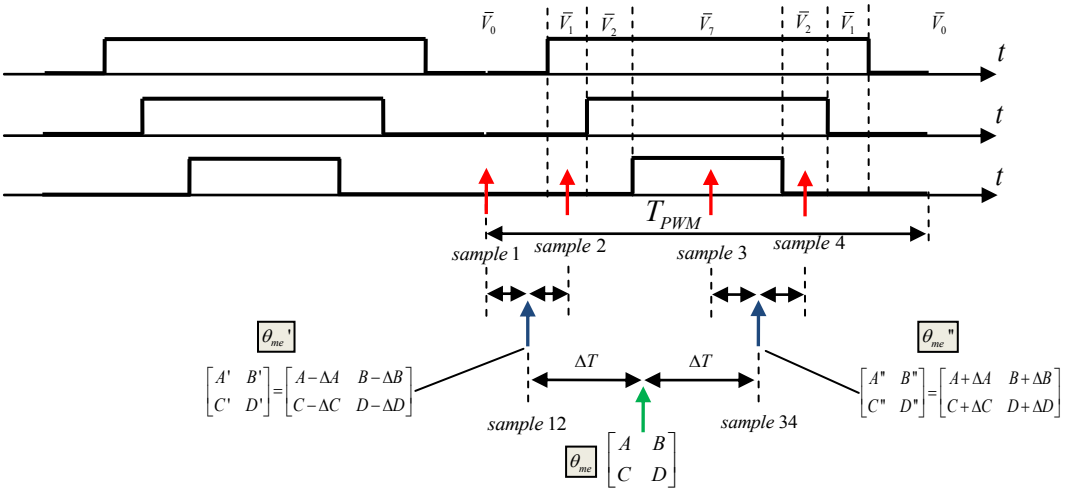

Fig. 4.19. Sampling instants within a symmetric double-edge PWM pattern (high speed operation).

As rotor position is supposed to vary linearly within the PWM period, the final estimated position will be referred to the mean point between ***sample* 12** and ***sample* 34**, as shown in Fig. 4.19 (θ_{me}, green arrow), to make the analytical calculations easier.

In particular this hypothesis allows to consider an inductance matrix (terms A, B, C and D in (4.36)) that can be expressed in the two equivalent sampling instants (i.e. ***sample* 12** and ***sample* 34**) as a function of the same variations ΔA, ΔB, ΔC and ΔD, as shown in Fig. 4.19.

Therefore (3.11) can be rewritten by considering the rotor position variation due to inductance matrix, i.e.:

$$\begin{aligned} \begin{bmatrix} u_\alpha^{(21)} \\ u_\beta^{(21)} \end{bmatrix} &= \begin{bmatrix} A-\Delta A & B-\Delta B \\ C-\Delta C & D-\Delta D \end{bmatrix} \frac{d}{dt} \begin{bmatrix} i_\alpha \\ i_\beta \end{bmatrix}^{(21)} \\ \begin{bmatrix} u_\alpha^{(43)} \\ u_\beta^{(43)} \end{bmatrix} &= \begin{bmatrix} A+\Delta A & B+\Delta B \\ C+\Delta C & D+\Delta D \end{bmatrix} \frac{d}{dt} \begin{bmatrix} i_\alpha \\ i_\beta \end{bmatrix}^{(43)} \end{aligned} \tag{4.40}$$

After some manipulations the following linear systems, equivalent to those of (4.33), can be obtained, allowing the estimation of inductance matrix $\underline{L}_{\alpha\beta}$ in the position θ_{me}:

$$\begin{bmatrix} \frac{di_\alpha}{dt}^{(21)} & \frac{di_\beta}{dt}^{(21)} \\ \frac{di_\alpha}{dt}^{(43)} & \frac{di_\beta}{dt}^{(43)} \end{bmatrix} \begin{bmatrix} A \\ B \end{bmatrix} = \begin{bmatrix} u_\alpha{}^{(21)} + \Delta A \frac{di_\alpha}{dt}^{(21)} & +\Delta B \frac{di_\beta}{dt}^{(21)} \\ u_\alpha{}^{(43)} - \Delta A \frac{di_\alpha}{dt}^{(43)} & -\Delta B \frac{di_\beta}{dt}^{(43)} \end{bmatrix}$$
$$\begin{bmatrix} \frac{di_\alpha}{dt}^{(21)} & \frac{di_\beta}{dt}^{(21)} \\ \frac{di_\alpha}{dt}^{(43)} & \frac{di_\beta}{dt}^{(43)} \end{bmatrix} \begin{bmatrix} C \\ D \end{bmatrix} = \begin{bmatrix} u_\beta{}^{(21)} + \Delta C \frac{di_\alpha}{dt}^{(21)} & +\Delta D \frac{di_\beta}{dt}^{(21)} \\ u_\beta{}^{(43)} - \Delta C \frac{di_\alpha}{dt}^{(43)} & -\Delta D \frac{di_\beta}{dt}^{(43)} \end{bmatrix} \tag{4.41}$$

The variation terms ΔA, ΔB, ΔC and ΔD can be calculated by Taylor series expansion, as stated before:

$$\begin{aligned} A + \Delta A &= \tilde{L}_\Sigma - \tilde{L}_\Delta cos(2\theta''_{me}) - \tilde{M}_{qd} sin(2\theta''_{me}) \\ &= \tilde{L}_\Sigma - \tilde{L}_\Delta cos(2\theta_{me}) - \tilde{M}_{qd} sin(2\theta_{me}) + \\ &+2\left(\tilde{L}_\Delta sin(2\theta_{me}) - \tilde{M}_{qd} cos(2\theta_{me})\right)\omega_{me}\Delta T + o(\Delta T)^2 \end{aligned} \tag{4.42}$$

where $o(\Delta T^2)$ represents all the higher order terms of the series. If the linear terms is considered only, ΔA is obtained:

$$\begin{aligned} \Delta A &\approx 2\left(\tilde{L}_\Delta sin(2\theta_{me}) - \tilde{M}_{qd} cos(2\theta_{me})\right)\omega_{me}\Delta T \\ &= 2\sqrt{\left(\tilde{L}_\Delta{}^2 + \tilde{M}_{qd}{}^2\right)} sin(2\theta_{me} + \alpha)\omega_{me}\Delta T \end{aligned} \tag{4.43}$$

The same approach can be adopted for the calculation of ΔB, ΔC and ΔD, i.e.:

$$\begin{aligned} \Delta B &= -2\sqrt{\left(\tilde{L}_\Delta{}^2 + \tilde{M}_{qd}{}^2\right)} cos(2\theta_{me} + \alpha)\omega_{me}\Delta T \\ \Delta C &= -2\sqrt{\left(\tilde{L}_\Delta{}^2 + \tilde{M}_{qd}{}^2\right)} cos(2\theta_{me} + \alpha)\omega_{me}\Delta T \\ \Delta D &= -2\sqrt{\left(\tilde{L}_\Delta{}^2 + \tilde{M}_{qd}{}^2\right)} sin(2\theta_{me} + \alpha)\omega_{me}\Delta T \end{aligned} \tag{4.44}$$

Then (4.46) can be calculated following the same steps used to obtain (4.38), where

$$\Delta_i = \frac{di_\alpha}{dt}^{(21)} \frac{di_\beta}{dt}^{(43)} - \frac{di_\alpha}{dt}^{(43)} \frac{di_\beta}{dt}^{(21)} \tag{4.45}$$

After some algebraic manipulations and considering that $\Delta A = -\Delta D$ and $\Delta B = \Delta C$, the following relations are obtained:

$$\begin{aligned}
-A + D &= 2\sqrt{\left(\tilde{L}_{\Delta}{}^2 + \tilde{M}_{qd}{}^2\right)}\cos(2\theta_{me} + \alpha) = -a{u_\alpha}^{(21)} - b{u_\alpha}^{(43)} + \\
&\quad c{u_\beta}^{(21)} + d{u_\beta}^{(43)} + \\
&+\sqrt{\left(\tilde{L}_{\Delta}{}^2 + \tilde{M}_{qd}{}^2\right)}\cos(2\theta_{me} + \alpha)\, 4\omega_{me}\Delta T \frac{\left(\frac{di_\alpha}{dt}^{(21)}\frac{di_\alpha}{dt}^{(43)} + \frac{di_\beta}{dt}^{(21)}\frac{di_\beta}{dt}^{(43)}\right)}{\left(\frac{di_\alpha}{dt}^{(21)}\frac{di_\beta}{dt}^{(43)} - \frac{di_\alpha}{dt}^{(43)}\frac{di_\beta}{dt}^{(21)}\right)} \\
-B - C &= 2\sqrt{\left(\tilde{L}_{\Delta}{}^2 + \tilde{M}_{qd}{}^2\right)}\sin(2\theta_{me} + \alpha) \\
&= -a{u_\beta}^{(21)} - b{u_\beta}^{(43)} - c{u_\alpha}^{(21)} - d{u_\alpha}^{(43)} + \\
&+\sqrt{\left(\tilde{L}_{\Delta}{}^2 + \tilde{M}_{qd}{}^2\right)}\sin(2\theta_{me} \\
&\quad + \alpha) 4\omega_{me}\Delta T \frac{\left(\frac{di_\alpha}{dt}^{(21)}\frac{di_\alpha}{dt}^{(43)} + \frac{di_\beta}{dt}^{(21)}\frac{di_\beta}{dt}^{(43)}\right)}{\left(\frac{di_\alpha}{dt}^{(21)}\frac{di_\beta}{dt}^{(43)} - \frac{di_\alpha}{dt}^{(43)}\frac{di_\beta}{dt}^{(21)}\right)}
\end{aligned} \tag{4.46}$$

It can be pointed out that equations (4.46) are very similar to (4.38), the last ones obtained in the case no variation of the inductance matrix is considered between the two couples of current derivative samples. The additional term is speed dependent, as previously discussed.

A simplified expression can be finally calculated

$$\begin{aligned}
&2\sqrt{\left(\tilde{L}_{\Delta}{}^2 + \tilde{M}_{qd}{}^2\right)}\cos(2\theta_{me} + \alpha) = \\
&= k\left(-a{u_\alpha}^{(21)} - b{u_\alpha}^{(43)} + c{u_\beta}^{(21)} + d{u_\beta}^{(43)}\right) \\
&2\sqrt{\left(\tilde{L}_{\Delta}{}^2 + \tilde{M}_{qd}{}^2\right)}\sin(2\theta_{me} + \alpha) = \\
&= k\left(-a{u_\beta}^{(21)} - b{u_\beta}^{(43)} - c{u_\alpha}^{(21)} - d{u_\alpha}^{(43)}\right)
\end{aligned} \tag{4.47}$$

where

$$k = \left(1 - 2\omega_{me}\Delta T \frac{\left(\frac{di_\alpha}{dt}^{(21)} \frac{di_\alpha}{dt}^{(43)} + \frac{di_\beta}{dt}^{(21)} \frac{di_\beta}{dt}^{(43)} \right)}{\left(\frac{di_\alpha}{dt}^{(21)} \frac{di_\beta}{dt}^{(43)} - \frac{di_\alpha}{dt}^{(43)} \frac{di_\beta}{dt}^{(21)} \right)} \right)^{-1} \tag{4.48}$$

About these last results, one can notice that:

- sine and cosine signals experience discontinuities at each sector change; this is due to the different PWM pattern for each sector and, consequently, to the different couples of active vectors and current derivatives;
- the ratio between the sine and cosine terms in (4.47) is still proportional to the tan of the electrical position, as the additional speed-dependent term is an identical gain for both the equations, that simplifies after ratio; that is the reason why, even at high speed and with discontinuities of the sine and cosine signals, the estimated speed is still correct, as it will be shown in the simulation investigation;

The additional term speed-dependent terms in (4.46) can however be compensated in order to obtain pure sinusoidal functions with no discontinuity, thus allowing the application of other position and speed calculation methods, e.g. PLL.

Even more complex models can be introduced for the variation of the inductance matrix with rotor position (especially at high speed), e.g. by considering a different value for each current derivative sampling instant (see Fig. 4.19). It can however be verified by simulation results that the improvements in the estimates are very limited. Therefore this analysis is not reported here.

4.3.3 Simulation results

Reliability of the proposed analysis has initially been verified by comparing the results of a complete electro-mechanical dynamical model simulation of the drive system, including sampled-time control and PWM modulation, and the analytical models discussed in the previous sections.

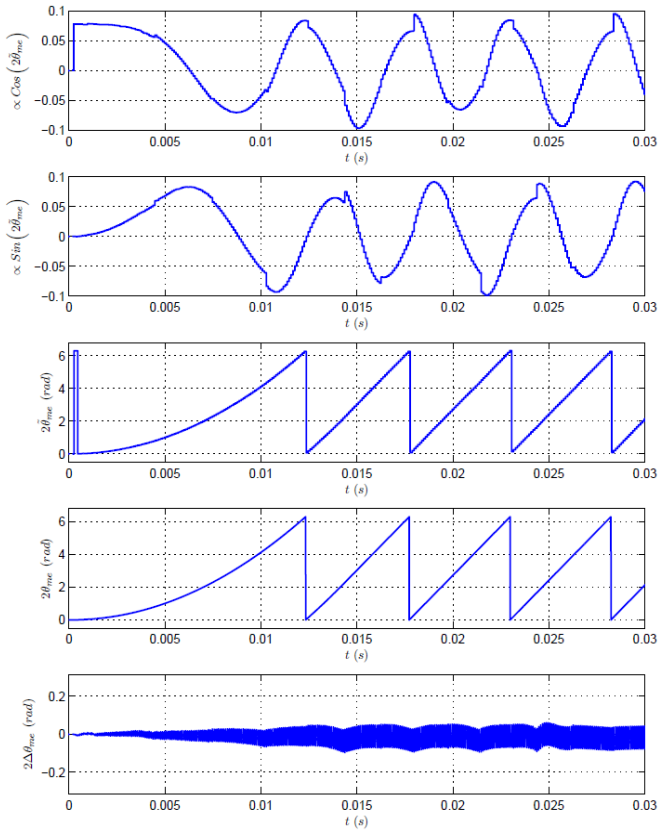

Fig. 4.20. Rotor position estimation during a speed transient with no compensation for the speed dependent term (simulation).

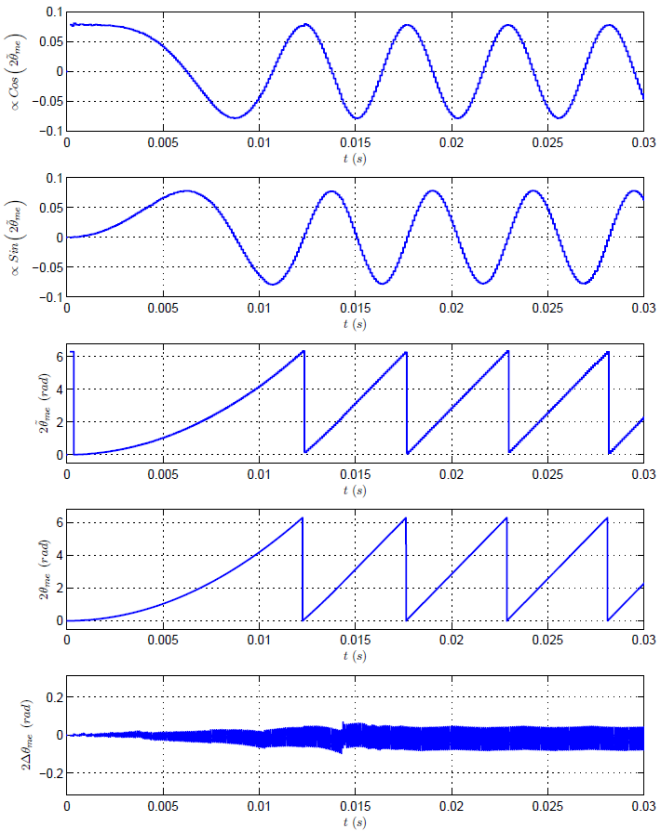

Fig. 4.21. Rotor position estimation during a speed transient with compensation for the speed dependent term (simulation).

In Fig. 4.20 and Fig. 4.21 a speed transient under load conditions is considered from 0 to $300\ rpm$. The aim is to show that rotor position estimation is possible and to highlight the effect of the rotor speed on the sine and cosine signals extracted from current derivatives measurements.

One can notice that discontinuities of those signals are present in the result of Fig. 4.20, due to the effect of speed dependent term that has been neglected in (4.38). Nevertheless, the estimated rotor position, as obtained by direct tan^{-1} of the ratio of those signals is correct, as discussed in the previous section.

The results of Fig. 4.21 prove that a compensation of that effect is possible as a function of motor speed, leading to the removal of discontinuities. This could provide a beneficial effect in the actual system due to the presence of measurement

noise and also allowing the application of more robust rotor position calculation techniques., such as a phase locked loop.

Actual machine will however experience saturation and cross-saturation effects that will worsen the obtainable results. Problems related to current derivative measurement would also cause estimation performance degradation. This topic will be discussed in the next section.

4.3.4 Implementation issues

Current derivative measurement

Direct measurement of current derivative by dedicated sensors is for sure the most effective and reliable method. Indirect measurement, through standard current measurement and derivative calculation (either analogically or digitally), is in fact very difficult to obtain mainly due to the resulting low value of the sensitivity and quantization noise.

The simplest approach is to use a simple inductor, providing a voltage proportional to the time derivative of the circulating current, but this leads to a number of drawbacks, e.g.:

- it is an invasive method, as modification of the measured circuits are introduced (both inductance and resistance);
- reduction of the equivalent inductance would lead to sensitivity problems;
- the sensor provides no galvanic insulation between its output and the measured circuit.

A better solution could be the use of a transformer (mutual inductor), whose mutual inductance provides the sensitivity of measurement. Proper solutions have to be considered in order to reduce any magnetic coupling with external magnetic field and cross-talk among different measuring channels. Also the coupling of primary and secondary circuits have to be properly chosen and any difference

among the channels would lead to a different sensitivity, that needs to be accurately tuned.

The solution adopted in this case is based instead on dedicated Rogowski coils, [68]–[70], mainly due to a simple construction, low cost and high accuracy and bandwidth of the measurements. Accurate modeling of the coils have been taken into account in order optimize the choice of its parameters as a function of the required bandwidth, encumbrance and sensitivity. Fig. 4.22 shows the arrangement of coils and signal conditioning circuit.

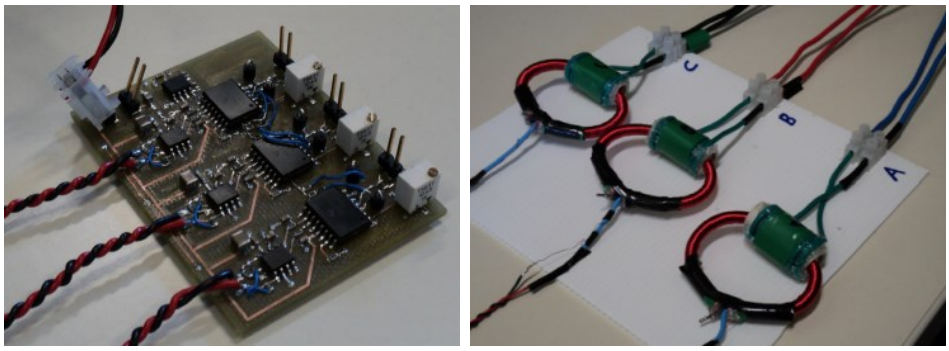

Fig. 4.22. Experimental arrangement of coils and signal conditioning circuit.

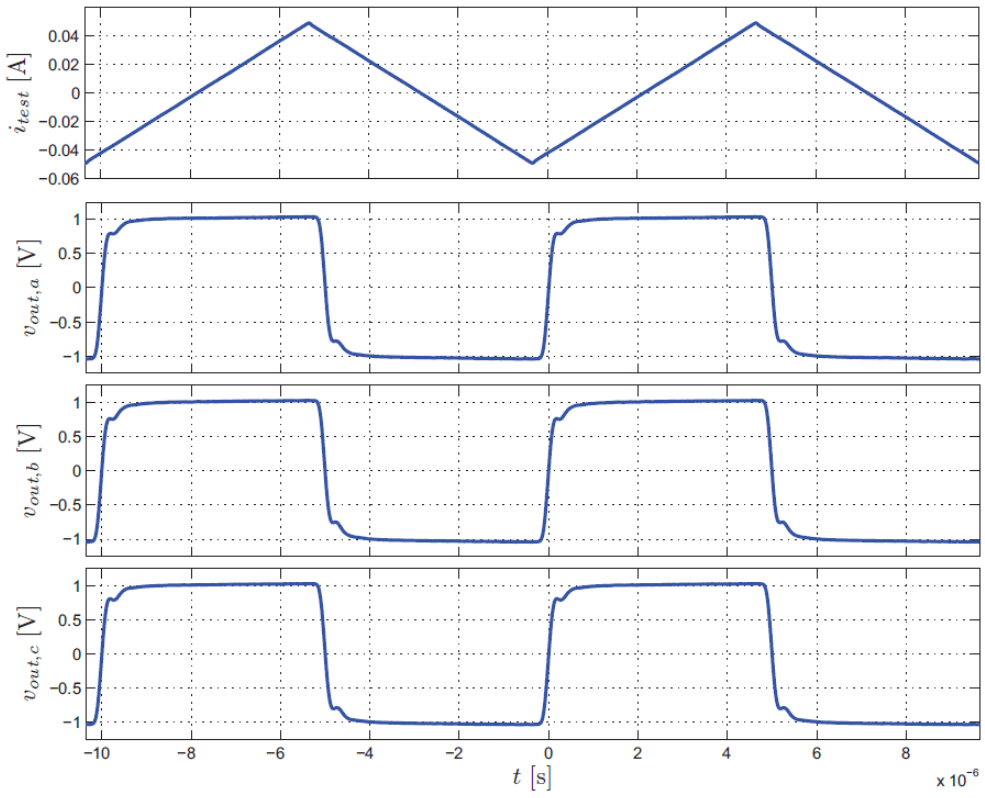

Fig. 4.23. Triangular current excitation across the thee-phases and measured current derivative responses.

Accurate tuning and equalization of the gains of the three current derivative measuring circuits (coils and signal conditioning) have been realized by by feeding all of the three sensors with a triangular current source. The three output voltages $v_{out,x}$ of the measuring circuitry in response to the test current i_{test} are shown in Fig. 4.23. As clearly visible, the system response during slope inversion of the current is not the one of a second order system, as theoretically considered. However the response time is fully compliant with system requirements and the bandwidth of the coils.

Edge-shifting of PWM signals

One of the main issues for the implementation of the discussed sensorless technique is to guarantee a minimum application time of each space vector in Fig. 4.18 under all the operating range of the machine. This requirement is related at least to the following considerations:

- the application time of one active voltage vector when a low amplitude voltage space vector is applied could be too low (even comparable to the response time of the power switches); therefore the resulting current response is not the one considered in the theoretical analysis and those results are not valid anymore;
- the resulting motor phase current oscillations during and immediately after each commutation of the power switches affect the reliability of current derivative measurement; some time has to be waited to make those oscillations decay before measurement can take place.

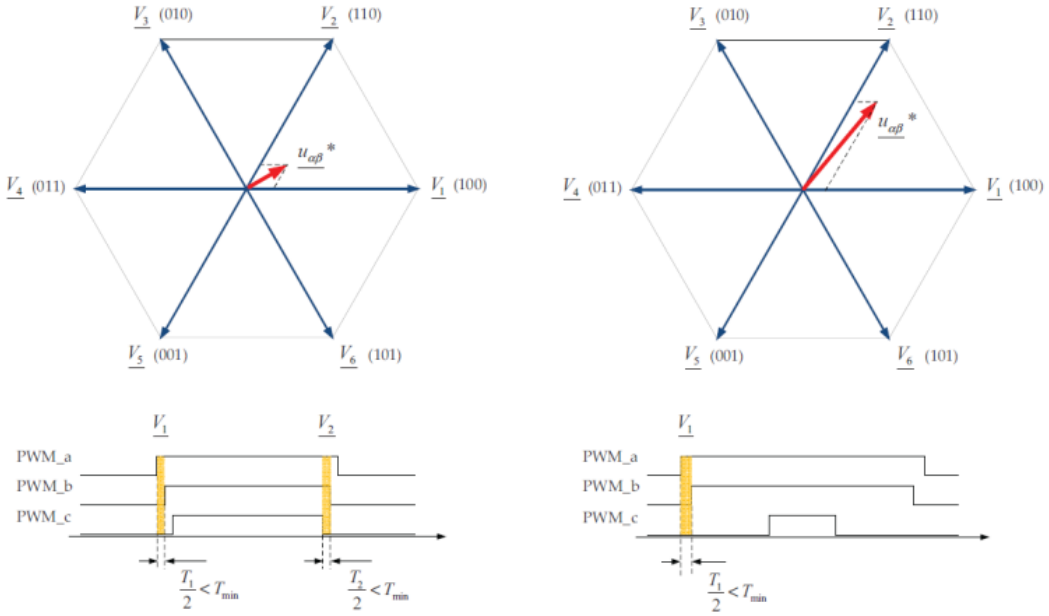

Fig. 4.24. Space vector representation and PWM pattern for low amplitude (left) and sector crossing (right) of the reference voltage space vector.

The most critical cases where the application time of one voltage vector becomes too low can be related to two main operating conditions:

- low-speed operation: application time of active voltage vectors are quite low;
- sector transition of the reference voltage space vector: even if the amplitude of the voltage is high enough, it happens that the application time of an active voltage vector becomes very low (even zero) at each sector transition.

The two cases are graphically recalled in Fig. 4.24. In those situations, the analyzed sensorless strategy can be applied only if a modification of the PWM pattern is introduced, aiming at guaranteeing enough duration of both zero and active voltage space vector, thus allowing reliable values of current derivative samples.

Two main limitation (i.e. constraints) have been considered to any modification strategy of the PWM pattern: the number of commutations within each modulation period and the average value of the reference voltage space vector have to be both maintained.

This necessarily requires the introduction of a modification of the PWM pattern by edge-shifting of the PWM signals, [62], which does not preserves symmetry of the pattern. Differently from the recalled reference, the four current derivative measurements are performed in the same modulation period, thus providing a more complex edge-shifting algorithm. A considerable amount of different cases are possible as a function of the original reference voltage space vector. A full investigation, although performed as part of the study and implementation, is not reported here, since does not represent the core of the proposal.

Edge-shifting of the PWM waveforms introduces a side effect related to the asymmetry of the resulting pattern, that is introduced but not in depth discussed hereafter for the same reason. When adopting a standard double-edge modulation pattern, average values of motor phase currents can be sampled in the symmetry points of the pattern thus removing the most part of the high frequency ripple and avoiding the use of low-pass filters, [71]. Edge-shifting introduces a modification of the pattern that moves the symmetry point and makes the sampling of the average current value more difficult. A compensation strategy implemented in software has been proposed to solve that problem.

Homopolar currents due to capacitive couplings

An IPM synchronous machine represents an asymmetrical three-phase load. The difference between the output voltage of the inverter (as referred to the midpoint of the dc bus) and the phase voltage is due to a homopolar voltage component. As the machine is wye connected, no homopolar current should be present in the ideal case.

But, the analysis of actual motor currents during inverters' switches commutations show that high-frequency oscillations are introduced, with a damped behaviour and time constant in the order of some to tenths of μs, that can be explained with the presence of a homopolar current component.

A simple model is discussed hereafter in order to explain the current behaviour immediately after each inverter commutation, as shown in Fig. 4.25. Lumped parameters C_{inv} and C_{mot} have been introduced to model the total inverter and motor stray capacitance respectively with respect to earth, that indeed are of distributed nature.

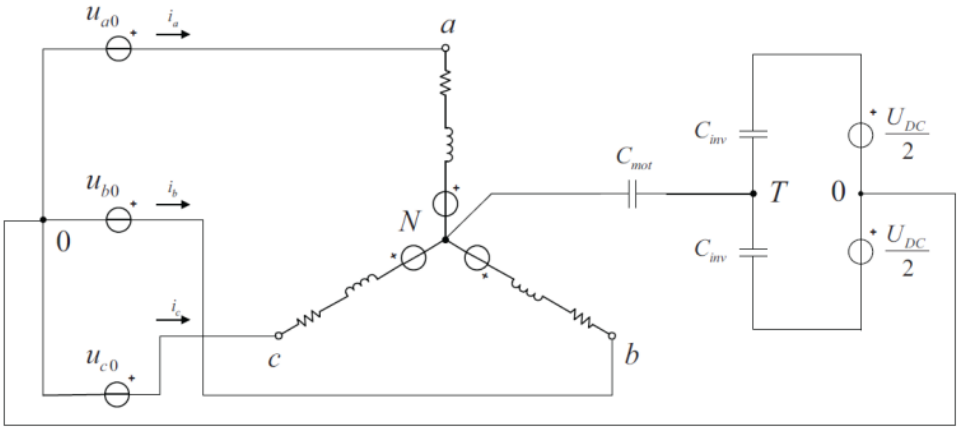

Fig. 4.25. Simplified model of the motor/inverter with parasitic earth capacitances.

From a zero sequence point-of-view, the circuit is a series RLC circuit and the damping factor is generally low due the small value of the series resistance. Oscillations are therefore expected on both motor currents and neutral to inverter

reference voltage, thus requiring a modification of the current derivative sampling instants.

4.3.5 Experimental results

A motor drive system for fractional power high speed IPMSM based on a last generation digital signal controller is considered as a test bench to prove the effectiveness of the sensorless strategy and the validity of the theoretical analysis (see A.3).

Measurement of current derivatives have been performed by dedicated Rogowski coils as previously discussed, oversampling and processing (averaging over a certain time window) of the measured values. This last feature is needed in order to reduce the effects of parasitic parameters of the system (e.g. capacitive couplings, hard switching transient effects, etc.) on the reliability of the measured values, as discussed in the next section.

The tests reported hereafter are mainly intended to highlight some of the problems in the implementation of the estimation method and suggest possible solutions.

The results of Fig. 4.26 refer to the measurement (with oversampling) and processing of the current derivatives within an electrical period of the machine. The four terms A, B, C and D discussed in (4.37) are shown, together with the sine and cosine functions (4.38), the estimated rotor position and the estimation error.

One can notice that terms A and D have different offsets and amplitudes, meaning that both differential sum ($\tilde{L}_{\Sigma}$) and difference ($\tilde{L}_{\Delta}$) indutances are different. This is the main cause of the offset that is visible in the cosine signal and that is the main source of estimation error. This can be explained by considering that actual motor inductances are non-linear and depend on the flux level, in turn depending on the permanent magnet and instantaneous current contributions. Even if the current ripple is very low, the average value of the motor phase current could be relatively different between the current derivative sampling instants. Moreover position estimation error experiences a relatively high value around π, probably due to the effect of the permanent magnet.

In Fig. 4.27 the measured current derivatives and currents in the $\alpha\beta o$ reference frame are shown. One can notice the effect of stray capacitance that provides an oscillating behavior after each commutation. Also a qualitative comparison between the oscillations in the α (or β) and the zero sequence components highlights that a small cross-coupling exists between those axes, as recently modelled in [72] and [73]. In those papers it is in fact demonstrated that, by adopting a proper model for the saturation induced in the stator teeth by the permanent magnet, the inductance matrix in the orthogonal stationary reference is not diagonal and contains some elements linking the homopolar component to both α and β axes. However the first transition of the current derivatives in the $\alpha\beta$ components can be explained by considering the actual model of the motor phase inductance, including a parallel capacitance (due to windings) that conducts a high initial current due to the voltage commutation. This means that current derivative measurement and averaging has to be performed only after that transient condition in order to obtain reliable values.

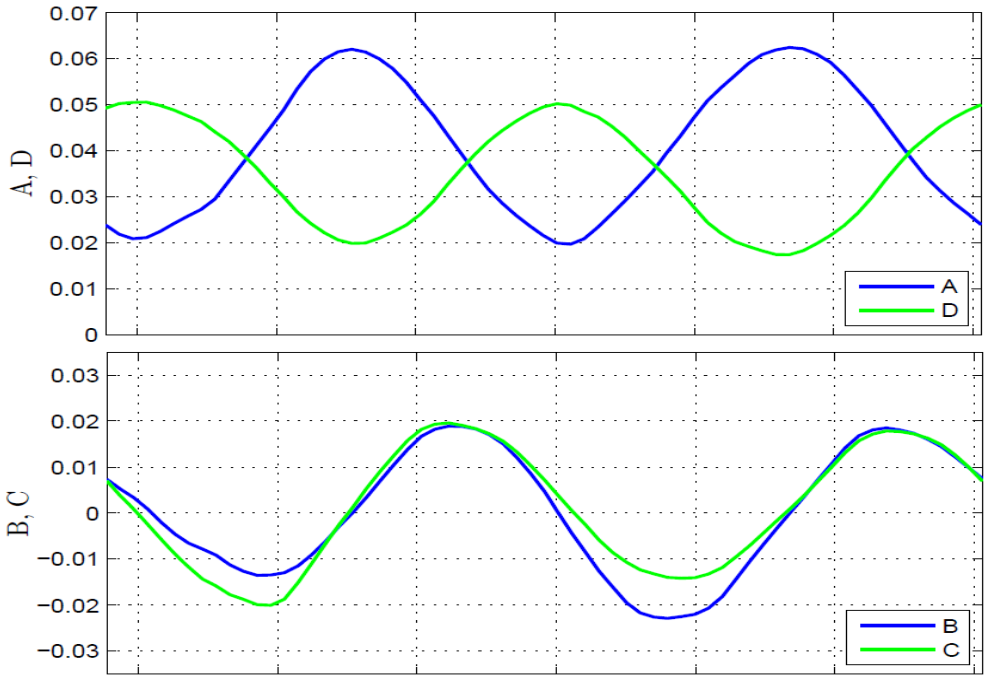

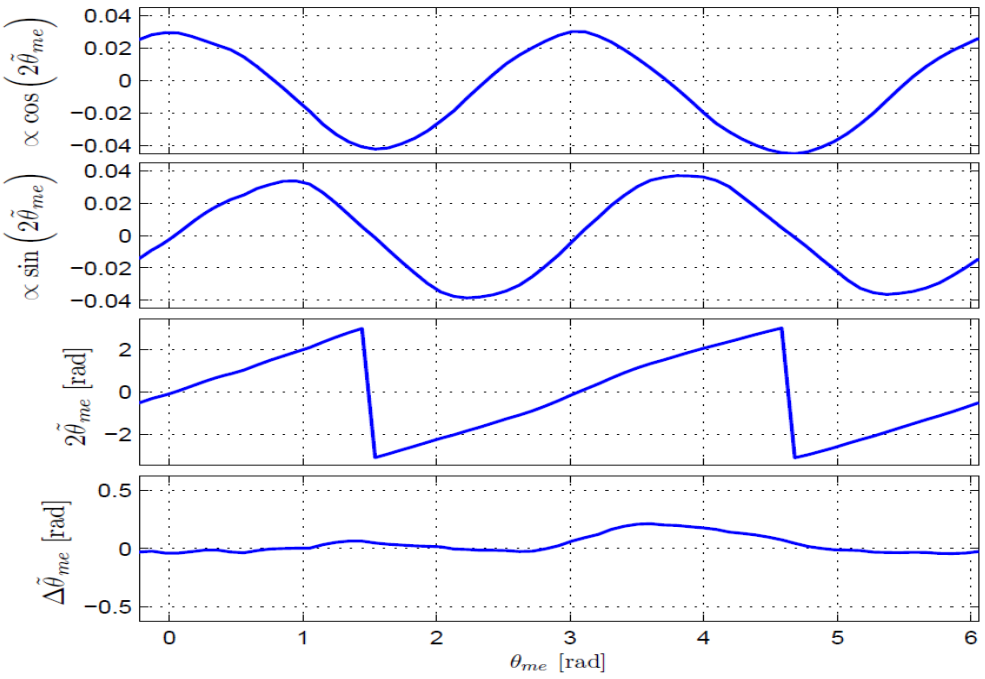

Fig. 4.26. Estimation results (average of current derivatives is done in the last $5\mu s$ of each PWM configuration)

Finally in Fig. 4.28 and Fig. 4.29 the measured current derivatives are shown when the permanent magnet axis is aligned along the α and β axis respectively. The two figures allow to highlight a very interesting phenomenon, that is completely neglected in the past literature. The two curves of each figure have been obtained with the permanent magnet north pole aligned along the positive direction of the winding (blue curves) or the negative direction (purple curves)

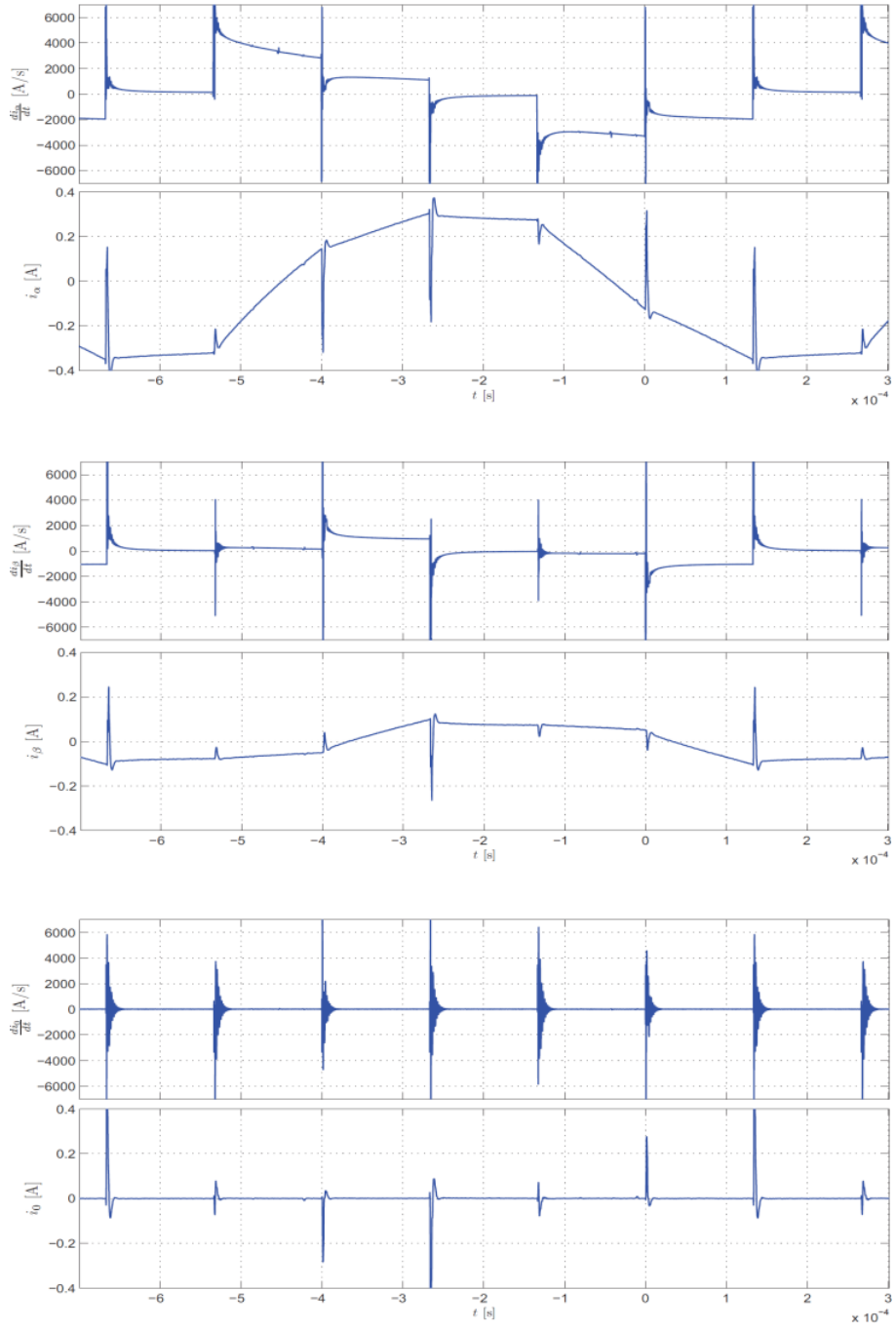

Fig. 4.27. Measured current derivatives and currents ($\theta_{me} = 0$, $U_{dc} = 100V$, voltage vectors $\bar{V}_0$, $\bar{V}_1$, $\bar{V}_2$, $\bar{V}_7$, $\bar{V}_4$ and $\bar{V}_5$) (from top: α, β and o components).

Fig. 4.28 is considered first, where the rotor position has been chosen in order to have the permanent magnet aligned with the α axis.

During the application of the zero voltage vectors ($\bar{V}_0$ and $\bar{V}_7$, 1st and 4th subperiods) the current derivatives are zero, as expected.

During the application of $\bar{V}_1$ (2nd subperiod) and considering the α axis, one can notice that the behavior of current derivative is different if the PM is in-phase or out-of-phase with that axis. When the PM is in-phase with the α axis the overall flux along that direction is increasing, due to the superposition of the (positive) PM flux linkage and that produced by the phase current (also positive in that period). The same applies in the 3rd subperiod, during the application of vector $\bar{V}_2$. The different behavior seems therefore to be related to the influence of the PM flux linkage, that increases or decreases the total flux linkage. This hypothesis is strengthened by considering the behavior of the β component of the current derivative, that is not affected by the in-phase or out-of-phase position of the rotor, as in both the cases it is in quadrature to that axis.

A similar situation is present in the results of Fig. 4.29, where the PM is aligned along β axis. In that case the α component of the current derivative is not affected by the rotor position.

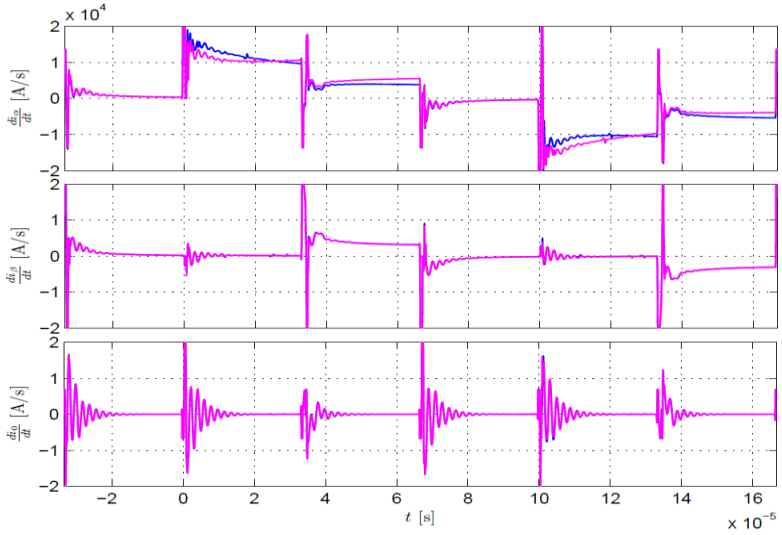

Fig. 4.28. $\alpha\beta o$ measured current derivatives (PM aligned along phase α, $U_{dc} = 300V$, voltage vectors $\bar{V}_0$, $\bar{V}_1$, $\bar{V}_2$, $\bar{V}_7$, $\bar{V}_4$ and $\bar{V}_5$).

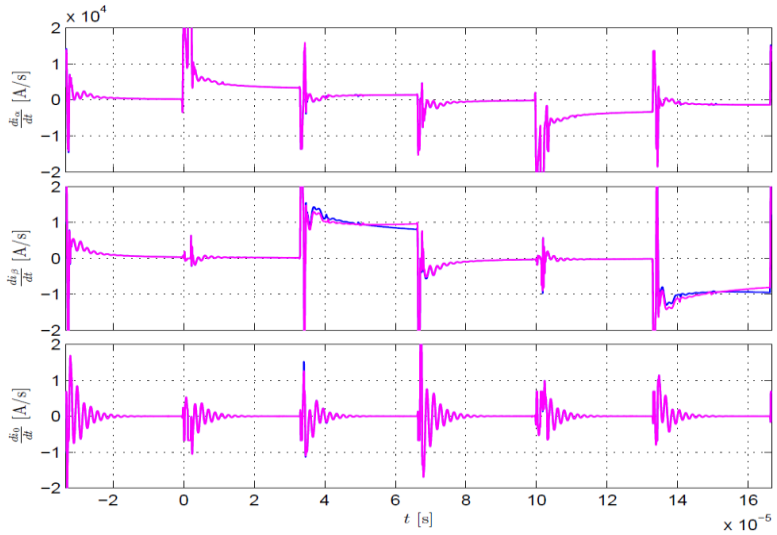

Fig. 4.29. $\alpha\beta o$ measured current derivatives (PM aligned along phase β, $U_{dc} = 300V$, voltage vectors $\bar{V}_0$, $\bar{V}_1$, $\bar{V}_2$, $\bar{V}_7$, $\bar{V}_4$ and $\bar{V}_5$).

4.4 Low-Frequency injection

The proposed position detection method is based on the superimposition of a sinusoidal current at relatively low frequency, causing a vibration of the rotor, according to the principle described in [74], [75]. Speed variation amplitude depends on the difference between injection angle and actual rotor position, and will be detected by means of the observed back-EMF, differently from previous techniques. Then rotor position is tracked by means of a phase-locked loop, both at low speed and at standstill. Moreover, the first harmonic of the produced oscillation provides the rotor axis direction, whilst the analysis of the second harmonic can be adopted to detect the polarity. Therefore absolute rotor position estimation is possible.

Two different application cases will be considered: an initial high-accuracy position detection at quasi-standstill and a position and speed tracking for closed-loop sensorless speed control. It must be noted that, since this kind of techniques involve rotor vibration, their performances are strongly dependent on mechanical

parameters, in particular to load and rotor inertia (which could also be time-varying, in certain applications). In some cases, the presence of a compliant coupling at the rotor shaft could avoid the transmission of vibration to the rest of the mechanical system, making the behavior at a certain frequency almost independent on the applied load. However, these are strong limitations in the applicability of the method, especially for the online position and speed tracking.

A complete theoretical analysis is reported to demonstrate the features of the proposal and highlight the dependence on certain design parameters. Then extensive simulation and experimental investigations based on an industrial drive system are included to prove the feasibility of the method and validity of the theoretical analysis.

4.4.1 Principle of operation

The proposed method relies on the inherent torque production characteristic of non-salient PMSMs, which only involves the permanent magnet field and the related orthogonal current component. The considered analysis is only based on the sinusoidal motor model, i.e. saturation and other non-idealities will not be considered. However it can be recognized that the method works also with typical nonlinearities of non-salient PMSMs.

Given the mechanical system model, a proper choice of amplitude and frequency of the oscillating current injection makes it possible to avoid sensible rotor movement, so that the mechanical position remains in the neighborhood of a certain operating point. Thus, the speed oscillation amplitude depends, besides parametric values, from the orthogonal portion of the injected current vector, which is obviously related to the difference between injection angle and rotor magnetic axis position. Processing the back-EMF amplitude can be used to obtain rotor position information.

This technique assumes that a position "estimation" is considered, so that the injection and back-EMF processing is done in the estimated reference frame, resulting in an error signal. If a position tracking is needed, the estimation value is obtained by regulating the error to zero in a PLL-type scheme.

If a pulsating current reference is imposed along the estimated direct-axis,

$$I_{\hat{d}}^{*} = \left|I_{\hat{d}}^{*}\right| \cdot sin\,\omega_i t \tag{4.49}$$

having frequency ω_i below the current control loop bandwidth (or a special controller topology is employed, [76]), it can be assumed that the reference is correctly followed, so that

$$I_{\hat{d}} \approx I_{\hat{d}}^{*} \tag{4.50}$$

Since the generated torque depends on the rotor reference frame quadrature-axis current and polar pairs pp and magnet-flux linkage Λ_{mg}, i.e.

$$T_e = \frac{3}{2} pp\Lambda_{mg} \cdot I_q \tag{4.51}$$

by expressing the torque current I_q through synchronous transformation of the injected current

$$I_q = I_{\hat{d}} \cdot sin\left(\hat{\theta}_{me} - \theta_{me}\right) \approx -I_{\hat{d}}^{*} \cdot sin\left(\theta_{me} - \hat{\theta}_{me}\right) \tag{4.52}$$

equation (4.51) can be rewritten as follows

$$\begin{aligned} T_e = \frac{3}{2} pp\Lambda_{mg} \cdot I_q &= \frac{3}{2} pp\Lambda_{mg} \cdot I_{\hat{d}} \cdot sin\left(\hat{\theta}_{me} - \theta_{me}\right) \\ &\approx -\frac{3}{2} pp\Lambda_{mg} \cdot I_{\hat{d}}^{*} \cdot sin\left(\theta_{me} - \hat{\theta}_{me}\right) \end{aligned} \tag{4.53}$$

where torque depends on injected current reference (4.49) and position estimation error $\theta_{me} - \hat{\theta}_{me}$.

The mechanical subsystem is considered to be first-order (inertia J and friction coefficient B)

$$\omega_m = \frac{T_e - T_L}{B + sJ} \tag{4.54}$$

If the injection frequency is sufficiently higher than the mechanical pole ($\omega_i \gg B/J$) and the load torque has dynamics not correlated to (4.49), the component of the mechanical-electrical speed at the injected frequency can be approximated as

$$\omega_{me,i} \approx T_e \frac{pp}{sJ} \tag{4.55}$$

Thus, by substituting the torque expression (4.53) in this last equation, the relation between position estimation error and speed oscillation amplitude can be obtained, in the time domain, as:

$$\begin{aligned}\omega_{me,i} &\approx -\frac{pp}{J}\cdot\frac{3}{2}pp\Lambda_{mg}\cdot\int I_{\hat{d}}^{*}\cdot sin\left(\theta_{me}-\hat{\theta}_{me}\right)\,dt = \\ &= -\frac{pp}{sJ}\cdot\frac{3}{2}pp\Lambda_{mg}\cdot\left|I_{\hat{d}}^{*}\right|\cdot\int sin\,\omega_i t\cdot sin\left(\theta_{me}-\hat{\theta}_{me}\right)\,dt\end{aligned} \tag{4.56}$$

If the peak angular speed due to injection is small (i.e. much lower than the injection pulsation, $|\omega_{me}| \ll \omega_i$), the multiplying term $sin\left(\theta_{me}-\hat{\theta}_{me}\right)$ can be considered as a constant. This approximation is acceptable if injection amplitude and frequency are properly chosen according to the mechanical load, so that the related position oscillation is almost negligible. For a constant position dependent term, the integration operator can be applied only to the higher frequency $\sin\omega_i$ term, resulting in

$$\omega_{me,i} = \frac{3}{2\cdot J}pp^2\Lambda_{mg}\cdot sin\left(\theta_{me}-\hat{\theta}_{me}\right)\cdot\frac{|I_{\hat{d}}|}{\omega_i}cos\,\omega_i t \tag{4.57}$$

If the back-EMF is calculated in the actual rotating synchronous frame (complex notation)

$$E_{dq} = E_d + jE_q = 0 + j\omega_{me}\Lambda_{mg} \tag{4.58}$$

the quadrature component due to injection can be written by using the speed expression in (4.57):

$$E_{q,i} = \omega_{me,i}\Lambda_{mg} = \frac{3}{2\cdot J}pp^2\Lambda_{mg}^2\cdot sin\left(\theta_{me}-\hat{\theta}_{me}\right)\cdot\frac{|I_{\hat{d}}|}{\omega_i}cos\,\omega_i t \tag{4.59}$$

The last signal is not available to the controller, since the actual rotor position is not known. However, if a stationary frame back-EMF observer with proper estimation bandwidth is adopted, [21], it can be assumed that estimates are equal the actual ones:

$$\hat{E}_{\alpha\beta} \approx E_{\alpha\beta} \tag{4.60}$$

Then, applying a Park transformation to obtain the back-EMF components in the estimated reference frame, the following expression can be calculated:

$$E_{\hat{d}\hat{q}} = j \cdot \frac{3}{2 \cdot J} pp^2 \Lambda_{mg}^2 \cdot sin\left(\theta_{me} - \hat{\theta}_{me}\right) \cdot \frac{|I_{\hat{d}}|}{\omega_i} cos\, \omega_i t \left[cos\left(\theta_{me} - \hat{\theta}_{me}\right) + jsin\left(\theta_{me} - \hat{\theta}_{me}\right)\right] \tag{4.61}$$

The two components are proportional to the cosine and sine of the estimation error, i.e.

$$E_{\hat{d}} = -\frac{3}{2 \cdot J} pp^2\, \Lambda_{mg}^2 \cdot \frac{1}{\omega_i} \cdot |I_{\hat{d}}| \cdot sin\left(\theta_{me} - \hat{\theta}_{me}\right) \cdot sin\left(\theta_{me} - \hat{\theta}_{me}\right) \cdot cos\, \omega_i t = \frac{3}{2 \cdot J} pp^2 \Lambda_{mg}^2 \cdot \frac{|I_{\hat{d}}|}{\omega_i} \cdot \frac{1}{2} \left\{cos\left[2\left(\theta_{me} - \hat{\theta}_{me}\right)\right] - 1\right\} \cdot cos\, \omega_i t \tag{4.62}$$

$$E_{\hat{q}} = \frac{3}{2 \cdot J} pp^2\, \Lambda_{mg}^2 \cdot \frac{1}{\omega_i} \cdot |I_{\hat{d}}| \cdot sin\left(\theta_{me} - \hat{\theta}_{me}\right) \cdot cos\left(\theta_{me} - \hat{\theta}_{me}\right) \cdot cos\, \omega_i t = \frac{3}{2 \cdot J} pp^2 \Lambda_{mg}^2 \cdot \frac{|I_{\hat{d}}|}{\omega_i} \cdot \frac{1}{2} sin\left[2\left(\theta_{me} - \hat{\theta}_{me}\right)\right] \cdot cos\, \omega_i t \tag{4.63}$$

The q-axis component can be demodulated and low-pass filtered, to extract rotor position information:

$$E_{\hat{q}_{demod}} = \frac{3}{2 \cdot J} pp^2 \Lambda_{mg}^2 \cdot \frac{|I_{\hat{d}}|}{\omega_i} \cdot \frac{1}{2} sin\left[2\left(\theta_{me} - \hat{\theta}_{me}\right)\right] \cdot cos\, \omega_i t \cdot cos\, \omega_i t \tag{4.64}$$

$$LPF_{E_{\hat{q}_{demod}}} \approx \frac{3}{2 \cdot J} pp^2 \Lambda_{mg}^2 \cdot \frac{|I_{\hat{d}}|}{\omega_i} \cdot \frac{1}{2} sin\left[2\left(\theta_{me} - \hat{\theta}_{me}\right)\right] \tag{4.65}$$

this last term being proportional to the sine of twice the rotor position estimation error.

As mentioned above, this last signal can be fed as the input error to a PLL processing block (instead of the simple **atan** function), as frequently done also in other estimation techniques, thus obtaining an on-line position tracking (and an average speed estimation), as in Fig. 4.30.

Since the error signal dependence is a sinusoidal function of twice the position error, axes polarity ambiguity exists (similarly to the case of anisotropy-based techniques). One possible solution is looking at the 2nd harmonic of back-EMF, [75],

or injecting a DC component on the estimated direct-axis to cause a motion of the rotor in the nearby of the actual d-axis position.

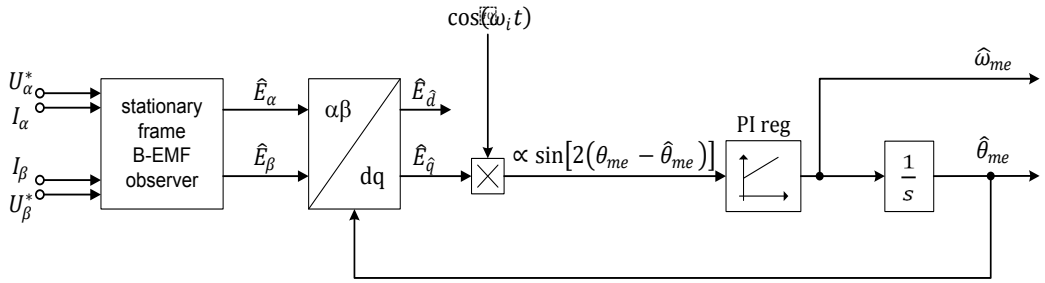

Fig. 4.30. Low-frequency injection based position and speed tracking.

In applications where only an initial rotor position detection is needed (i.e. where external torque is not present at standstill, but reliable startup is required), a different approach can be adopted, leading to a higher position estimation accuracy. The injection and processing reference frame axes are rotated at an arbitrary low speed, thus allowing to map the back-EMF response in a certain position span (half electrical revolution or multiples), obtaining an off-line position estimation, which is the result of an averaging over the imposed axes rotation.

Considering the previous equations, the estimated rotor position is substituted with a low-slope ramp, so that pulsating current injection moves along half electrical revolution or multiples of it. In particular, for a null starting angle, and a frame rotation $\omega_{rot} \ll \omega_i$:

$$\hat{\theta}_{me} \rightarrow \omega_{rot} \cdot t \tag{4.66}$$

The demodulated and filtered back-EMF signals (4.65) are acquired during this injection and will have the form of one or more sine periods, with a phase being the difference between the actual rotor position and the injection starting angle:

$$LPF_{E_{\hat{q}_{demod}}} \propto sin[2(\theta_{me} + \omega_{rot} t)] \tag{4.67}$$

The phase θ_{me} can be obtained off-line by extracting the 2nd harmonic at ω_{rot} frequency by means of a Fourier series decomposition, i.e.:

$$\mathcal{F}_{sin}\left\{LPF_{E_{\hat{q}_{demod}}}\right\} = \\ = \frac{1}{n\pi}\int_{0}^{n\pi} LPF_{E_{\hat{q}_{demod}}} \cdot \sin n\omega_{rot}t \cdot dt \tag{4.68}$$

$$\mathcal{F}_{cos}\left\{LPF_{E_{\hat{q}_{demod}}}\right\} = \\ = \frac{1}{n\pi}\int_{0}^{n\pi} LPF_{E_{\hat{q}_{demod}}} \cdot \cos n\omega_{rot}t \cdot dt \tag{4.69}$$

$$atan2\frac{\mathcal{F}_{cos}\left\{LPF_{E_{\hat{q}_{demod}}}\right\}}{\mathcal{F}_{sin}\left\{LPF_{E_{\hat{q}_{demod}}}\right\}} = n(\theta_{me} + k\pi) \tag{4.70}$$

where k is introduced to take into account the polarity ambiguity and $n = 2$. It is worth noticing that, even though the result is obtained off-line, the memory and computational burden of this processing is low, since each sample requires few multiplication and accumulation operations that can be processed on-line, thus avoiding excessive memory usage.

To obtain control in the whole speed range of the drive, a fundamental back-EMF based algorithm is adopted above a minimum speed. Particular care in the management of the two different estimation techniques must be taken. In this case, an hysteresis switching between the two methods according to two different thresholds on estimated and reference speeds has been implemented. Moreover, position and speed tracking is kept active also for the unused method, at least for a certain speed range. As mentioned, management of the two methods can be performed in many ways, but this very simple one is sufficient to guarantee a smooth transition.

4.4.2 Simulation results

Reliability of the proposed analysis has been verified by comparing the results of a complete electro-mechanical dynamical model simulation of the drive system,

including sampled-time control and PWM modulation, and the analytical models discussed in the previous sections. Simulations have been carried out principally with the aim of verifying the correctness of the theoretical analysis.

The observer and PLL gains choice has been analytically proven to be acceptable, then confirmed by simulation and tuned empirically, since the system noise plays a very relevant role in the estimation performances (practically limiting the usable bandwidth), and a noise model is very difficult to obtain. The observer with $\tilde{\omega}_{me} = 0$ has been considered in this results. The injection frequency is set to $50\ Hz$.

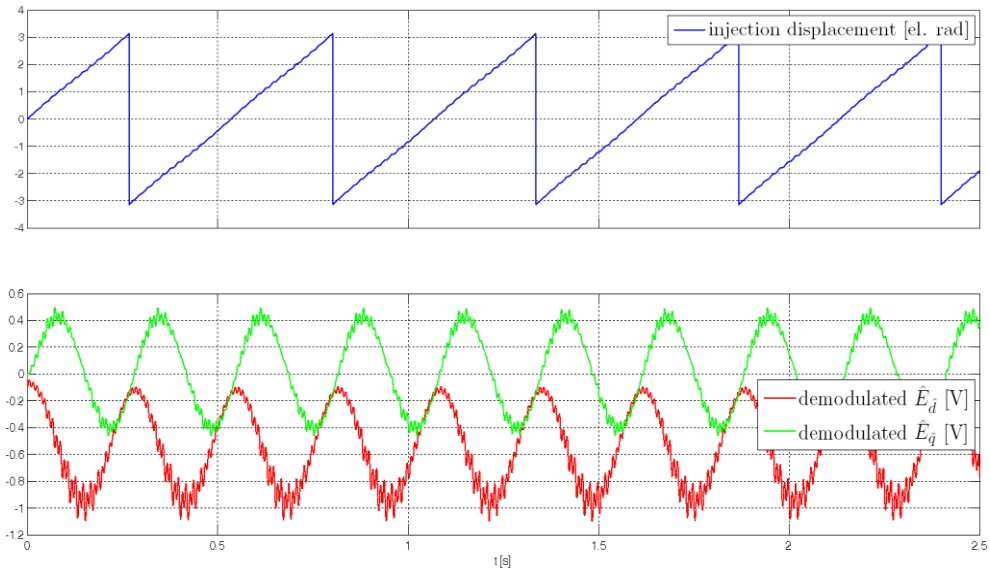

Fig. 4.31. Injection displacement and demodulated back-EMF at standstill with injection reference frame rotating at very low frequency ($\omega_i = 2\pi \cdot 50 \frac{rad}{s}$)

A confirmation of the validity of the theoretically analysis is provided by the results in Fig. 4.31. Injection displacement (i.e. the difference between the actual rotor position and the injected position, $\theta_{me} - \omega_{rot} t$) is shown in the top part of the diagram, whilst back-EMF signals (demodulated and low-pass filtered) are shown in the bottom part. Standstill operations are considered and the injection reference frame is forced to rotate at a constant and very low speed ω_{rot}. It can be highlighted that both the d-axis and q-axis components have a qualitative

behavior which is consistent with the theoretical analysis, i.e. (4.62). The q-axis component has two zero crossings within each electrical period, at about 0 and π (due to the low-pass filter effect), allowing the estimation of the injection displacement and therefore of the rotor position. The d-axis signal does not hit zero (but is very close) due to again the effect of the low-pass filter, that reduces its amplitude, and of back-EMF observer delays. The same simulation has been repeated after arbitrarily increasing the saliency ratio of the machine up to 1.6 and the injected frequency up to $250\,Hz$ in order to highlight any effect of the saliency itself. The q-axis component continues to track the injection displacement, therefore allowing also in this case the estimation of the rotor position. The d-axis component is more affected by saliency, but it is not considered in the estimation process.

Fig. 4.32 shows estimation tracking capabilities when the rotor is dragged by an auxiliary motor (the estimates are not used for motor control). The estimation accuracy and the achieved tracking bandwidth and ripple level allow to use the estimated speed and position signals for closed-loop control, as shown in Fig. 4.33, where a full sensorless control is considered in the same conditions.

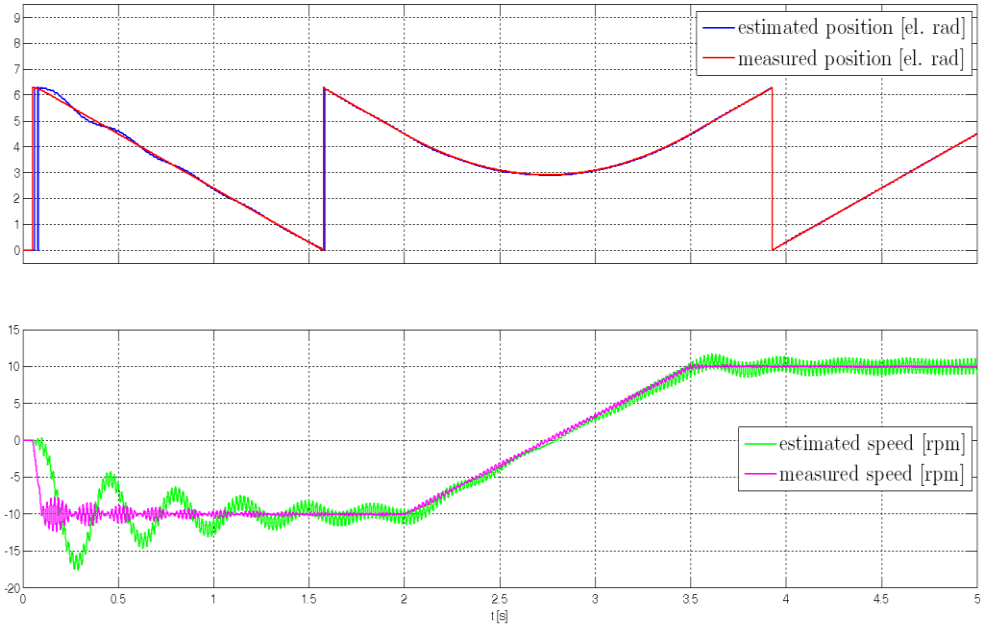

Fig. 4.32. Tracking a slow transition from -10 to 10 rpm.

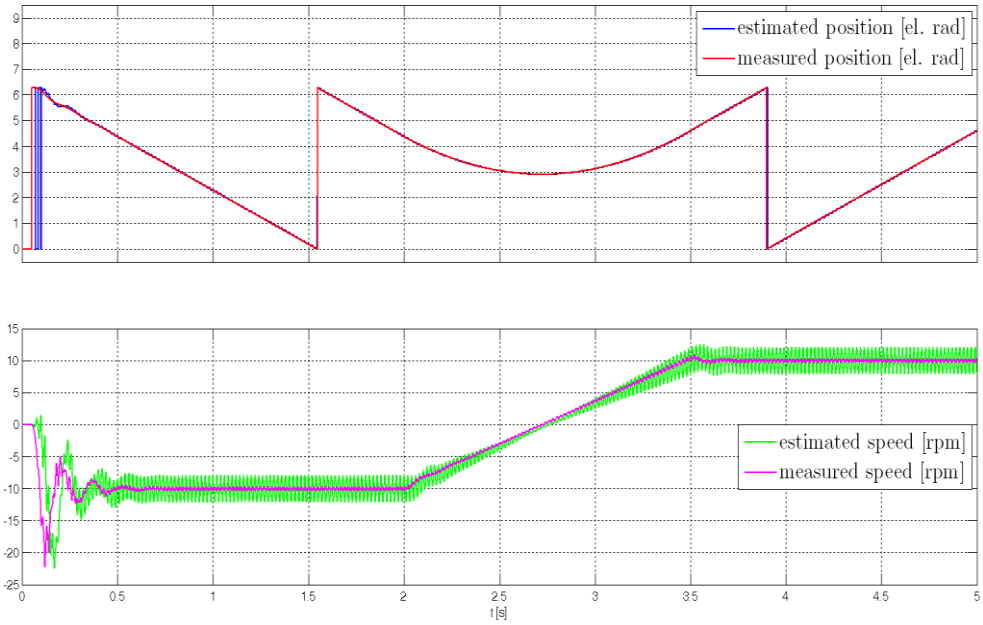

Fig. 4.33. Sensorless closed-loop speed control
(slow ramp from -10 to 10 rpm).

4.4.3 Experimental results

Extensive experimental investigation, using the same setup considered in Chapter 4 (see A.1), is provided hereafter to confirm the correctness of the theoretical approach and to show the effectiveness of the estimation technique. Both stand-still position detection and tracking performance will be considered, the former to be used for open-loop fail-safe startup and the latter for closed-loop sensorless control. Also the effects of a small residual saliency component of the motor used for the experiments will be highlighted, whose effect is however not detrimental to rotor position estimation (even though it has not been proved analytically here and will be the topic of a future investigation).

During the experimental investigations, quite a high-frequency injection (i.e. $250\,Hz$) has proved to provide the best results in terms of estimation bandwidth and signal-to-noise ratio, while causing acceptable small vibrations on the

low-inertia system under test (no sensible rotation was produced). The approximations used in the formal description of the method are based on a simple first-order mechanical load model and ideal behavior of both the back-EMF observer and the current control loop. In particular, the estimation bandwidth of the observer can be evaluated by using the approach presented in [21]. While the above assumptions can be reasonable for low-frequency injection (e.g. in the tens-Hertz range), some adjustments have to be made, in particular on demodulation, for higher frequencies. This does not limit the applicability of the technique, since off-line or on-line phase adjustment can be applied, for example by means of a numerical PLL, similarly to what is usually done for magnetic saliency tracking HF-injection. All the considered experimental tests are in no-load conditions, except for the last one showing the torque rejection capabilities of the system at standstill.

The results of Fig. 4.34 have been obtained at standstill when the injection reference frame is forced to rotate at a constant and very low speed ω_{rot}, as done in the simulation section, Fig. 4.31. The results are quite comparable, confirming the reliability of the analysis and of the implementation. Any saliency in the machine has negligible effect in this frequency condition. The same test has been repeated after increasing the injection frequency in order to boost the effect of saliency. The results are similar to the simulation ones.

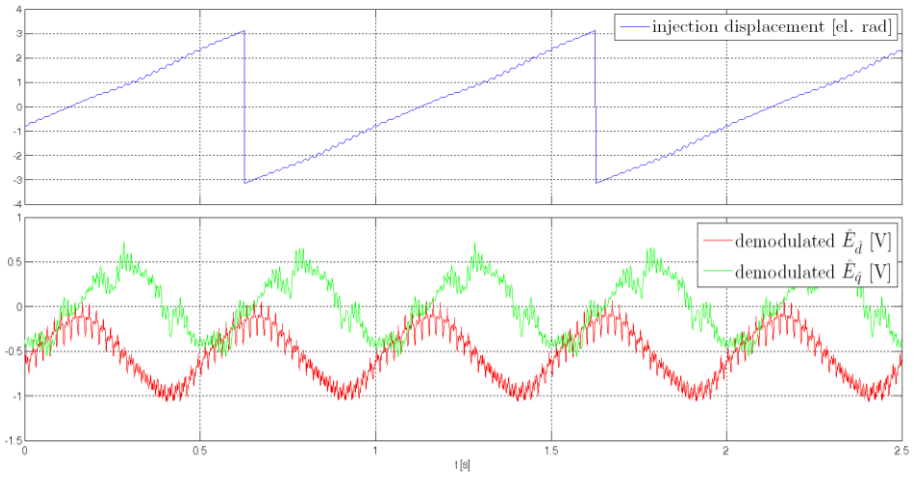

Fig. 4.34. Injection displacement and demodulated back-EMF at standstill with injection reference frame rotating at very low frequency ($\omega_i = 2\pi \cdot 50 \frac{rad}{s}$).

Fig. 3.29 and Fig. 4.36 show estimation tracking capabilities when the rotor is dragged by an auxiliary motor, as done for the simulation analysis, i.e. Fig. 4.32. The estimation accuracy and the achieved tracking bandwidth and noise level allow also in this case to use the estimated speed and position signals for closed-loop control, as shown in Fig. 4.37 and

Fig. 4.38, where a full sensorless control is considered. As shown, both for slow and fast transient conditions the behavior of the controller is quite good, also when the speed is crossing zero.

In Fig. 4.39 the disturbance rejection of the sensorless control at standstill is considered. Rated load torque is applied by an auxiliary drive following a step reference. The top, middle and bottom diagrams show the response of the speed control loop, the torque current and the rotor position estimation error respectively. At time $t = 0.05\ s$ rated load torque is applied and the sensorless drive experience a speed control error that is compensated in about $0.1\ s$ and whose peak amplitude is about $200\ rpm$. Then the torque is maintained at rated value and, during steady-state zero speed condition, a small rotor position estimation error is present. Finally at about $1.2\ s$ load torque is removed.

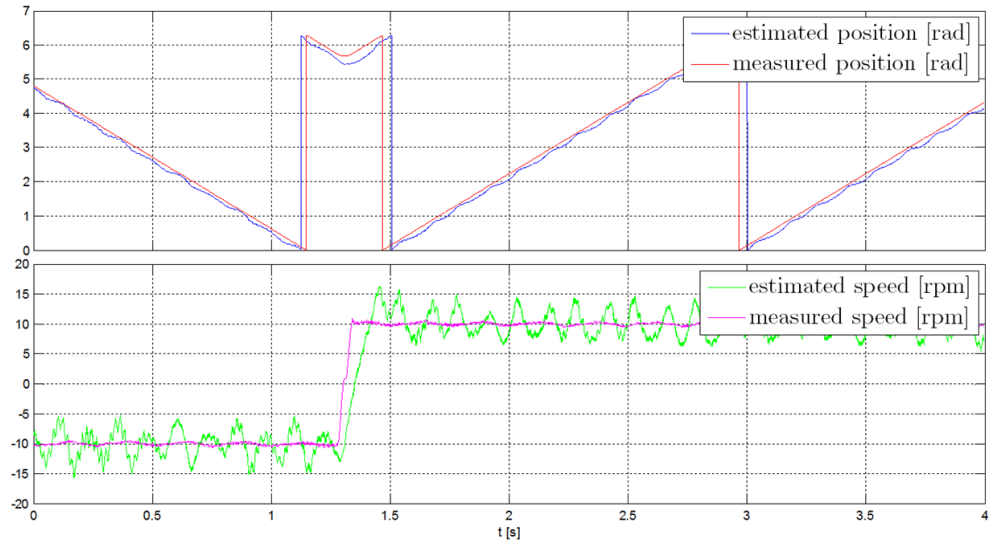

Fig. 4.35. Tracking of fast transition from -10 to 10 rpm.

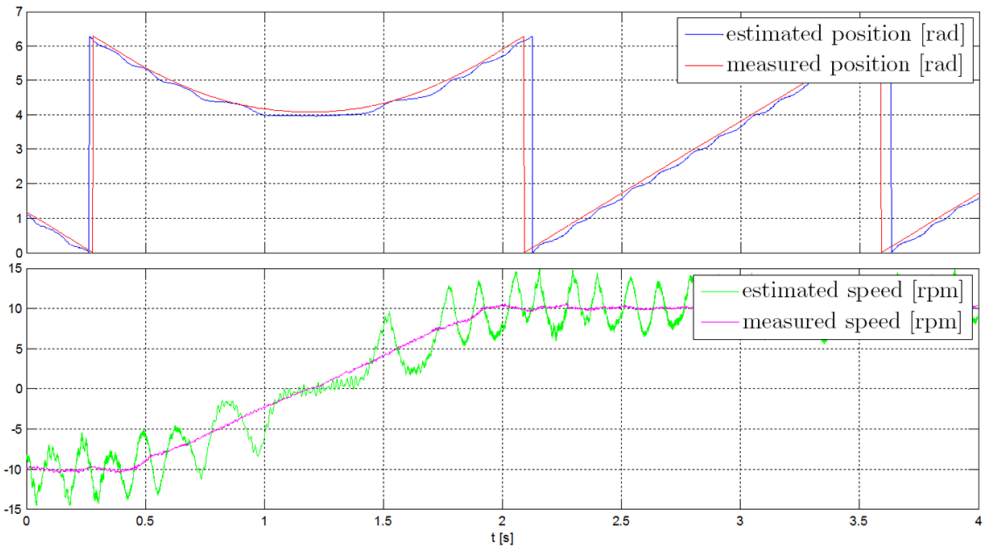

Fig. 4.36. Tracking of slow transition from -10 to 10 rpm.

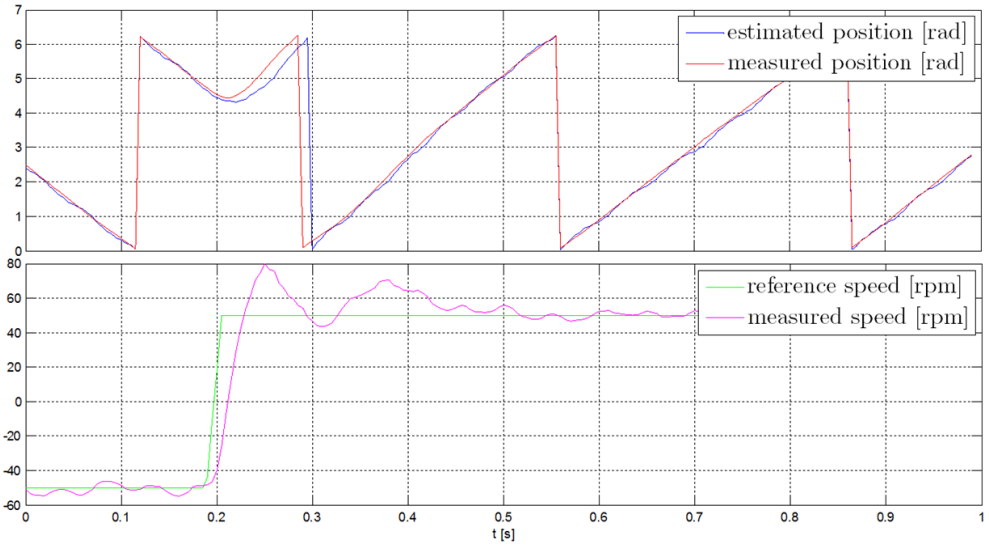

Fig. 4.37. Sensorless closed-loop speed control
(fast ramp from -50 to 50 rpm).

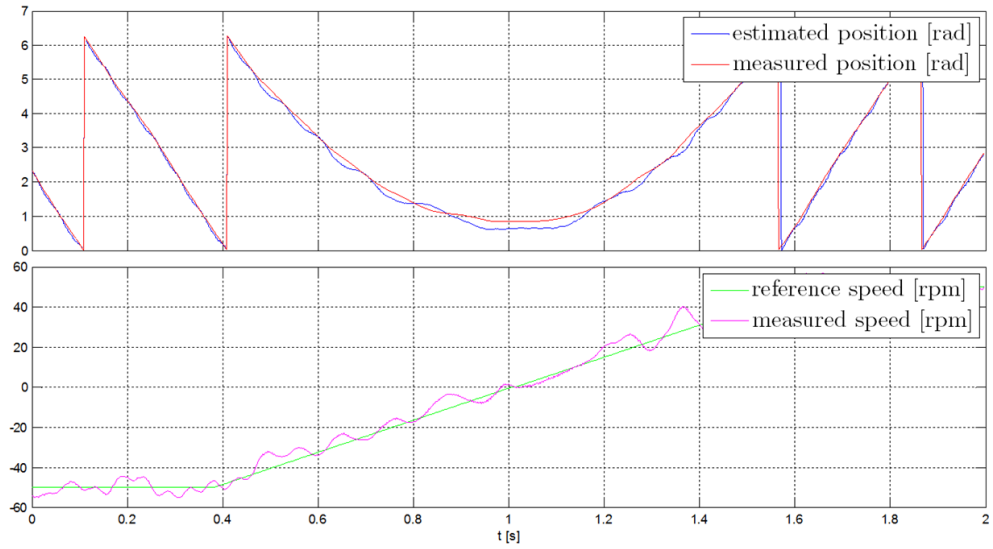

Fig. 4.38. Sensorless closed-loop speed control
(slow ramp from -50 to 50 rpm).

Finally in Fig. 4.40 the result of standstill initial rotor position detection method is reported. As discussed in 4.4.1, this approach is based on an injection and processing in a reference frame axes which is rotated at an arbitrary low speed, thus allowing to map the estimated back-EMF response in a certain position span (e.g. half electrical revolution or multiples), obtaining a high accuracy position estimation, as it is the result of an averaging over the imposed rotation period. In the top part of the figure the unknown injection displacement, the quadrature component of the estimated back-EMF and its 2nd harmonic according to (4.68) and (4.69) Fourier decomposition are shown (back-EMFs are amplified as their amplitude is very low). As it is clearly visible the estimated back-EMF is proportional to the sine of twice the injection displacement, confirming that it can be adopted for the estimation of the rotor position, as $\omega_{rot}t$ is known. The detection time in the considered test is fixed to $1\,\mathrm{s}$, as shown in the bottom diagram of the same figure. The detection error is statistically limited to about 3 electrical degrees, a value being sufficiently accurate for proper motor start-up and comparable with other methods, [77]–[79]. A trade-off has been experimentally proved between accuracy and detection time, i.e. the frequency of the injection frame rotation.

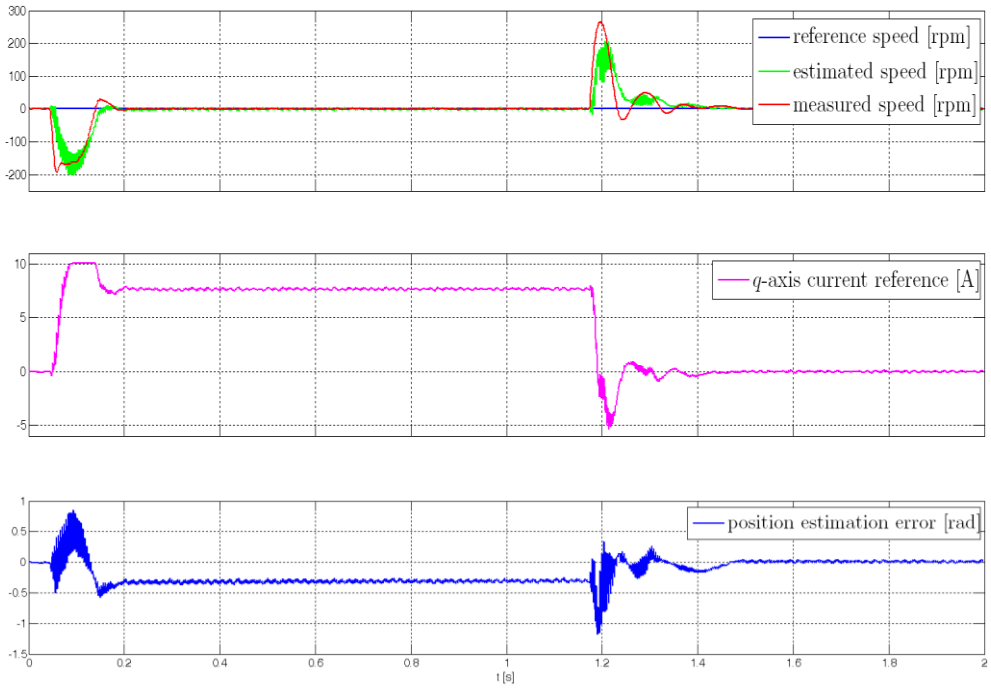

Fig. 4.39. Sensorless rated torque step load disturbance rejection at standstill.

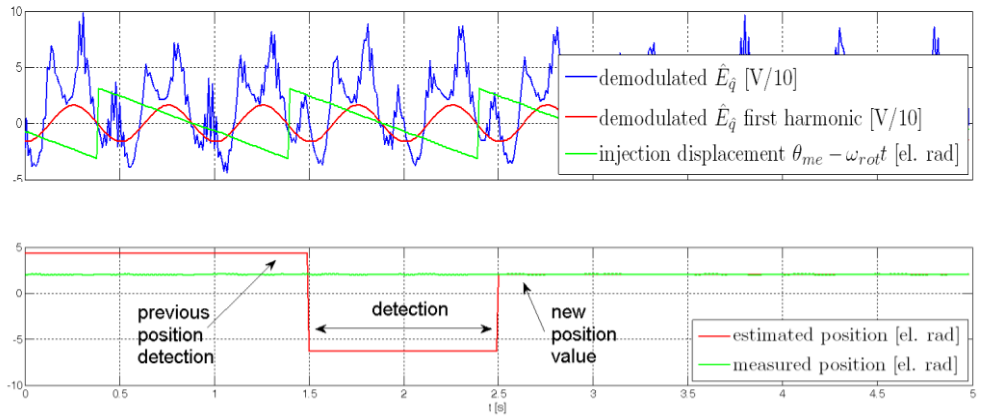

Fig. 4.40. Stand-still initial rotor position detection
with slow reference frame rotation.

4.5 Conclusions

The issue of the demodulation process for high-frequency injection-based sensorless control of salient rotor PM motors has been considered in the first part of this chapter. A novel approach based on Discrete Fourier Transform (DFT) and non-conventional reference frame transformation has been proposed allowing a simple and robust non-coherent demodulation, i.e. in which no information about the carrier phase is needed. The implementation is straightforward as DFT can be seen as a simple low-order (i.e. having a relatively low number of samples) FIR digital filtering. As an example, in the experimental implementation the DFT window length was half the carrier period, thus resulting in 4 samples for each filtering, since the injection frequency was $1.25\,kHz$, while the sampling one was $10\,kHz$. A total of 4 filtering operations with 4 samples long filters must be performed at each control period, which represents an acceptable computational burden. DFT demodulation can therefore represent a good alternative to classical approaches.

The analytical development of the sensorless algorithm including the demodulation technique has been reported. A complete simulation investigation has been carried out aiming at validating the performance of the proposed method. Finally, experimental results have been presented based on a prototype motor drive for city-scooters.

In 4.3, the issue of rotor position estimation in IPMSMs based on persistent PWM excitation and current derivative measurement has been investigated. A complete mathematical model has been developed, by taking also into account the dependence of the rotor position estimation error on the mutual inductance, which is neglected in the past literature adopting similar sensorless approaches.

Measurement of current derivatives is performed by dedicated and optimally designed Rogowski coils, oversampling and processing of the measured values.

Simulation results confirm the reliability of the analytical developments. Experimental investigations prove the feasibility of the method but highlights some phenomena related to the presence of parasitic in the actual system and unmodelled effects of the permanent magnet flux linkage that requires further investigations.

The rotor position estimation method proposed in 4.4 for non-salient PMSMs has been analytically demonstrated and validated by simulation and experimental investigations. Test results prove the feasibility of the proposal and the possibility to attain sensorless closed-loop control even at zero speed, also being able to sustain step rated torque load insertion and removal. Further analytical investigations are needed to gain a full understanding of saliency effects.

Finally the same principle of operation is adopted to obtain the initial rotor position estimation at stand-still. The obtained performance are comparable and even better than stat-of-the-art proposal.

Chapter 5
Flux-Weakening

This chapter reports the results of a study on feedback based deep flux-weakening techniques, which were also published in [80]–[82]. A review and comparison of some state-of-the-art flux-weakening algorithms for the Interior Permanent Magnet Synchronous Motor (IPMSM) will be presented, having voltage exploitation, dynamical performances and implementation (development efforts and utilized resources) as key parameter in the comparison. All of the considered algorithms have at least one feed-back path (thus providing steady-state voltage control even in the presence of parameters mismatch), but different strategies are adopted, leading to completely different dynamical characteristics. One of the three different approaches that will be analyzed is based on the direct control of the synchronous reference frame currents, one relies on mixed feed-back and feed-forward voltage saturation control via the torque vs. flux characteristics and the third acts by means of the voltage vector angle, setting a constant magnitude.

The voltage control by means of the typical synchronous current regulation (which gives the better simulation results) is then analyzed in deep, obtaining a complete characterization of its static and dynamical behavior. The study, which highlights the strongly non-linear characteristics of the controlled plant, is validated by means of simulation. These results allow to develop a linearization strategy for the control loop, by means of a gain scheduling, which results in almost constant bandwidth over a large speed range, thus maximizing the performances in operation under voltage limitation. In fact, application of the gain scheduling leads to important improvements in current control (and, consequently, speed regulation), especially during operation at the boundary between unsaturated and saturated voltage operation, which have been verified both in simulation and experimental tests.

5.1 PMSM field-weakening background

From the physical point of view, motor operation is constrained by limits in current and power, mainly related to thermal issues, speed (for the mechanical construction of the motor) and voltage, due to the dielectric rigidity of the phase windings. However, when considering the voltage, usually insulation is not the most stringent limitation, since inverter voltage supply capability imposes a saturation value to the output voltage amplitude, which is typically much more restrictive.

The usual representation of the effect of electrical limits on the mechanical performances is the well-known maximum torque vs. speed characteristic. From this curve different information can be extrapolated, and some conventional values are defined. In particular, the typical characteristic for a PMSM shows a constant torque capability from stand-still up to a certain speed value, which is named the base speed. Unfortunately, definition of the base speed is not homogeneous in technical literature, but for the purpose of voltage limitation issues, base speed can be conveniently defined as the maximum speed at which the nominal torque can be achieved, given the inverter DC voltage supply value. This is quite different from the nominal speed definition used in the motor datasheets, which is usually referred to a specified voltage.

Nominal torque below the base speed is a characteristic of the motor and of its thermal rating, and is defined as the torque obtained at the nominal current vector amplitude on the MTPA curve. Since, usually, the electronic power stage is designed for higher currents than the motor (allowing short-time overloading and non-destructive transients), the nominal torque is mostly an intrinsic characteristic of the motor, while the voltage limit related characteristics (base speed and maximum torque curve above it) are typically related to the maximum fundamental wave voltage that the inverter generates.

These performances are heavily affected by the control algorithm operation, which determines the actual maximum voltage of the fundamental wave (i.e. the the first harmonic content) that will be supplied to the motor phases. When supplied by a classical three-phase inverter, the maximum output at the motor

leads is determined by the inverter input (DC bus) voltage. As represented in Fig. 5.1, the linear operating range of the inverter is represented by the inscribed circle in the voltage vectors hexagon, which can be geometrically found to be $U_{DC}/\sqrt{3}$, where U_{DC} is the DC bus voltage. If the presence of low-order harmonics is accepted, slightly higher fundamental wave voltages can be obtained in the over-modulation region, moving toward the six-step operation (where only the hexagon vertices are utilized).

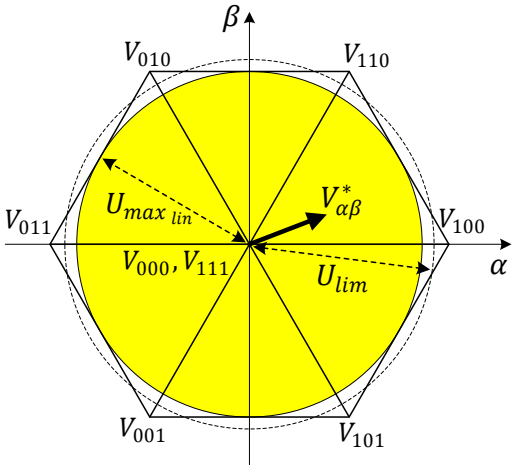

Fig. 5.1. Vector representation of the inverter output voltage capability.

At sinusoidal steady-state and high speed, voltage vector magnitude is mainly related to the induced voltage (derivative of flux), while the contribution of resistive voltage drop is negligible. To keep control above the base speed, a stator flux reduction is imposed ("flux-weakening" or "field-weakening"). Although this can result in a lower torque output, it allows to maintain the current control, since the voltage vector resulting from current regulation can be kept within the magnitude limit. On the torque vs. speed characteristic, above the base speed, a constant apparent power characteristic is followed, which means that, approximately, the maximum torque decreases as inversely proportional to speed. The maximum torque achievable at a given speed increased with the maximum allowed voltage (an example is shown in Fig. 5.2).

Among the many techniques that have been developed for field-weakening, both open-loop and closed-loop techniques can be found. While open-loop methods must provide flux reduction in excess, in order to take into account the worst-case parameter uncertainty, in the feedback based ones control dynamic behavior is critical when the motor is operating next to the voltage limit. In fact, since the limited bandwidth, to avoid temporary saturation of the voltage vector (and consequent loss of the current control) a voltage margin is usually imposed between the limitation value and the actual inverter voltage limit. A faster response of the voltage limitation loop allows the narrowing of the margin, resulting in a higher torque vs. speed curve (Fig. 5.2), finally resulting in an expansion of the speed control range.

In certain applications that require the maximum possible torque to be generated at high speeds, this is a very important target. As an example, this is crucial in home appliances like washing machines (which need to work both at low-speed and spin-dry), but also in electric or hybrid traction, where torque vs. speed curve is an important performance figure from the user point of view.

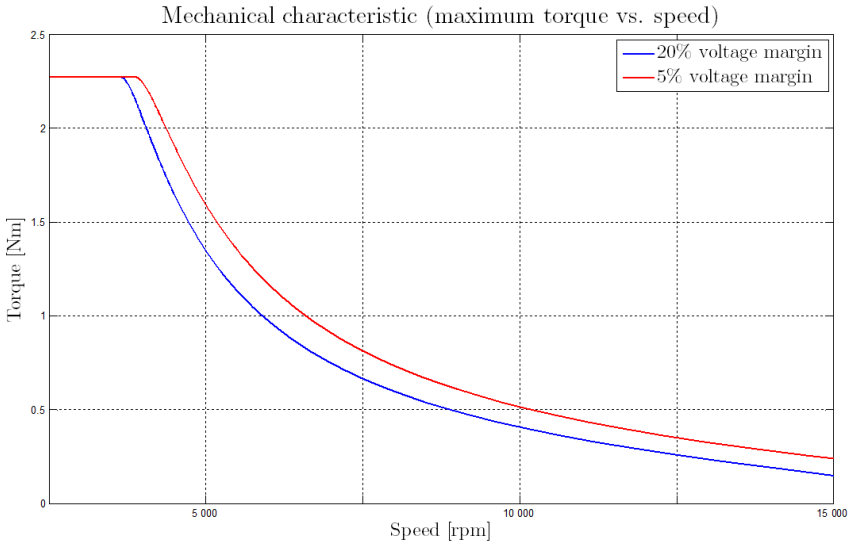

Fig. 5.2. Example of torque versus speed characteristic for two different voltage limit values.

As the capability of controlling motor current at higher phase voltages leads to an increase in maximum torque at high speed; on the other side, the same torque value can be achieved with a lower current magnitude. It must be noted that, in many cases, resistive power losses are the most relevant ones in the motor (from the electrical point of view), and the converter losses are mostly dependent on current level (both resistive and switching). For this reason, when operating the motor in the constant apparent power range (flux-weakening), operating at the highest possible voltage means keeping the losses the lowest possible, thus significantly improving the drive efficiency, especially in the cases where sustained operation above the base speed is required by the application.

Maximizing the DC bus voltage exploitation while avoiding control stability and accuracy loss is one of the targets that research in this field has tried to optimize, because of the important implications on the drive performances (torque or speed control at high speed). In fact, if the current controllers are maintained in a condition where their output represents a voltage vector whose magnitude is significantly higher than the maximum value the inverter can supply, current control can be lost, definitely preventing correct drive operation. Typically, current control loss causes a temporary reduction of the output torque and a consequent speed decrease that allows the drive to recover its torque capability (as voltage is not saturated yet). Then the motor enters in the high speed range, where again control loss occurs, resulting in a cyclic behavior. Besides being a problem from the mechanical performances point of view, especially for motors that are operated in deep flux-weakening (i.e. many times above the base speed) uncontrolled operation can cause potentially damaging overcurrent or overvoltage conditions on the inverter, due to the high voltage generated by the permanent magnet flux, if not properly counteracted by means of d-axis current.

Even if flux-weakening is also adopted in the control of SM-PMSMs, IPMSMs are the machine where this topic has been most intensively investigated, especially in the recent years. This becomes quite obvious if the peculiar characteristics of IPMSMs are considered. In fact, as a first reason, it can be noted that anisotropic machines usually have lower PM flux levels for the same power and torque, leading to a larger capability of counteracting the PM flux with direct-axis current. But, most of all, they allow to partially compensate the PM related torque decrease associated with flux-weakening by exploiting the reluctance torque, which comes

almost automatically with proper field-weakening operation. This has led to an intense research in field-weakening of anisotropic motors, especially for automotive and home appliances.

5.1.1 Principle of operation

From the voltage equation in the dq synchronous reference frame

$$U_{dq} = R_s I_{dq} + sL_{dq} I_{dq} + \omega_{me} \lambda_{dq} \tag{5.1}$$

it can be easily pointed out that, in the two orthogonal components at high-speed steady-state, the axes coupling components $\omega_{me}\lambda_{dq}$ are the dominant ones. Thus, if the resistive drop is neglected, voltage at a certain speed can be simply considered as linearly dependent on the total flux-linkage vector magnitude

$$|U_{dq}| = |\omega_{me}| \cdot |\lambda_{dq}| \tag{5.2}$$

This means that a certain voltage magnitude can be obtained at steady-state by generating a proper flux-linkage magnitude. Flux vector components are composed by the permanent magnet contribution and by the inductive ones

$$\lambda_d = \Lambda_{mg} + L_d I_d \tag{5.3}$$

$$\lambda_q = L_q I_q \tag{5.4}$$

From their expression it is possible to deduce that introduction of a negative direct-axis current counteracts the permanent magnet flux, and a decrease in the quadrature-axis current also leads to a reduction of the voltage amplitude. Almost all the flux-weakening schemes work on this principle, either by imposing a predefined direct-axis current reference depending on the operating conditions (mainly speed, also torque reference can be involved in the calculation), or by adopting a feedback approach, closing a regulation loop on the voltage vector magnitude which synthesizes online a proper value for the current references.

Obviously, the flux-weakening action must be performed contemporarily to the torque or speed control. One of the main issues the this arises is related to the fact that, in principle, the speed control (or torque control), the voltage limitation

(flux-weakening control) and current limitation can have conflicting current requirements. As an example, if a torque command rise is considered, quadrature current should be increased, resulting in a larger magnitude flux vector, finally causing an excessive voltage command to be imposed to the inverter (above its amplitude limits). On the other hand, voltage limitation could be achieved by introducing an additional negative direct-axis current, but this is only possible if the current limit is not exceeded. As a conclusion, obeying both voltage and current saturation limits results in a decreased torque capability, as seen from the torque vs. speed characteristics (Fig. 5.2).

5.2 Literature analysis on Flux-Weakening methods for IPMSM

Many techniques for effective flux-weakening have been reported in literature, aiming at optimizing some different features like a simple implementation, control robustness or accuracy or DC bus voltage exploitation. Typically, the simplest methods rely on a known model of the machine, whether analytical or empirical, to provide a current reference, which takes into account the need for counteracting the PM flux above the base speed. This usually translates into a d-axis current reference, varying as a function of speed, to be subtracted to the MTPA one. These methods, represented in Fig. 5.3, are referred to as "open-loop", since the flux-weakening action is only based on previous knowledge on the model, rather than on a real-time measurement and correction. Besides the fact that, in many cases, open-loop implementation requires large memory resources (e.g. if using Look-Up Tables, LUTs), these methods also have the obvious disadvantage of being prone to parametric errors, and can require a considerable safety voltage margin for ensuring control stability and robustness.

The best performances are certainly provided by those methods adopting at least a feed-back approach [48], [83]–[96], in some cases also incorporating feed-

forward features,[48], [92], and often based on the direct control of the motor feeding voltage magnitude. Closed-loop methods Fig. 5.4introduce significant advantages with respect to open-loop techniques, while not necessarily being more complex in their principle of operation and implementation. In most of the schemes, magnitude of the inverter reference voltage vector is calculated and regulated to a value which can be predetermined or calculated as a function of the DC-bus voltage. Even if a voltage margin is in many cases considered (i.e. the reference voltage amplitude is slightly lower than the maximum the inverter can supply), the degree of confidence with which the voltage limit is respected is, at a first approximation, not dependent on parameters. Critical issues, in this case, are moved to the dynamic behavior, since the non-linearity of the controlled loop. In fact, regulation gains and parametric errors affect stability and bandwidth, while the steady-state voltage value, once stability is ensured, can be correctly achieved since the very nature of the feed-back approach.

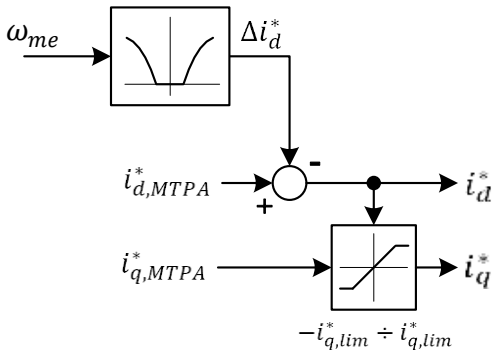

Fig. 5.3. Principle of operation of a common open-loop method.

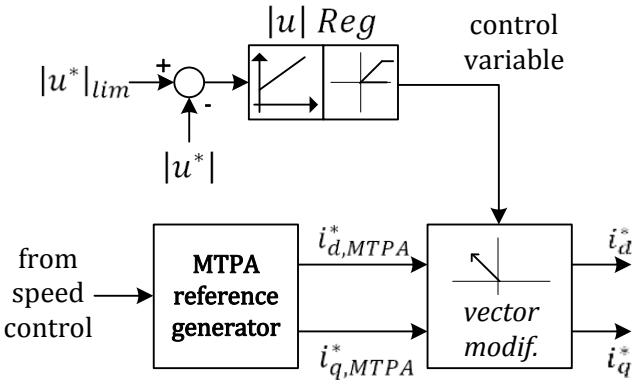

Fig. 5.4. Principle of operation of a common closed-loop method.

Dynamic performances of the voltage control loop can have an important impact on the current control behavior, which is in turn crucial for the speed regulation. In fact, if a typical vector control scheme is adopted, a sudden torque request increase at high speed can cause the current regulators to synthesize transient voltage references which exceed the limit imposed by the inverter. The voltage vector must then be distorted according to some strategy, leading current regulation action to be altered and control to be lost for a certain recovery time. This can cause instability or, at least, a deterioration of the dynamic response both in current control and speed regulation.

In the choice and implementation of a flux-weakening algorithm, some important aspects need to be taken into account. As already mentioned, it can be easily seen that better dynamic performances and accuracy of the voltage command regulation loop allow to adopt higher voltage limits (while still avoiding current control loss), which means improving the torque capability at high speed or achieving the same output torque at a lower current. Another important characteristic which is desirable for a field-weakening algorithm is the possibility to ensure seamless transition between normal MTPA control and the flux-weakneing region, where current must be controlled to obey the voltage limitation. If an outer speed regulation loop is considered, control must be maintained in both the operating regions and at their boundary. This qualitative criteria can be translated into the more technical requirements of control variables continuity and, of course, robust stability. A good knowledge of the dynamic properties of the control loop is

vital for its tuning, also obtaining stability margins for dealing with parametric variations.

Summarizing the main desired characteristics, the design of a flux-weakening control scheme should obtain:

- Steady-state accuracy and fast dynamic response in limiting the voltage demand, which leads to a narrow voltage margin or better current control
- Smooth transitions between MTPA and FW operating regions (control variables continuity)
- Robustness against parameter dispersion and variation
- Reasonable utilization of processing resources (feasibility of implementation)

5.3 Comparison of three flux-weakening control approaches

As already mentioned in the chapter opening, some state-of-art flux-weakening strategies are considered in this paragraph, and their main features recalled in the next sections. The choice of the methods has been done with the aim of comparing typical and simple techniques, a very innovative and quite promising one, and a more complex variant. The three following methods have been individuated:

- voltage magnitude control by means of direct (or quadrature) or phase angle of the current space vector, [83], [93] (vector current control, VCC);
- voltage magnitude control by means of commanded torque and flux, [48] (torque and flux control, TFC);
- single current regulator with voltage angle control, featuring a sort of "hybrid" control behavior between flux-weakening and MTPA regions, [94], [95] (SCR+VAC).

Comparison by means of preliminary analysis and simulation have been carried out. In Fig. 5.5 a general block diagram of a drive system incorporating speed control, current vector control, MTPA trajectory generation and flux-

weakening control is shown. The output of the speed regulator could be the torque reference T_e^* or the current reference i_s^* (amplitude with sign) as a function of the adopted flux-weakening algorithm.

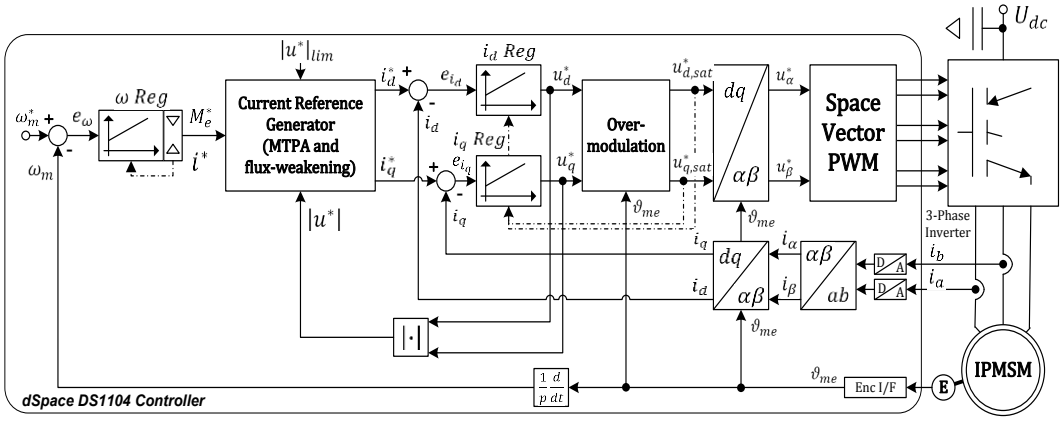

Fig. 5.5. Block diagram of the drive system.

The block diagrams of the considered flux-weakening strategies are shown in Fig. 5.6-Fig. 5.10. They share at least a general feed-back behavior, being linear in the case of direct control of motor phase voltage amplitude (VCC and TFC), i.e. Fig. 5.6-Fig. 5.9, and "switching" for the SCR+VAC approach, i.e. Fig. 5.10.

In the linear control of the voltage amplitude, the voltage control error is calculated by comparing the motor voltage reference and a certain limiting value $|u^*|_{lim} = \epsilon U_N$, where ϵ is a value slightly smaller or equal to one. The voltage error is regulated to zero by commanding a variation of the dq components of the current space vector in order to operate the motor within voltage and current limitations. The main difference among the various algorithms here considered is the strategy used for manipulating the voltage command regulation error to adjust the value of motor currents components.

Some flux-weakening proposals ([48], [88]) consider the modulation duty-cycles of the inverter states instead of the actual voltage reference, which however are tightly related to voltage magnitude values. It can be proved that the over-modulation capabilities claimed in the description of these techniques can be obtained by a proper over-modulation strategy of the dq components of the voltage space vector. This is the reason why in the block diagram of Fig. 5.5, the electrical position θ_{me} is considered as an input of the over-modulation block.

It can be noticed that at least two options can be chosen for the speed control. The schemes where the current reference space vector amplitude is considered as the speed regulator output, involves non-linear relationship between current and torque, but has some implementation advantages. For example, the application of anti-windup for the speed regulator is very easy, since the limit value is constant and equal to the nominal current while, where the torque command mode is used, the limit value (which is important for anti-windup, as it will be demonstrated later) needs to be updated, decreasing above the base speed. Moreover, the choice of the dq current components from the commanded amplitude value and laying on the MTPA locus has a low computational cost, and can be usually implemented without the use of any tabulated data. On the other hand, since the solution of the reverse problem (finding a current vector satisfying the commanded torque, while ensuring it has the minimum magnitude), is more complex, usually LUTs must be adopted. The non-linearity introduced by the first simpler solution is usually acceptable for the speed control loop, especially in the case of a small permanent magnet flux-linkage.

5.3.1 Synchronous current frame based voltage feedback controllers (VCC)

According to this field-weakening approach, the current vector reference coming from the MTPA calculation (fed by the speed controller), is modified by applying the output of a voltage amplitude feedback regulator, in order to achieve the desired flux-weakening effect. As shown in Fig. 5.6-Fig. 5.8 this can be done at least in three different ways, i.e. by imposing a reference for three different variables, operating on the d current component or on the current vector phase angle (and also, but it is not shown here, on the q current component).

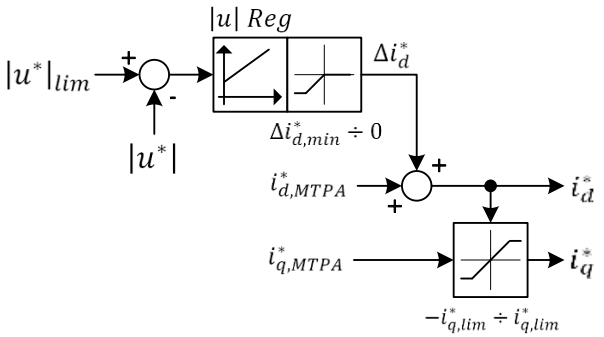

Fig. 5.6.Voltage feedback control (VCC) through additive d-axis current.

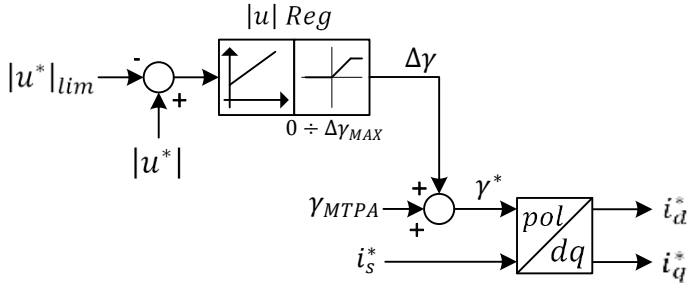

Fig. 5.7. Voltage feedback control (VCC) through additive current vector phase.

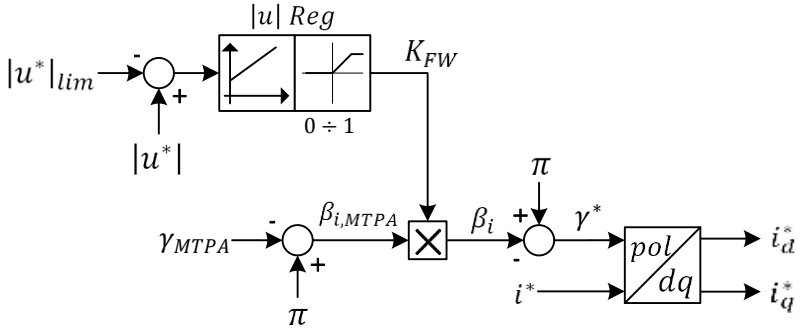

Fig. 5.8. Voltage feedback control (VCC) through product variation of current vector phase.

The first algorithm is illustrated in Fig. 5.6. The voltage controller R_u processes the voltage error and provides a variation Δi_d of the d component of the current space vector. That value is added to the one providing MTPA control (i.e. i_d^{MTPA}), [48], [93]. The q component i_q^{MTPA} should then be processed accordingly, in order to keep the amplitude of the current space vector equal to the output of the speed regulator.

The second scheme shown in Fig. 5.7 directly adjusts the angle of the current space vector, whereas the amplitude $|\bar{\imath}_s|^*$ is provided by the speed regulator. Phase angle variation $\Delta\vartheta_i$ is the output of the voltage regulator added to the MTPA reference current vector phase.

In the scheme of Fig. 5.8 a proportional change of current space vector phase angle is imposed, [83], [86], by means of the factor K_{FW}, being the output of the voltage regulator and whose value is limited in the range $[0; 1]$. The angle β_i^{MPTA} is calculated as the complementary value of the current space vector phase angle γ_i^{MTPA} with respect to π. The value of β_i^{MPTA} is then multiplied by $0 \leq K_{FW} \leq 1$. In this way, MTPA operation is maintained until voltage reaches the reference value U_{lim}, so upper saturation level is set at $K_{FW} = 1$, whilst flux-weakening is obtained by reducing the value of K_{FW} towards zero, thus phase-shifting the current reference vector towards π.

Under flux-weakening operation, phase voltage amplitude is forced to the reference value by generating a current vector which is out of the MTPA trajectory, and so reaching the intersection point between the required torque hyperbola and the reference voltage ellipse. This will be the condition satisfying the voltage limit and having the lower current vector magnitude. A higher d-axis current component or a phase angle lying on the left of the MTPA trajectory results in weakening the flux value, and so reducing steady-state voltage amplitude. Proper limitation of the voltage regulator output ensures the current reference phase is always limited between the MTPA angle for the commanded current amplitude and the negative d-axis (i.e. always to the left with respect to the MTPA trajectory), so that MTPA is followed until flux-weakening is strictly needed.

From a dynamical point of view, each of these three schemes has different gain characteristics, but they all share the same underlying approach and act on a portion of the system which has the same small-signal behavior, i.e. specifically the transfer function relating the current vector to the voltage amplitude. They can

thus be studied together, just applying simple modifications to the gain analysis (see next sections and [81]).

5.3.2 Feed-forward and feed-back voltage control by commanded torque and flux (FTC)

A mixed feed-forward and feed-back strategy based on torque and flux control is considered inFig. 5.9, [48]. The dq current components are a function of both commanded torque T_e^* and proper flux level λ^* and are obtained by means of two two-dimensional look-up tables. Both analytical (i.e. from motor model) and measured values can be considered to build up the tables. The flux magnitude command is obtained as the sum of two contributions, namely λ_{FF} and λ_{FB}. The first one is obtained in a feed-forward manner as a function of commanded torque through an additional look-up-table, depending on motor speed. While MTPA control substantially relies on the feed-forward path, the voltage limitation feed-back modifies the flux reference. An error signal is calculated as the difference between the magnitude of the synchronous current regulators outputs and the saturated voltage (where the saturation is imposed by PWM modulator over the six-step hexagon or an inner hexagon). This path only contains low-pass filters (there are no pure integrators), then does not provide steady-state null error (i.e. no voltage saturation at all), but allows to use an average voltage range comprised in between the inscribed circle and the outer circle with respect to the physical limit being the hexagon (whose radiuses are respectively $1/\sqrt{3}$ and $2/3$ of the DC bus voltage). The relationship between the gain on this path ($1/\omega_{MIcon}$) and the resulting average voltage limit value is quite complex, and has not been provided in the reference paper. However, it can be stated that a higher gain leads to a lower non-linear modulation, while a lower gain moves the PWM modulation range towards the six-step mode.

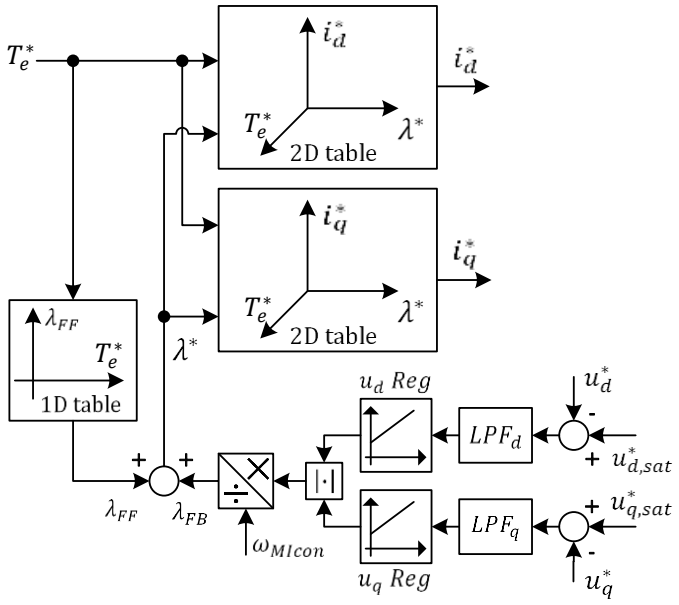

Fig. 5.9. Feed-forward and feed-back voltage control by torque and flux (TFC).

5.3.3 Single current regulator and voltage angle control (SCR+VAC)

A very recent and completely different approach is the one shown in Fig. 5.10, [94], [95]. Standard MTPA vector current control is performed below base speed (having the speed regulator output as the current magnitude reference), whilst the phase angle of the voltage space vector (instead of current) is imposed in flux-weakening region to achieve d-axis current control. During this last mode, the speed control loop provides a reference value for d current regulator, whose output represents the phase angle of voltage space vector. The amplitude is fixed at a constant value $|u|^*$ being less than or equal to the voltage capability of the inverter, given the applied modulation strategy. The reference d axis current i_d^* is calculated from the speed regulator output i_s^* and the measured quadrature current i_q, so that their quadratic sum must satisfy the current limit at steady-state. Since a direct current control is not performed on both axes, it does not prevent modulus of current from

being out of the specified limit for sensible time amounts. The condition for passing from MTPA to single current regulation is the voltage amplitude (i.e. the current regulators output modulus) being higher than the voltage limit $|u|^*$, while the opposite transition happens when the current vector angle is lower than the MTPA reference phase.

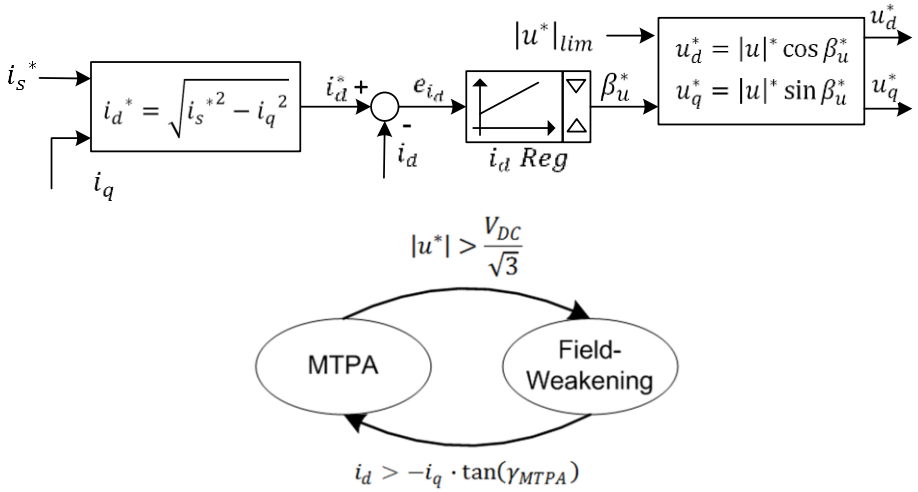

Fig. 5.10. Single-current regulator and voltage angle control (SCR + VAC).

5.3.4 Preliminary comparison

The considered flux-weakening techniques can be evaluated according to various aspects, including effectiveness in exploiting the available dc bus voltage, implementation complexity/requirements and dynamical properties.

The main advantages of the synchronous current frame based controllers (VCC) are related to their simple implementation, providing a seamless integration with the standard vector control, and also leading to an automatic management of transitions between MTPA and flux-weakening control. This means that any traditional MTPA technique can be used, besides the recently introduced on-line tracking, [11], [12]. In fact, the flux-weakening controller produces no effect until the voltage limit is exceeded and, thanks to a proper anti-windup action on the PI regulator, it guarantees smooth operation when working across the limitation

boundary (between MTPA and flux-weakening regions). Moreover, it does not require any look-up-table, thereby no discretization effect is introduced, and large memory, processing performance and parameter-dependent off-line calculations are not needed. A gain scheduling could also be implemented to adapt the regulator's dynamics to the varying operating conditions (see next sections for details), both analytically or by using look-up-tables. But, in this last case, discretization is present in the stored gain values only, which typically requires a lower number of points and generates lower noise on the controlled variables with respect to the case of feed-forward approaches. Finally, all the controller gains and limitations are obtained from few motor and inverter parameter values, such as the voltage-current limits, maximum speed, inductances and permanent magnet flux linkage amplitude.

The FTC technique involves a large memory usage in order to store the look-up-tables, and a complex implementation to manage some out-of-domain operating conditions. Moreover, an extensive off-line measurement and post-processing effort should be carried out to fill in the tables, making it not feasible to apply any gain recalculation inside the drive controller, based on just the main motor and inverter parameters. An advantage in the overall control could be pointed out in the case of strong magnetic saturation effects, but this will likely be more evident under MTPA conditions, while has little influence on the flux-weakening operation, since this last operating region relies mainly on the feed-back component of the voltage controller.

In the referenced paper, the advantage of this approach is claimed to be related to the lack of an anti-windup back-calculation for the current regulators. In fact, it is shown that the interaction between current regulators anti-windup algorithms (which limiting values are taken from the over-modulation calculation) and the voltage feedback path are conflicting each other during quasi-six step operation. The simulations carried out for the scheme in Fig. 5.7 however show that the adopted feedback controller avoids excessive integral accumulation of the current regulators, if correct flux-weakening voltage control is attained. Therefore current controllers saturation limits for anti-windup are designed to be never reached, while the actual saturation on the inverter hexagon is applied maintaining voltage vector phase. This means that over-modulation mode can be also adopted, even if a current ripple arises due to voltage variable magnitude saturation (hexagon limit), similarly to what happens in the approach of Fig. 5.9, translating

into a torque oscillation. This obviously represents a trade-off between control accuracy and voltage exploitation, that must be managed according to the application requirements. The choice of voltage reference value can be done continuously from less than $V_{DC}/\sqrt{3}$ (linear range with a voltage margin), to $V_{DC}/\sqrt{3}$ (inscribed circle, linear range limit), up to V_{DC} (circumscribed circle), obtaining different performances.

The SCR+VAC approach demonstrates weak stability and high sensitivity to gain parameters. In particular, it would be difficult to ensure the current magnitude value will obey the nominal limit during transients, since only the d-axis component is being directly controlled. For the same reason, it is also difficult to find a relationship between the instantaneous values of the controlled variables and the resulting torque. On the other hand, this method ensures operation at a fixed voltage value ($V_{DC}/\sqrt{3}$), which means the whole linear range is well exploited.

Smooth transition between the two different control regions is claimed in the reference paper, but the experimental results show some oscillations, especially if looking at the currents in the synchronous reference frame. This result can be expected, since the method relies on steady-state equations and current vector components are not both directly controlled. This represents the main disadvantage with respect to other techniques, as it means that torque generation and current limitation are not always under full control.

5.3.5 Simulation comparison

Comparative simulations between the discussed flux-weakening control schemes have been carried out under the Matlab/Simulink environment. A motor drive system for home appliances has been considered, whose main parameters are listed in Table I (reported after the conclusions). A test speed reference pattern is considered following a rising and a falling ramp, each followed by speed and torque steady-state conditions. The ramp slope is set to the maximum acceleration achievable by the drive, given the torque limit under MTPA control and the load inertia. This means that, when entering the flux-weakening region, the actual speed

slope decreases with speed. The reduced value of produced torque depends on the voltage limitation imposed by the considered flux-weakening controller, and then qualifies the voltage exploitation characteristics of the adopted technique or, from another point-of-view, allows to evaluate the maximum torque as a function of speed. The results show a similar steady-state behavior, as expected from the qualitative analysis. Some differences arise during transient conditions.

The scheme providing the best stability is the vector control based one with the proposed adaptation of the voltage command regulation loop gains (results are shown in Fig. 5.11), since it maintains full current control under all of the operating conditions, even when a voltage limitation outside the linear region (quasi-six step operation) is considered, i.e. the voltage margin is chosen to be $\epsilon = 1.05$. The experienced heavy ripple on voltage, currents and torque can therefore be justified by the over-modulation condition. Another interesting feature is that the method does not require any switching among different controllers and is only based on feedback regulation. This last characteristic reduces discontinuities and ensures null steady-state voltage error, due to the integral action in the feedback branch.

Fig. 5.12 shows the results of the FTC flux-weakening approach in the same quasi-six step operating conditions. One can notice that the speed transient duration is very similar to that of the VCC approach, thus proving that FTC adds an excessive complexity to the flux-weakening control scheme, which cannot be shown to bring significant improvements. Looking more in detail, it can be noted that FTC experiences some problems during transient conditions due to the low-pass action of the feedback loop, that also does not incorporate any integration feature, leading to non-zero steady-state voltage control error.

In Fig. 5.13 SCR+VAC flux-weakening is considered. Good steady-state results in particular for the voltage are obtained, but current limitations cannot be obeyed. A short but heavy overshoot is present at the torque demand transitions, which may be or not acceptable, depending on the application, but does not provide a corresponding torque boost, demonstrating a transient inefficiency.

It must be pointed out that, thanks to its simpler structure, a dynamical analysis has been performed for the VCC based technique, and the gains have been adjusted based upon the open-loop transfer function bode plots, as discussed in the previous section. Since in the other two flux-weakening schemes gains have been tuned empirically, it can be possible that the best performances are not fully

obtained. However, this would demonstrate how these schemes are more difficult to deal with.

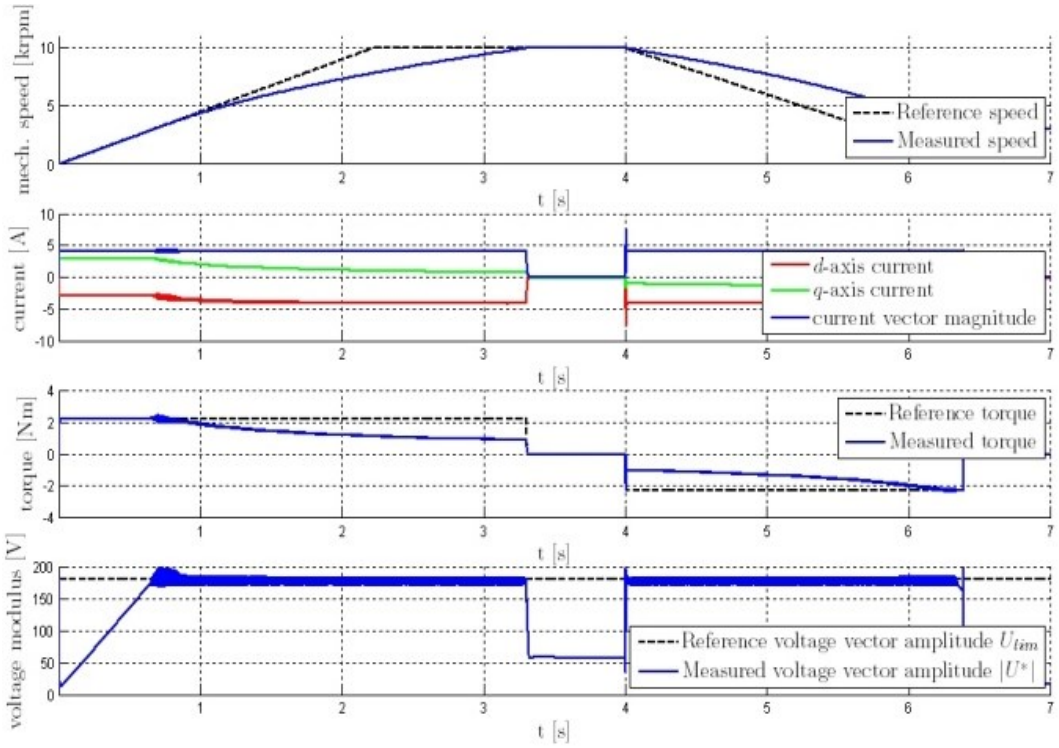

Fig. 5.11. Speed response of VCC.

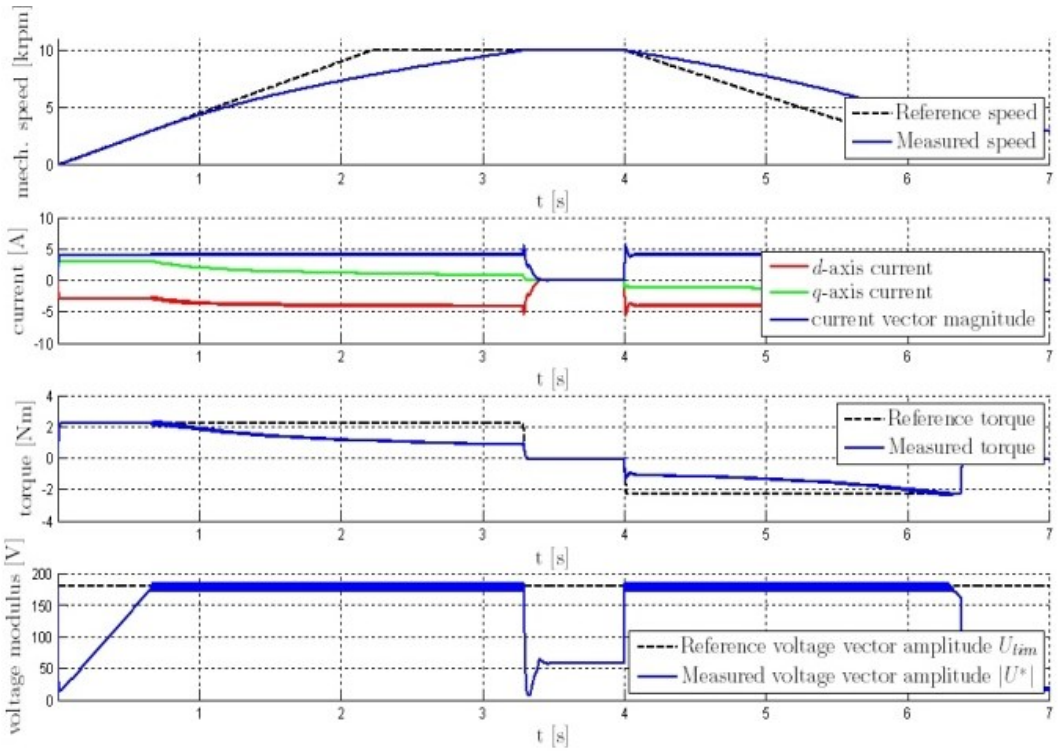

Fig. 5.12. Speed response of FTC.

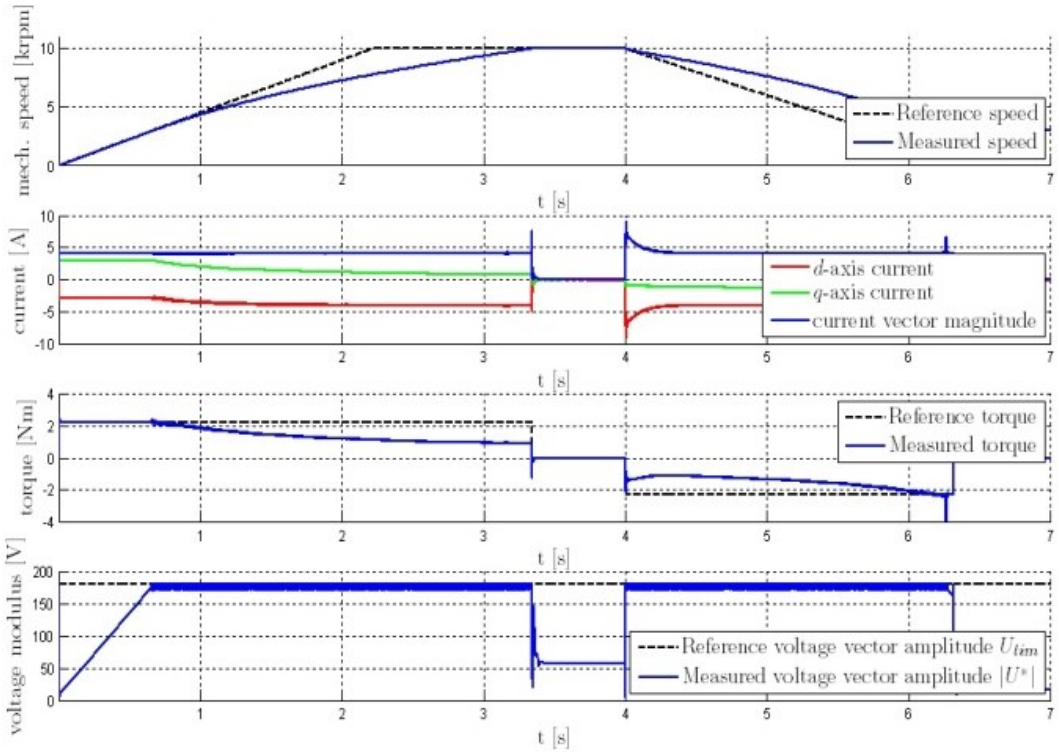

Fig. 5.13. Speed response of SCR+VAC.

5.4 Gain scheduling for the synchronous current frame based voltage feedback controllers (VCC)

The techniques proposed in this section, which have been developed after the analytical and simulative investigation of a voltage magnitude control loop integrated within the typical vector control for an IPMSM, have demonstrated some improvements towards the goals described in the last part of 5.2, if compared

to some state-of-art methods. Moreover, the dynamics analysis will hopefully represent a small contribution for further work on the design of more accurate, fast and stable field-weakening controllers. This work, was presented partially in [80], and was further extended in the papers [81], [82].

The analyzed voltage controller is based on the difference between the amplitude of the reference voltage space vector and a proper reference value, related to the feeding inverter limitations, and adopts the phase angle of reference current space vector as the control variable. Normal MTPA control below the base speed is achieved, while the field-weakening regulation starts operating only when voltage saturation is reached, with a smooth transition between the two control modes ensured by proper voltage controller saturation and anti-windup. A novel theoretical analysis of the overall dynamics of the voltage control loop is carried out, also taking into account non-linear effects and discrete-time implementation delays. The design of the controller can therefore be optimized for each operating condition by an adaptive approach, allowing to define stability properties and to maximize bandwidth of the voltage control loop. Maximization of the dynamical performance provides the main advantage of the proposal, i.e. allows a lower voltage (control) margin to be considered with respect to standard approaches, leading to a higher torque and system efficiency and/or a reduced value of the dc-bus capacitance. A motor drive system for home appliances has been used as a test bench to prove the effectiveness of the proposal.

When a very high-speed condition is considered, some effects related to the non-linear behavior of the voltage control loop (e.g. also related to cross-coupling effects) and to discrete time implementation become extremely important, [90], and can lead to instability of the controller or to a non-optimized bandwidth of the loop. Unfortunately no analytical development can be found in literature allowing the optimized design of the flux-weakening controller and a manual tuning is normally considered in actual drive systems.

A novel theoretical analysis of the overall dynamics of the voltage control loop is proposed, which allows the design of the controller to be optimized for each operating condition. Therefore stability properties and maximization of the loop bandwidth can be guaranteed, e.g. by a proper dynamical adaptation of the voltage control loop regulator gain. This last feature provides the main advantage of the presented approach, i.e. allows a lower voltage (control) margin to be

considered with respect to standard approaches based on a fixed design of voltage controller, definitively leading to a higher torque and system efficiency and/or a reduced value of the dc-bus capacitance. A motor drive system for home appliances is considered as a test bench for both simulation and experimental investigations. Obtained results prove the effectiveness and importance of the proposal.

Referring to the scheme in Fig. 5.7, a novel theoretical analysis of the voltage control loop adopted in the flux-weakening operating region has been carried out, showing that optimized design of the controller can be obtained for each speed condition. Therefore stability properties can be fixed and maximization of the bandwidth of the loop can be obtained by a proper choice of the voltage control loop transfer function, leading to the increment of the available dc bus voltage exploitation.

5.4.1 Voltage equations

From this paragraph, and through the following until 5.4.5, an analytical description of the static and dynamical behavior of the voltage control loop adopted in the flux-weakening operating region will be obtained. The results can be adopted for the optimized design of the controller for each speed operating condition. Therefore stability properties can be specified and maximization of the bandwidth of the loop obtained through a proper choice of the voltage control loop transfer function.

The conventional voltage equation of IPM motor in the dq reference frame synchronous with permanent magnet flux-linkage is considered, i.e.:

$$\bar{u}_{dq} = R\bar{\imath}_{dq} + \boldsymbol{L}\frac{d\bar{\imath}_{dq}}{dt} + \omega_{me}\boldsymbol{JL}\bar{\imath}_{dq} + \omega_{me}\boldsymbol{J}\bar{\lambda}_{mg} \tag{5.5}$$

where $\bar{u}_{dq}$, $\bar{\imath}_{dq}$ and $\bar{\lambda}_{mg}$ are voltage, current and permanent magnet flux linkage vectors, i.e.

$$\bar{u}_{dq} = \begin{bmatrix} u_d \\ u_q \end{bmatrix}, \bar{\imath}_{dq} = \begin{bmatrix} i_d \\ i_q \end{bmatrix}, \bar{\lambda}_{mg} = \begin{bmatrix} \Lambda_{mg} \\ 0 \end{bmatrix} \tag{5.6}$$

and matrices $\boldsymbol{L}$ and $\boldsymbol{JL}$ are related to motor synchronous inductances, i.e.:

$$\boldsymbol{L} = \begin{bmatrix} L_d & 0 \\ 0 & L_q \end{bmatrix}, \boldsymbol{J} = \begin{bmatrix} 0 & -1 \\ 1 & 0 \end{bmatrix}, \boldsymbol{JL} = \begin{bmatrix} 0 & -L_q \\ L_d & 0 \end{bmatrix} \tag{5.7}$$

Electromagnetic torque is therefore:

$$T_e = \frac{3}{2} pp\left[\Lambda_{mg} i_q + (L_d - L_q) i_d i_q\right] \tag{5.8}$$

where pp is the number of pole-pairs. In this analysis, an IPM motor (parameters are reported in the Appendix) is considered theoretically allowing infinite speed in deep field-weakening conditions, i.e. the voltage ellipse centre is inside the rated current circle, as shown in Fig. 5.14.

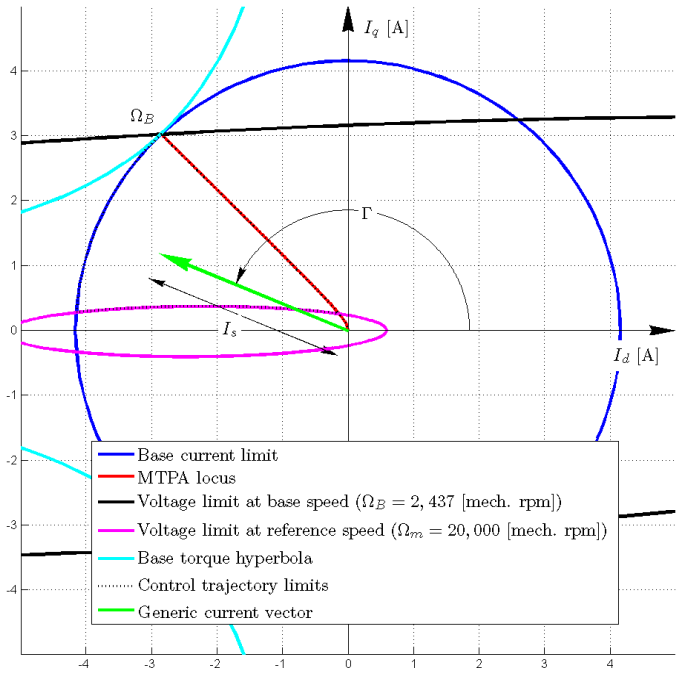

Fig. 5.14. Control trajectories and limit loci in the I_d vs. I_q plane.

Since the vector current control is usually implemented, the machine operating condition is normally studied by drawing the *current–limit locus* and *voltage–limit locus* in the I_d and I_q plane [93], as shown in Fig. 5.14. The former is represented by a circle with radius I_N and center in the origin, the latter by a set of ellipses

whose size is inversely proportional to the electrical angular speed. The center of the ellipses is defined by the short circuit direct current $I_{cc} = -\Lambda_{mg}/L_d$.

In Fig. 5.14, the three different *current loci* can be identified, that set the operating region boundaries: the maximum-torque-per-ampere (MTPA) trajectory, the flux–weakening curve along the limit circle and the voltage limit ellipse at maximum speed. Along the first trajectory the available torque is constant (equal to the nominal torque T_N) up to a certain value of electrical motor speed (i.e. base speed, Ω_B) and amplitude of current and voltage space vectors is lower than machine limits. MTPA control strategy is commonly adopted and the corresponding current operating points are on the red curve in Fig. 5.14. Above the base speed, maximum available torque is determined by the intersection of the current limit circle and the voltage limit ellipse. Depending on the torque command and operating speed, the working point can lie on the MTPA trajectory (for lower speed values) or in the space below it (i.e. having a higher phase angle), when field-weakening is needed. Therefore, the maximum torque decreases with speed. The aim of the flux-weakening control is to provide correct operation with the maximum available torque at any speed (within current and voltage limits) by means of a proper regulation of the current space vector.

It is important to notice that in Fig. 5.14 the Maximum Torque per Voltage (MTPV) characteristic is missing. This last locus contains the tangent points between torque curves and voltage limits ellipses that fall inside the current limit circle. This line joins a point on the limit circumference the d-axis at $-\Lambda_{mg}/L_d$, where null total flux is achieved (inductance flux totally neutralizes the PM component). Following this curve would virtually allow operation up to an infinite speed. If the PM flux magnitude is low, transition to the MTPV would be needed at a very high speed, which can even be out of the operating range (for mechanical reasons), as for the motor considered in this work. For these reasons, the MTPV problem has been neglected. Moreover, differently from flux-weakening and MTPA, at the moment there are no simple methods for MTPV curve on-line tracking, which requires complete parameter knowledge, and is therefore heavily dependent on it.

5.4.2 Considered control scheme

The considered drive control scheme implementing the proposed flux-weakening strategy is shown in Fig. 5.15. Flux-weakening is based on a proper choice of the current space vector (both angle γ and amplitude I_s) based on the direct feed-back control of the amplitude of the reference voltage space vector $|u|$ and rotor speed ω_m, as shown in

Fig. 5.16. The difference between the amplitude of the reference voltage and a proper limit value, U_{lim} related to the feeding inverter limitations, is controlled to zero by varying the phase angle γ of the reference current space vector.

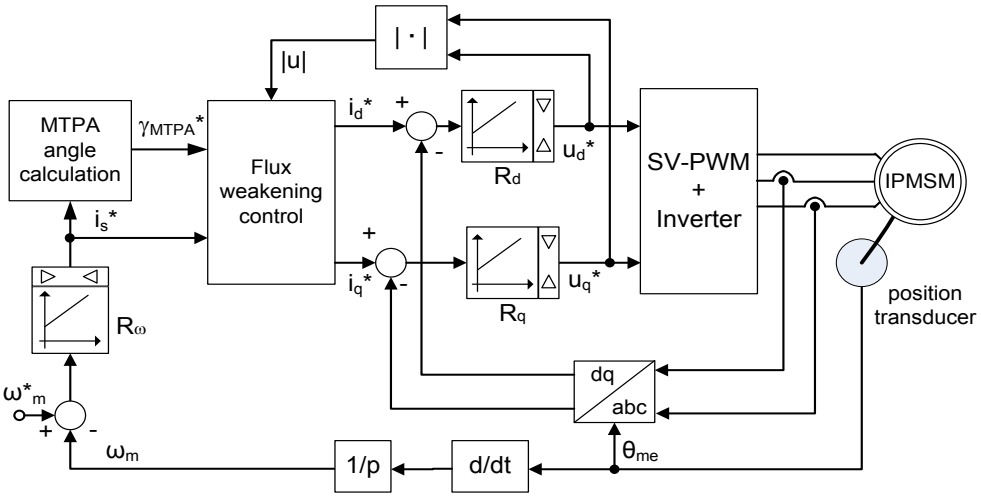

Fig. 5.15. IPMSM drive control scheme.

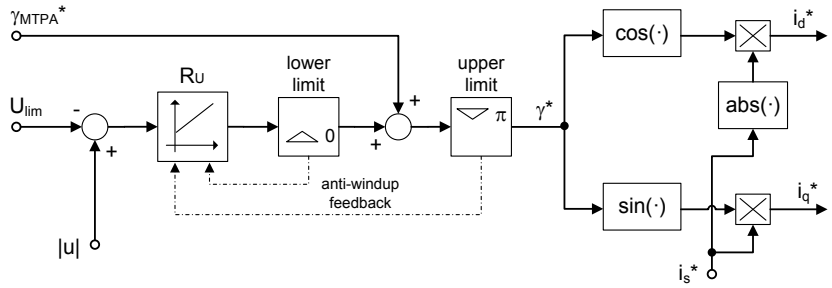

Fig. 5.16. Flux-weakening voltage amplitude control.

This solution can be analytically proved to provide important advantages with respect to classical approaches based on the variation of the direct current component, [48]. The voltage control loop adopted in the flux-weakening operating region can be represented by means of a non-linear block diagram, as shown in Fig. 5.15. A first order approximation of control delays taking into account the discrete time implementation and pulse-width-modulation have been considered both in the forward loop and in the feedback loop. Electrical angular speed Ω_{me} is considered at steady-state condition, as the dynamical behavior of the electrical quantities is analyzed. Voltage regulator $R_u(s)$, current regulators $R_{i_d}(s)$ and $R_{i_q}(s)$, control delays $CD(s)$ and motor model $\boldsymbol{M}_{\Omega_{me}}(s)$ (matrix) transfer functions are shown in the diagram. Λ_{mg} is the permanent magnet flux-linkage, R_s, L_d and L_q are phase resistance and synchronous inductances respectively. The equivalent analytical model is highly non-linear due to the presence of angular speed dependent terms (i.e. back-electromotive force) as well as non-linear terms (both transcendent and modulus functions).

Current space vector angle γ is saturated to stay in the range $[\gamma_{MTPA}, \pi]$, where γ_{MTPA} is the value assuring (until possible) MTPA control. Anti-windup action ensures a smooth transition from MTPA to flux-weakening operations. Bottom limitation imposed to the MTPA angle automatically activates flux-weakening only when needed (i.e. when the voltage limit is exceeded). A trade-off between the need for preserving a voltage margin with respect to the inverter limitation (i.e. avoiding saturation) for current control stability by one side and exploiting full power capabilities by the other thus exists also with the considered scheme.

5.4.3 Steady-state (static) small-signal analysis

Static gain of the transfer function linking the variation of the stator voltage amplitude as a consequence of the variation of the current space vector angle will be calculated for different values of the steady-state condition of speed (i.e. current space vector angle). Based on the obtained results, the sensitivity analysis of different flux-weakening voltage-control schemes (i.e. adopting either i_d, i_q or Γ as

control output) is studied. Control of current angle space vector is proved to be the best approach (i.e. the gain variance over the flux-weakening region is the smallest one), when deep field-weakening operating conditions are considered. Moreover a novel proposal aiming at maintaining constant loop gain at different speed by proper gain scheduling is sketched, whose beneficial effects are proved in the simulation and experimental results.

At speed and torque steady-state operating conditions and with constant amplitude of the current space vector, a unique mapping exists between rotor speed and current space vector angle. This is commonly shown in graphical format in the $i_d i_q$ plane by the intersection between the constant amplitude current circle and constant voltage ellipse at a given (constant) speed, as already shown in Fig. 5.14.

From an analytical point of view equation (5.9) can be obtained,

$$\begin{aligned}\Omega_{me} = -2I_s R_s\left[\Lambda_{mg} + I_s\left(L_d - L_q\right)\cos\Gamma\right]\sin\Gamma \\ + + \left(\frac{I_s^2 R_s^2\left[\Lambda_{mg} + I_s\left(L_d - L_q\right)\cos\Gamma\right]^2 \sin^2\Gamma}{\left(\Lambda_{mg} + I_s L_d \cos\Gamma\right)^2 + I_s^2 L_q^2 \sin^2\Gamma} \right. \\ \left. - \frac{\left(I_s^2 R_s^2 - U_{lim}^2\right)\left[\left(\Lambda_{mg} + I_s L_d \cos\Gamma\right)^2 + \frac{I_s^2 L_q \sin\Gamma}{4}\right]}{\left(\Lambda_{mg} + I_s L_d \cos\Gamma\right)^2 + I_s^2 L_q^2 \sin^2\Gamma} \right)^{\frac{1}{2}}\end{aligned} \tag{5.9}$$

providing speed as a function of the stator current space vector (both amplitude I_s and angle Γ) and voltage space vector upper limit U_{lim}. Cross coupling terms, current reference generation and voltage modulus calculation (i.e. square and square root) are taken into account. Motor speed is slowly changing as compared to the electrical variables and its value can therefore be approximated to be constant inside the cross coupling terms. Similar considerations allow to consider the amplitude of the current reference space vector constant within the field-weakening region as speed control loop has narrower bandwidth (especially above base speed, where maximum achievable torque is strongly below nominal value). Moreover, during speed transients, the commanded torque is often

saturated, thus providing a current reference module at its nominal value for relatively long time.

A small variation $\hat{\Gamma}$ of the current space vector angle in the neighborhood of the steady-state operating point $\bar{\Gamma}$ (i.e. a certain steady-state value of angular speed $\bar{\Omega}_{me}$) is considered. This variation will move motor currents and voltage around their respective steady-state values.

In particular the voltage vector module can be represented with a constant component and a small variation, i.e.:

$$|U| = \sqrt{\left(\bar{U}_d + \hat{U}_d\right)^2 + \left(\bar{U}_q + \hat{U}_q\right)^2} \triangleq \overline{|U|} + \widehat{|U|} \tag{5.10}$$

where the former is the limitation value imposed by the steady-state output of the voltage controller, i.e. $\overline{|U|} = U_{lim}$.

Linear approximation for the small-signal terms leads to:

$$\widehat{|U|} \cong \left.\frac{\partial(|U|)}{\partial \Gamma}\right|_{\Gamma=\bar{\Gamma}} \cdot \hat{\Gamma} \tag{5.11}$$

Derivative is calculated at the operating point, where:

$$\left.\frac{\partial(|U|)}{\partial \Gamma}\right|_{\Gamma=\bar{\Gamma}} = \frac{1}{2|U|}\left.\frac{\partial(|U|^2)}{\partial \Gamma}\right|_{\Gamma=\bar{\Gamma}} = \frac{1}{2U_{lim}}\left.\frac{\partial\left(U_d^2 + U_q^2\right)}{\partial \Gamma}\right|_{\Gamma=\bar{\Gamma}} \tag{5.12}$$

Substitution of steady-state voltage expressions obtained from motor model, static gain can easily be calculated, i.e.:

$$\begin{aligned}\left.\frac{\partial(|U|)}{\partial \Gamma}\right|_{\Gamma=\bar{\Gamma}} = \frac{1}{2U_{lim}}\big[&2\left(\Lambda_{mg}\bar{\Omega}_{me} + I_s L_d \bar{\Omega}_{me}\cos\bar{\Gamma} + I_s R_s \sin\bar{\Gamma}\right) \\ &\cdot \left(I_s R_s \cos\bar{\Gamma} - I_s R_s L_d \bar{\Omega}_{me}\sin\bar{\Gamma}\right) \\ &+ 2\left(-I_s L_q \bar{\Omega}_{me}\cos\bar{\Gamma} - I_s R_s \sin\bar{\Gamma}\right) \\ &\cdot \left(I_s R_s \cos\bar{\Gamma} - I_s L_q \bar{\Omega}_{me}\sin\bar{\Gamma}\right)\big]\end{aligned} \tag{5.13}$$

Analysis of (5.13) for each steady-state value of angular speed (i.e. each value of $\bar{\Gamma}$) provides sensitivity of the voltage control loop to a (small) variation of the current space vector angle.

Similar relations can be obtained if the output of the voltage regulator is in turn considered to be the direct or quadrature component of stator current reference, since simple variable substitution can be applied:

$$\left.\frac{\partial(|U|)}{\partial I_d}\right|_{\Gamma=\bar{\Gamma}} = -\left.\frac{\partial(|U|)}{\partial \Gamma}\right|_{\Gamma=\bar{\Gamma}} \cdot \frac{1}{I_s \sin \bar{\Gamma}} \tag{5.1}$$

$$\left.\frac{\partial(|U|)}{\partial I_q}\right|_{\Gamma=\bar{\Gamma}} = \left.\frac{\partial(|U|)}{\partial \Gamma}\right|_{\Gamma=\bar{\Gamma}} \cdot \frac{1}{I_s \cos \bar{\Gamma}} \tag{5.2}$$

Plots of different sensitivity functions normalized against their maximum values in the considered range are shown in Fig. 5.17. The situation is very different among the three control choices, i.e. heavy gain variation occurs in the deep flux-weakening region. This is especially true when using a scheme in which d-axis current is the voltage regulator output. This was expected since circular current trajectory (constant amplitude) has a high slope, for angle values near to π. The results of this analysis are true for the actual motor considered in this work (i.e. having a high reluctance torque component). Adopting the current space vector angle γ or the q-axis current as the control output, results in similar variations of the static gain. Even in these cases, however, the voltage control loop static gain exhibit large variations over the whole speed operating range, thus suggesting an adaptive voltage controller in order to provide a globally optimized bandwidth. The dynamical analysis of the voltage control loop will first be carried out in the next section in order to confirm that statement and suggest possible solutions.

Finally, if (5.13) is re-arranged as a function of both direct and quadrature currents (i.e. with variable $\mathrm{I_s}$ and $\bar{\Gamma}$), the behaviour of the static gain in the whole dq plane is obtained, as shown in Fig. 5.18. The rated current limit locus (blue circular trace) and the MTPA trajectory (red trace) are also shown for completeness. One can notice that the static gain is also a function of the current space vector amplitude and the maximum-to-minimum ratio at about a half of the rated current is even higher than at rated current. This proves that gain adaptation of the voltage controller is needed even in the case a lower limitation on the current value is adopted.

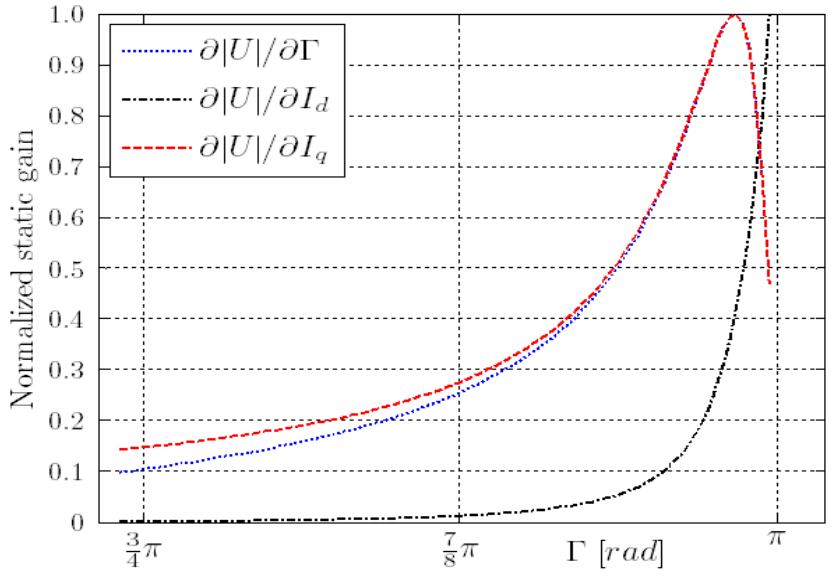

Fig. 5.17. Normalized static gains (gain values to their maximum ratio) at rated amplitude of the current space vector.

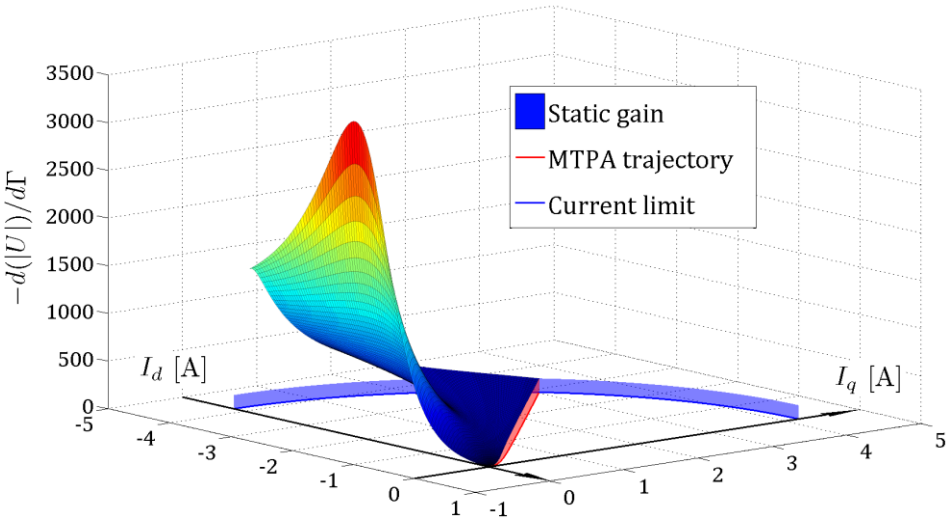

Fig. 5.18. Static gain as a function of direct and quadrature current.

5.4.4 Dynamical analysis and gain scheduling

The voltage control loop adopted in the flux-weakening operating region can be represented by means of the block diagram shown in Fig. 5.19. A first order approximation of control delays taking into account the discrete time implementation and pulse-width-modulation have been considered both in the forward loop and in the feedback loop. The dynamical behavior of the electrical quantities is analyzed, while the mechanical system dynamics is considered to be much slower than the electrical one, thus the electrical angular speed $\boldsymbol{\Omega_{me}}$ is considered as a constant (steady-state condition). Voltage regulator $\boldsymbol{R_u(s)}$, current regulators $\boldsymbol{R_{i_d}(s)}$ and $\boldsymbol{R_{i_q}(s)}$, control delays $\boldsymbol{CD(s)}$ and motor model $\boldsymbol{M_{\Omega_{me}}(s)}$ (matrix) transfer functions are shown in the diagram. $\boldsymbol{\Lambda_{mg}}$ is the permanent magnet flux-linkage, $\boldsymbol{R_s}$, $\boldsymbol{L_d}$ and $\boldsymbol{L_q}$ are phase resistance and synchronous inductances respectively. The equivalent model is highly non-linear due to the presence of angular speed dependent terms (i.e. back-electromotive force) as well as non-linear terms (both transcendent and modulus functions). Linearization of the voltage control loop in the neighborhood of a certain operating condition allows to study the dynamical behavior in the Laplace domain as a function of frequency by means of the open-loop transfer function, comprising the motor model, currents regulation loop, control and inverter delays, voltage modulus (feedback) calculation, voltage command magnitude regulation and reference current generation.

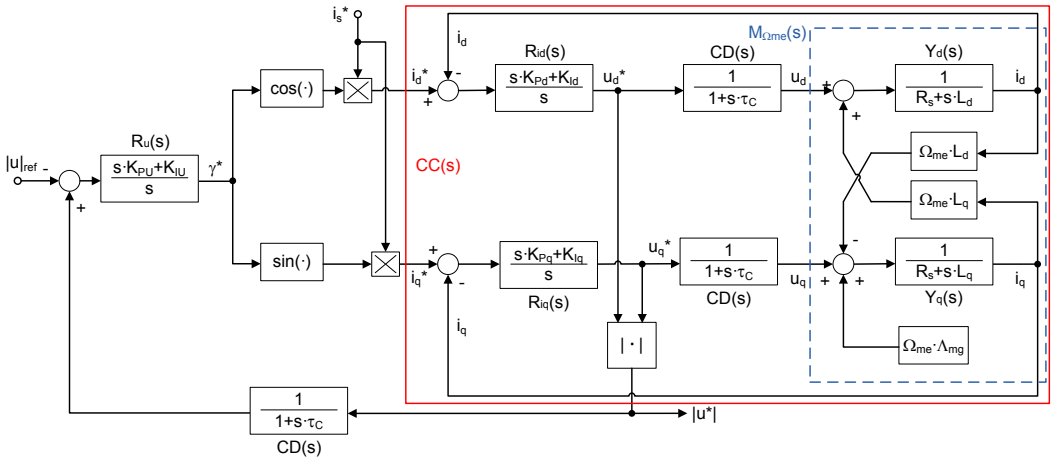

Fig. 5.19. Voltage vector amplitude control loop model.

If the motor electrical model (in the dq reference frame) at constant speed Ω_{me} is considered for small-signal analysis, a linear MIMO (multiple input multiple output, i.e. two-input two-output) dynamical system is obtained, with voltages as inputs and currents as outputs. In this way, motor model can be seen as a $2x2$ Laplace transfer function matrix $\boldsymbol{M}_{\Omega_{me}}(s)$:

$$\begin{bmatrix} i_d(s) \\ i_q(s) \end{bmatrix} = \underbrace{\begin{bmatrix} \left.\frac{i_d(s)}{u_d(s)}\right|_{u_{q\,(s)}=0} & \left.\frac{i_d(s)}{u_q(s)}\right|_{u_{d\,(s)}=0} \\ \left.\frac{i_q(s)}{u_d(s)}\right|_{u_{q\,(s)}=0} & \left.\frac{i_q(s)}{u_q(s)}\right|_{u_{d\,(s)}=0} \end{bmatrix}}_{\boldsymbol{M}_{\Omega_{me}}(s)} \begin{bmatrix} u_d(s) \\ u_q(s) \end{bmatrix} \tag{5.14}$$

$$\begin{aligned} \left.\frac{i_d(s)}{u_d(s)}\right|_{u_{q\,(s)}=0} &= \frac{Y_d}{1 + Y_d Y_q (L_d \Omega_{me})(L_q \Omega_{me})} \\ \left.\frac{i_d(s)}{u_q(s)}\right|_{u_{d\,(s)}=0} &= \frac{Y_d Y_q (L_q \Omega_{me})}{1 + Y_d Y_q (L_d \Omega_{me})(L_q \Omega_{me})} \\ \left.\frac{i_d(s)}{u_q(s)}\right|_{u_{d\,(s)}=0} &= \frac{-Y_d Y_q (L_q \Omega_{me})}{1 + Y_d Y_q (L_d \Omega_{me})(L_q \Omega_{me})} \\ \left.\frac{i_d(s)}{u_d(s)}\right|_{u_{q\,(s)}=0} &= \frac{Y_q}{1 + Y_d Y_q (L_d \Omega_{me})(L_q \Omega_{me})} \end{aligned} \tag{5.15}$$

$Y_d(s), Y_q(s)$ are the phase admittances, i.e.:

$$Y_d \triangleq \frac{1}{R_s + sL_d}, Y_q \triangleq \frac{1}{R_s + sL_q} \tag{5.16}$$

Commanded voltage vector can be expressed as:

$$\begin{bmatrix} u_d^*(s) \\ u_q^*(s) \end{bmatrix} = \underbrace{\begin{bmatrix} R_{i_d}(s) & 0 \\ 0 & R_{i_q}(s) \end{bmatrix}}_{\boldsymbol{R}_{i_{dq}}(s)} \begin{bmatrix} i_d^*(s) - i_d(s) \\ i_q^*(s) - i_q(s) \end{bmatrix} \tag{5.17}$$

where $R_{i_d}(s)$ and $R_{i_q}(s)$ are the current regulators transfer functions. Motor actual voltage is a delayed version of commanded voltage, as PWM cycle and calculation delay of the digital control subsystem are taken into account, i.e.:

$$\begin{bmatrix} u_d(s) \\ u_q(s) \end{bmatrix} = CD(s) \begin{bmatrix} u_d^*(s) \\ u_q^*(s) \end{bmatrix} \cong \frac{1}{1 + s\tau_C} \begin{bmatrix} u_d^*(s) \\ u_q^*(s) \end{bmatrix} \tag{5.18}$$

The first order Padé approximation of the time delay is considered, with time constant $\tau_C = 3/2 \cdot T_C$, [90]. Substitution of (5.17) into (5.18) and then into (5.14), yields the current closed-loop transfer function $\boldsymbol{CC}(s)$ (actual to reference), i.e.:

$$\begin{aligned} \begin{bmatrix} i_d(s) \\ i_q(s) \end{bmatrix} &\triangleq \boldsymbol{CC}(s) \begin{bmatrix} i_d^*(s) \\ i_q^*(s) \end{bmatrix} \\ &\triangleq \left[\boldsymbol{I}_{2\times2} + \boldsymbol{M}_{\Omega_{me}}(s) CD(s) \boldsymbol{R}_{i_{dq}}(s) \right]^{-1} \\ &\cdot \boldsymbol{M}_{\Omega_{me}}(s) CD(s) \boldsymbol{R}_{i_{dq}}(s) \begin{bmatrix} i_d^*(s) \\ i_q^*(s) \end{bmatrix} \end{aligned} \tag{5.19}$$

where $\mathbf{I}_{2\times2}$ is the 2^{nd} order identity matrix.

Equation (5.17) can therefore be re-arranged as:

$$\begin{bmatrix} u_d^*(s) \\ u_q^*(s) \end{bmatrix} = \boldsymbol{R}_{i_{dq}}(s) [\boldsymbol{I}_{2\times2} - \boldsymbol{CC}(s)] \begin{bmatrix} i_d^*(s) \\ i_q^*(s) \end{bmatrix} \tag{5.20}$$

Reference currents can be expressed as a function of reference current space vector angle γ^* through an approximated linear model starting from non-linear sine and cosine functions shown in Fig. 5.19, i.e.:

$$\begin{bmatrix} i_d^*(s) \\ i_q^*(s) \end{bmatrix} \cong \begin{bmatrix} -\bar{I}_s \sin \bar{\Gamma} \\ \bar{I}_s \cos \bar{\Gamma} \end{bmatrix} \gamma^*(s) \tag{5.21}$$

Upper-case over-lined symbols represent the operating point values. Modulus of the voltage space vector can be computed by a linear approximation through partial derivatives, i.e.:

$$|u^*|(s) \cong \frac{\bar{U}_d}{U_{lim}} u_d^*(s) + \frac{\bar{U}_q}{U_{lim}} u_q^*(s) = \begin{bmatrix} \frac{\bar{U}_d}{U_{lim}} & \frac{\bar{U}_q}{U_{lim}} \end{bmatrix} \begin{bmatrix} u_d^*(s) \\ u_q^*(s) \end{bmatrix} \tag{5.22}$$

Substitution of (5.20) into (5.22) and considering (5.21) allows to obtain a comprehensive transfer function linking reference current vector angle γ^* to voltage amplitude $|u^*|$, i.e.:

$$\frac{|u^*|(s)}{\gamma^*(s)} = \begin{bmatrix} \frac{\bar{U}_d}{U_{lim}} & \frac{\bar{U}_q}{U_{lim}} \end{bmatrix} \left(\boldsymbol{R}_{i_{dq}}(s) [\boldsymbol{I}_{2\times2} - \boldsymbol{CC}(s)] \begin{bmatrix} -\bar{I}_s \sin \bar{\Gamma} \\ \bar{I}_s \cos \bar{\Gamma} \end{bmatrix} \right) \tag{5.23}$$

Finally, referring to the block diagram of Fig. 5.19, a set of open-loop transfer functions parameterized by angular speed value can be calculated by including the voltage regulator $R_u(s)$ and the control delay model of the feed-back loop, as shown in Fig. 5.21 (top). Control bandwidth, stability range and margins can easily be calculated for each operating condition.

5.4.5 Implementation issues in gain scheduling

Analysis of the open-loop gain curves shows that heavy variation of static gain occurs (about 20dB in this case). A simple approach to guarantee a proper stability margin for each operating condition is to dynamically vary the static gain of the voltage controller compensating for the plant variations. An adaptive voltage controller is considered, as it will be shown hereafter. Accurate design of the closed-loop response bandwidth is therefore possible, approximately maintained for the whole needed speed range, as shown in Fig. 5.21 (bottom).

An adaptation of the voltage controller's static gain can be done in different ways, e.g. gain scheduling or analytically, referring to the previously performed static analysis. Analytical adaptation can be obtained by considering (5.13) or a simplified version resulting from some substitutions, as it will be shown later. However both the approaches have been implemented and tested in simulation and experimentally.

The nominal gains for the regulator are chosen achieving the desired response and stability margin at a certain operating point. The most obvious choice is preserving a minimum stability margin (i.e. maximizing the gains) at the most critical conditions, i.e. at the maximum operating speed and maximum current magnitude. This can be achieved analytically, based upon the previously depicted dynamics model, or by empirical tuning on the real system.

The gain adaptation is then implemented as a multiplicative factor K_{adapt} applied to both integral and proportional values of the voltage regulator. The scaling value is obtained by dividing the static gain at the nominal condition (i.e. the one calculated off-line at the tuning point) by the calculated value of the static gain updated for the actual operating condition:

$$K_{adapt} = \frac{\left.\frac{\partial(|U|)}{\partial \Gamma}\right|_{\Gamma=\bar{\Gamma}_{nom}}}{\frac{\partial(|U|)}{\partial \Gamma}(t)} \tag{5.24}$$

Gain analysis above developed leads to a long and non-trivial expressions, also involving trigonometric calculations. However, further manipulation on the static gain equation (5.13) can significantly simplify the gain adaptation procedure, by introducing electrical quantities which are already known from the current control loop (synchronous voltages and currents).

In fact, from (5.12), the derivative is the sum of two terms

$$\left.\frac{\partial(|U|)}{\partial \Gamma}\right|_{\Gamma=\bar{\Gamma}} = \frac{1}{2U_{lim}}\left(\left.\frac{\partial(U_d^2)}{\partial \Gamma}\right|_{\Gamma=\bar{\Gamma}} + \left.\frac{\partial\left(U_q^2\right)}{\partial \Gamma}\right|_{\Gamma=\bar{\Gamma}}\right) \tag{5.25}$$

which can be further expressed as

$$\left.\frac{\partial(|U|)}{\partial \Gamma}\right|_{\Gamma=\bar{\Gamma}} = \frac{1}{2U_{lim}}\left(2U_d\left.\frac{\partial(U_d)}{\partial \Gamma}\right|_{\Gamma=\bar{\Gamma}} + 2U_q\left.\frac{\partial\left(U_q\right)}{\partial \Gamma}\right|_{\Gamma=\bar{\Gamma}}\right) \tag{5.26}$$

By considering the expressions for the steady-state voltage

$$\begin{aligned} U_d &= R_s I_d - \Omega_{me} L_q I_q \\ U_q &= R_s I_q + \Omega_{me} L_d I_d + \Omega_{me} \Lambda_{mg} \end{aligned} \tag{5.27}$$

the last equation can be expanded in

$$\begin{aligned} \left.\frac{\partial(|U|)}{\partial \Gamma}\right|_{\Gamma=\bar{\Gamma}} = \frac{1}{2U_{lim}}\big[&2\bar{U}_d\left(-R_s\bar{I}_s \sin\bar{\Gamma} - L_q\bar{\Omega}_{me}\bar{I}_s \cos\bar{\Gamma}\right) \\ &+ 2\bar{U}_q(R_s\bar{I}_s \cos\bar{\Gamma} - L_d\bar{\Omega}_{me}\bar{I}_s \sin\bar{\Gamma})\big] \end{aligned} \tag{5.28}$$

leading to:

$$\left.\frac{\partial(|U|)}{\partial \Gamma}\right|_{\Gamma=\bar{\Gamma}} = \frac{1}{U_{lim}}\left[\bar{U}_d\left(-R_s\bar{I}_q - L_q\bar{\Omega}_{me}\bar{I}_d\right) + \bar{U}_q\left(R_s\bar{I}_d - L_d\bar{\Omega}_{me}\bar{I}_q\right)\right] \tag{5.29}$$

Indeed both steady-state and transient conditions are here approximated by a sequence of quasi-steady-state points. Calculation of the adaptation factor (5.24) by using (5.29) is done on-line (i.e. at each sampling period, see Fig. 5.20), requiring only small calculation efforts. In fact only few product/sum operations on

the values of current, speed and voltage are required, values already available to the vector controller.

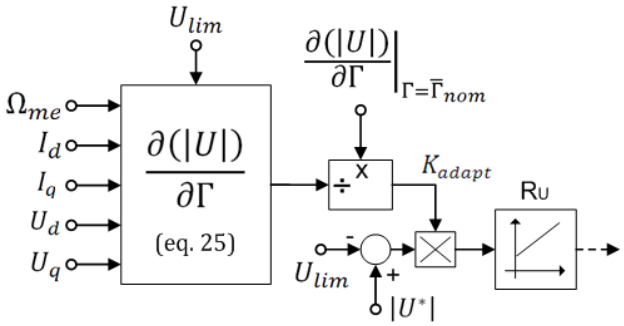

Fig. 5.20. Block diagram of the adaptation algorithm.

Since a voltage margin is needed during current transients following a torque request, the technique used for voltage vector saturation and current control during limitation conditions heavily affects the overall drive control stability and robustness, obviously reflecting into torque ripple and efficiency performances. In general, a trade-off between DC bus voltage exploitation and current ripple exists since operation at higher voltage amplitude (i.e. around or above U_N) causes transient voltage saturation.

In the case both speed and voltage are controlled by means of a closed-loop scheme, the steady-state operating point under field-weakening can be reached by proper regulation, without the need for calculation or use of tabled characteristics from measurements. This is true even in the presence of parametric errors and non-idealities (such as those due to magnetic saturation effects), because these will only affect regulation dynamics, causing usually acceptable variations.

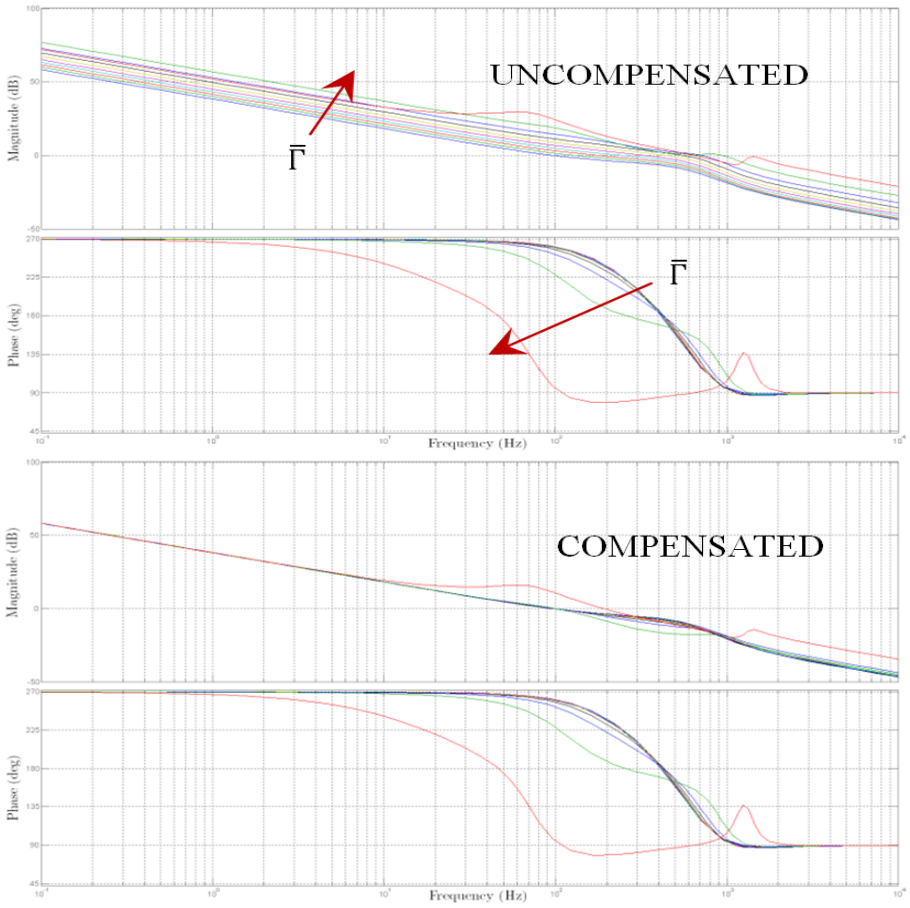

Fig. 5.21. Open-loop magnitude (top) and phase (bottom) responses at various speeds (i.e. current angle $\bar{\Gamma}$), $\bar{\Gamma} \in [\Gamma_{\mathrm{MTPA}}\,;\pi - 0.01]$, $\bar{I_s} = I_{sN}$.

5.4.6 Simulation results

Reliability of the proposed analysis has initially been verified by comparing the results of a complete electro-mechanical dynamical model simulation of the drive system, including sampled-time control and inverter delay, and the linearized continuous-time analytical model discussed in the previous sections.

A simple validation is obtained by comparing the small-signal response to a square-wave voltage reference $|u|^*$, as shown in Fig. 5.22, at two different rotor

speed conditions in the flux-weakening region, at rated current and with a certain design of the voltage loop controller. An optimal matching is obtained in both conditions but a nearly unstable behavior is present at very high speed, due to a reduced phase margin of the control loop, confirming the dynamical analysis of the previous section.

A comparison between fixed and gain scheduling voltage controllers (designed for the same maximum speed value of $22000\ [rpm]$) is shown in Fig. 5.23. A load torque step disturbance (low-pass filtered at $1\ kHz$) at steady-state and high-speed condition is applied and the response of the voltage control loop analyzed. The reference voltage has been chosen to be lower than the maximum allowable voltage of the inverter in order to study the behavior of the controller in non saturated conditions. As shown in the zoomed boxes the peak voltage reached during load torque removal is much lower when gain scheduling controller is considered, thus confirming the reliability of the proposed analysis and the effectiveness of the gain adaptation. Optimization of voltage control loop allows therefore to increase the voltage limiting value and to maximize bus voltage exploitation.

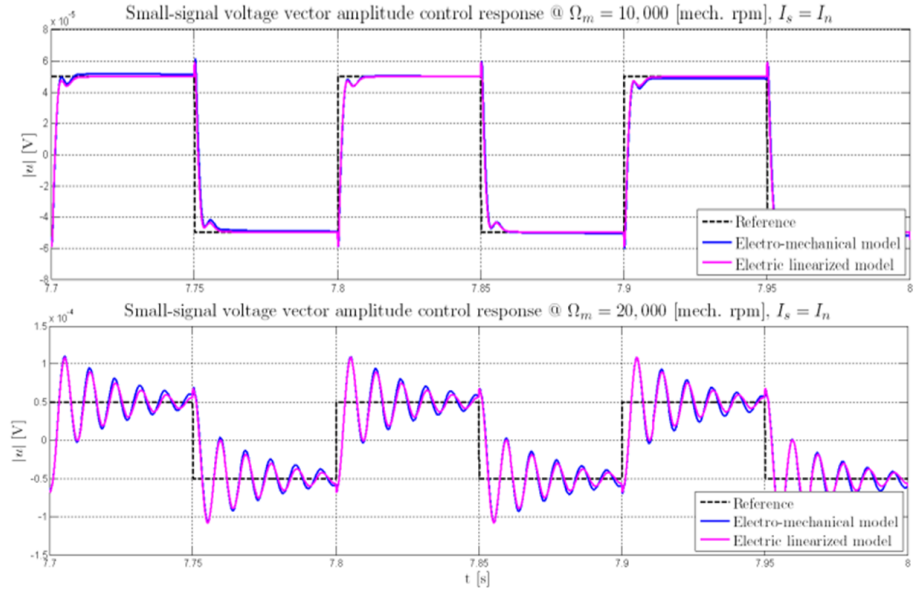

Fig. 5.22. Dynamic response to a square-wave voltage reference, under two different speed operating conditions (10,000 and 20,000 rpm).

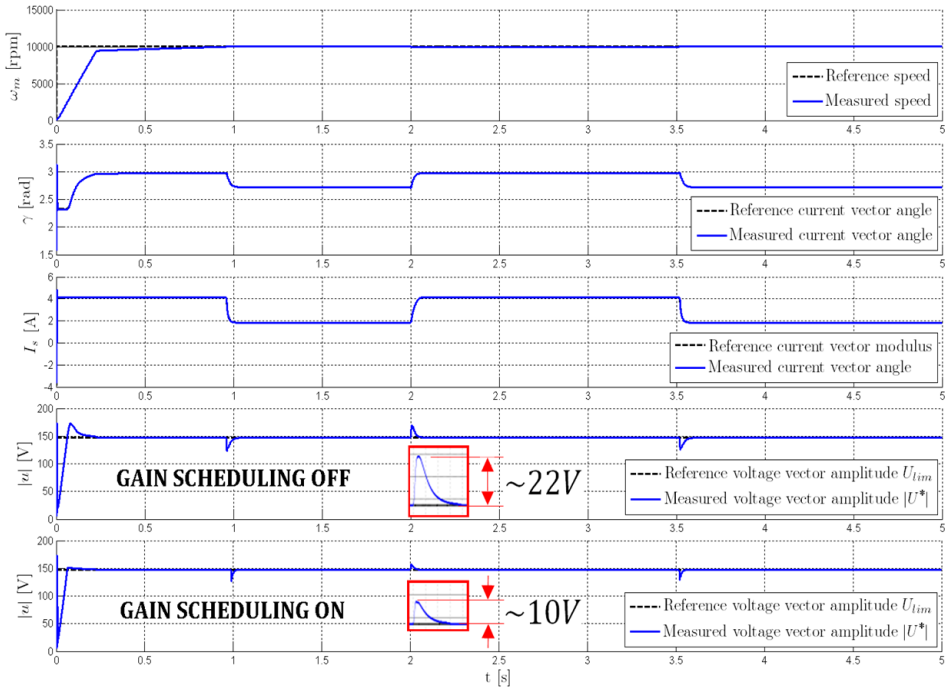

Fig. 5.23. Load torque disturbance rejection at $10000\,rpm$ (simulation).

5.4.7 Experimental results

The three VCC flux-weakening approaches discussed above have been verified by means of an experimental test bench equipped with an IPM motor for home appliances and a controlled induction motor acting as a load (see section A.3). Differently from the simulated model, in this case the voltage amplitude reference is calculated on-line as a function of the actual value of the dc bus voltage, ensuring that the PWM modulation always remains inside the linear range, with an utilization factor $\epsilon = 0.95$. Since some measurement noise and inverter non-idealities is present in the experimental system, proper filtering is applied to the measured dc bus voltage, considering that the dynamical performances of the voltage control is lower than those of the current control.

The results of the tests with the three flux-weakening approaches are very similar, even if some minor differences arise, mainly due to the different values of

the voltage controller gains. The results of the flux-weakening adopting a regulation through a multiplicative factor on the current phase angle are shown in Fig. 5.24. One can notice that a proper voltage and current control is obtained both in transient and during steady-state conditions. The reference voltage amplitude is slightly higher at the end of the speed transient as the DC bus voltage increases due to a reduction of the power drawn from the input rectifier. The reference torque is the value of the torque that the MTPA would provide in that condition and the "measured" torque is indeed an estimated value based on the motor parameters, as no torque sensor is available in the experimental setup. Since the current speed regulator provides a reference for the current vector magnitude instead of torque (to avoid the use of tabulated data), under flux-weakening an inconsistency arises between the commanded torque (calculated according to the MTPA curve) and the "measured" value, since the current vector is rotated out of the MTPA curve.

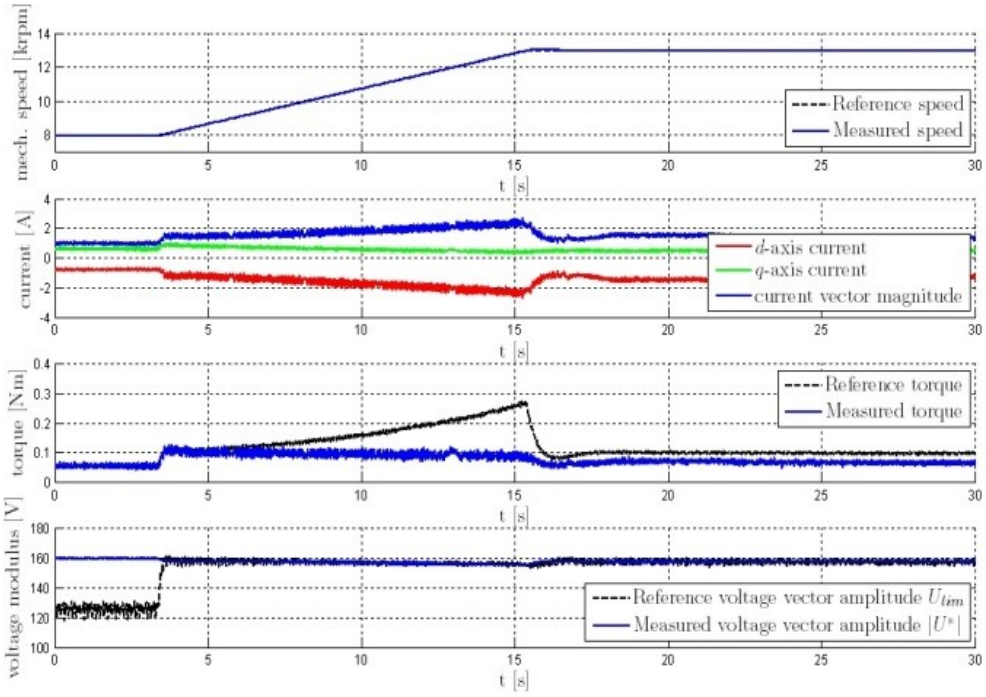

Fig. 5.24. Speed reference from **8000** to **13000** rpm (VCC, angle multiplicative factor flux-weakening control, experimental).

A prototype motor drive system for home appliances is considered as a test bench to prove the effectiveness of the proposal. The results shown hereafter are mainly intended to prove that optimal design of voltage command magnitude regulation loop is possible and provides better dynamical response for each speed operating condition, as demonstrated by the analytical developments of previous sections. In all the results on-line adaptation of voltage regulator's gains is implemented. Maximization of the bandwidth of the voltage command regulation loop is therefore obtained in the whole flux-weakening range and a lower voltage (control) margin could be considered, especially at very high speed.

In the result of Fig. 5.25 a similar test to those of Fig. 5.23 is considered, showing that a good agreement is obtained between theoretical analysis, simulations and experiments. As in the results of Fig. 5.23 the reference voltage has been chosen to be lower than the maximum allowable voltage out of the inverter in order to study the behavior of the voltage controller in non-saturated conditions. It should be noted that the experimental set-up does not allow a step torque disturbance generation as in the simulation results, since an induction motor drive is adopted as load in this case.

The design and optimization of the voltage regulator's gains are done by considering the open-loop transfer function (magnitude and phase) at e.g., $10000\,rpm$. Gain scheduling is considered for the voltage regulator in these experiments.

Referring to Fig. 5.25, when a lower value of the speed is commanded, i.e. $5000\,rpm$, and voltage regulator's gain is kept constant, a relatively high value of actual voltage overshoot is obtained as response to a sudden variation of load torque. As a higher gain margin is available at lower speed, voltage regulator's gain can be adapted (increased) consequently. Then the response of voltage command regulation loop to the same load torque variation provides a lower dynamical error. Only one response for speed, current space vector phase and amplitude are shown in the figure as the difference between the two cases (i.e. with or without gain scheduling) is hardly appreciable. Different tests, conducted under similar conditions, with gain scheduling activated and with a higher value of the voltage regulator's gain (an increase of 50% is considered, i.e. $3\,dB$) leads to instability. This indirectly proves the consistency of the theoretical analysis, since it demonstrates that, following the adaptation law, the stability limit gains are independent on speed.

In the results of Fig. 5.26 and Fig. 5.27 similar load torque disturbance tests at $5000\,rpm$ are considered, respectively without and with gain adaptation. Adaptation law coming from (5.24) and (5.29) is implemented in these cases, instead of gain scheduling. Moreover the difference with respect to the results of Fig. 5.25 refer to the voltage limitation value, that is now very close to the actual inverter's limitation, i.e. the voltage regulator will operate in saturated conditions during transients.

The results show that the adaptation provides better overall results. Particularly one can notice that the speed undershoot is highly reduced and current control is maintained during the whole torque transient, definitively proving that higher voltage control bandwidth is attained with the proposed adaptive approach. This in turn means that a reduction of the voltage margin can be considered in the voltage control loop, thus providing higher torque for the same speed value.

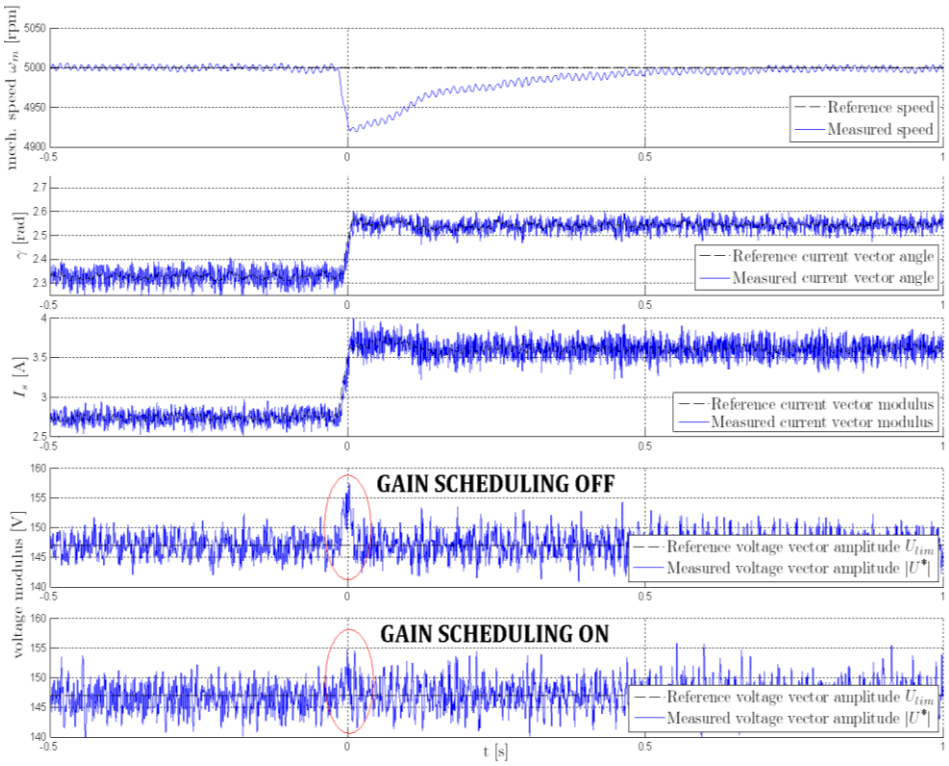

Fig. 5.25. Load torque disturbance rejection at $5000\,rpm$ (experimental, voltage regulator operates in linear conditions).

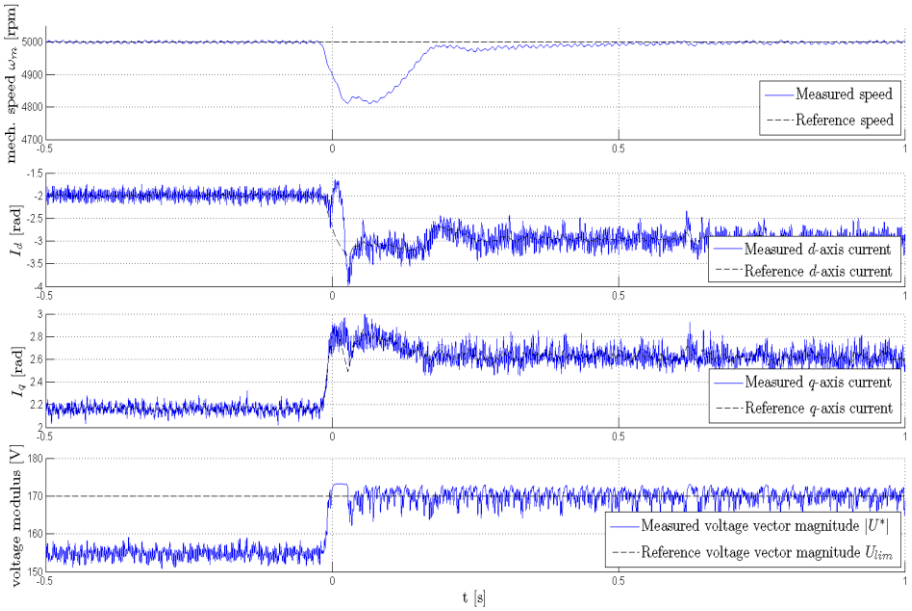

Fig. 5.26. Load torque disturbance rejection at $5000\,rpm$ (experimental, gain adaptation is off).

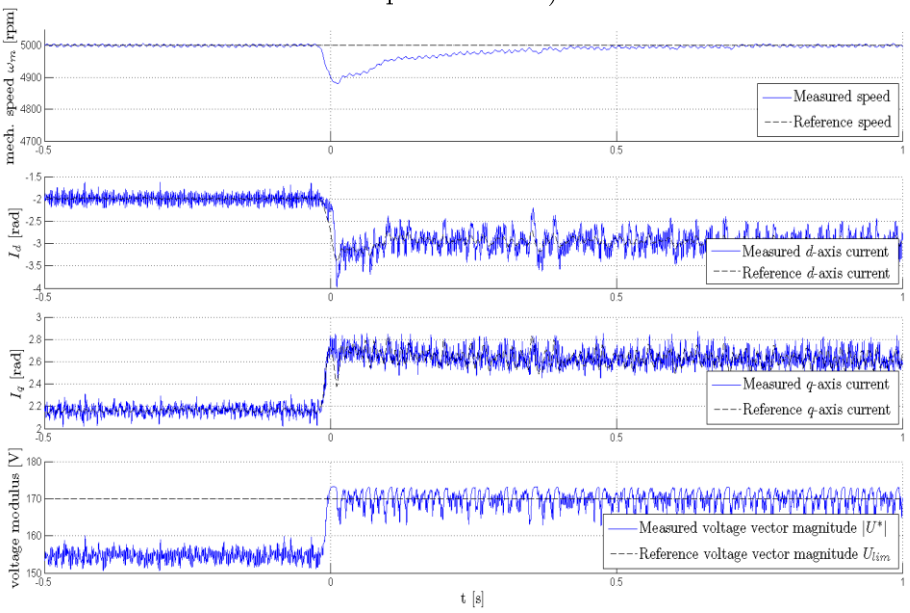

Fig. 5.27. Load torque disturbance rejection at $5000\,rpm$ (experimental, gain adaptation is on).

5.5 Conclusions

A selection of state-of-art feedback algorithms for deep flux-weakening control of IPMSM drives have been compared both analytically and by means of simulation, namely voltage magnitude control by means of direct (or quadrature) or phase angle of the current space vector (VCC), voltage magnitude control by means of commanded torque and flux (TFC) and single current regulator with voltage angle control (SCR+VAC).

These techniques offer a feasible implementation and the inherent characteristics of closed-loop control. In fact, good accuracy and robustness in voltage limiting and current control is achieved. However, they differ in many aspects related to dynamics, robustness to parameters and implementation

complexity. Below, Table 5.1 summarizes the results of analytical and simulative comparison between the three methods, according to the main aspects considered.

Table 5.1. Field-weakening methods comparison summary.

	VCC	**FTC**	**SCR+VAC**
Voltage exploitation	Good (overmodulation allowed)	Good (overmodulation allowed)	Excellent (constant voltage magnitude, overmodulation allowed)
Smoothness	Very Good	Good (issues in flux-weakening to MTPA transition)	Poor (oscillatory current transients)
Responsiveness	Good	Good	Poor (current is indirectly controlled)
Robustness	Very good (low sensitivity to gain parameters)	Good (sensitivity to parameters mitigated by feedback)	Poor (high sensitivity to gain parameters)
Implementation cost/complexity	Normal (std. FOC+voltage magnitude regulator)	Large LUTs (and heavy offline measurement work)	Normal
Analytical dynamics comprehension/design	Good (possibility to adapt gains optimally)	Limited	Poor (static analysis only)

Moreover, for the methods based on regulation on the synchronous current frame via the normal vector control, a novel theoretical static and dynamical investigation has been proposed in this chapter. The analytical results prove that voltage control loop dynamics can be analytically designed, which allows to

guarantee stability and to maximize exploitation of the inverter bus voltage. A simple approach for on-line gain adaptation has been presented, based either on gain scheduling or on real-time calculation of the adaptation gain as a function of the motor operating condition. The obtained experimental results based prototype motor drive for home appliances prove that a lower voltage (control) margin can adopted with the proposed approach with respect to standard solutions based on a fixed design of the flux-weakening controller, and to easily exploit the PWM over-modulation range, too. This leads to achieve a higher torque vs. speed curve with the most stable and fast response possible. On the other hand, at a first approximation, to achieve the same torque under constant apparent power, a lower current level is needed, possibly leading to higher system efficiency and/or a reduced value of the DC-bus capacitance (in the case of grid voltage rectifier fed inverters, which is very common, especially in home appliances).

Conclusions

New applications of Permanent Magnet Synchronous Motors (PMSMs), other than the typical high-accuracy and high dynamical performances servo drives, set different requirements in the control of the related electric drives, thus efficiency, cost and speed operating range become crucial parameters. In this perspective, research issues as avoiding the use of mechanical sensors ("sensorless" control), and ensuring the best exploitation of the supply voltage at high speeds ("flux-weakening" control) gain a relevant role. In this work, different aspects about these two topics have been investigated, starting from the study of state-of-the-art to the proposal of new techniques, implementations or analytical approaches.

Chapters 3 and 4 have described the activity in the sensorless field, dividing the two chapters according to the two main classes of techniques, i.e. model-based and injection-based methods. The development of a sensorless strategy for a general-purpose Surface Mount-PMSM industrial drive has been carried out, adopting a back-EMF observer in the stationary reference frame followed by PLL-based position and speed estimates extraction. The advantages in simplicity and easiness of modeling of this solution are exploited, obtaining a full analytical description of the dynamics involved. This has led to the hints necessary for the development of an automatic tuning procedure and of drive management and supervision techniques, also introducing alternative means for speed estimation checking. Finally, the introduction of a stabilizing direct-axis current component for the low-speed operation is addressed by means of a novel linearized model, characterizing the effects of this reactive current on the closed-loop speed control.

In the second chapter on sensorless control, some original contributions have been proposed, all related to techniques in which the injection of a test voltage or current test signal is adopted. For the demodulation of the high-frequency current signal related to sinusoidal injection for anisotropy tracking, a technique based on

DFT calculation has been proposed, which overcomes the issues related to the unknown phase lag between carrier and measured signal. A different kind of injection is instead considered in 0, where the PWM harmonic content is exploited as an injection signal. This introduces many issues, since the transitions related to PWM ripple happen during the single modulation period. Multiple current derivative measurements by means of Rogowsky coils are performed and processing of the acquired samples leads to an information on the rotor position. The analysis is validated by simulations and preliminary experimental implementation, however the technique requires more development in order to be applied to closed-loop control. Finally, in 4.4 a novel injection-based technique is illustrated, which does not rely on rotor anisotropy, only involving the torque generation characteristic of PMSM, thus being suitable to isotropic rotor motors. Although dynamical performances are not very high, both an online estimation technique for closed-loop control and an initial position detection method are experimentally demonstrated.

In the last chapter, a selection of state-of-art feedback algorithms for deep flux-weakening control of IPMSM drives have been compared both analytically and by means of simulation, highlighting the advantages of the techniques relying on the synchronous current frame. Moreover, for this class of methods, a novel theoretical static and dynamical investigation has been proposed in this chapter. The analytical results prove that voltage control loop dynamics can be analytically designed, which allows to guarantee stability and to maximize exploitation of the inverter bus voltage. A simple approach for on-line gain adaptation has been presented, based either on gain scheduling or on real-time calculation of the adaptation gain as a function of the motor operating condition. The obtained experimental results, obtained on a prototype motor drive for home appliances, prove that a lower voltage control margin can adopted with the proposed approach with respect to standard solutions based on a fixed design of voltage controller. This can lead to a higher torque vs. speed characteristic, or a higher system efficiency for a given torque. Moreover, the improved dynamic performances in the flux-weakening voltage limitation control allow improved performances to be obtained in the current and speed control of the machine.

Appendix A
Experimental setups

In this appendix the main technical data and pictures representing experimental setups referenced in the previous sections are shown. The first, comprising a SM-PMSM and general-purpose drive, has been used for the experimental tests relating the model-based and low-frequency injection (vibration based) estimation for sensorless control. On the second system, which consists of a custom drive board and IPMSM designed for an electric scooter powertrain, the DFT demodulation method has been tested for sensorless control based on high-frequency injection (anisotropy based). In the last case an IPMSM for home appliances was the machine on which the flux-weakening regulation and PWM injection estimation methods were tested, using a commercial drive as the power hardware and a dSPACE DS1104 system as the controller.

A.1 Model-based and LF-injection sensorless

Table A.1. Parameters of the SM-PMSM considered in simulations and experimental setup on the back-EMF and LF-injection based sensorless control (Chapter 3 and section 4.4).

Pole pairs, pp	4
Rated frequency, f_n	200 $[Hz]$
Stator resistance, R	1.095 $[\Omega]$
Synchronous inductance, L_s	0.008 $[H]$
PM flux linkage (amplitude), Λ_{mg}	0.204 $[Vs]$
Rated current, $\|i\|_{n,rms}$	5.8 $[Arms]$
Rated torque, T_n	10 $[Nm]$

Fig. A.1. Experimental setup for the SM-PMSM for the back-EMF and LF-injection based sensorless control (3.5, 3.6.2, 3.7.3 and 4.4.3).

A.2 DFT demodulation for HF-injection sensorless

Table A.2. Parameters of the IPM motor considered in simulations and experimental setup on the DFT demodulation for HF injection based sensorless (section 4.2).

Pole pairs, pp	2
Rated frequency, f_n	86.7 $[Hz]$
Stator resistance, R	0.026 $[\Omega]$
Direct inductance, L_d	0.4 $[\mathrm{m}H]$
Quadrature inductance, L_q	1.45 $[mH]$
PM flux linkage (amplitude), Λ_{mg}	0.022 $[Vs]$
Rated current, $\|i\|_{n,rms}$	63.64 $[Arms]$
Electromagnetic torque	17.5 $[Nm]$

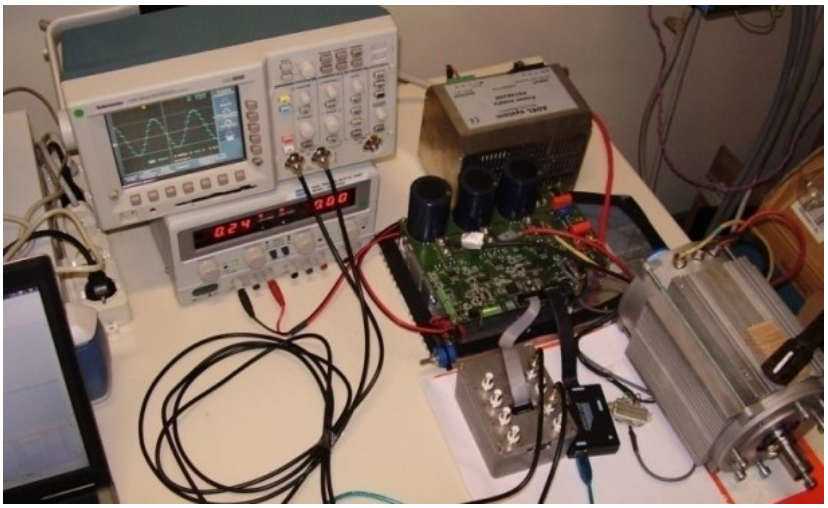

Fig. A.2. Experimental set-up for the DFT demodulation for the HF injection based sensorless technique (4.2.7).

A.3 Flux-weakening control and PWM excitation sensorless

Table A.3. Parameters of the IPM motor considered in simulations and experimental setup on the flux-weakening control and PWM excitation sensorless control (Chapter 5 and 0).

Pole pairs, pp	2
Stator resistance, R	2.86 [Ω]
Direct inductance, L_d	0.012 $[H]$
Quadrature inductance, L_q	0.087 $[H]$
PM flux linkage (amplitude), Λ_{mg}	0.028 $[Vs]$
Rated current, $\|i\|_{n,rms}$	3 $[Arms]$
Electromagnetic torque, $T_{e,}$@500rpm	1.3 $[Nm]$
Electromagnetic torque, $T_{e,}$@18000rpm	0.4 $[Nm]$

Fig. A.3. Experimental set-up for the the flux-weakening control and PWM excitation sensorless (5.4.7 and 4.3.5).

Bibliography

[1] DoE EERE, Advanced Manufacturing Office, "U.S. Department of Energy's Motor Challenge Program: A National Strategy for Energy Efficient Industrial Motor-Driven Systems." 2012.

[2] R. McElveen, K. Lyles, B. Martin, and W. Wasserman, "Reliability of Cooling Tower Drives: Improving Efficiency with New Motor Technology," *IEEE Industry Applications Magazine*, vol. 18, no. 6, pp. 12 –19, Dec. 2012.

[3] A. de Almeida, P. Fonseca, and F. Ferreira, "Improving the Penetration of Energy-Efficient Motors and Drives." University of Coimbra, prepared for the SAVE Programme, European Commission, DG - TREN, Brussels, 2000.

[4] W. C. Duesterhoeft, M. W. Schulz, and E. Clarke, "Determination of Instantaneous Currents and Voltages by Means of Alpha, Beta, and Zero Components," *American Institute of Electrical Engineers, Transactions of the*, vol. 70, no. 2, pp. 1248 –1255, Jul. 1951.

[5] R. H. Park, "Two-reaction theory of synchronous machines-II," *American Institute of Electrical Engineers, Transactions of the*, vol. 52, no. 2, pp. 352 – 354, Jun. 1933.

[6] M. Depenbrock, "Direct self-control (DSC) of inverter-fed induction machine," *IEEE Transactions on Power Electronics*, vol. 3, no. 4, pp. 420 –429, Oct. 1988.

[7] F. Blaschke and F. Blaschke, "Apparatus for Field-Oriented Control or Regulation of Asynchronous Machines," U.S. Patent 380513516-Apr-1974.

[8] A. R. Munoz and T. A. Lipo, "On-line dead-time compensation technique for open-loop PWM-VSI drives," *IEEE Transactions on Power Electronics*, vol. 14, no. 4, pp. 683 –689, Jul. 1999.

[9] S. Bolognani, M. Ceschia, P. Mattavelli, A. Paccagnella, and M. Zigliotto, "Improved FPGA-based dead time compensation for SVM inverters," in *Power Electronics, Machines and Drives, 2004. (PEMD 2004). Second International Conference on (Conf. Publ. No. 498)*, 2004, vol. 2, pp. 662 – 667 Vol.2.

[10] A. Cichowski and J. Nieznanski, "Self-tuning dead-time compensation method for voltage-source inverters," *IEEE Power Electronics Letters*, vol. 3, no. 2, pp. 72 – 75, Jun. 2005.

[11] S. Bolognani, R. Petrella, A. Prearo, and L. Sgarbossa, "Automatic Tracking of MTPA Trajectory in IPM Motor Drives Based on AC Current Injection," *IEEE Transactions on Industry Applications*, vol. 47, no. 1, pp. 105 –114, Feb. 2011.

[12] S. Bolognani, R. Petrella, A. Prearo, and L. Sgarbossa, "On-line tracking of the MTPA trajectory in IPM motors via active power measurement," in *2010 XIX International Conference on Electrical Machines (ICEM)*, 2010, pp. 1 –7.

[13] S. Kim, Y.-D. Yoon, S.-K. Sul, K. Ide, and K. Tomita, "Parameter independent maximum torque per ampere (MTPA) control of IPM machine based on signal injection," in *2010 Twenty-Fifth Annual IEEE Applied Power Electronics Conference and Exposition (APEC)*, 2010, pp. 103 –108.

[14] P. Guglielmi, M. Pastorelli, G. Pellegrino, and A. Vagati, "Position-sensorless control of permanent-magnet-assisted synchronous reluctance motor," *IEEE Transactions on Industry Applications*, vol. 40, no. 2, pp. 615 – 622, Apr. 2004.

[15] J. Holtz, "Speed estimation and sensorless control of AC drives," in , *International Conference on Industrial Electronics, Control, and Instrumentation, 1993. Proceedings of the IECON '93*, 1993, pp. 649 –654 vol.2.

[16] Y. Inoue, K. Yamada, S. Morimoto, and M. Sanada, "Accuracy Improvement of IPMSM Sensorless Drives with On-line Parameter Identification," in *Power Conversion Conference - Nagoya, 2007. PCC '07*, 2007, pp. 860 –866.

[17] D. Raca, M. C. Harke, and R. D. Lorenz, "Robust Magnet Polarity Estimation for Initialization of PM Synchronous Machines with Near Zero Saliency," in *Conference Record of the 2006 IEEE Industry Applications Conference, 2006. 41st IAS Annual Meeting*, 2006, vol. 1, pp. 481 –487.

[18] F. Parasiliti, R. Petrella, and M. Tursini, "Initial rotor position estimation method for PM motors," in *Conference Record of the 2000 IEEE Industry Applications Conference, 2000*, 2000, vol. 2, pp. 1190 –1197 vol.2.

[19] M. Tursini, R. Petrella, and A. Scafati, "Speed and Position Estimation for PM Synchronous Motor using self-compensated Back-EMF Observers," in *IECON 2006 - 32nd Annual Conference on IEEE Industrial Electronics*, 2006, pp. 5087 –5092.

[20] H. Rasmussen, P. Vadstrup, and H. Borsting, "Sensorless field oriented control of a PM motor including zero speed," in *Electric Machines and Drives Conference, 2003. IEMDC'03. IEEE International*, 2003, vol. 2, pp. 1224 – 1228 vol.2.

[21] S. Bolognani, S. Calligaro, and R. Petrella, "Design issues and estimation errors analysis of back-EMF based position and speed observer for SPM synchronous motors," in *2011 Symposium on Sensorless Control for Electrical Drives (SLED)*, 2011, pp. 138 –145.

[22] Z. Zheng, Y. Li, and M. Fadel, "Sensorless control of PMSM based on extended kalman filter," in *2007 European Conference on Power Electronics and Applications*, 2007, pp. 1 –8.

[23] M. Jansson, L. Harnefors, O. Wallmark, and M. Leksell, "Synchronization at startup and stable rotation reversal of sensorless nonsalient PMSM drives," *IEEE Transactions on Industrial Electronics*, vol. 53, no. 2, pp. 379 – 387, Apr. 2006.

[24] M. Tursini, R. Petrella, and A. Scafati, "Speed and position estimation for PM synchronous motor with back-EMF observer," in *Industry Applications Conference, 2005. Fourtieth IAS Annual Meeting. Conference Record of the 2005*, 2005, vol. 3, pp. 2083 – 2090 Vol. 3.

[25] S. Chi, Z. Zhang, and L. Xu, "Sliding-Mode Sensorless Control of Direct-Drive PM Synchronous Motors for Washing Machine Applications," *IEEE Transactions on Industry Applications*, vol. 45, no. 2, pp. 582 –590, Apr. 2009.

[26] F. Parasiliti, R. Petrella, and M. Tursini, "Sensorless speed control of a PM synchronous motor by sliding mode observer," in *, Proceedings of the lEEE International Symposium on Industrial Electronics, 1997. ISIE '97*, 1997, pp. 1106 –1111 vol.3.

[27] J. Lee, J. Hong, K. Nam, R. Ortega, L. Praly, and A. Astolfi, "Sensorless Control of Surface-Mount Permanent-Magnet Synchronous Motors Based on a Nonlinear Observer," *IEEE Transactions on Power Electronics*, vol. 25, no. 2, pp. 290 –297, Feb. 2010.

[28] D. Janiszewski, "Extended Kalman Filter Based Speed Sensorless PMSM Control with Load Reconstruction," in *IECON 2006 - 32nd Annual Conference on IEEE Industrial Electronics*, 2006, pp. 1465 –1468.

[29] R. P. Burgos, P. Kshirsagar, A. Lidozzi, J. Jang, F. Wang, D. Boroyevich, P. Rodriguez, and S.-K. Sul, "Design and Evaluation of a PLL-Based Position

Controller for Sensorless Vector Control of Permanent-Magnet Synchronous Machines," in *IECON 2006 - 32nd Annual Conference on IEEE Industrial Electronics*, 2006, pp. 5081 –5086.

[30] S. Calligaro and R. Petrella, "Accuracy and robustness improvement in sensorless PMSM drives at low-speed by direct-axis current injection," in *2012 Symposium on Sensorless Control for Electrical Drives (SLED)*, 2012, pp. 138 –145.

[31] R. Petrella, A. Revelant, and P. Stocco, "Robust grid synchronisation in three-phase distributed power generation systems by synchronous reference frame pre-filtering," in *Universities Power Engineering Conference (UPEC), 2009 Proceedings of the 44th International*, 2009, pp. 1 –5.

[32] J. Holtz and J. Quan, "Sensorless vector control of induction motors at very low speed using a nonlinear inverter model and parameter identification," *IEEE Transactions on Industry Applications*, vol. 38, no. 4, pp. 1087 – 1095, Aug. 2002.

[33] I. R. Bojoi, E. Armando, G. Pellegrino, and S. G. Rosu, "Self-commissioning of inverter nonlinear effects in AC drives," in *Energy Conference and Exhibition (ENERGYCON), 2012 IEEE International*, 2012, pp. 213 –218.

[34] P. Kshirsagar, R. P. Burgos, A. Lidozzi, J. Jang, F. Wang, D. Boroyevich, and S.-K. Sul, "Implementation and Sensorless Vector-Control Design and Tuning Strategy for SMPM Machines in Fan-Type Applications," in *Conference Record of the 2006 IEEE Industry Applications Conference, 2006. 41st IAS Annual Meeting*, 2006, vol. 4, pp. 2062 –2069.

[35] S. Bolognani, S. Calligaro, R. Petrella, and M. Tursini, "Sensorless Control of IPM Motors in the Low-Speed Range and at Standstill by HF Injection and DFT Processing," *IEEE Transactions on Industry Applications*, vol. 47, no. 1, pp. 96 –104, Feb. 2011.

[36] S. Bolognani, S. Calligaro, R. Petrella, and M. Sterpellone, "Sensorless control for IPMSM using PWM excitation: Analytical developments and implementation issues," in *2011 Symposium on Sensorless Control for Electrical Drives (SLED)*, 2011, pp. 64 –73.

[37] S. Calligaro, R. Petrella, and S. Bolognani, "Sensorless quasi-standstill and very low-speed position detection in non-salient PMSMs based on current injection and back-EMF observer," in *2012 Symposium on Sensorless Control for Electrical Drives (SLED)*, 2012, pp. 138 –145.

[38] Y. Yoon, S. Sul, S. Morimoto, and K. Ide, "High bandwidth sensorless algorithm for AC machines based on square-wave type voltage injection," in *IEEE Energy Conversion Congress and Exposition, 2009. ECCE 2009*, 2009, pp. 2123 –2130.

[39] M. J. Corley and R. D. Lorenz, "Rotor position and velocity estimation for a salient-pole permanent magnet synchronous machine at standstill and high speeds," *IEEE Transactions on Industry Applications*, vol. 34, no. 4, pp. 784 – 789, Aug. 1998.

[40] M. J. Corley and R. D. Lorenz, "Rotor position and velocity estimation for a salient-pole permanent magnet synchronous machine at standstill and high speeds," *IEEE Transactions on Industry Applications*, vol. 34, no. 4, pp. 784 – 789, Aug. 1998.

[41] D. Raca, P. Garcia, D. Reigosa, F. Briz, and R. Lorenz, "A comparative analysis of pulsating vs. rotating vector carrier signal injection-based sensorless control," in *Twenty-Third Annual IEEE Applied Power Electronics Conference and Exposition, 2008. APEC 2008*, 2008, pp. 879 –885.

[42] M. Schroedl, "Sensorless control of AC machines at low speed and standstill based on the INFORM method," in *, Conference Record of the 1996 IEEE Industry Applications Conference, 1996. Thirty-First IAS Annual Meeting, IAS '96*, 1996, vol. 1, pp. 270 –277 vol.1.

[43] S. Sato, H. Iura, K. Ide, and S.-K. Sul, "Three years of industrial experience with sensorless ipmsm drive based on high frequency injection method," in *2011 Symposium on Sensorless Control for Electrical Drives (SLED)*, 2011, pp. 74 –79.

[44] S.-C. Yang and R. D. Lorenz, "Surface permanent magnet synchronous machine position estimation at low speed using eddy-current-reflected asymmetric resistance," *IEEE Transactions on Power Electronics*, vol. 27, no. 5, pp. 2595 –2604, May 2012.

[45] P. Garcia, D. Reigosa, F. Briz, C. Blanco, and J. M. Guerrero, "Sensorless control of surface permanent magnet synchronous machines using the high frequency resistance," in *2011 IEEE Energy Conversion Congress and Exposition (ECCE)*, 2011, pp. 2709 –2716.

[46] P. Garcia, F. Briz, D. Reigosa, C. Blanco, and J. M. Guerrero, "On the use of high frequency inductance vs. high frequency resistance for sensorless control of

AC machines," in *2011 Symposium on Sensorless Control for Electrical Drives (SLED)*, 2011, pp. 90 –95.

[47] S.-C. Yang and R. D. Lorenz, "Comparison of resistance-based and inductance-based self-sensing controls for surface permanent-magnet machines using high-frequency signal injection," *IEEE Transactions on Industry Applications*, vol. 48, no. 3, pp. 977 –986, Jun. 2012.

[48] J.-M. Kim and S.-K. Sul, "Speed control of interior permanent magnet synchronous motor drive for the flux weakening operation," *IEEE Transactions on Industry Applications*, vol. 33, no. 1, pp. 43 –48, Feb. 1997.

[49] H. Kim, M. C. Harke, and R. D. Lorenz, "Sensorless control of interior permanent-magnet machine drives with zero-phase lag position estimation," *IEEE Transactions on Industry Applications*, vol. 39, no. 6, pp. 1726 – 1733, Dec. 2003.

[50] F. Parasiliti, R. Petrella, and M. Tursini, "Sensorless speed control of salient rotor PM synchronous motor based on high frequency signal injection and Kalman filter," in *Proceedings of the 2002 IEEE International Symposium on Industrial Electronics, 2002. ISIE 2002*, 2002, vol. 2, pp. 623 – 628 vol.2.

[51] S. Shinnaka, "A New Speed-Varying Ellipse Voltage Injection Method for Sensorless Drive of Permanent-Magnet Synchronous Motors With Pole Saliency - New PLL Method Using High-Frequency Current Component Multiplied Signal," *IEEE Transactions on Industry Applications*, vol. 44, no. 3, pp. 777 –788, Jun. 2008.

[52] J.-H. Jang, S.-K. Sul, J.-I. Ha, K. Ide, and M. Sawamura, "Sensorless drive of surface-mounted permanent-magnet motor by high-frequency signal injection based on magnetic saliency," *IEEE Transactions on Industry Applications*, vol. 39, no. 4, pp. 1031 – 1039, Aug. 2003.

[53] M. Linke, R. Kennel, and J. Holtz, "Sensorless position control of permanent magnet synchronous machines without limitation at zero speed," in *IECON 02 [Industrial Electronics Society, IEEE 2002 28th Annual Conference of the]*, 2002, vol. 1, pp. 674 – 679 vol.1.

[54] S. Shinnaka, "New 'mirror-phase vector control' for sensorless drive of permanent-magnet synchronous motor with pole saliency," *IEEE Transactions on Industry Applications*, vol. 40, no. 2, pp. 599 – 606, Apr. 2004.

[55] J.-I. Ha, M. Ohto, J.-H. Jang, and S.-K. Sul, "Design and selection of AC machines for saliency-based sensorless control," in *Industry Applications*

Conference, 2002. 37th IAS Annual Meeting. Conference Record of the, 2002, vol. 2, pp. 1155 –1162 vol.2.

[56] F. Briz, M. W. Degner, P. Garcia, and R. D. Lorenz, "Comparison of saliency-based sensorless control techniques for AC machines," *IEEE Transactions on Industry Applications*, vol. 40, no. 4, pp. 1107 – 1115, Aug. 2004.

[57] D. Raca, P. Garcia, D. D. Reigosa, F. Briz, and R. D. Lorenz, "Carrier-Signal Selection for Sensorless Control of PM Synchronous Machines at Zero and Very Low Speeds," *IEEE Transactions on Industry Applications*, vol. 46, no. 1, pp. 167 –178, Feb. 2010.

[58] N. Bianchi, S. Bolognani, J.-H. Jang, and S.-K. Sul, "Comparison of PM Motor Structures and Sensorless Control Techniques for Zero-Speed Rotor Position Detection," *IEEE Transactions on Power Electronics*, vol. 22, no. 6, pp. 2466 –2475, Nov. 2007.

[59] Y. Li, Z. Q. Zhu, D. Howe, C. M. Bingham, and D. A. Stone, "Improved Rotor-Position Estimation by Signal Injection in Brushless AC Motors, Accounting for Cross-Coupling Magnetic Saturation," *IEEE Transactions on Industry Applications*, vol. 45, no. 5, pp. 1843 –1850, Oct. 2009.

[60] P. Guglielmi, M. Pastorelli, and A. Vagati, "Cross-Saturation Effects in IPM Motors and Related Impact on Sensorless Control," *IEEE Transactions on Industry Applications*, vol. 42, no. 6, pp. 1516 –1522, Dec. 2006.

[61] D. D. Reigosa, P. Garcia, D. Raca, F. Briz, and R. D. Lorenz, "Measurement and Adaptive Decoupling of Cross-Saturation Effects and Secondary Saliencies in Sensorless Controlled IPM Synchronous Machines," *IEEE Transactions on Industry Applications*, vol. 44, no. 6, pp. 1758 –1767, Dec. 2008.

[62] Y. Hua, G. M. Asher, M. Sumner, and Q. Gao, "Sensorless Control of Surface Mounted Permanent Magnetic Machine Using the Standard Space Vector PWM," in *Conference Record of the 2007 IEEE Industry Applications Conference, 2007. 42nd IAS Annual Meeting*, 2007, pp. 661 –667.

[63] Y. Hua, M. Sumner, G. Asher, and Q. Gao, "Sensorless control for a PM machine with reduced current distortion using space vector PWM excitation," in *13th European Conference on Power Electronics and Applications, 2009. EPE '09*, 2009, pp. 1 –10.

[64] R. Raute, C. Caruana, J. Cilia, C. S. Staines, and M. Sumner, "A zero speed operation sensorless PMSM drive without additional test signal injection," in

2007 European Conference on Power Electronics and Applications, 2007, pp. 1 –10.

[65] M. A. Vogelsberger, S. Grubic, T. G. Habetler, and T. M. Wolbank, "Using PWM-Induced Transient Excitation and Advanced Signal Processing for Zero-Speed Sensorless Control of AC Machines," *IEEE Transactions on Industrial Electronics*, vol. 57, no. 1, pp. 365 –374, Jan. 2010.

[66] A. Faggion and S. Bolognani, "A new proposal of rotor position estimation in IPM motor drives based on PWM current harmonics," in *2010 First Symposium on Sensorless Control for Electrical Drives (SLED)*, 2010, pp. 86 – 92.

[67] J. Holtz and J. Juliet, "Sensorless acquisition of the rotor position angle of induction motors with arbitrary stator windings," *IEEE Transactions on Industry Applications*, vol. 41, no. 6, pp. 1675 – 1682, Dec. 2005.

[68] W. Rogowsky and W. Steinhaus, *Die messung der megnetische spannung*. 1912.

[69] J. Cooper, "On the high-frequency response of a Rogowski coil," *Journal of Nuclear Energy. Part C, Plasma Physics, Accelerators, Thermonuclear Research*, vol. 5, no. 5, pp. 285–289, Jan. 1963.

[70] W. F. Ray and R. M. Davis, "Wide bandwidth Rogowski current transducers : Part 1 - The Rogowski coil," *EPE Journal*, pp. 51–59, Mar-1993.

[71] M. M. Bech, F. Blaabjerg, and J. K. Pedersen, "Random modulation techniques with fixed switching frequency for three-phase power converters," *IEEE Transactions on Power Electronics*, vol. 15, no. 4, pp. 753 –761, Jul. 2000.

[72] R. Leidhold, "Position Sensorless Control of PM Synchronous Motors Based on Zero-Sequence Carrier Injection," *IEEE Transactions on Industrial Electronics*, vol. 58, no. 12, pp. 5371 –5379, Dec. 2011.

[73] R. Leidhold and P. Mutschler, "Sensorless position detection in PM synchronous motors by injecting a high-frequency zero-sequence carrier," in *13th European Conference on Power Electronics and Applications, 2009. EPE '09*, 2009, pp. 1 –10.

[74] M. Eskola and H. Tuusa, "Sensorless control of salient pole PMSM using a low-frequency signal injection," in *2005 European Conference on Power Electronics and Applications*, 2005, p. 10 pp. –P.10.

[75] D. Basic, F. Malrait, and P. Rouchon, "Initial rotor position detection in PMSM based on low frequency harmonic current injection," in *Power*

Electronics and Motion Control Conference (EPE/PEMC), 2010 14th International, 2010, pp. T4–1 –T4–7.

[76] D. Basic, F. Malrait, and P. Rouchon, "Current Controller for Low-Frequency Signal Injection and Rotor Flux Position Tracking at Low Speeds," *IEEE Transactions on Industrial Electronics*, vol. 58, no. 9, pp. 4010 –4022, Sep. 2011.

[77] J. S. Kim and S. K. Sul, "New stand-still position detection strategy for PMSM drive without rotational transducers," in *Applied Power Electronics Conference and Exposition, 1994. APEC '94. Conference Proceedings 1994., Ninth Annual*, 1994, pp. 363 –369 vol.1.

[78] D.-W. Chung, J.-K. Kang, and S.-K. Sul, "Initial rotor position detection of PMSM at standstill without rotational transducer," in *Electric Machines and Drives, 1999. International Conference IEMD '99*, 1999, pp. 785 –787.

[79] M. Tursini, R. Petrella, and F. Parasiliti, "Initial rotor position estimation method for PM motors," *IEEE Transactions on Industry Applications*, vol. 39, no. 6, pp. 1630 – 1640, Dec. 2003.

[80] S. Bolognani, S. Calligaro, R. Petrella, and F. Pogni, "Flux-weakening in IPM motor drives: Comparison of state-of-art algorithms and a novel proposal for controller design," in *Proceedings of the 2011-14th European Conference on Power Electronics and Applications (EPE 2011)*, 2011, pp. 1 –11.

[81] S. Bolognani, S. Calligaro, and R. Petrella, "Optimal voltage feed-back flux-weakening control of IPMSM," in *IECON 2011 - 37th Annual Conference on IEEE Industrial Electronics Society*, 2011, pp. 4170 –4175.

[82] S. Bolognani, S. Calligaro, and R. Petrella, "Adaptive flux-weakening controller for IPMSM drives," in *2011 IEEE Energy Conversion Congress and Exposition (ECCE)*, 2011, pp. 2437 –2444.

[83] T. M. Jahns, "Flux-Weakening Regime Operation of an Interior Permanent-Magnet Synchronous Motor Drive," *IEEE Transactions on Industry Applications*, vol. IA-23, no. 4, pp. 681 –689, Jul. 1987.

[84] S. Morimoto, K. Hatanaka, Y. Tong, Y. Takeda, and T. Hirasa, "Servo drive system and control characteristics of salient pole permanent magnet synchronous motor," *IEEE Transactions on Industry Applications*, vol. 29, no. 2, pp. 338 –343, Apr. 1993.

[85] N. Bianchi and T. M. Jahns, "Design, Analysis and control of interior PM Synchronous Machines," *Tutorial IEEE Course Note, IEEE IAS Annual Meeting*, Oct. 2004.

[86] J. Wai and T. M. Jahns, "A new control technique for achieving wide constant power speed operation with an interior PM alternator machine," in *Conference Record of the 2001 IEEE Industry Applications Conference, 2001. Thirty-Sixth IAS Annual Meeting*, 2001, vol. 2, pp. 807 –814 vol.2.

[87] T.-S. Kwon and S.-K. Sul, "Novel Antiwindup of a Current Regulator of a Surface-Mounted Permanent-Magnet Motor for Flux-Weakening Control," *IEEE Transactions on Industry Applications*, vol. 42, no. 5, pp. 1293 –1300, Oct. 2006.

[88] T.-S. Kwon, G.-Y. Choi, M.-S. Kwak, and S.-K. Sul, "Novel Flux-Weakening Control of an IPMSM for Quasi-Six-Step Operation," *IEEE Transactions on Industry Applications*, vol. 44, no. 6, pp. 1722 –1731, Dec. 2008.

[89] T.-S. Kwon, S.-K. Sul, L. Alberti, and N. Bianchi, "Design and Control of an Axial-Flux Machine for a Wide Flux-Weakening Operation Region," *IEEE Transactions on Industry Applications*, vol. 45, no. 4, pp. 1258 –1266, Aug. 2009.

[90] N. V. Olarescu, M. Weinmann, S. Zeh, and S. Musuroi, "Novel flux weakening control algorithm for PMSMS," in *International Conference on Power Engineering, Energy and Electrical Drives, 2009. POWERENG '09*, 2009, pp. 123 –127.

[91] B.-H. Bae and S.-K. Sul, "A compensation method for time delay of full-digital synchronous frame current regulator of PWM AC drives," *IEEE Transactions on Industry Applications*, vol. 39, no. 3, pp. 802 – 810, Jun. 2003.

[92] Y.-D. Yoon, W.-J. Lee, and S.-K. Sul, "New flux weakening control for high saliency interior permanent magnet synchronous machine without any tables," in *2007 European Conference on Power Electronics and Applications*, 2007, pp. 1 –7.

[93] N. Bianchi, S. Bolognani, and M. Zigliotto, "High-performance PM synchronous motor drive for an electrical scooter," *IEEE Transactions on Industry Applications*, vol. 37, no. 5, pp. 1348 –1355, Oct. 2001.

[94] Z. Lei, X. Shan, W. Xuhui, L. Yaohua, and K. Liang, "A new deep field-weakening strategy of IPM machines based on single current regulator and

voltage angle control," in *2010 IEEE Energy Conversion Congress and Exposition (ECCE)*, 2010, pp. 1144 –1149.

[95] Y. Zhang, L. Xu, M. K. Güven, S. Chi, and M. Illindala, "Experimental Verification of Deep Field Weakening Operation of a 50-kW IPM Machine by Using Single Current Regulator," *IEEE Transactions on Industry Applications*, vol. 47, no. 1, pp. 128 –133, Feb. 2011.

[96] S. Chi and L. Xu, "A special flux-weakening control scheme of pmsm - incorporating and adaptive to wide-range speed regulation," in *Power Electronics and Motion Control Conference, 2006. IPEMC 2006. CES/IEEE 5th International*, 2006, vol. 2, pp. 1 –6.

Acknowledgments

Thanks to...

Curiosity and technology.

Roberto (prof. Petrella). He took me as a trainee and helped me find my trade.
It's no small matter.

People studying and working with us in the lab and in companies. I had the chance to breathe the smell of a good old shop, a place for working and living (laughing when it's all OK, and getting angry when things don't work).

All friends. Especially Paolo "TaboPa", who led me to broken English ("Laughing and calling people to laugh!", [1]).

My family, they supported me all time long, and especially when I decided to start my PhD.

My father, example of dedication and inventiveness.

Martina, "holy woman", [2]. Walking at her side made heavy things lighter and joyful ones richer. It's not easy to be an engineer's wife, but it's even worse if he's a PhD student!

The Lord, who liked me to reach this point.

[1] N. Vattolo "Aphorisms", *some time ago.*
[2] R. Petrella, *about an hour before discussing my M.S. thesis*, April 2008.

Ringraziaments

J dîs grazie...

Ae tecniche e ae semence di curiôs.

A Roberto (el prof. Petrella, ma dopo agns mi sint di dai dal tu). Mi à cjapât su di garzon e mi à judât a cjatâ el gno mistîr. Nol è pôc.

A ducj chêi ch'e an studiât e lavorât cun nô, in laboratori e tes aziendes. J ai podût respirâ chel ajar di buteghe di une volte, un puest par lavorâ, ma ancje par vîvi (ridi quant ch'e vâ drete, e inrabiâsi quant che nol funzione nie).

A ducj i amîs. Specialmentri a Paolo "Chinchine", che mi à obleât a scrivi par ingles macaronic ("Rîdi e clamâ dongje înt a rîdi!", [1]).

Ai mêi, che mi an sapuartât, scoltât e sburtât dut el timp, ancje e soredut quant ch'j ai decidût di tacâ el dotorât.

A gno pari, esempli di dedizion e di inventive.

A Martina, "sante femine", [2]. Cjaminâ dongje di je al à sliserît les robes pesantes e ingrandît chês bieles. Nol è facil sei le femine di un inzegnîr, Diu nus vuardi s'al fâs el dotorât!

Al Signôr, che al à volût fâmi rivâ fin chi.

[1] N. Vattolo "Frases famôses", *cuisà nie trop timp indaûr*.
[2] R. Petrella, *circhе un'ore prin di presentâ le tesi dai cinc agns*, avrîl 2008.